



Politecnico  
di Torino

ScuDo  
Scuola di Dottorato ~ Doctoral School  
WHAT YOU ARE, TAKES YOU FAR

Doctoral Dissertation  
Doctoral Program in Civil and Environmental Engineering (33<sup>th</sup> Cycle)

# Application of Virtual Element Methods for geomechanical assessment of fluid storage in deep geological formations

By

**Cristina Serazio**

\*\*\*\*\*

## Supervisor(s):

Prof. Francesca Verga, Supervisor  
Prof. Stefano Berrone, Co-Supervisor

## Doctoral Examination Committee:

Prof. Claudio Alimonti, Referee, Università di Roma “La Sapienza”  
Prof. Corrado Fidelibus, Università del Salento  
Prof. Paolo Macini, Referee, Università di Bologna  
Prof. Vera Rocca, Politecnico di Torino  
Prof. Dario Viberti, Politecnico di Torino

Politecnico di Torino  
2021

## **Declaration**

I hereby declare that, the contents and organization of this dissertation constitute my own original work and does not compromise in any way the rights of third parties, including those relating to the security of personal data.

Cristina Serazio

2021/07/29

\* This dissertation is presented in partial fulfillment of the requirements for  
**Ph.D. degree** in the Graduate School of Politecnico di Torino (ScuDo).





## **Abstract**

Renewable sources are considered key to decarbonize energy systems and reduce dependency on fossil fuels. However, despite the availability of solar energy and wind power, technologies relying on these sources are not fully viable yet due to their unstable and intermittent nature. Therefore, solutions to match the high-frequency variation of renewable energy production with the electricity demand are fundamental for energy transition. In this view, large-scale energy storage can provide means for balancing supply and demand, increasing energy security, promoting a better management of the grid and allowing convergence towards a low carbon economy. To this end, chemical storage is currently under investigation. Chemical storage implies transforming electrical power into chemical energy in the form of H<sub>2</sub>. One way to ensure large-scale storage of chemical energy is to use the storage capacity of deep geological formations. Furthermore, long-term CO<sub>2</sub> underground storage is regarded as an essential mitigation option to reduce greenhouse gases in the atmosphere and contrast climate change. Temporary underground storage is also envisioned, as a strategy to efficiently match the quantity of captured CO<sub>2</sub> and the quantity of CO<sub>2</sub> that can be transformed CO<sub>2</sub> into value-added fuels and chemicals. Thus, it is evident that underground storage systems can play a fundamental role in the transition to a more sustainable energy future.

The goal of this research was to apply the recently formalized Virtual Element Method (VEM) to build 3D geomechanical models and address the safety issues associated to fluid storage in deep geological formations, namely rock integrity and compaction/expansion due to fluid withdrawal/injection causing ground level subsidence/rebound. The advantage of using VEM mainly resides in their versatility to

reproduce complex geometries while maintaining a certain computational “simplicity” without losing solution accuracy.

The development of the project required that knowledge and skills on numerical analysis were merged with competences and experience gained on fluid storage in underground formations. The main tasks were (1) the validation of the 3D VEM library (*GeDim+VemElast*) developed for the solution of boundary differential problems that describe the stress-strain behavior of deep formations subject to underground storage operation in the linear-elastic-domain; (2) the integration of stratigraphic and fault surfaces deriving from seismic interpretation within the tetrahedral discretization process of the investigated geological volumes, which was achieved by developing and implementing an effective triangulation algorithm implemented; (3) the grid construction using simplexes (tetrahedral cells), which also represented the preparatory step for the construction of generic polyhedral grids obtained through gluing algorithms.

The libraries necessary to generate the models were coded in an opensource environment (*QTCreator + CMake + MinGW*) and integrated in a unitary product which support the cross-compiling between MS Windows and GNU/Linux.

Extensive validation tests of the new model to calculate compaction/expansion due to fluid withdrawal/injection and corresponding ground level subsidence/rebound in the linear-elastic domain were performed. First simplified cases were considered. Then, tests on realistic models of the Italian Adriatic offshore and of the Po Plain panorama. The simulation results proved very satisfactory and consistent with the ones obtained by a commercial FEM solver dedicated to geomechanical simulations and typically used in the oil&gas field. Validation tests were mainly performed in the linear-elastic domain because the technical literature consistently shows that the formations behave elastically. However, tests were also performed in the elasto-plastic domain. Convergence issues highlighted the need to modify the iterative algorithm implemented to solve the constitutive problem to obtain consistent results under any investigated scenario.



# Contents

Introduction .....	1
Theoretical Background .....	7
Stress and strain state in a continuous medium .....	7
Linear momentum balance .....	9
Effective stress.....	10
Elasto-plastic constitutive models .....	11
The Mohr-Coulomb criterion.....	17
Safety Factor .....	20
Stress state of the lithosphere .....	23
Induced subsidence and rebound .....	25
Analytical and semi-analytical approaches.....	27
Numerical model .....	30
Model construction .....	30
Static model.....	31
Static model at a regional scale.....	34
Dynamic model .....	34
Mechanical model .....	36
FEM and VEM .....	37
Gridding.....	40
Corner point gridding parser.....	41
Unstructured grid construction workflow.....	45
Stratigraphical surface triangulation .....	51
Fault surface triangulation .....	62
Lateral surface triangulation .....	67

Intersection between faults and stratigraphic surfaces.....	68
Domain vertical refinement .....	72
Region identification and characterization .....	74
Validation test in the linear-elastic domain .....	76
VEM formalization for the solution of the elastic problem.....	76
Implementation details.....	78
Validation .....	79
Disk-shaped reservoir model .....	79
Offshore Adriatic model .....	87
UGS model.....	104
Validation test in the elasto-plastic domain.....	114
Return-mapping algorithms .....	116
Validation .....	119
Analytical scaled model.....	119
Disk-shaped reservoir model .....	122
Underground Natural Gas Storage Test.....	127
Code development and GUI prototyping for model validation and data analysis .....	134
Conclusion and future development.....	146
Appendix .....	150
References .....	172



# List of Figures

Figure 1: stress tensor components representations on a rectangular parallelepiped.....	8
Figure 2: constitutive models of a continuum medium: (a) linear elastic (b) non-linear elastic (c) elastic with hysteresis (d) elasto-plastic.....	12
Figure 3: stress-strain behavior of a geomaterial under compressive strength: (a) strain softening (b) strain hardening.....	13
Figure 4: sketch of yielding and failure surfaces .....	14
Figure 5: creep phenomenon: time-dependent behavior of the continuous medium .....	17
Figure 6: Maxwell model (a); Kelvin model (b); Burgers model(c).....	17
Figure 7: (a) Mohr-Coulomb Yield criterion in the plane $\sigma' - \tau$ . (b) sketch of the rock plug subjected to loading. (c) Mohr-Coulomb Yield Criterion in the $\sigma' \mathbf{1} - \sigma \mathbf{3}'$ plane.....	18
Figure 8: (a) representation of the yield function defined by the Mohr-Coulomb criterion in the space of the principal stresses. As an example, $c = 2.5$ bar and $\varphi = 25^\circ$ were imposed. In (b) projection of the function on the deviatoric plane .....	19
Figure 9: failure envelope for the Mohr-Coulomb criterion .....	20
Figure 10: shear failure according to Mohr-Coulomb failure criteria.....	21
Figure 11: tensile stress cut-off on the Mohr-Coulomb failure criteria .....	22
Figure 12: $\sigma' - \tau$ Mohr's circle representation of effective stress: (a) pressure decreasing and (b) pressure increasing effects .....	22
Figure 13: sketch of fault types (Fjær et al., 2008) .....	24
Figure 14: sketch of induced compaction/expansion as a consequence of withdrawal/injection of fluids in deep geological formations .....	25
Figure 15: corner-point grid cell (yellow) defined through the specification of eight vertices (red bullets) identified by the $ijk$ index triplet. Red lines represent the pillars. ....	42
Figure 16: example of pillar gridding model with a single fault and layers given by sinusoidal surfaces (fault faces are marked in red). ....	43

---

Figure 17: cells splitting procedure: (a) original hexahedral cell. (b) polyhedral cell obtained by triangulation of not planar faces through insertion of face barycenter. (c) tetrahedral decomposition. ....	43
Figure 18: workflow of the corner-grid parser.....	44
Figure 19: workflow for the grid generation.....	46
Figure 20: main steps of Surface Reconstruction of Geological Surface from Point Cloud (Serazio et al., 2021).....	47
Figure 21: sequence of stratigraphic surfaces defining the model domain (Step 1). ....	47
Figure 22: triangulation of the reference stratigraphic surface (red) and projection of the triangulation on the underlying surfaces (Step 3 and Step 4)....	48
Figure 23: triangulation of the lateral faces (Step 7). In evidence the intersection between the lateral faces and the intermediate stratigraphic surfaces (a). Section of the model orthogonal to the Y direction (b). ..	49
Figure 24: sectional view of the tetrahedralized computing domain (Step 13). The stratigraphic surfaces that represent the constraints in the process of generating the 3D grid are highlighted. ....	50
Figure 25: sectional view of the tetrahedralized computing domain. Regions identified by the <i>Tetgen</i> library (Step 12) are highlighted with different colors. ..	50
Figure 26: stratigraphic surface reconstruction from 3D point cloud .....	51
Figure 27: detail of the XY-plane point cloud projection (black). Points result equally spaced and aligned with diagonals. the initial <i>Convex Hull</i> and corresponding <i>Concave Hull</i> , in green and red, respectively. ....	53
Figure 28: detail of the XY-plane point cloud projection. The colormap refers to edge ratio of the triangles of the triangulation constrained to the Convex Hull (red nodes). The mean value of the edge length distribution it is approximately 14. Triangles external to the final <i>Concave Hull</i> (green) show edge-ratio that deviate from the mean becoming candidates to be removed from the triangulation. ....	53
Figure 29: <i>case Surf Top</i> - detail of the XY-plane point cloud projection: initial <i>Convex Hull</i> constrained triangulation ( <i>red</i> ) (a) and corresponding <i>Concave Hull</i> constrained triangulation ( <i>green</i> ) (b) (Serazio et al., 2021).....	55
Figure 30: <i>case Surf Top</i> - original Cartesian coordinate system comparison between the initial <i>Convex Hull</i> constrained triangulation ( <i>red</i> ) (a) and	

corresponding *Concave Hull* constrained triangulation (*green*) (b) (Serazio et al., 2021).....55

Figure 31: *case Erosional 50* - detail of the XY-plane point cloud projection: initial *Convex Hull* constrained triangulation (*red*) (a) and corresponding *Concave Hull* constrained triangulation (*green*) (b) (Serazio et al., 2021).....56

Figure 32: *case Erosional 50* - original Cartesian coordinate system comparison between the initial *Convex Hull* constrained triangulation (*red*) (a) and corresponding *Concave Hull* constrained triangulation (*green*) (b) (Serazio et al., 2021).....56

Figure 33: XY-plane projections of stratigraphic surface point cloud. In (a) the surface need extension and the outer boundary need to be identified: in red points at high-resolution and in gray the area occupied by the extended stratigraphic surface. In (b) the uploaded surface does not need extension. Conversely the high-resolution zone needs to be identified (points in red). In blue the boundary polygons defined in workflow in Figure 26, step 4-5, a and b, respectively.....57

Figure 34: detail of the triangulation of an extended stratigraphic surface: measure of the quality mesh is given by the minimum angle of each triangle. Triangulation results from the 30° minimum angle constraints in the *Triangle* library routine. ....58

Figure 35: resulting triangulation of stratigraphic surface.....59

Figure 36: comparison of two triangulation strategies. Above (a) a high level of detail is preserved only on in the portion of interest of the investigation domain and extrapolation of depth values is applied. Below (b) a high level of detail is guaranteed for the entire extension of the geomechanical model and interpolation algorithm is applied outside the high-resolution zone. ....60

Figure 37: comparison between the stratigraphic surface extended obtained from the interpolation phase (grey) and the triangulation of the interpolated stratigraphic surface point cloud (blue). In the graph an amplification factor of 2 in the Z direction was applied to appreciate differences.....61

Figure 38: intersection P 'on the XY plane between the *Convex Hull* (blue line) of the surface point cloud and the segment that connects the center of CH (C) and the point P external to CH.....61

Figure 39: fault surface reconstruction from 3D point cloud.....62

Figure 40: (a) point cloud in $\mathbb{R}^3$ , representative of a fault surface. (b) Intersection of the point cloud with the BFP (grey) in $\mathbb{R}^3$ (c) Point cloud projection on the BFP. (Serazio et al., 2021) .....	63
Figure 41: "digging" algorithm evolution example. Boundary polygons corresponding to five steps are shown. The initial <i>Convex Hull</i> (red) of 40 nodes, iterations at 100, 150, 200 nodes and the final <i>Concave Hull</i> (green) of 216 nodes. (Serazio et al., 2021) .....	64
Figure 42: <i>case Fault 12</i> - XY-plane point cloud projection: initial <i>Convex Hull</i> constrained triangulation ( <i>red</i> ) (a) and corresponding <i>Concave Hull</i> constrained triangulation ( <i>green</i> ) (b) (Serazio et al., 2021). .....	65
Figure 43: <i>case Fault 12</i> - original Cartesian coordinate system comparison between the initial <i>Convex Hull</i> constrained triangulation ( <i>red</i> ) (a) and corresponding <i>Concave Hull</i> constrained triangulation ( <i>green</i> ) (b). (Serazio et al., 2021). .....	65
Figure 44: <i>case H53</i> - XY-plane point cloud projection: initial <i>Convex Hull</i> constrained triangulation ( <i>red</i> ) (a) and corresponding <i>Concave Hull</i> constrained triangulation ( <i>green</i> ) (b)(Serazio et al., 2021) .....	66
Figure 45: <i>case H53</i> - original Cartesian coordinate system comparison between the initial <i>Convex Hull</i> constrained triangulation ( <i>red</i> ) (a) and corresponding <i>Concave Hull</i> constrained triangulation ( <i>green</i> ) (b) (Serazio et al., 2021). .....	66
Figure 46: lateral surface triangulation workflow .....	67
Figure 47: triangulation of the lateral faces of the model .....	68
Figure 48: stratigraphic surface sample (orange in Figure 22) used to illustrate the evolution of triangulation afterward the identification of intersections with fault surfaces. .....	70
Figure 49: spatial position of the fault surfaces (in red and blue) with respect to the sample stratigraphic surface.....	70
Figure 50: updating of the stratigraphic surface triangulation after the identification of intersections with the red fault surface of Figure 49. Added points and segments with respect to the starting triangulation are highlighted in red.....	71
Figure 51: updating of the stratigraphic surface triangulation after the identification of intersections with the blue fault surface of Figure 49. Added points and segments with respect to the starting triangulation are highlighted in red.....	71

Figure 52: conforming triangulation resulting from the identification of intersections between the sample stratigraphic surface and the fault surfaces.....	72
Figure 53: vertical discretization of the geomechanical model constrained by the depth values assigned to each surface of the model (white boxes).....	74
Figure 54: sketch of the model defined for the comparison of VEM numerical solution against Geertsma analytical one. (a) disk-shaped reservoir in red and black boundary of the refinement cylinder. (b) cells of the domain interested by a vertical displacement higher than 0.5 cm in absolute value .....	80
Figure 55: section orthogonal to Y-axis of the volume discretization with unstructured grid (a) and corner-point gird (b). The color map refers to the cell volumes ( $m^3$ ).....	81
Figure 56: section orthogonal to Y-axis of the volume discretization with unstructured grid (a) and corner-point gird (b). The color map refers to the cell quality (edge ratio).....	81
Figure 57: section orthogonal to Y-axis of the two grid models: on the left (a) unstructured grid for VEM simulation and, on the right (b), corner-point grid for FEM simulation, respectively. In red the reservoir where pore pressure variation is imposed.....	82
Figure 58: top view of the two grid models: on the left (a) unstructured grid for VEM simulation and, on the right (b), corner-point grid for FEM simulation, respectively. In both grids a refinement zone in correspondence of the subsidence bowl was defined.....	82
Figure 59: (a) top view of the model. The colormap refers to the subsidence expressed in cm. (b) comparison of the subsidence along the dotted red segment HH' in (a).....	83
Figure 60: (a) top view of the model. The colormap refers to the displacement along x-axis expressed in cm. (b) comparison of the subsidence along the dotted red segment HH' in (a). .....	84
Figure 61: (a) top view of the model. The colormap refers to $\Delta\sigma_{xx}$ , expressed in MPa, induced by the imposed $\Delta p$ . (b) comparison of the induced $\Delta\sigma_{xx}$ along the dotted red segment HH' in (a). .....	84
Figure 62: (a) top view of the model. The colormap refers to $\Delta\sigma_{yy}$ , expressed in MPa, induced by the imposed $\Delta p$ . (b) comparison of the induced $\Delta\sigma_{yy}$ along the dotted red segment HH' in (a). .....	85

---

Figure 63: (a) section orthogonal to Y-axis of the model. The colormap refers to the displacement along z-axis expressed in cm. (b) comparison of the z-axis displacement along the dotted red segment OO' in (a) .....	85
Figure 64: (a) section orthogonal to Y-axis of the model. The colormap refers to $\Delta\sigma_{xx}$ , expressed in MPa, induced by the imposed $\Delta p$ . (b) comparison of the induced $\Delta\sigma_{xx}$ along the dotted red segment HH' in (a). ....	86
Figure 65: (a) section orthogonal to Y-axis of the model. The colormap refers to $\Delta\sigma_{zz}$ , expressed in MPa, induced by the imposed $\Delta p$ . (b) comparison of the induced $\Delta\sigma_{zz}$ along the dotted red segment HH' in (a).....	86
Figure 66: Structural top of the reservoir.....	88
Figure 67: zoning of the geomechanical model (thicknesses amplification factor of 5 applied in the z-direction).....	89
Figure 68: geomechanical classes defined in the model (thicknesses amplification factor of 5 applied in the z-direction) .....	90
Figure 69: sectional view of the pressure map @ 23/03/2022 model (thicknesses amplification factor of 5 applied in the z-direction). ....	91
Figure 70: domain discretization by pillar-gridding: (a) top view and (b) 3D view. Reservoir cells are highlighted in green. In (b) a thicknesses amplification factor of 5 applied in the z-direction) to highlight the progression of the discretization.....	91
Figure 71: domain discretization by unstructured grid construction workflow: (a) top view and (b) 3D view. Reservoir cells are highlighted in green. In (b) a thicknesses amplification factor of 5 applied in the z-direction to highlight the progression of the discretization.....	92
Figure 72: surfaces constraining the unstructured grid. Amplification factor of 5 applied in the z-direction. ....	93
Figure 73: vertical section of the defined grid: (a) corner-point grid and (b) unstructured grid. Amplification factor of 5 applied in the z-direction.....	93
Figure 74: region identification from tetrahedralization process. Amplification factor of 5 applied in the z-direction.....	94
Figure 75: Young's modulus assignment. Amplification factor of 5 applied in the z-direction. ....	95
Figure 76: reservoir's cells identification.....	95

Figure 77: top view of the reservoir cells: (a) corner-point hexahedral grid, (b) polyederal grid obtained by adding a node in correspondence of the barycenter of not planar faces in (a), (c) tetrahedral grid from decomposition of polyhedron in (b).	96
.....	96
Figure 78: top view of the model. Colormap refers to the z-component of the FEM displacement. It ranges between 45mm and 10 mm.....	97
Figure 79: y-axis orthogonal section of the model. Colormap refers to the z-component of the FEM displacement. It ranges between 45mm and 10 mm.....	97
Figure 80: Top view of the reservoir cells. The colormap refers to the z-component displacement relative discrepancy between FEM reference solution and VEM solution calculated on the original hexahedral corner-point grid (a), in the “spit faces” grid (b) and in the “refine reservoir” grid. .....	99
Figure 81: top view of the model. The colormap refers to the z-component displacement relative discrepancy between FEM reference solution and VEM solution calculated on the original hexahedral corner-point grid (a), in the “spit faces” grid (b) and in the “refine reservoir” grid. .....	100
Figure 82: y-axis orthogonal section of the model. The colormap refers to the z-component displacement relative discrepancy between FEM reference solution and VEM solution calculated on the original hexahedral corner-point grid (a), in the “spit faces” grid (b) and in the “refine reservoir” grid. .....	101
Figure 83: (a) top view and (b) y-axis orthogonal section of the subsidence bowl identified by the FEM solution calculated on the Corner-Point Grid (surface) and the VEM solution calculated on the Unstructured Grid (wireframe). Amplification factor of 2 applied in the z-direction.....	102
Figure 84: (a) model top-view. Colormap refers to the z-component of displacement (subsidence W) obtained by FEM on the original Corner-Point Grid. (b) Plot along the HH' line shown in (a). Comparison between the reference FEM solution on the corner point grid (hexa) (dotted red) against the VEM solutions calculated on the hexa corner point-grid (green) and on the tetra unstructured grid (blue) is shown.....	102
Figure 85: (a) model top-view. Colormap refers to the x-component of displacement (U) obtained by FEM on the original Corner-Point Grid. (b) Plot along the HH' line shown in (a). Comparison between the reference FEM solution on the corner point grid (hexa) (dotted red) against the VEM solutions calculated on the	

---

hexa corner point-grid (green) and on the tetra unstructured grid (blue) is shown.	103
Figure 86: (a) model top-view. Colormap refers to the y-component of displacement (V) obtained by FEM on the original Corner-Point Grid. (b) Plot along the HH' line shown in (a). Comparison between the reference FEM solution on the corner point grid (hexa) (dotted red) against the VEM solutions calculated on the hexa corner point-grid (green) and on the tetra unstructured grid (blue) is shown.	103
.....	103
Figure 87: UGS dynamic model: 7 superimposed gas pools are simulated. UGS strategy considered 12 wells.	105
Figure 88: gas rate history of the UGS scenario: 10 gas storage cycles of 6 months of production followed by 6 months of injection. A week of closure between two cycles. In red the cycle under analysis.	106
Figure 89: field gas pressure history of the UGS scenario. In red the cycle under analysis.	106
Figure 90: y-axis orthogonal slice of the geomechanical grid. Colored cells represent the reservoir. Amplification factor of 10 applied in the z-direction.	107
Figure 91: (a) top view and (b) y-axis orthogonal section of the subsidence bowl identified by the FEM (surface) and the VEM (wireframe) solution. Amplification factor of 2 applied in the z-direction.	108
Figure 92: (a) model top-view. Colormap refers to the x-component of displacement (U) obtained by FEM at the end of production ( $\Delta p1$ ). (b) Plot along the HH' line shown in (a). Comparison between the reference FEM solution on (dotted red) against the VEM solutions (blue) is shown.	108
.....	108
Figure 93: (a) model top-view. Colormap refers to the y-component of displacement (V) obtained by FEM at the end of production ( $\Delta p1$ ). (b) Plot along the HH' line shown in (a). Comparison between the reference FEM solution on (dotted red) against the VEM solutions (blue) is shown.	109
.....	109
Figure 94: (a) model top-view. Colormap refers to the z-component of displacement (W subsidence) obtained by FEM at the end of production ( $\Delta p1$ ). (b) Plot along the HH' line shown in (a). Comparison between the reference FEM solution on (dotted red) against the VEM solutions (blue) is shown.	109
.....	109
Figure 95: (a) y-axis orthogonal section view of the model. Colormap refers to variation of the xx-effective stress component obtained by FEM at the end of	

production ( $\Delta p_1$ ). (b) Plot along the OO' segment shown in (a). Comparison between the reference FEM solution on (dotted red) against the VEM solutions (blue) is shown.....110

Figure 96: (a) y-axis orthogonal section view of the model. Colormap refers to variation of the zz-effective stress component obtained by FEM at the end of production ( $\Delta p_1$ ). (b) Plot along the OO' segment shown in (a). Comparison between the reference FEM solution on (dotted red) against the VEM solutions (blue) is shown.....110

Figure 97: (a) model Top-view. Colormap refers to the x-component of displacement (U) obtained by FEM at the end of injection ( $\Delta p_2$ ). (b) Plot along the HH' line shown in (a). Comparison between the reference FEM solution on (dotted red) against the VEM solutions (blue) is shown.....111

Figure 98: (a) model Top-view. Colormap refers to the y-component of displacement (V) obtained by FEM at the end of injection ( $\Delta p_2$ ). (b) Plot along the HH' line shown in (a). Comparison between the reference FEM solution on (dotted red) against the VEM solutions (blue) is shown.....111

Figure 99: (a) model Top-view. Colormap refers to the z-component of displacement (W subsidence) obtained by FEM at the end of injection ( $\Delta p_2$ ). (b) Plot along the HH' line shown in (a). Comparison between the reference FEM solution on (dotted red) against the VEM solutions (blue) is shown.....112

Figure 100: (a) y-axis orthogonal section view of the model. Colormap refers to variation of the xx-effective stress component obtained by FEM at the end of injection ( $\Delta p_2$ ). (b) Plot along the OO' segment shown in (a). Comparison between the reference FEM solution on (dotted red) against the VEM solutions (blue) is shown.....112

Figure 101: (a) y-axis orthogonal section view of the model. Colormap refers to variation of the zz-effective stress component obtained by FEM at the end of injection ( $\Delta p_2$ ). (b) Plot along the OO' segment shown in (a). Comparison between the reference FEM solution on (dotted red) against the VEM solutions (blue) is shown.....113

Figure 102: implicit Return-Mapping Algorithm for the solution of the initial value elasto-plastic constitutive problem.....117

Figure 103: qualitative scheme of the Return-Mapping algorithm.....118

---

Figure 104: representation on the deviatoric plane of the flow potential $\Psi$ deriving from the Mohr-Coulomb criterion. Flow vectors normal to the surface are identified by $N$ .....	118
Figure 105: section view (XZ plane) of the pore pressure variation imposed as forcing term.....	119
Figure 106: Comparison between the SS-MC-NP-3D Matlab (red line) and the VEM C++ (blue line) trend of the maximum value of the yield function ( $\Phi$ ) over the entire domain with respect to the load steps .....	121
Figure 107: Comparison between the vertical displacement $W$ (cm) on the XY plane calculated by the SS-MC-NP-3D code (a) and the VEM solver (b).....	121
Figure 108: (a) top view of the model scheme: disk-shaped reservoir (in red) with the identification of the zone (green square) zoomed in (b) , where are shown VEM tetrahedron (green) and FEM hexahedron (blue) cells whose safety factors are compared in Table 9.....	123
Figure 109: (a) model top-view. Colormap refers to the x-component of displacement ( $U$ ) obtained by FEM at the end of injection ( $\Delta p$ ). (b) Plot along the HH' line shown in (a). Comparison between the reference FEM solution on (dotted red) against the VEM solutions (blue) is shown.....	124
Figure 110: (a) model Top-view. Colormap refers to the z-component of displacement ( $W$ rebound) obtained by FEM at the end of production ( $\Delta p$ ). (b) Plot along the HH' line shown in (a). Comparison between the reference FEM solution on (dotted red) against the VEM solutions (blue) is shown. ....	125
Figure 111: (a) y-axis orthogonal section view of the model with a thicknesses amplification factor of 2 applied along the z-direction. Colormap refers to the z-component of displacement ( $W$ rebound) at the end of injection ( $\Delta p$ ). (b) Plot along the OO' segment shown in (a). Comparison between the reference FEM solution on (red) against the VEM solutions (blue) is shown. ....	125
Figure 112: (a) y-axis orthogonal section view of the model with a thicknesses amplification factor of 2 applied along the z-direction. Colormap refers to variation of the xx-effective stress component obtained by FEM at the end of injection ( $\Delta p$ ). (b) Plot along the OO' segment shown in (a). Comparison between the reference FEM solution on (dotted red) against the VEM solutions (blue) is shown. ....	126
Figure 113: (a) y-axis orthogonal section view of the model with a thicknesses amplification factor of 2 applied along the z-direction. Colormap refers to variation of the xx-effective stress component obtained by FEM at the end of injection ( $\Delta p$ ).	

(b) Plot along the OO' segment shown in (a). Comparison between the reference FEM solution on (dotted red) against the VEM solutions (blue) is shown. ....126

Figure 114: Mohr's circle representation of the initial state of stress (blue) and the one assessed after injection (green) in correspondence of the centroid of a disk-shaped reservoir cell. Mohr-Coulomb failure criteria is represented as a black line. ....127

Figure 115: Mohr's circle representation of the state of stress for the selected reservoir cell obtained from VEM solution. Three states are represented: initial (blue), end of primary production (green) and end of injection period (dotted red). Projections on the Mohr-Coulomb failure line are used to evaluate the Safety Factor. ....129

Figure 116: (a) model top-view. Colormap refers to the x-component of displacement ( $U$ ) obtained by FEM at the end of injection ( $\Delta p2$ ). (b) Plot along the HH' line shown in (a). Comparison between the reference FEM solution on (dotted red) against the VEM solutions (blue) is shown.....130

Figure 117: (a) model top-view. Colormap refers to the z-component of displacement ( $W$  subsidence) obtained by FEM at the end of production ( $\Delta p2$ ). (b) Plot along the HH' line shown in (a). Comparison between the reference FEM solution on (dotted red) against the VEM solutions (blue) is shown.....130

Figure 118: (a) y-axis orthogonal section view of the model. Colormap refers to the z-component of displacement ( $W$  subsidence) at the end of injection ( $\Delta p2$ ). (b) Plot along the OO' segment shown in (a). Comparison between the reference FEM solution on (dotted red) against the VEM solutions (blue) is shown. ....131

Figure 119: (a) y-axis orthogonal section view of the model. Colormap refers to variation of the xx-effective stress component obtained by FEM at the end of injection ( $\Delta p2$ ). (b) Plot along the OO' segment shown in (a). Comparison between the reference FEM solution on (dotted red) against the VEM solutions (blue) is shown. ....131

Figure 120: (a) y-axis orthogonal section view of the model. Colormap refers to variation of the zz-effective stress component obtained by FEM at the end of injection ( $\Delta p2$ ). (b) Plot along the OO' segment shown in (a). Comparison between the reference FEM solution on (dotted red) against the VEM solutions (blue) is shown. ....132

Figure 121: Mohr's circle representation of the state of stress for the selected reservoir cell obtained from VEM solution. Three states are represented: initial

(bleu), end of primary production (green) and end of injection period (red). Projections on the Mohr-Coulomb failure line are used to evaluate the Safety Factor.....	132
Figure 122: Software architecture .....	136
Figure 123: sketch of STEP1 of the evolution process.....	137
Figure 124: sketch of STEP2 of the evolution process.....	138
Figure 125: sketch of STEP4 of the evolution process.....	138
Figure 126: scheme of signal/slot connection between objects (The Qt Company, 2021a).....	140
Figure 127: Current Development Flowchart .....	141
Figure 128: <i>Main Application</i> GUI – menu item for selection of the grid file to be processed.....	142
Figure 129: <i>Main Application</i> GUI – logging window for grid upload.....	142
Figure 130: <i>Main Application</i> GUI – successful upload of unstructured gridding with attributes .....	143
Figure 131: <i>Main Application</i> GUI – grid attributes visualization through combobox.....	143
Figure 132: <i>Main Application</i> GUI – dialog box for threshold filtering. By way of example, reservoir is identified by selecting cells with associated dP equal to 40 bar.....	144
Figure 133: <i>Main Application</i> GUI – visualization of the threshold filter's output .....	144
Figure 134: <i>Main Application</i> GUI – dialog box for association of grid attributes to the VEM simulation input parameters .....	145

## List of Tables

Table 1: example of reconstruction of stratigraphic surfaces. The main parameters are reported: number of cloud points, sampling increment, dimension of the <i>Convex Hull</i> and the <i>Concave Hull</i> and corresponding triangulation (Serazio et al., 2021) .....	54
Table 2: example of reconstruction of fault surfaces. The main parameters are reported: number of the cloud points, <i>nDig</i> , dimension of the <i>Convex Hull</i> and the <i>Concave Hull</i> and corresponding triangulation (Serazio et al., 2021).....	64
Table 3: Geertsma's test model parameters .....	80
Table 4: zoning of the geomechanical model on the basis of the stratigraphy	89
Table 5: geomechanical classes defined in the model.....	90
Table 6: UGS dynamic model parameters .....	104
Table 7: parameters of the elasto-plastic constitutive model .....	120
Table 8: disk-shaper reservoir model. Load term and elasto-plastic constitutive model parameters .....	122
Table 9: Safety Factor calculated in correspondence of the centroid of test cell of the disk-shaped reservoir, both at the initial equilibrium ( $t_0$ ) and after injection ( $t_1$ ) .....	124
Table 10: Mohr-Coulomb yield criteria parameters.....	127
Table 11: Safety Factor values of a reservoir and a caprock cells at the initial state ( $t_0$ ), at the end of primary production ( $t_1$ ) and after an injection period ( $t_2$ )	128
Table 12: Safety Factor values of a reservoir and a caprock cells at the initial state ( $t_0$ ), at the end of primary production ( $t_1$ ) and after an injection period ( $t_2$ )	133
Table 13: pre-existing Software Development Ecosystem Actors.....	135

# **Chapter 1**

## **Introduction**

Renewable sources are considered key to decarbonize energy systems and reduce dependency on fossil fuels, as stated by the Mission Innovation Program (“Mission Innovation,” 2021). Since the Paris Agreement was adopted at the United Nations Climate Change Conference in 2015 (“The Paris Agreement | UNFCCC,” 2016) most of the involved countries increased their investment in the development of low and zero-carbon solutions and new markets arose, especially in the power and transport sectors in order to meet the key targets of the 2030 climate & energy framework (European Commission Website, 2016). However, despite the availability of solar energy and wind power, technologies relying on these sources are not fully viable yet due to their unstable and intermittent nature (Benetatos et al., 2019; Rodrigues et al., 2014). Therefore, solutions to match the high-frequency variation of renewable energy production with the electricity demand are fundamental for energy transition. In this view, large-scale energy storage can provide means for balancing supply and demand, increasing energy security, promoting a better management of the grid and allowing convergence towards a low carbon economy. To this end, both electrical storage technologies - such as rechargeable batteries and supercapacitors (Lamberti et al., 2015; Scalia et al., 2021) - and chemical storage are currently under investigation. Chemical storage implies transforming electrical power into chemical energy in the form of H<sub>2</sub>, which can then be used as such or combined with captured CO<sub>2</sub> to produce green CH<sub>4</sub> (referred to as the gas-to-power technology), thus it is very versatile. One way to ensure large-scale storage of chemical energy is to use the storage capacity of

deep geological formations, since underground reservoirs have the potential to store large volumes of fluids with minimal impact to the environment and society (Matos et al., 2019).

Furthermore, long-term CO<sub>2</sub> underground storage is regarded as an essential mitigation option to reduce greenhouse gases in the atmosphere and contrast climate change. Strategies for CO<sub>2</sub> capture and permanent storage have been developed to compensate for CO<sub>2</sub> emissions from burning fossil fuels and to meet the challenge of drastically reducing CO<sub>2</sub> emissions in the next future. Already back in 2005, the Special Report on Carbon Dioxide Capture and Storage (CCS) (Rubin et al., 2005), issued by the Intergovernmental Panel on Climate Change, illustrated strategies for CO<sub>2</sub> capture, transport and permanent storage that have to be developed to compensate for CO<sub>2</sub> emissions from burning fossil fuels. In this report the potential of CCS to mitigate the climate change was shown, pointing out that the success on CCS would have mainly depended on financial incentives spent for scientific research and technical deployment and on the capability of successfully manage the risks associated to CO<sub>2</sub> storage. As opposed to permanent geological sequestration, temporary underground storage could be a strategy to efficiently match the quantity of captured CO<sub>2</sub> and the quantity of CO<sub>2</sub> that can be transformed CO<sub>2</sub> into value-added fuels and chemicals. In this approach, the storage the storage would act like a “buffer” and would be fully integrated with the valorization technologies.

Based on the above, it is evident that underground storage systems can play a fundamental role in the transition to a decarbonized and more sustainable energy future.

Two of the most important characteristics of an underground storage are its ability to hold natural gas for future use and the rate at which that gas can be withdrawn. The concept of storing natural gas underground in geologic formations dates back to the beginning of the last century, with the first successful underground storage of natural gas in a depleted natural gas reservoir developed in 1915 in Ontario, Canada. Since then, hundreds of facilities have been developed worldwide: depleted gas and oil reservoirs, deep saline formations, salt caverns and un-minable coal beds are the favorite candidates for safe geological storage of natural gas, but several reconditioned mines are also in use as gas storage facilities.

Depleted gas or partially depleted gas reservoirs (fields located deep underground where most of the recoverable hydrocarbons have been extracted) are the most sizeable and commonly used formations for natural gas storage. A depleted

field typically represents the most suitable option because of its ability to contain and trap gas (given the reservoir has contained gas on a geological timescale, it should be capable of doing so again). Pressure is used to force the gas into and out of the porous and permeable geological formations while a sealing caprock prevents vertical fluid migration. Deep saline aquifers represent a common alternative for UGS. The development and management of saline aquifers require that the original formation pressure is exceeded to displace the water initially saturating the pores of the rock to accommodate the gas. Therefore, the sealing capacity of the caprock, the presence of spill points (depths below which the gas may “escape” from the geological structure) as well as the rock mechanical integrity must be assessed in order to prevent gas leakage. Salt caverns and excavated rock caverns are generally developed in regions where reservoirs are not available. They are typically much smaller in volume than either depleted reservoirs or aquifers but can provide high delivery rates (Benetatos et al., 2013).

The successful development of an underground storage must include an appropriate site selection based on subsurface information and subsequent performance analysis, preferably based on an integrated geological, geochemical, fluid-dynamic and geomechanical approach. To this end, the same basic sets of information as a typical reservoir study are used: geophysics, geology, well logging and core analysis, well testing and production history, rock mechanic properties. Furthermore, an adequate monitoring program to satisfy technical and safety regulations together with social and environmental concerns must also be conceived to ensure the long-term feasibility of the project. Even though the UGS industry has borrowed much of its knowledge from other industries (primarily oil and gas reservoir engineering and production), it has also developed a technology of its own to meet specific challenges and concerns (Verga, 2018).

In the context of energy transition, the know-how and gained experience in underground storage of natural gas (UGS) can be profitably exploited and applied to CO<sub>2</sub> and H<sub>2</sub> middle to long term confinement to guarantee both the efficiency of the system and the existence of safety conditions. In fact, most of the past and ongoing underground CO<sub>2</sub> and H<sub>2</sub> storage projects use the experiences of the underground natural gas storage in each and every aspect, such as site specifications, storage techniques, monitoring, cost life cycle or economic viability and safety. To this end, the hydraulic sealing capacity of the caprock, the risk of lateral gas migration and the system geomechanical response must be assessed. In fact, pressure changes caused in geological formations by fluid production and/or storage affect the rock stress state. If the variations of the rock stress state are

significant, they could jeopardize the formation integrity and induce (micro)fracturing, potential faults (re)activation and rock deformation, which can propagate to the surface and induce ground movements. Both current regulations and public concerns call for geomechanical analyses to assess safety conditions in terms of stored gas containment, earthquake hazard and subsidence magnitude and extension. Therefore, the mechanical behavior of an underground storage system is a key aspect to be investigated. Given the extension and complexity of the system in terms of geometry, stratigraphy, rock heterogeneity, original stress field and stress variations induced by pressure changes, 3D numerical models are needed to simulate the mechanical behavior.

A geomechanical model relies on the geological (or static) model of the volume of interest, which comprises the depleted reservoir or aquifer to be converted into a storage and the neighboring formations up to the surface. In turn, the geological model is a representation of the structural, stratigraphic, lithological and petrophysical aspects of the underground and is defined based on 2/3D seismic datasets, well logs and rock core data. The time and space evolution of pressure and fluid saturations in the geological formations are obtained from fluid-flow (or dynamic) simulations, which require the following input: fluids thermodynamic (PVT) behavior, rock-fluid interaction properties, pressure and temperature at initial conditions, well data, and future storage targets (such as injection and withdrawal fluid rates) and constraints (such as minimum or maximum pressure values). Furthermore, variable gas composition, reservoir temperature (slight) reduction due to repeated “cold” fluid injection, enhanced effects of petrophysical heterogeneities on the pressure response due to the cyclical withdrawal and injection of gas at high rates resulting in rapid and significant pressure variations and hysteresis of gas-water relative permeabilities should be taken into account (Verga, 2018). Production history if any is used to calibrate the model and confirm its reliability to forecast the storage dynamic behavior.

Based on the geological and the fluid-flow models, the geomechanical model is defined and characterized with additional data about the deformation and the strength parameters of the system (i.e., intact rock and discontinuities), gathered from well log, core data and analogues. If historical production/storage data and surface movement surveys are available, the geomechanical model can be back-analyzed so as to tune the most uncertain parameters. Ground movements can be monitored with the Interferometric *Synthetic Aperture Radar* (InSAR) acquisition technique, which is widely adopted due to its high accuracy (millimeters) on large areas (A. Ferretti et al., 2001; Berardino et al., 2003).

Typically, a one-way coupling approach is adopted for analyzing the stress/strain evolution induced by gas storage activities, namely the input to the geomechanical model is updated according to the outcome of the dynamic model. Thus, the time and space pressure evolution obtained from the dynamic model represents the forcing function applied to the geomechanical model, which implies that the information must be transferred from one model to the other. This introduces two strictly correlated, key aspects, i.e., the investigated volume discretization and the numerical methods applied to solve the differential problem under analysis.

Discretization is the first key aspect because it is common practice to describe the investigated volume with a finite number of geometrical elements identified by vertices, edges and faces. They can be organized on a regular structure or not. The process which drives the domain discretization is strongly influenced by the geometry and the physics of the problem. In geomodelling problems, geological units need to be represented with high accuracy because the material properties strongly influence the response of the system. Fault and stratigraphic surfaces usually lead the construction of the grid because they can separate zones characterized by properties that differ by orders of magnitude. In this context two main approaches can be identified: structured hexahedral corner point grids (K. Ponting, 1989), based on the concept of pillar gridding, which represent the industry standard methodology, and generic unstructured grids with different underlying mathematical frameworks, such as the time-space grids introduced by Mallet (Gringarten et al., 2008; Mallet, 2004). The two types of grids are widely represented in codes developed both in academic/open-source (Pellerin et al., 2017) and in industrial/governmental projects (Emerson, 2021; LANL, 2016; Schlumberger, 2020a) focused on geomodelling and earth science applications.

Once the volume of interest has been discretized, the second key aspect is the selection of the numerical method to solve the problem under investigation. For reservoir fluid flow simulations and rock mechanics applications the Finite Difference Methods (FDM) and the Finite Element Methods (FEM) are the reference methods (Jing and Hudson, 2002). The finite difference software Flac (Itasca Consulting Group, 2021) and the finite element simulators Visage (Schlumberger, 2020b) and Diana FEA (DIANA FEA, 2021) developed for geotechnical and geomechanical analysis are worth mentioning. Although classical FDMs and FEMs represent the state of the art in the solution of generic problems in differential and variational form, these methods are constantly evolving to improve the stability and accuracy of the solutions for specific application problem.

The recently introduced virtual elements method (VEM) (Beirão da Veiga et al., 2013a) derives from the finite difference mimetic methods (MFD)(Lipnikov et al., 2014) and is considered a generalization of FEMs because it overcomes some limitations of the original method, especially related to the shape of the elements which constitutes the discretized volume. The mathematical formulation behind VEM allows an easy solution of the PDEs on highly elongated or highly irregular deformed cells which typically characterize a pillar gridding mesh. The method can be applied to polyhedral grids and on meshes which are not conforming and it allows mixing different order of solutions without extra coding effort. Given their recent formulation, VEM application to engineering problems is still limited. However, they are a promising candidate to solve linear elastic equations, characteristic of geomechanical problems, on grid with complex geometry such as the ones which describes sedimentary formations, as shown in (Andersen et al., 2017).

Based on the above premises, the ultimate goal of this research project was the development and implementation of a geomechanical model suited to address the safety issues associated to fluid storage in deep geological formations, namely rock integrity and compaction/expansion due to fluid withdrawal and/or injection and induced ground level subsidence/rebound. So, the following two main challenging issues had to be tackled: discretization of the underground volume and numerical modeling of the storage geomechanical behavior.

# Chapter 2

## Theoretical Background

The theoretical fundamentals used in the study of the mechanical behavior of porous media are briefly recalled in the following. For a more detailed discussion, reference can be made to the reference technical literature:(Mase and Mase, 1999); (Lancellotta, 2012), (Fjær et al., 2008), (Neto et al., 2008), (Drucker, 1956), (Davis and Selvadurai, 2002), (Atkinson, 1993), (Brady, 2012),(Wood, 1991).

### Stress and strain state in a continuous medium

The mathematical representation of the mechanical behavior of porous media is based on the general principles of the continuum mechanics. In particular, under the basic continuum assumption the minimum element is a representative element volume (REV) of the analyzed material.

In this framework, let us recall the Cauchy's Theorem and the following theory, according to which the complete stress state of a point in  $\mathbb{R}^3$  within a continuous medium can be represented by a second-order tensor ( $\sigma$ ) called *Cauchy stress tensor* or *simply stress tensor*:

$$\sigma = \begin{bmatrix} \sigma_x & \tau_{xy} & \tau_{xz} \\ \tau_{yx} & \sigma_y & \tau_{yz} \\ \tau_{zx} & \tau_{zy} & \sigma_z \end{bmatrix} \quad (1)$$

In other words, the complete stress state of a point can be determined by the knowledge of the state of stress acting on 3 mutually orthogonal planes ( $\pi_x, \pi_y, \pi_z$ ) passing through that point. In Figure 1 a schematic of the stress tensor components acting on a rectangular parallelepiped is represented, where the normal components to the plane  $\pi_i$  are identified by  $\sigma_i$  and the shear stresses orthogonal to the i-direction and parallel to the j-direction by  $\tau_{ij}$ .

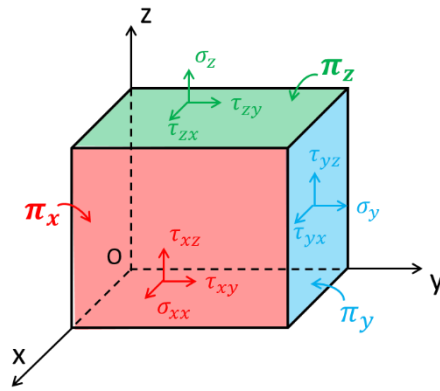


**Figure 1:** stress tensor components representations on a rectangular parallelepiped

If the analyzed infinitesimal element is at rest, as a consequence of the balance of momentum, it is possible to prove that  $\sigma$  is symmetric, i.e.,  $\sigma_{ij} = \sigma_{ji}$ . It follows that the number of independent components of the stress tensor reduces to six. It is also possible to prove that, solving the characteristic equation of the stress tensor for a generic point of the continuum medium:

$$|\sigma - \hat{\sigma}\mathbb{I}| = 0 \quad (2)$$

Three orthogonal planes are identified, called principal planes, on which only normal stresses act ( $\tau_{ij} = 0$ ) ( $\delta_{ij}$  is the Kronecker delta). The normal stress acting on these planes are called principal stress and are indicated as:  $\sigma_1$  (maximum principal stress),  $\sigma_2$  (intermediate principal stress) and  $\sigma_3$  (minimum principal stress).

Focusing on the analysis of small deformations, the state of deformation of each point of the continuum medium is represented by means of a second order tensor called infinitesimal *strain tensor*:

$$\boldsymbol{\varepsilon} = \begin{bmatrix} \varepsilon_x & \gamma_{xy} & \gamma_{xz} \\ \gamma_{yx} & \varepsilon_y & \gamma_{yz} \\ \gamma_{zx} & \gamma_{zy} & \varepsilon_z \end{bmatrix} \quad (3)$$

Its definition descends from the *Cauchy-Green tensors* of deformation and it has expression

$$\boldsymbol{\varepsilon} = \frac{1}{2} (\nabla \mathbf{u} + \nabla \mathbf{u}^T) \quad (4)$$

where  $\mathbf{u}$  is the displacement vector.  $\boldsymbol{\varepsilon}$  is symmetric, thus only 6 components are independent ( $\gamma_{ij} = \gamma_{ji}$ ). The above expression inherently assumes that the deformations are small or infinitesimal, i.e., the displacement is sufficiently small to neglect second order terms ( $\nabla \mathbf{u} \cdot \nabla \mathbf{u}^T$ ) in the strain tensor definition.

As for stresses, planes on which only longitudinal deformations act ( $\gamma_{ij} = 0$ ) can be derived. Analogously to stresses, they are called principal strains:  $\varepsilon_1, \varepsilon_2, \varepsilon_3$ . In an isotropic medium, the directions of the main stresses and deformations coincide.

## Linear momentum balance

Now let us recall the differential equations that represent the focus of the validation described in the following chapters.

The linear momentum balance equations for a general body  $\Omega$  subject to body forces  $\mathbf{b}$  is:

$$\int_{f(\partial\Omega)} \mathbf{t}(\mathbf{n}) ds + \int_{f(\Omega)} \mathbf{b} dv = \int_{f(\Omega)} \rho \ddot{\mathbf{u}} dv \quad (5)$$

where  $f(\Omega)$  represent the deformed configuration of the internal points of the body and  $f(\partial\Omega)$  the deformed boundary configuration.  $\rho$  is the mass density and  $\ddot{\mathbf{u}}$  represents the acceleration field of the body. The Cauchy stress vector applied to  $f(\partial\Omega)$  is  $\mathbf{t}(\mathbf{n}) = \boldsymbol{\sigma} \cdot \mathbf{n}$  where  $\mathbf{n}$  is the outer normal versor to  $f(\partial\Omega)$ .

In the following it will be assumed:

- infinitesimal deformations, i.e. reference and deformed configurations coincide:  $f(\Omega) = \Omega$  and  $f(\partial\Omega) = \partial\Omega$ .
- quasistatic conditions, i.e. the inertial terms are neglected:  $\rho\ddot{\mathbf{u}} = 0$

Therefore, the *pointwise* or *strong* expression of equations (5) becomes:

$$\begin{aligned} \nabla \cdot \boldsymbol{\sigma} + \mathbf{b} &= 0 && \text{in } \Omega \\ \mathbf{t}(\mathbf{n}) &= \boldsymbol{\sigma} \cdot \mathbf{n} && \text{in } \partial\Omega \end{aligned} \tag{6}$$

In turn, the *weak* expression is

$$\int_{\partial\Omega} \mathbf{t} \cdot \boldsymbol{\eta} \, dS + \int_{\Omega} \mathbf{b} \cdot \boldsymbol{\eta} \, dV = \int_{\Omega} \boldsymbol{\sigma} : \nabla \boldsymbol{\eta} \, dV \quad \forall \boldsymbol{\eta} \in \mathcal{V} \tag{7}$$

Where  $\mathcal{V}$  is the space of virtual displacements  $\boldsymbol{\eta}$ . This equation is usually denoted as *Principle of Virtual Work* and represents the starting point for the finite difference method and virtual element method formulations.

## Effective stress

Deep geological formations used for storage are typically sedimentary rocks, i.e. porous and permeable media whose interstitial voids are filled with fluids. To understand the effects induced by a variation of the stress field and therefore to be able to express the internal distribution of the stresses applied to a generic element of rock or soil, it is necessary to establish an interaction law between the solid and fluid phases. Terzaghi's principle of effective stress (Terzaghi, 1936), initially developed for soils, constitutes the universally adopted law of interaction between phases for soils and porous rocks (Bouteca and Guéguen, 1999).

According to Terzaghi, “all the measurable effects of a change of the stress, such as compression, distortion and a change of the shearing resistance are exclusively due to changes in the effective stresses”. The effective stress is related to the total stress through the relation:

---


$$\sigma' = \sigma - \alpha p \mathbb{I} \quad (8)$$

where  $\sigma_{ij}$  is the total stress tensor,  $\sigma'_{ij}$  is the effective stress tensor,  $p$  is the neutral pressure (or pore pressure), and  $\alpha$  is called the Biot's coefficient. The theoretical formalization of the effective stress concept and its generalization to three dimensional problems was performed by Biot in the soil consolidation framework (Biot, 1941) and it constitutes the basis of poroelasticity theory. Biot's coefficient can be expressed as:

$$\alpha = 1 - \frac{K'}{K_s} \quad (9)$$

where  $K'$  is the frame modulus, i.e. the bulk modulus of the solid skeleton, and  $K_s$  is the bulk modulus of the rock grains. Since  $K' \ll K_s$ ,  $\alpha$  is assumed to be equal to unity (Geertsma, 1973a).

## Elasto-plastic constitutive models

Geomaterials show very complex responses even when subject to simple loading conditions. Many characteristics of their response, such as non-linearity, irreversibility, stress path and time dependence, are taken into account by means of constitutive laws. The constitutive laws are represented by equations that describe the deformation of a medium subject to a stress field:

$$\sigma = C \epsilon \quad (10)$$

where  $\sigma$  is the total stress tensor,  $\epsilon$  is the strain tensor and  $C$  is a fourth order tensor (with 81 parameters) describing the behavior of the material.

In the scientific literature, several types of constitutive laws have been defined which define the deformation behavior of continuous media subject to a stress field with the desired level of complexity and accuracy. However, the difficulty of exhaustively describing all the involved phenomena using a single mathematical model is evident. For this reason, results provided by the application of simplified

models are commonly accepted, that is only those phenomena that are believed to influence the behavior of the rock in a significant way are taken into account.

The general form of a constitutive model, which is commonly applied for geomaterial deformation analysis, is summarized below.

The behavior of a continuous medium is defined as elastic when the stress-strain relation is described by a bijective function (Figure 2a and Figure 2b). In such conditions, during a loading-unloading cycle, not only the deformation is recovered but also the deformation work.

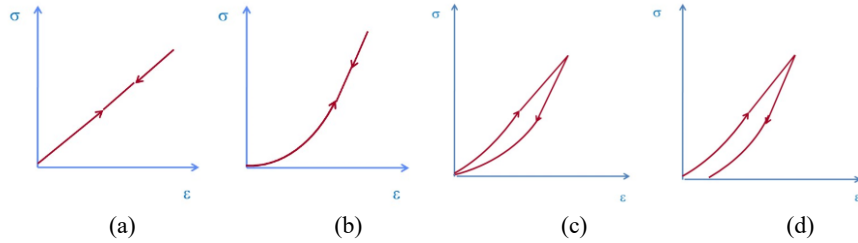


Figure 2: constitutive models of a continuum medium: (a) linear elastic (b) non-linear elastic (c) elastic with hysteresis (d) elasto-plastic

If the material is assumed to be homogeneous, isotropic, linear and elastic (ILE), the C tensor is completely defined by two independent constant parameters and the generalized Hooke's law describes the stress-strain relation in  $\mathbb{R}^3$ :

$$\sigma = 2\mu\varepsilon + \lambda\text{tr}(\varepsilon)\mathbb{I} \quad (11)$$

where  $\mu$  and  $\lambda$  are the *Lamé Elastic Constant*

$$\mu = \frac{E}{2(1+\nu)} \quad \lambda = \frac{Ev}{(1+\nu)(1-2\nu)} \quad (12)$$

and E is the Young's modulus and v is the Poisson's ratio. It follows that in terms of effective stress it becomes:

$$\sigma' = 2\mu\varepsilon + [\lambda\text{tr}(\varepsilon) - \alpha p]\mathbb{I} \quad (13)$$

Several materials, including rocks and soils, are subject to hysteresis (Figure 2c). In such cases, although the deformation is completely recovered during the loading-unloading cycle, some of the deformation work is dissipated in the deformation process. Thus, there is no longer a one-to-one correspondence between stresses and strains and the constitutive law describing the process is more complex than the generalized Hooke's law.

Eventually, if during a loading-unloading cycle the deformations are not completely recovered (irreversible process), the behavior of the material is defined as elasto-plastic (Figure 2d). In this situation, the constitutive law has to model the elastic part of the response and the plastic - or irreversible - one. Permanent deformations occur when stresses exceed a value called *yield point* ( $\sigma_y$ ). After reaching the yield point, if the material can still support the load, the behavior is defined *ductile*, as shown in the section A-B of Figure 3a and in Figure 3b. conversely, if the stress-strain curve reaches a peak (point B in Figure 3a) and the material shows a reduction in resistance, the behavior is defined as *brittle*. As the confinement stress varies, geomaterials exhibit the two types of behavior shown in Figure 3. The behavior of Figure 3a is called *strain softening* and, in general, occurs at no or moderate confinement stresses, while the one of Figure 3b is called *strain hardening* and it typically occurs at high confinement stress.

Behaviors illustrated in Figure 3 show that it is difficult to define what the failure of a material is. Conventionally, we speak of failure when the peak resistance is reached, commonly called the *strength* of the rock, as in the case of Figure 3a (point B); however, although there is a reduction in resistance, the material can still carry a load. The behavior shown in Figure 3b poses greater difficulties in defining the phenomenon of failure.

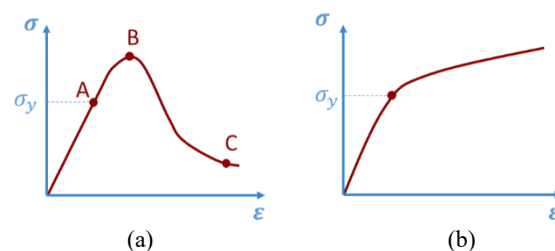


**Figure 3: stress-strain behavior of a geomaterial under compressive strength: (a) strain softening (b) strain hardening**

Sometimes the failure is defined as the point where the stress-strain curve exhibits a change in slope, but this definition may seem inappropriate since the

material can carry an increasing load even if it "reached the failure". In other situations, a condition in which deformations are unacceptable for engineering applications can also be defined as "failure". For this reason, the term "resistance criterion" is sometimes preferred to the term "failure criterion".

From what highlighted so far, it becomes relevant to describe the behavior of the material after reaching the yield stress through the concepts of the *Theory of Plasticity*. A fundamental assumption of this theory is that the strain can be decomposed in the sum of an elastic or reversible component ( $\boldsymbol{\varepsilon}^e$ ) and a plastic or irreversible one ( $\boldsymbol{\varepsilon}^p$ ):

$$\boldsymbol{\varepsilon} = \boldsymbol{\varepsilon}^e + \boldsymbol{\varepsilon}^p \quad (14)$$

In this framework, the definition of a constitutive model able to describe the irreversible behavior of a continuous medium requires:

- A *yield condition* to establish the existence of plastic deformations.
- A *hardening law* to establish the modulus of plastic deformations.
- A *flow rule* to establish the direction of plastic deformations.

In Figure 3a yield stress  $\sigma_y$  has been set as a threshold between the reversible and the plastic behavior. However, in the more general case of the three-dimensional principal stress domain, assuming to apply increasing principal stresses according to infinite stress paths, the corresponding yielding points set represent the locus of the points which separate the elastic and plastic domains (as sketched in Figure 4), commonly known as *yielding surface*.

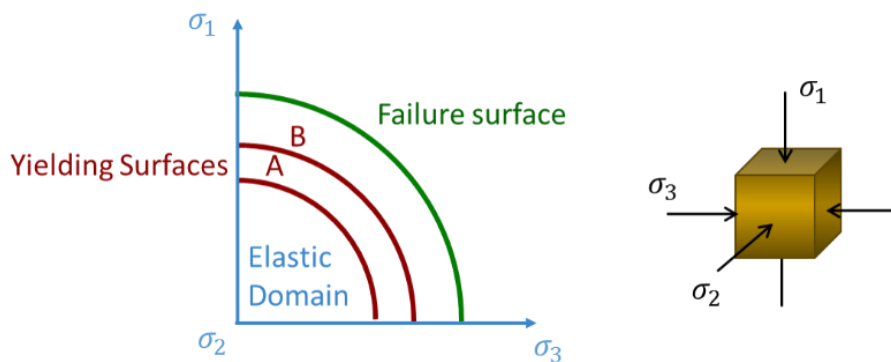


Figure 4: sketch of yielding and failure surfaces

A relation between  $\sigma'$  and  $\kappa$  describes a general yielding surface

$$\Phi(\sigma', \kappa) = 0 \quad (15)$$

where  $\sigma$  is the stress tensor and  $\kappa$  are internal hardening variables.

During plastic deformation, this surface can change size and shape. The evolution of the yield surface is called hardening and the relation between the variation in yield stress and plastic deformation is known as *hardening law*:

$$\dot{\kappa} = \gamma H(\sigma', \kappa) \quad (16)$$

where  $\gamma$  is called plastic multiplier and  $\dot{\kappa}$  represent the rate of variation of the hardening variables.

Inside the yield surface the behavior of the material is elastic and yielding occurs on the boundary of the surface. Consequently, if the material is subject to a loading process until it reaches the yield surface A (Figure 4) and is then unloaded, part of the deformations will be irreversible. If the material is subject to a loading process again, its behavior will be elastic until it reaches the yield surface A again. If the yield surface evolves (hardening) up to B, the behavior of the material from A to B (and B to A) will be elasto-plastic.

If during the plastic deformation the yield surface does not change, the behavior of the medium is defined *perfectly plastic*. It is noticed that, for a perfectly plastic material, the yield condition coincides with the failure criterion.

The direction of the plastic strain increment is independent of the stress increment direction, but it depends on the stress field applied to the body. Thus, the plastic flow rule is introduced. Its general expression is

$$\dot{\epsilon}^p = \gamma N(\sigma', \kappa) \quad (17)$$

where  $N$  is the flow vector.

---

Usually, the *plastic flow rule* can be expressed through the introduction of a function of the stress components, called *flow potential* ( $\Psi$ ) and the plastic strain rate is defined orthogonal to that surface:

$$N(\sigma', \kappa) = \frac{\partial \Psi}{\partial \sigma'} \quad (18)$$

If the potential function and the yield function coincide ( $\Psi \equiv \Phi$ ) we speak of an *associated plastic flow*. In the more general case, the potential function and the yield function do not coincide, and the plastic flow criterion is defined as *unassociated*.

To guarantee the admissibility of the solution, the definition of the constitutive model requires that the following conditions are fulfilled:

$$\Phi(\sigma', \kappa) \leq 0 \quad \gamma \geq 0 \quad \gamma \Phi(\sigma', \kappa) = 0 \quad (19)$$

The first is named the *consistency condition* and assures the actual state of stress is plastically admissible, the second is the Lagrangian multiplier constraint and the third is the so-called *complementarity condition*. In the plasticity theory they are referred to as *loading/unloading conditions*, and they are nothing else than the Karush-Kuhn-Tucker optimality conditions for nonlinear problems (Luenberger et al., 1984).

The literature reports different failure criteria formulated for the different types of material. For example, the Tresca criterion, the Von Mises criterion and the Drucker & Prager criterion are cited. However, the simplest and most widely used criterion of failure or plasticization in the field of soil and rock mechanics is the Mohr-Coulomb criterion.

An elasto-plastic model specifically formulated for soils is the *Cam Clay model* (Schofield and Wroth, 1968). This model is based on the experimental evidence of triaxial tests performed on clays and it represents the first application of the theory of plasticity to soils with the purpose of predicting their behavior in a realistic way. Recently the *Modified Cam Clay* model has been applied to analyze the mechanical response of sedimentary rocks. Examples can be found in (Capasso and Mantica, 2006; Cuss et al., 2003; Firme et al., 2014).

In all the cases described above, the stress-strain relation is independent of time. However, rocks and soils can exhibit viscous, i.e. time-dependent, behavior that is commonly called *creep*. Figure 5 schematically shows the creep phenomenon: even if the loading process stops at point A, the material deforms – at constant stress – from A to B in time  $t$ .

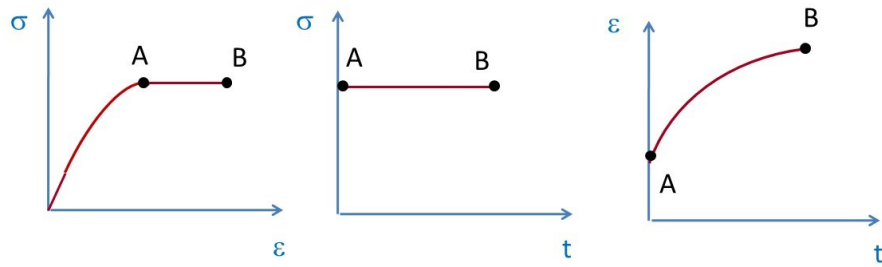


Figure 5: creep phenomenon: time-dependent behavior of the continuous medium

Viscous behavior is generally associated with elastic and/or plastic behavior, giving rise to the viscoelastic or – visco-elastoplastic constitutive models, respectively. The most known viscoelastic models are the Maxwell model, the Kelvin model and the Burgers model which are sketched as an elastic spring and a viscous damper connected in series and/or in parallel as shown in Figure 6.

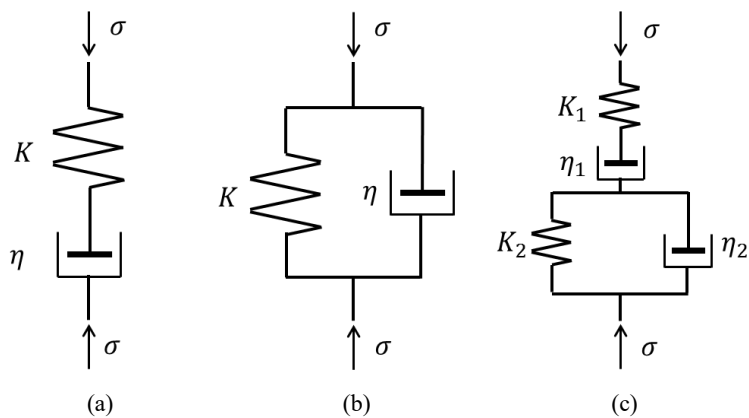


Figure 6: Maxwell model (a); Kelvin model (b); Burgers model(c).

## The Mohr-Coulomb criterion

Coulomb (Coulomb, 1776) postulated that the shear strength of rocks and soils was composed of two parts: a constant cohesion and a friction component dependent on the normal stress (in reality the criterion was formulated in terms of forces, because the Cauchy's stress vector was introduced later). Consequently, the

shear resistance  $\tau_f$  that develops on a plane within an isotropic material is expressed as:

$$\tau_f = c + \sigma \tan \varphi \quad (20)$$

where  $\varphi$  is the friction angle,  $c$  is the cohesion and  $\sigma$  is the normal stress acting on the failure plane. In presence of fluids the Terzaghi's effective stress principle is applied and the equation is expressed in terms of effective stress, and the corresponding cohesion and friction angle are considered:

$$\tau_f = c' + \sigma' \tan \varphi' \quad (21)$$

In the  $\sigma' - \tau$  plane, the shear resistance ( $\tau_f$ ) is represented by two straight lines (red lines in Figure 7a). If represented through the Mohr circles, the failure condition occurs when the Mohr circle, which represents the state of stress of the element subjected to loading, is tangent to the failure envelope. Figure 7b shows the failure of a rock element subject to a stress state  $\sigma'_1 - \sigma'_3$ . The Mohr-Coulomb criterion provides that the *failure plane* is inclined by angle  $\beta = \frac{\pi}{4} + \varphi'$  with respect to the direction of the minimum main stress.

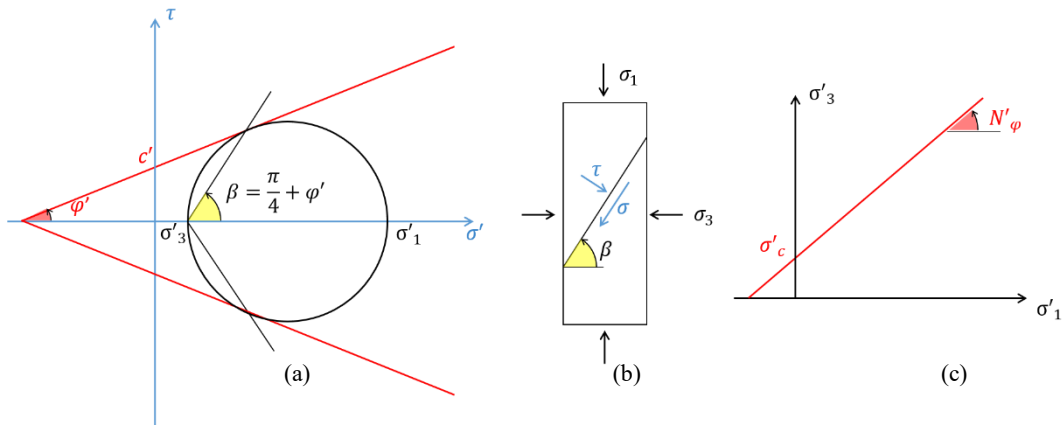


**Figure 7: (a) Mohr-Coulomb Yield criterion in the plane  $\sigma' - \tau$ . (b) sketch of the rock plug subjected to loading. (c) Mohr-Coulomb Yield Criterion in the  $\sigma'_1 - \sigma'_3$  plane**

Using the stress transformation law, the Mohr-Coulomb criterion can be reported in the plane  $\sigma'_1 - \sigma'_3$  (Figure 7c):

$$\sigma'_c = \frac{2c \cos \varphi'}{1 - \sin \varphi'} \quad N'_{\varphi} = \frac{1 + \sin \varphi'}{1 - \sin \varphi'} \quad (22)$$

where  $\sigma_c$  is the uniaxial compressive strength and  $N_c$  is the slope of the straight line representing the criterion.

When generalized to the three-dimensional case, the expression of the yield surface becomes:

$$\Phi_{i_1, i_2}(\boldsymbol{\sigma}') = (1 - \sin \varphi) \sigma'_{i_1} - (1 + \sin \varphi) \sigma'_{i_2} - 2c' \cos \varphi' \quad (23)$$

$$i_1, i_2 = 1, 2, 3 \quad i_1 \neq i_2$$

The multi-surface representation in the space of the principal stresses is a pyramid with a hexagonal base and axis coinciding with the hydrostatic axis, as shown in Figure 8 where it is assumed that  $\sigma_1 \geq \sigma_2 \geq \sigma_3$ .

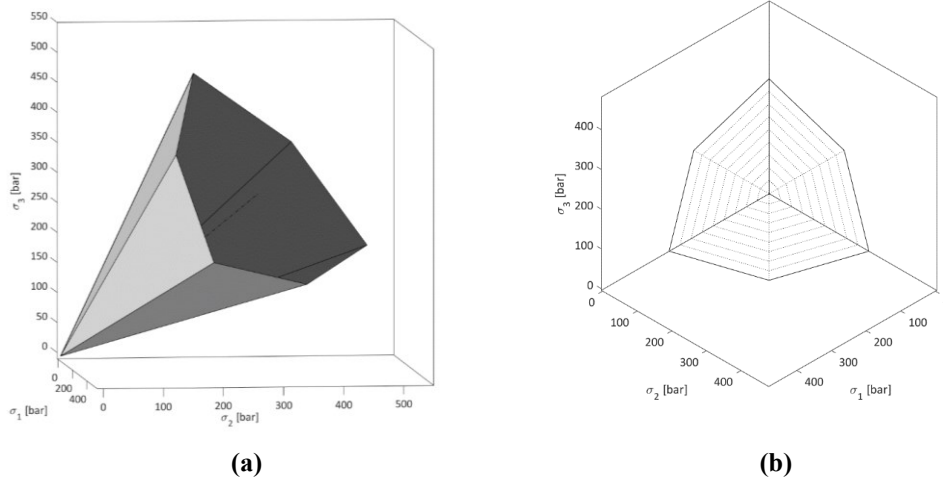


**Figure 8: (a) representation of the yield function defined by the Mohr-Coulomb criterion in the space of the principal stresses. As an example,  $c = 2.5$  bar and  $\varphi = 25^\circ$  were imposed. In (b) projection of the function on the deviatoric plane**

When applying Mohr-Coulomb yield criterion to rock materials, a non-associated plastic flow is usually introduced and a flow potential  $\Psi$  defined. Such a choice is due to the necessity to control the dilatancy effect usually overestimated by associative plastic flow. For the Mohr-Coulomb yield model the flow potential is similar to yield surface, i.e. the friction angle  $\varphi$  is substituted by the *dilatancy angle*  $\psi$  (Fjær et al., 2008; Neto et al., 2008):

$$\Psi_{i_1, i_2}(\sigma') = (1 - \sin \psi)\sigma'_{i_1} - (1 + \sin \psi)\sigma'_{i_2} - 2c \cos \psi \quad (24)$$

$$i_1, i_2 = 1, 2, 3 \quad i_1 \neq i_2$$

## Safety Factor

The formation pressure and stress fields variations during fluids withdrawal/injection are strongly related to safety issue. The modification of the stress state can cause borehole instability, jeopardize the reservoir cap-rock integrity, induce deformations that propagate to the surface generating subsidence/rebound and even lead to the (re)activation of discontinuities such as faults or fractures at reservoir and regional scale with possible induced (micro)seismicity.

The aim of failure mechanics is the reliable characterization of the constitutive laws describing the rock stress-strain behavior through laboratory tests, and the application of adequate criteria to assess the risks of failure. For this reason, in geotechnical analysis it is common practice to quantify the level of risks with a *safety factor* ( $S$ ). In the technical literature the Mohr-Coulomb criterion is commonly assumed as a *failure envelope* and applied for this purpose (Fjær et al., 2008; Mao et al., 2020; S. Kwon et al., 2013). For an isotropic material, its representation in the  $\sigma - \tau$  plane is depicted in Figure 9:

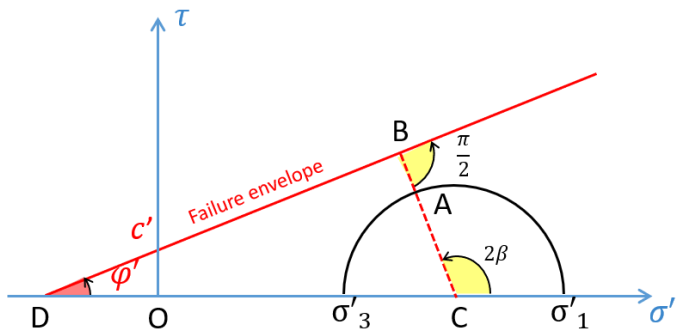


Figure 9: failure envelope for the Mohr-Coulomb criterion

where:

- $DC = \frac{1}{2}(\sigma'_1 + \sigma'_3) + \frac{c'}{\tan \varphi'}$
- $AC = \frac{1}{2}(\sigma'_1 - \sigma'_3)$  represents the stress acting on the material
- $BC = DC \sin \varphi'$  represents the strength of the material, i.e. the stress level at which the material fails

and  $S$  is defined as

$$S = \frac{AC}{BC} = \frac{\frac{1}{2}(\sigma'_1 - \sigma'_3)}{\left[ \frac{1}{2}(\sigma'_1 + \sigma'_3) + \frac{c'}{\tan \varphi'} \right] \sin \varphi'} \quad (25)$$

It follows that if the Mohr's circle lies below the failure envelope,  $S \in [0,1]$  and it approaches 1 when the circle is tangent to the envelope as depicted in Figure 10:

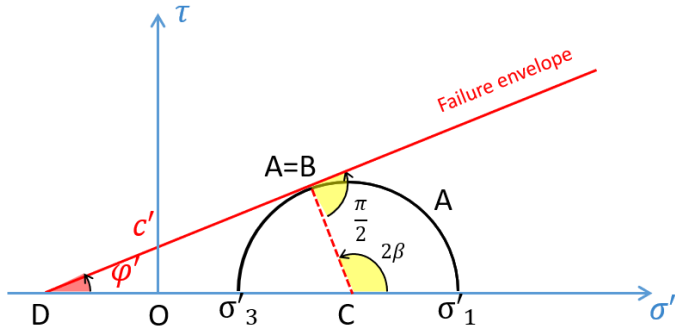
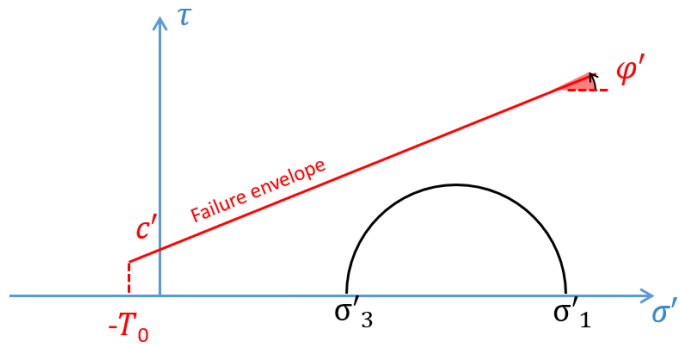


Figure 10: shear failure according to Mohr-Coulomb failure criteria

The tangent condition means that the material reached a *shear failure*: it occurs when the shear stress along a plane (*failure plane*) is sufficiently high, thus a fault zone can develop, and a relative translation can occur between two bodies in contact and separated by the failure plane. It is also observed that frictional forces that oppose to the movement depend on the compressive stress which presses the two bodies together.

From a general point of view failure of a material can also occur when the tensile stress exceeds a value called *tensile strength* ( $T_0$ ) which is a characteristic property of the rock. Most sedimentary rocks are characterized by tensile strength values (typically in the order of few MPa) smaller than shear strength. This is the

reason why in many applications this value is assumed equal to zero. In the  $\sigma' - \tau$  plane Mohr's circle representation *tensile failure* occurs when the minimum principal stress is lower than  $T_0$ . In the safety assessment Mohr-Coulomb failure envelope can be modified by introducing a tensile cut-off ( $T_0$ ) (Figure 11) in order to keep into account tensile failure mode (although the criterion is specific for predicting shear failure) (Brady, 2012)



**Figure 11: tensile stress cut-off on the Mohr-Coulomb failure criteria**

It is worth mentioning that pore pressure plays a crucial role in the evaluation of the safety factor  $S$ . As already discussed, effective stress variations are responsible for skeleton deformation and the pore pressure only influences the normal components of the total stress. Generally speaking, production induces more stable stress states (i.e. translation of the Mohr's circle towards higher values of the normal stress in the  $\sigma$ - $\tau$  plane), if the variations of the deviatoric stress are limited or negligible compared to the plastic deviatoric stress. Conversely, injection induces stress configuration closer to failure state as sketched in Figure 12.

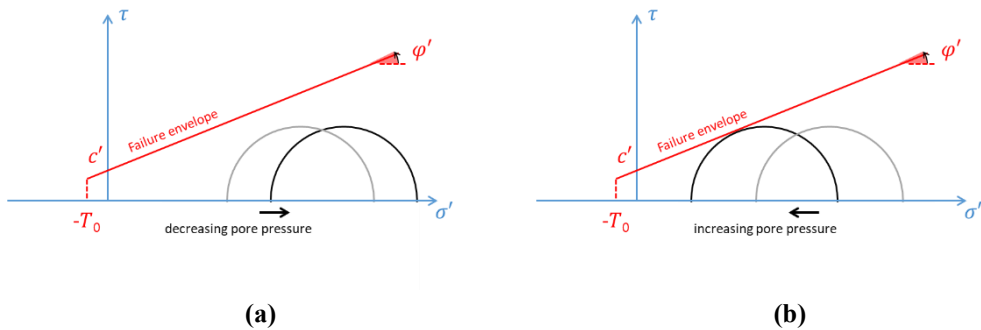


**Figure 12:  $\sigma' - \tau$  Mohr's circle representation of effective stress: (a) pressure decreasing and (b) pressure increasing effects**

Finally, it is observed that Biot's coefficient was originally derived for linear elastic intact rock, and it should not be applied to failure analysis. However, Terzaghi's

effective stress definition is generally applied to failure analysis (Bouteca and Guéguen, 1999)

## Stress state of the lithosphere

The knowledge of the active stress field in the Earth's crust is of fundamental importance for the understanding of the geodynamic processes that govern the evolution of the lithosphere, for the evaluation of the seismic hazard, to verify the stability of underground constructions and for the optimization of reservoir management (Sperner et al., 2003). From a modelling point of view, it represents the initial stress equilibrium state of the investigated volume.

Within the lithosphere, stress is conventionally described by three main components of compressive stress: a vertical component ( $\sigma_v$ ) and two horizontal components ( $\sigma_{or}$ ) corresponding to the maximum horizontal stress ( $\sigma_H$ ) and minimum ( $\sigma_h$ ). When that the Earth's surface does not have an elevated and irregular topography, and in the absence of discontinuities, it can be assumed that the components  $\sigma_V$ ,  $\sigma_H$  and  $\sigma_h$  coincide with the main stress axes. The vertical component depends on gravity and, for a rock volume located at a given depth, it depends on the weight of the overburden rock. This component is called *lithostatic pressure* and depends on the thickness and nature of the sediments and saturating fluids as well as on the depositional history. The value of the  $\sigma_H$  component is the most difficult to calculate and is typically derived from direct correlation with the value of  $\sigma_h$ . Different correlations between,  $\sigma_H$ ,  $\sigma_h$  and  $\sigma_V$  have been proposed as a function of rock type and tectonic regime (Zang et al., 2012).

The stress field inside the lithosphere is therefore the result of the interaction, at different scales, between the gravitational force, processes involved in the movement and tectonics of plates, lithological variations, heterogeneity of the mechanical properties of rocks, changes of temperature and pore pressure. The two main components are represented by the stress connected to the lithostatic pressure and by that connected to tectonic processes, respectively:

$$\sigma_v = \sigma_{lito} = \rho g z \quad (26)$$

$$\sigma_{or} = K\sigma_v + \sigma_{tec} \quad (27)$$

In (26)  $\sigma_{lito}$  is the lithostatic pressure [MPa],  $\rho$  is the density [kg/m<sup>3</sup>], g is the acceleration of gravity [m/s<sup>2</sup>] and z is the depth [m]. In the Italian geological context, Montone and Mariucci (Montone and Mariucci, 2015) calculated the lithostatic stress gradients representative for the eastern Po Valley, the northern Apennines and the North-Western Adriatic. In particular, a lithostatic gradient of about 21 MPa/km was calculated for the Adriatic off-shore and about 22 MPa/km for the Po Plain (Montone and Mariucci, 2015). In (27) K is the *lateral stress coefficient* which represents the ratio between the average horizontal stress and the vertical one:

$$K = 0.5 \frac{\sigma_H + \sigma_h}{\sigma_v} \quad (28)$$

K is characterized by a strongly non-linear behavior, and it decreases significantly as the depth increases (Brown and Hoek, 1978; Taherynia et al., 2016; Zang and Stephansson, 2009).

According to Anderson's theory, the orientation of the axes  $\sigma_1$ ,  $\sigma_2$  and  $\sigma_3$  controls the orientation and the type of faults that can potentially form in a given tectonic regime. Figure 13 shows the most common types of faulting, under the hypothesis that one principal stress is vertical (Fjær et al., 2008).

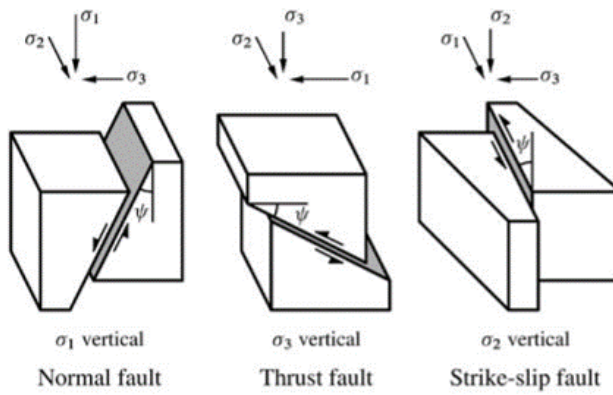


Figure 13: sketch of fault types (Fjær et al., 2008)

## Induced subsidence and rebound

In the case of a saturated porous medium, such as deep geological formations, the pressure exerted by the lithostatic load is distributed between effective stress, i.e. the part supported by the solid skeleton, and interstitial pressure, which represents the fraction supported by fluids saturating the porous medium (Terzaghi, 1936).

The withdrawal/injection of fluids, whether liquid or gaseous, generates a progressive variation in the interstitial pressure of the porous medium and, consequently, a variation in the effective stresses, which insist on the solid skeleton; in turn the skeleton reacts to the new stress state with a deformation. In other words, the void index  $e$  (or porosity  $\phi$ ) is reduced/increased. The void index is defined by the following relationship:

$$e = \frac{V_v}{V_s} \quad (29)$$

where  $V_v$  is the volume of the voids and  $V_s$  is the volume of the solid phase. The void index is related to porosity  $\phi$  by the following relation:

$$\phi = \frac{e}{1 + e} \quad (30)$$

At the macroscale, the reduction/increase of the void index, or porosity, corresponds to a volumetric change known as compaction/expansion (Figure 14).

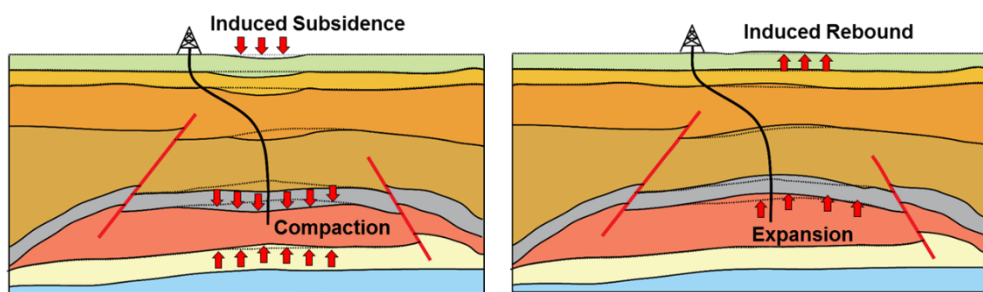


Figure 14: sketch of induced compaction/expansion as a consequence of withdrawal/injection of fluids in deep geological formations

Before starting any withdrawal/injection operations, the effective stress field of rock is at equilibrium. During the production or storage operations the fluid pressure in the pores decreases/increases, causing an increase/decrease in the effective stresses. As a result, the rock formations compact/expand and the degree of compaction/expansion is essentially governed by the variation of effective stresses, the compressibility of the formation rock and its thickness (Nagel, 2001). The volume variation, caused by the compaction/expansion of the rock, propagates to the surface, causing subsidence/rebound (or uplift) phenomena. The extent of subsidence/rebound depends on the compaction/expansion magnitude, on geometric factors, such as the depth and size of the interested formations, and on the fluid-dynamic and mechanical properties of the geological bodies located above (*overburden*), to the sides (*sideburden*) and below (*underburden*) the formations affected by production or storage.

The compaction/expansion phenomena and the induced subsidence/uplift by production or withdrawal/injection from deep rock formations are widely described in the technical-scientific literature. Subsidence studies are typically related to oil and gas production, which can induce significant variations in the pore pressure. Starting from the first analyzed case related to the Goose Creek field (Texas) in 1918, recent examples of important subsidence phenomena (over 6 meters) are those of the Ekofisk and Valhall fields in the Norwegian sector of the North Sea. In the 90's, the subsidence due to the extraction of gas from the huge fields of Groningen and Ameland (on-shore and off-shore) in the Netherlands received particular attention. However, most hydrocarbon fields are subject to modest compaction and, consequently, the corresponding subsidence on the surface is negligible. In particular Fjær et al. (Fjær et al., 2008) report that subsidence becomes appreciable when one or more of the following conditions exist: the formation rock is highly compressible, the pressure drop in the formation is considerable, the reservoir has a significant thickness, the mechanical properties of the overburden are similar to those of the reservoir. It follows that important subsidence phenomena are expected only in certain circumstances and therefore in a limited number of cases.

Injection of fluids in deep formations has gained an increasing interest in the last decades and currently occurs worldwide for different purposes. For example, underground gas storage (UGS) in depleted gas/oil fields is a common strategy to meet daily and seasonal oscillations in energy needs and enhanced oil recovery (EOR) by fluid (water, CO<sub>2</sub>) injection in the oil fields for reservoir productivity optimization is a widespread practice. Similarly, aquifer storage and recovery

(ASR) practice is at the center of many projects with the aim of recharging aquifer systems and mitigate land subsidence. There is also a revived interest in the Carbon Capture and Storage (CCS) practice, i.e. underground storage of CO<sub>2</sub> in order to mitigate climate change by reducing greenhouse gas emissions, and CCS is at the center of international scientific projects (reference can be found in (Rubin et al., 2005).

As already mentioned, injection of fluids can cause land uplift that can range from few millimeters to tens of centimeters making necessary an accurate feasibility analysis and a close monitoring of the system evolution. A survey of sites where induced land uplift was observed can be found in (Pietro Teatini et al., 2011).

## Analytical and semi-analytical approaches

The assessment and monitoring of induced subsidence/rebound is one of the goals of geomechanical analyses performed on deep formations subject to withdrawal/injection of fluids to prevent safety issues. There are many contributors in the scientific literature who proposed analytical and semi-analytical solutions to the problem. By nature, analytical approaches to evaluate subsidence represent quick investigation techniques that generally offer an approximate but rapid evaluation of the phenomenon. Conversely, the numerous simplifying hypotheses underlying these methods often do not allow one to correctly reproduce the effects of the heterogeneity or structural characteristics of the investigated volume. Furthermore, the analytical solution of particularly complex models may not be feasible due to the nature of the mathematical laws and/or the geometry of the domain.

One of the most known analytical models in the oil and gas industry was proposed by Geertsma (Geertsma, 1973b, 1973a). It was derived in the framework of the nuclei of strain theory and based on a parallelism with thermo-elasticity (Mindlin, 1936; Mindlin and Cheng, 1950; Sen, 1951). The model provides the order of magnitude of both compaction and related subsidence generated by a decrease in the interstitial pressure in a disk-shaped underground porous medium with radius  $R$  and thickness  $H$ .

Reservoir compaction,  $\Delta H$ , is defined by eq. (31) with, Biot's coefficient  $\alpha$  set equal to 1, that is:

---


$$\Delta H = c_M \Delta p H \quad (31)$$

while the vertical displacement induced on the surface at a distance  $r$  from the symmetry axis of the reservoir,  $u_z(r, 0)$ , is:

$$u_z(r, 0) = -2c_M(1-\nu)\Delta p H A(\rho, \eta) \quad (32)$$

Since radial symmetry is assumed, the solution of the model is provided in cylindrical coordinates. Therefore, the radial displacement at a distance  $r$  from the reservoir  $u_r(r, 0)$  has the expression:

$$u_r(r, 0) = 2c_M(1-\nu)\Delta p H B(\rho, \eta) \quad (33)$$

where:

- $c_M$ : uniaxial compressibility coefficient expressed as  $\frac{(1+\nu)(1-2\nu)}{E(1-\nu)}$
- $\nu$ : Poisson's ratio
- $\Delta p$ : pressure reduction in the reservoir
- $H$ : depth of the reservoir
- $\rho$ : ratio between the distance from the axis of the reservoir  $r$  and the radius of the reservoir  $R$  ( $r/R$ )
- $\eta$ : ratio between depth and radius of the reservoir ( $H/R$ )
- $A(\rho, \eta)$  and  $B(\rho, \eta)$ : Hankel integrals functions parametrized by  $\rho$  and  $\eta$ . Details in (Geertsma, 1973b)

It can be shown that the maximum subsidence,  $u_z(0, 0)$ , i.e. the vertical displacement at the axis of the reservoir, can be obtained from equation (32) and is equal to:

$$u_z(0, 0) = -2c_M(1-\nu)\Delta p H \left(1 - \frac{\eta}{\sqrt{1+\eta^2}}\right) \quad (34)$$

The simplicity and ease of application of the method counterbalance the simplifying hypotheses underlying it (among which the main ones are disk-shaped reservoir with high areal dimension with respect to its thickness, constant and instantaneous reduction of interstitial pressure, constant parameters throughout the domain, uniaxial and elastic deformations).

Numerous other authors have formulated analytical solutions to the subsidence problem, in some cases adopting less simplifying hypotheses to make the models more realistic. As an example, the work of Morita et al. (Morita et al., 1989) constitutes an extension of Geertsma's results to a more realistic case with different Young's moduli for the reservoir and its cap rock.

More recently, semi-analytical models were formulated, in which the analytical solutions are associated with numerical integration techniques to describe the spatial variation of the pressure field obtained from an external fluid dynamic model of a reservoir with generic shape. Furthermore, thanks to the effect of superposition, it is possible to estimate the first approximation subsidence expected from multi-layered producing fields (as the sum of the subsidence induced by each level). As an example, the approach formulated by Fokker and Orlic (Fokker and Orlic, 2007) is worth mentioning. This semi-analytical model, developed through the TNO's AEsubs subsidence modelling tool, uses linear combinations of analytical solutions of elastic (or viscoelastic) equations to approximate boundary conditions. The number of unknown parameters to be estimated is limited and, consequently, the calculation is very fast. The model is also applicable to multi-layer systems (with variable viscoelastic parameters per level) and allows the adoption of an arbitrary history of reservoir pressure changes.

# **Chapter 3**

## **Numerical model**

### **Model construction**

The purpose of a 3D numerical model of the reservoir interested by withdrawal/injection operations and of the neighboring formations is to describe the spatial and temporal pressure evolution due to fluid flow and the consequent deformation response of the system. This is achieved through integration of all the available information, whether of geological, geophysical, petrophysical or geotechnical type or related to production/injection of fluids. When properly calibrated, the model becomes a reliable tool to forecast the performance of the system according to different scenarios.

The definition of a comprehensive model that allows the analysis of all the involved phenomena requires the integration of three reference models, each dedicated to describing a specific aspect of the problem in detail:

1. Geological (*static*) model
2. Fluid dynamic (*dynamic*) model
3. Mechanical model

The construction and characterization of a static model allows geologists to accurately describe the structural characteristics and the distribution of the lithological/petrophysical properties of the formations under analysis. The static model, integrated with the PVT (pressure, volume and temperature) parameters

describing the thermodynamic behavior of the fluids that saturate the porous media, the well type and completion characteristics and the production/injection data (such as well flow rates, cumulatively produced volumes, static bottom hole pressures), are the basis for the analysis of flow phenomena. The geological model, suitably extended to the neighboring formations and characterized from a geotechnical point of view with resistance and deformability parameters, can then be integrated with the dynamic model to define the mechanical model. Mechanical analyses are aimed at evaluating the effects of production/injection on the stress-strain response of the rock as well as at assessing the variations of the petrophysical parameters induced by rock matrix deformation.

One possible approach to define a geomechanical model that integrates static and dynamic information is articulated as follows. Initially, the *static model* is built. It is represented by a 3D grid with high areal and vertical resolution, and it includes all the structural, stratigraphic and petrophysical characteristics of the formation. In the case of hydrocarbon reservoirs this model is mainly used for estimating the volume of fluids originally in place. The grid of the static model, with all its properties, is then converted into a new grid, with lower resolution and therefore better suited for dynamic simulations. It represents the starting point of the *dynamic model*, used to simulate the pressure and saturation variations induced by fluid production/injection in the reservoir. In turn, the calculated pressure fields represent a fundamental input for geomechanical simulations. At last, the 3D grid used for geomechanical simulations is constructed by extending the grid of the static model to a regional scale to include all the formations interested by the phenomena under analysis. Thus, the extended grid also describes the geometry of the geological units surrounding the reservoir, including the main regional discontinuity systems within the modeled area (*geological model on a regional scale*). The related *geomechanical model* integrates this grid with all the information relative to the geomechanical and dynamic properties needed for the mechanical simulations.

## Static model

The reservoir study is divided into several phases. The workflow is meant to integrate geological and geophysical data but also dynamic information useful to understand if layers or zones are hydraulically separated. Each phase and its contribution to the construction of the geological model are presented in the following paragraphs.

### *Construction of the database and quality check*

The definition of the reservoir model begins with the collection of data that will constitute the integrated database necessary for the reconstruction of the geometries and geological characteristics of the reservoir. It follows that the quality of the available data affects the results of the reservoir study. The database typically includes data of different nature related to sedimentological-stratigraphic understanding of the system, seismic, wells, logs, and cores.

### *Construction of the structural model*

The model construction consists in the definition of the maps of the structural *top* and of the faults intercepting the reservoir. In most cases *top* maps derive from seismic interpretation. The horizons are defined starting from the interpreted seismic reflections to build 3D maps in the time domain. Subsequently, using a velocity model, the maps are converted in the space domain (depth) and integrated with the well data for the construction of the static model. The presence of faults can be identified through the analysis of seismic data, log data or pressure data. Seismic data provide information about the geometry of the faults through lines or polygons. The reconstructed fault surfaces constitute the basis of the 3D grid.

### *Construction of the stratigraphic model*

The stratigraphic model is defined through the correlation of the horizons, that limit the main stratigraphic units of the reservoir, adjusted at the wells. Information on the size of the sedimentary bodies, their geometry and their 3D organization can derive from the conceptual geological model and from regional stratigraphy. The stratigraphic correlation can be relatively simple in the case of bodies characterized by high lateral continuity, as in the case of turbiditic lobes; conversely, it can be extremely complex in the case of bodies characterized by rapid variations in orientation, thickness, and lateral continuity, as in the case of channelized deposition environments.

### *Facies and petrophysics characterization*

During this phase, the depositional and lithological facies and the associated petrophysical characteristics are defined. For the definition of the depositional and lithological facies it is necessary to refer to a sedimentological model; this model is generally based on core data, which provide information on the lithologies present within the reservoir and on their petrophysical properties. The association of

petrophysical characteristics to the lithological facies is carried out through the analysis and integration of the available logs and core data (RCAL, SCAL). Properties such as porosity ( $\phi$ ) and irreducible water saturation ( $S_{wi}$ ) are necessary for the calculation of the hydrocarbon volume; the permeability values ( $k$ ) are indispensable for the subsequent fluid dynamic simulations.

#### *Construction of the 3d geometric model*

The 3D geometric model of the reservoir is the result of the integration of the structural and stratigraphic models with the well data within the grid. The grid is an object which spatially describes the investigated volume, and it consists of a number of cells which can have a structured or unstructured organization. The nature of the grid strictly depends on the physical properties/phenomena that are represented/simulated and on the methods applied to perform such simulations. In case of geomechanics, grids with a vertical discretization following the stratigraphic sequence of the formations and suitable for the integration of the well data are typically generated; the areal dimensions of the cells are mainly defined based on the areal spacing of the wells and the desired total number of cells.

#### *Distribution of facies and petrophysical distribution*

Starting from the wells, the facies identified along the wells are distributed within the grid of the static model using geostatistical algorithms for a realistic reconstruction of the depositional bodies.

#### *Up-scaling of the static model*

To ensure the geological representativeness of the static reservoir model, the 3D grid is normally characterized by a high areal and vertical resolution, i.e. by a high number of cells. However, to optimize the computational times of dynamic simulations, the number of cells must be reduced.

The conversion from a geological grid to a dynamic grid is carried out through a coarsening process which involves the areal and vertical resizing of the cells. All previously distributed petrophysical properties are transferred in the new grid through an *up-scaling* process. At the end of these operations the new grid can be conveniently used for dynamic simulations.

## Static model at a regional scale

Geomechanical simulations require a grid of much larger dimensions than those of the static/dynamic grid to reproduce all the formations interested by the phenomena under analysis. The areal and vertical extension must be optimized on a case-by-case basis according to the size and depth of the reservoir, the presence of a bounding aquifer as well as the numerical modeling technique adopted in the mechanical simulation phase. The extension of the model to a regional scale involves a series of changes compared to the original model, which may include the extension of the main reservoir horizons and faults and integration of faults of regional significance external to the reservoir. For this purpose, it is necessary to expand the database with information relative to the regional geology, such as: geological and structural maps at regional scale, geological sections and 2D seismic sections, location, and profiles of wells outside the reservoir, information on studies related to neighboring fields and analogues.

Usually, outside the reservoir area there is no 3D seismic data coverage and the number of wells available is very low.

Particular attention must be paid to the modeling of the units above the reservoir as they are affected by the effects of pressure variations induced by the production/injection operations in the reservoir.

To keep the number of cells relatively low (thus limiting computational times) the dimensions of the model cells are progressively increased from the reservoir area (where the original dimensions are maintained) towards the peripheral and deep areas of the model, which are scarcely affected by the consequences of pressure variations in the reservoir.

The grid thus defined will subsequently be used for mechanical analyzes.

## Dynamic model

The purposes of a fluid-dynamic numerical model (*dynamic model*) are many, but the main one is certainly the evaluation of the expected performance of the wells and the estimation of the final recovery/injection of fluids under different development and/or production/injection scenarios.

The definition of a dynamic model requires the integration of data of different nature and from different sources:

- permeability and its anisotropy through laboratory tests (*Routine Core Analysis*)
- rock-fluid interaction parameters such as capillary pressures and relative permeability curves, obtained from laboratory tests (*Special Core Analysis*)
- chemical and thermodynamic properties of fluids sampled and analyzed in the laboratory
- well tests
- production data such as flow rates of injected/produced fluids
- static and dynamic well pressures
- well completions

Preliminary to the construction of the model, according to the available data and past production/injection history, a series of analysis are carried out:

- interpretation of the static pressure data acquired at different wells in different moments during the life of the reservoir
- interpretation of well tests
- application of analytical methods based on the material balance equation.

The information that can be obtained about any hydraulic compartmentalization of the system, volume of fluids originally in place and production mechanism are fundamental for acquiring a better knowledge of the system and therefore for the subsequent fine-tuning and calibration of the dynamic model.

Once characterized by all the petrophysical parameters, PVT, rock-fluid interaction properties, fluid contacts, initial thermodynamic conditions and well location, type and completion, the dynamic model is initialized and, in the presence of a previous production/injection history, subject to a calibration process by which the most uncertain input parameters are fine-tuned in order to reproduce the historical behavior of the reservoir in terms of recorded flow rates and static pressures measured at the wells. At the end of the calibration process, the dynamic model is assumed to represent a reliable tool for predicting the future behavior of the reservoir (Mattax et al., 1990).

## Mechanical model

The mechanical model allows us to predict the stress field variation and the deformation response of the reservoir and neighboring formations due to production/injection of fluids and therefore, to assess rock integrity and fault stability and to investigate the spatial and temporal evolution of subsidence.

The definition of a mechanical model requires the integration of the static and dynamic study with about the stress-strain behavior of the modeled formations. The geotechnical parameters are generally obtained both from laboratory tests and in situ investigations. Laboratory mono or triaxial compression tests on rock samples are performed to define the deformation behavior (i.e.: Young's modulus, Poisson's ratio, etc.) and resistance of the material (e.g.: cohesion and friction angle relative to the Mohr - Coulomb criterion). Young's modulus can also be obtained at the well or field level through the analysis of sonic and density logs and through the interpretation of the seismic data, respectively. By nature, laboratory data provide accurate but very local information, while data at the well or reservoir scale are able to capture the heterogeneity of the system - although to the detriment of accuracy or resolution of the information. In the following the analysis of flow phenomena and deformation phenomena will be considered one-way coupled and consequently the corresponding model solved sequentially. Conversely, in the case of a totally coupled approach, correlations between the matrix deformation behavior and variation of the petrophysical parameters are also necessary. In addition to the cited strain and strength parameters, information about the principal stresses is also required, the minimum of which can be obtained by in situ fracturing tests.

Since the volumes simulated by mechanical models are often considerable (extension in the order of tens of kilometers), the direct characterization of the geological formations is excessively expensive and, moreover, does not bear any significant added value. It is therefore common practice to analyze samples retrieved from the reservoir or from the aquifer, directly affected by the stress changes and deformations induced by the production/injection operations, and their cap rock.

Once suitably characterized through the assignment of deformability and resistance parameters, the geomechanical model is initialized, i.e. the distribution of the interstitial pressures and the stress field of the undisturbed formations are assigned accordingly to depth, lithology, depositional history and saturating fluids.

If the mechanical analysis is carried out separately from the dynamic one, the link between them is constituted by the variation of the field pressure: it is provided by the dynamic simulator and represents the input to the mechanical model. In such approach the calibration processes of the two models are completely independent and generally sequential.

## FEM and VEM

The *Principle of Virtual Work* formulation of the linear momentum balance equations (recalled in the previous Chapter) represents the starting point of the formulation of Finite Element Methods (FEM). FEM belong to the family of numerical resolution methods and allow one to evaluate an approximation of the solution of the variational problem in discrete points of the domain. The Finite Element Methods (FEM) theory was formulated starting from the 1950s and since then has found application in the numerical modeling of physical systems in a wide variety of engineering disciplines (Gockenbach, 2006). In brief, FEMs solve differential problems, expressed in their variational form, partitioning the domain in blocks of simple form (elements) such as triangle/tetrahedra or quadrilateral/hexahedra. On each element the solution of the problem is expressed by the linear combination of piecewise polynomial functions of fixed degree whose coefficients (degrees of freedom) become the unknowns of the resulting algebraic problem descending from the spatial discretization. In practice, on three-dimensional geometries, the analysis domain is partitioned into elements typically of tetrahedral or hexahedral shape since some limitations arise to the definition of low order basis on more complex shaped elements. The method is applicable, however, only on grids that comply with the conformity criterion, i.e. it is necessary that adjacent elements share the same degrees of freedom at their interface. It follows that on particularly complex geometries (for example with discontinuities) it is necessary to define a high number of elements, and consequently degrees of freedom, to satisfy the conformity principle.

Recently, an innovative method of numerical simulation has been proposed which takes the name of the Virtual Elements Method (VEM). It is the latest evolution of the Mimetic Finite Difference (MFD), with various points of contact with the FEM so as to represent an important generalization ((Beirão da Veiga et al., 2017, 2016a, 2014, 2013a). Although very recent, this method has already found application in the modeling of problems related to different engineering disciplines

including problems of fluid dynamics and linear elasticity (Andersen et al., 2017; Beirão da Veiga et al., 2013b; Benedetto et al., 2016; Gain et al., 2014).

The key aspect of this approach consists in preserving the polynomial accuracy that is ensured on tetrahedron (three-dimensional simplex) on not necessarily convex polyhedral elements and in the presence of hanging nodes. The innovative feature consists in the use of a local approximation space which includes polynomial functions that do not have explicit expression (hence the name of *virtual elements*). Indeed, explicit integration of shape functions for the stiffness matrix evaluation is avoided, thus it is only necessary to carefully choose the degree of freedom of the elements where the solution is calculated to preserve the method stability and accuracy. All this is possible by applying suitable projection operators (which can be evaluated thanks to the choice of the degrees of freedom) in place of the unknown polynomial functions for the determination of the components necessary for the evaluation of the solution (Ahmad et al., 2013). Thus, VEM is based on a theoretical framework sufficiently general to allow some of the FEM limitations to be overcome such as typology of elements used to discretize the domain or the applicability to non-conforming grids (Gain et al., 2014). Furthermore, with the same order of convergence, the VEM solution provides a representation of the exact solution with an accuracy similar to that obtained by the FEM.

From these first considerations, it is evident that the discretization of the domain plays a fundamental role in the solution process not only in terms of accuracy of the solution, but also in terms of necessary computational time. In the case of geomechanical applications, such as subsidence/rebound assessment and safety analyses, complex geometries must be discretized due to the presence of pinch-outs, i.e. progressively thinner geological bodies, as well as structural discontinuity (such as faults) characterized by strong throw that must be adequately reproduced in the grid construction. Using only hexahedral/tetrahedral elements for discretization could therefore generate problems of numerical stability caused by the presence of degenerate or excessively irregular elements. For this reason, the best choice for the discretization of the domain is the use of elements of different types that offer an adequate representation of the structural model. Although both FEM and VEM methods do not have theoretical limitations to the use of generic polyhedrons for the numerical solution of PDE, the use of FEMs on hybrid grids often requires a laborious implementation while the VEM formulation preserves a certain degree of "simplicity". Furthermore, since VEMs do not require conformity between adjacent elements, it is possible to use different degrees of approximation

in distinct elements, reproducing the solution with great accuracy only on the portions of main interest of the domain, with a consequent saving in terms of computational cost.

# Chapter 4

## Gridding

The process of volume discretization for simulation purposes is strictly linked to the process of structural modelling introduced in the previous chapter which integrates information coming from different data sources with the aim of describing with accuracy the stratigraphic structure of the underground. In summary, sedimentary formations are the expression of three main phenomena: sedimentation - which produces thin layers; faulting - which can cause connection between layers not originally communicating; and erosion - which produces degenerated layers. Therefore, the gridding process begins from creating a structural mesh by exploiting available information about faults and stratigraphy. In the technical literature two different approaches can be identified for volume discretization, namely the definition of structured hexahedral grids (*corner-point grids*) that follow the profile of faults and stratigraphic surfaces, and the generation of unstructured tetrahedral or polyhedral grids "which fill the regions" identified by the above-mentioned constraining surfaces or derive the grid from parametric transformation. Corner-point grids are results of the pillar-gridding approach and represent the standard approach in the oil&gas industry (K. Ponting, 1989). This approach is currently implemented in the Petrel E&P software platform (Schlumberger, 2020a) and exploited by the integrated reservoir simulator Eclipse (Schlumberger, 2020c) and the mechanical simulator Visage (Schlumberger, 2020b). In the resulting hexahedral discretized volume, the structural constraints produce elongated cells in the areal direction, sometimes degenerated with respect to the original topology and with evident distortions at the faulting surfaces. The

second approach has a relevant example in the SKUA-GOCAD software (Emerson, 2021), which implements the *uvr-transform* (from the geological grid to a parametric grid) formalized by Mallet (Mallet, 2004). The algorithm tries to overcome some limitations of the pillar-gridding approach in the accuracy of the description of the sedimentary formations, having the capability of representing complex geological structures and introducing highly deformed cells.

Recognizing the importance that pillar-gridding strategy still currently holds in UGS related simulation, in the present project the choice was made to integrate a C++ parser that is able to read the grid generated by Visage and to convert it into the open source format *vtu* (Visualization Toolkit Unstructured grid) (Schroeder et al., 2006) as it is briefly described in the next paragraph.

Subsequently, the formalized and implemented process for the generation of unstructured tetrahedral grids, constrained to stratigraphic and fault surfaces resulting from geological modeling, is described. In the presented validation cases it was assumed that the surfaces derive from a Petrel E&P modelling process. However, the proposed algorithms are of completely general validity.

## Corner point gridding parser

From a general point of view corner-point grids can be defined as the hexahedron tessellation of the  $\mathbb{R}^3$  Euclidean space. Each cell is defined by the assignment of eight not necessarily distinct vertices (*corners*) which, in turn, belong to a two-dimensional Cartesian partition of the xy-plane called *pillars*, identified by the couple of  $ij$  indexes. Pillars are straight lines with dominant vertical direction defined by two end points which respectively belong to the top and to the bottom surfaces bounding the discretization domain. Pillar directions derive from fault modelling whereas the discretization along pillars (span by  $k$  index) depends on the horizons position. The number of discretization points along the pillars is set constant. It follows that each node in the grid is identified both by spatial coordinates  $xyz$  and by a corresponding index triplet  $ijk$ . The cell volume is defined connecting four couples of nodes belonging to four distinct adjacent pillars as shown in Figure 15. In Figure 16 a corner-point grid with a single fault (in red) and layers given by sinusoidal surfaces is represented. It was generated with the Matlab® Reservoir Simulation Toolbox (MRST) 2021a (SINTEF, 2021), a free open-source software for reservoir modelling and simulation, developed primarily by the Computational Geosciences group at the Department of Mathematics and Cybernetics at SINTEF Digital (Lie et al., 2012; Lie, 2019).

In the specific case of the Petrel E&P platform, information related to the pillar-gridding structure are encoded in ASCII DATA format shared with the Eclipse reservoir simulator, for which the model information is organized in a set of keywords (Schlumberger, 2020d). The ones of interest related to the grid are:

- SPECGRID identifies specification of grid characteristics: number of grid blocks along the coordinates Cartesian axes.
- MAPAXES identifies the input of pre-processor map origin: transformation from the global to the local model coordinates.
- COORD identifies coordinate lines: two triplets of xyz-coordinates for each pillar representing two distinct points on it. The number of specified items is equal to  $2(n_x + 1)(n_y + 1)$  where  $n_x$  and  $n_y$  are the number of cells in the xy-plane in the x and y direction, respectively.
- ZCORN identifies depths of grid block corners. The number of specified items is equal to  $6n_x n_y n_z$ . The depth values for each vertex of each cell of the grid is specified by scanning the grid by  $i$ -rows starting from the top surface.

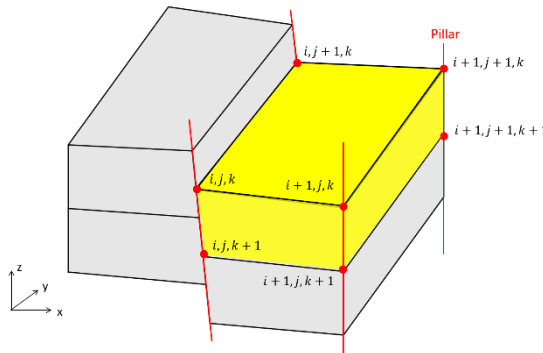


**Figure 15:** corner-point grid cell (yellow) defined through the specification of eight vertices (red bullets) identified by the  $ijk$  index triplet. Red lines represent the pillars.

The decoded pillar gridding was then transformed in the corresponding unstructured grid object available in the Visualization ToolKit (VTK) (Schroeder et al., 2006). This is an open-source software for manipulating and displaying 3D scientific data which found application to a wide variety of real-world problems. Moreover, the VTK's fundamental data structures are particularly well-suited to engineering problems that involve finite difference and finite element solutions. In the following, the generic `vtkUnstructureGrid` class, a concrete implementation of `vtkDataset` class, is exploited (I. Kitware, 2021). An unstructured grid object can be

made up of any combinations of any cell types: 0D (points), 1D (lines, polylines), 2D (triangles, polygons), and 3D (hexahedron, tetrahedron, polyhedron, etc.). It provides random access to cells, as well as topological information.

The coded parser, then, converts each cell deriving from corner-point grid structure into a mix of hexahedron and polyhedral cells. Since the original discretization tolerates the presence of degenerated cells and possibly not planar faces, specific routines were implemented to recognize elements with coincident vertices. To study the impact of the presence of not planar faces, instead, the triangulation strategy of not planar quadrilateral proposed in the MRST library was applied: the barycenter of not planar faces is introduced, converting a hexahedron into a generic polyhedron. A grid refinement process is then implemented by splitting polyhedral cells into a set of tetrahedrons to verify the impact of the grid refinement in the reservoir. An example of the sequence for the transformation of a generic cell is depicted in Figure 17. Simulations performed on grid derived from the Petrel E&P workflow are processed to validate the methodology using the parser here introduced and whose main steps are recapped in Figure 18.

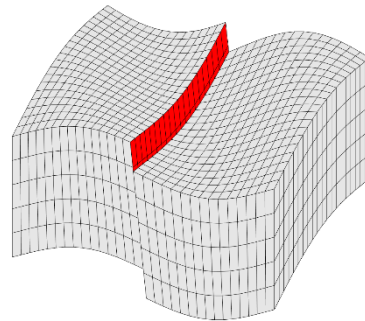


**Figure 16:** example of pillar gridding model with a single fault and layers given by sinusoidal surfaces (fault faces are marked in red).

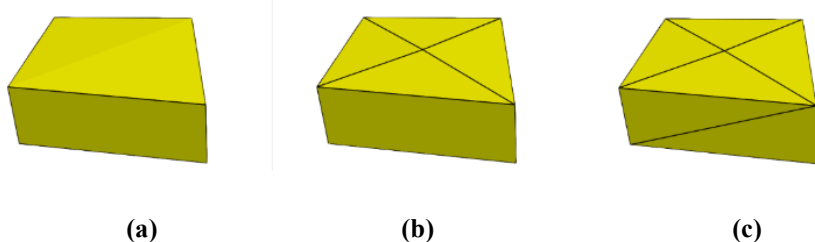


**Figure 17:** cells splitting procedure: (a) original hexahedral cell. (b) polyhedral cell obtained by triangulation of not planar faces through insertion of face barycenter. (c) tetrahedral decomposition.

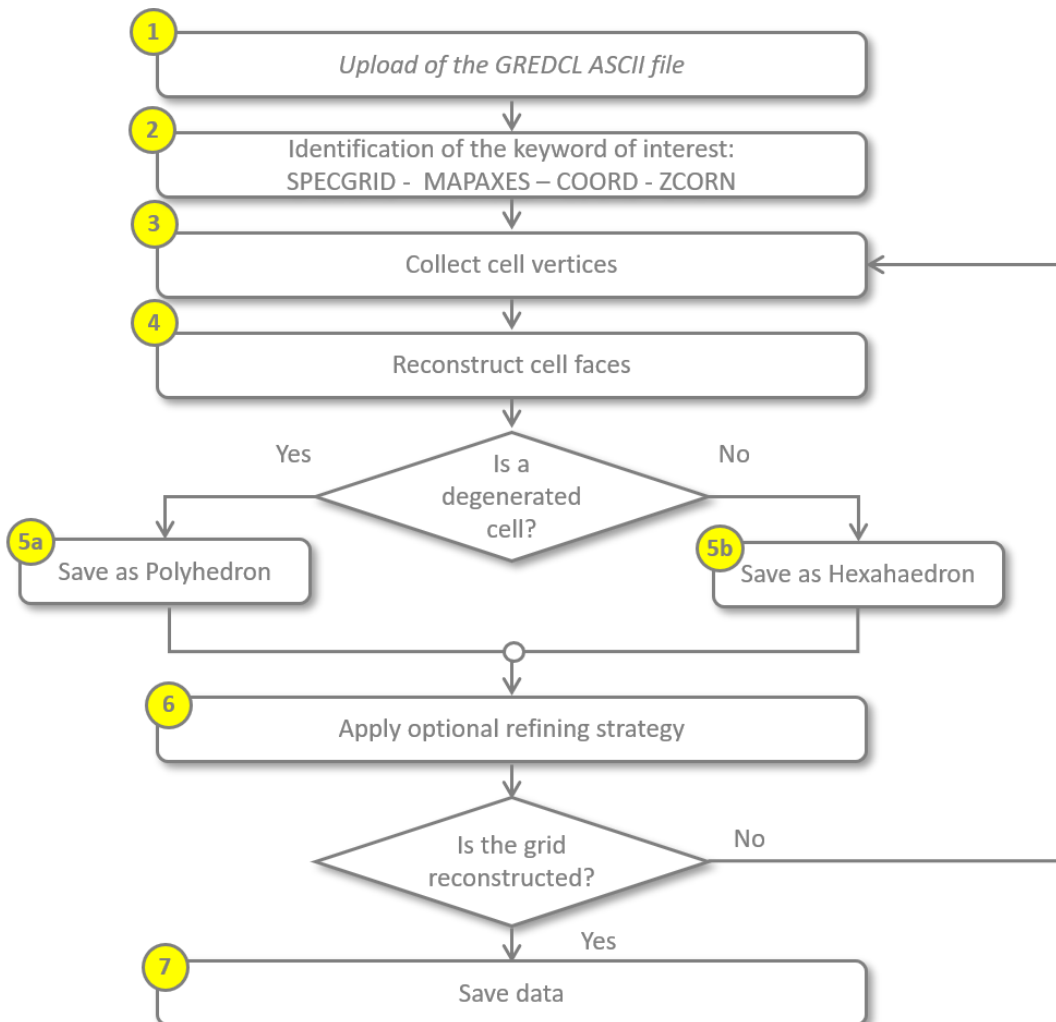


**Figure 18:** workflow of the corner-grid parser

## Unstructured grid construction workflow

As previously mentioned, the definition of the numerical mesh for geological applications is historically constrained to stratigraphic and fault surfaces that represent the main spatial elements guiding both the zoning process and the numerical discretization of the volume of interest. In the following the formalized and implemented workflow for the construction of the mesh is presented. It is defined according to the step sequence shown in Figure 19 and it allows one:

- to generate a 2D Delaunay triangulation of each surface with quality mesh control in terms of minimum angle and maximum area of each triangle, with a reduced computational cost. The triangulation is constrained to the *Planar Straight Line Graph* constituted by the *Concave Hull* of the 3D point cloud projected on the *Best Fitting Plane*. The presented process is based on the algorithm proposed by Park and Oh (Park and Oh, 2012) and on the derived Geological Surface Reconstruction method sketched in Figure 20 and published in (Serazio et al., 2021). The *Eigen* library (Guennebaud et al., 2010) was exploited to perform linear algebra operations and the *Triangle* library (Shewchuk, 1996) for the *Convex Hull* calculations and constrained Delaunay Triangulation.
- to integrate all the surface triangulations in an object conforming to the input required by the tetrahedrization library *Tetgen* (Si, 2015) which represents the core of the discretization process of the modeled volume.

Necessary input require that the stratigraphic surfaces come from a geological interpretation, or that they have been adjusted at the wells. In the implemented code, an interpolation function of the stratigraphic surface points has been integrated, thus making unnecessary that all the stratigraphic surfaces are sampled at the same points of the plane to evaluate possible intersections.

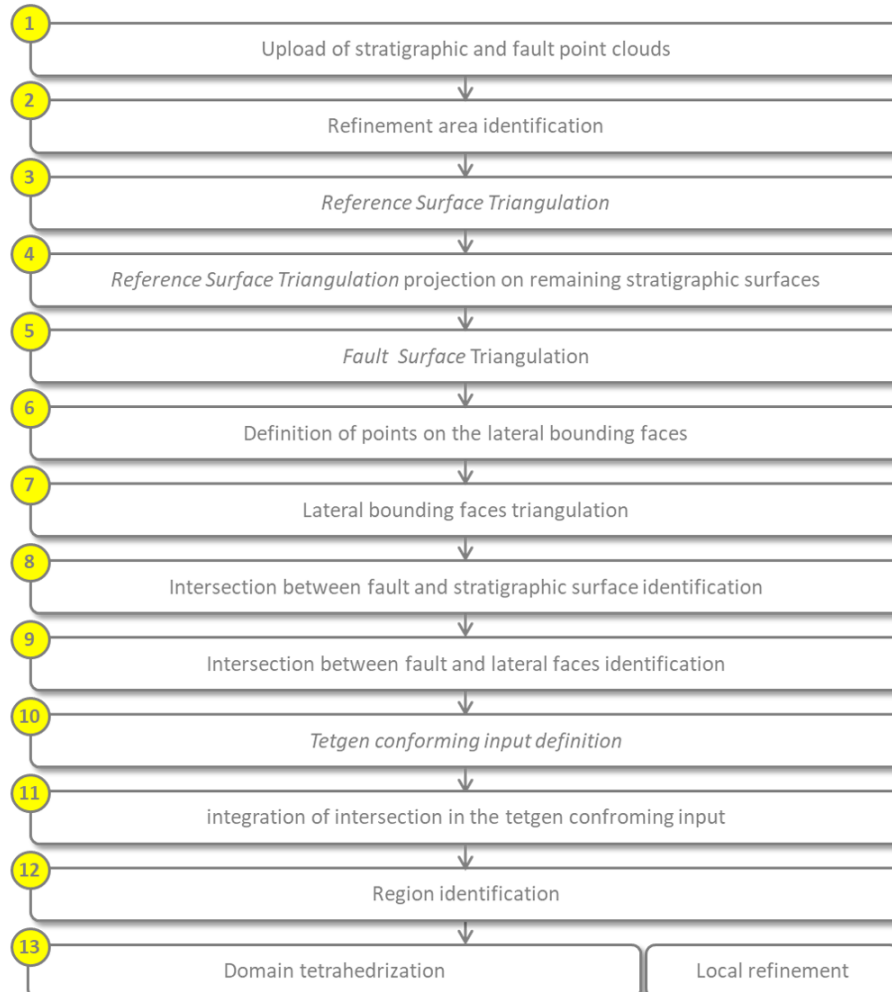


**Figure 19: workflow for the grid generation**

As already mentioned, it is also possible to upload and triangulate fault surfaces, which are not necessarily flat and with an arbitrary orientation in the space. In the following paragraphs the methodologies and algorithms used for the triangulation of the individual stratigraphic surfaces (Step 3) and of the fault surfaces (Step 5) are illustrated.

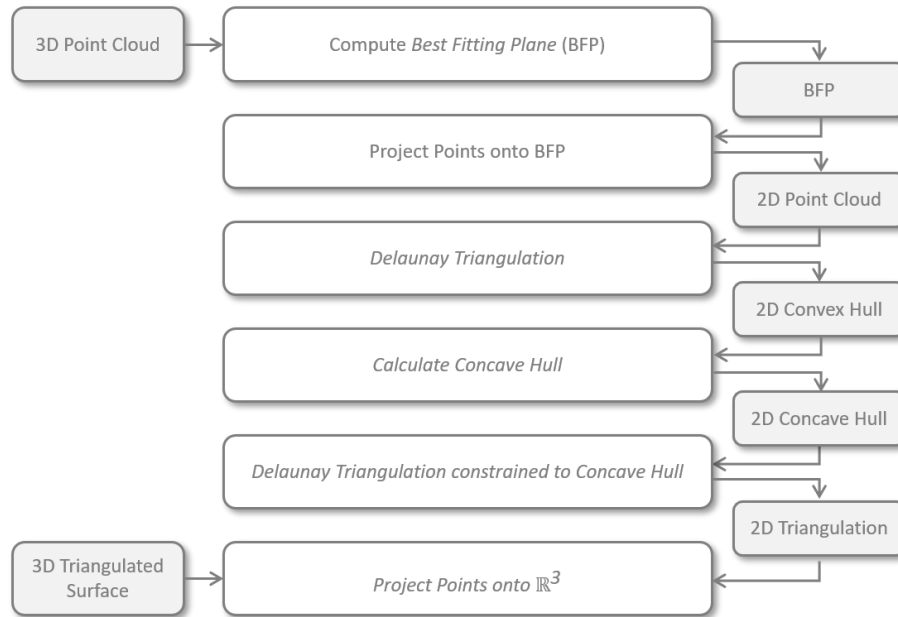


**Figure 20: main steps of Surface Reconstruction of Geological Surface from Point Cloud (Serazio et al., 2021)**

By way of example, Figure 21, Figure 22 and Figure 23, respectively sketch steps 1, 3, 4, 7 and 10 of the above workflow, through the generation of the grid for a synthetic case. In particular, it is assumed that the geometry of the model is defined by four already extended stratigraphic surfaces (Figure 21), i.e. whose areal dimensions correspond to those of the geomechanical model.

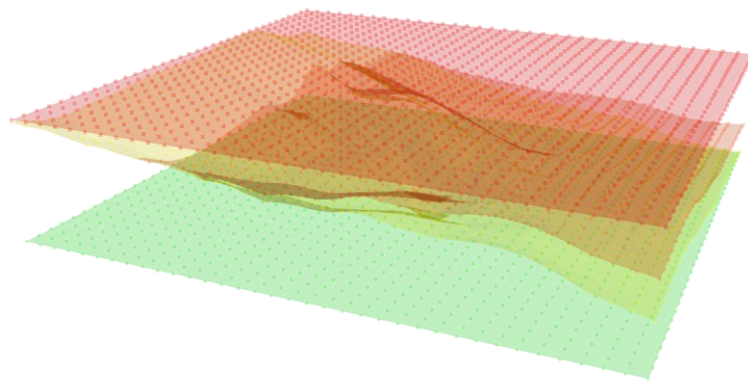


**Figure 21: sequence of stratigraphic surfaces defining the model domain (Step 1).**

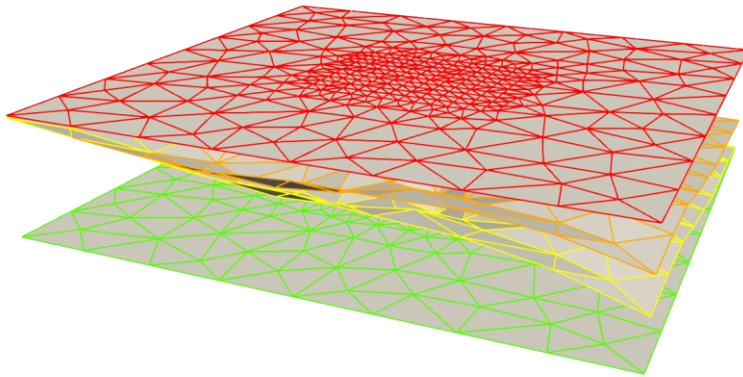


**Figure 22: triangulation of the reference stratigraphic surface (red) and projection of the triangulation on the underlying surfaces (Step 3 and Step 4).**

In the implemented process, it was decided to apply the triangulation algorithm only to the reference surface, typically ground level, and to project the obtained discretization on the underlying surfaces, interpolating points on the surfaces, if necessary, as illustrated in Figure 22.

Successively, the option of adding "fictitious" stratigraphic surfaces to the current mesh was also implemented to increase the level of detail of the vertical discretization or to define portions of the model with homogeneous geomechanical behavior (this comes very handy for the subsequent characterization phase); in particular, such "fictitious" surfaces can be defined in three different ways:

1. constant depth assignment for the entire areal extension of the model
2. grid translation of a pre-existing surface
3. convex combination of two pre-existing surfaces

Therefore, in the following all the stratigraphic surfaces share the same sampling on the XY plane: this allows one to easily verify and manage the presence of intersections between surfaces or pinch-outs. Furthermore, a threshold distance (equal to 0.05 m) between two points of distinct surfaces was defined. Below such a value, two points are considered coincident.

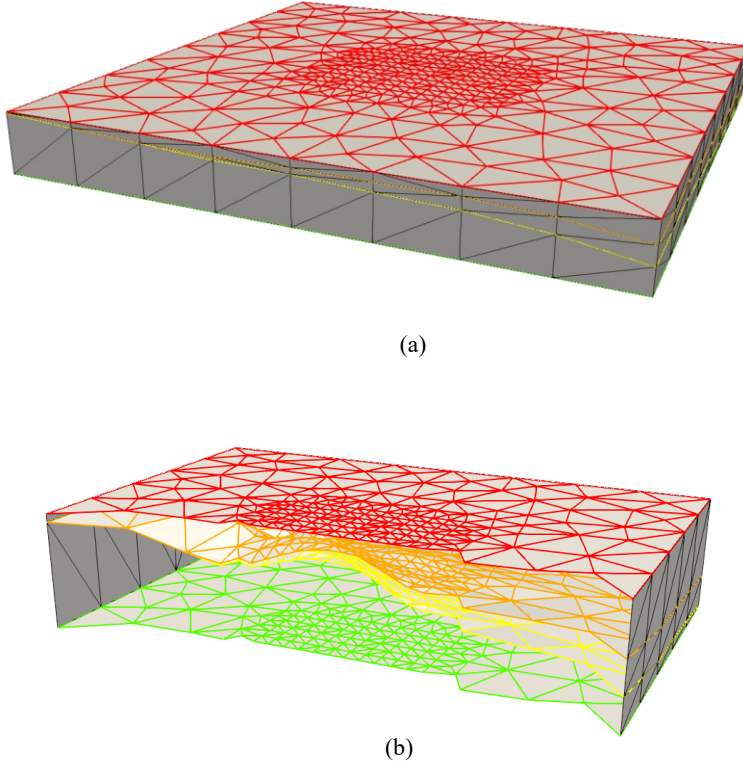


**Figure 23: triangulation of the lateral faces (Step 7). In evidence the intersection between the lateral faces and the intermediate stratigraphic surfaces (a). Section of the model orthogonal to the Y direction (b).**

The sequence of triangulated surfaces represents the input data of the next processing step which involves the identification of the boundary points for each surface and the assignment to the corresponding side faces. Figure 23a and Figure 23b illustrate the result of the triangulation process (constrained to the edge points of the stratigraphic surfaces) of the single lateral faces, both in perspective and along the section orthogonal to the Y direction.

The global constraining mesh is obtained from the incremental union of the triangulations of all the surfaces which define the model geometry. It must be conforming, i.e. the triangles must not have reciprocal intersections, in order to be set, in turn, as a constraint for the tetrahedrization algorithm implemented in the *Tetgen* library. As result of the discretization process, a tetrahedral volume is thus obtained. In Figure 21, a section orthogonal to the Y direction of the global mesh is

shown. In the example the obtained grid has a spatial extension of about 17 km x 17 km for a depth of 2 km and includes about  $6.3 \cdot 10^3$  nodes.

The *Tetgen* library provides a functionality for the identification of regions delimited by the stratigraphic and fault surfaces (and laterally constrained by the lateral surfaces), as shown in Figure 25. This algorithm allows one to characterize the obtained discretized volume referring to the region indexes assigned to each cell.

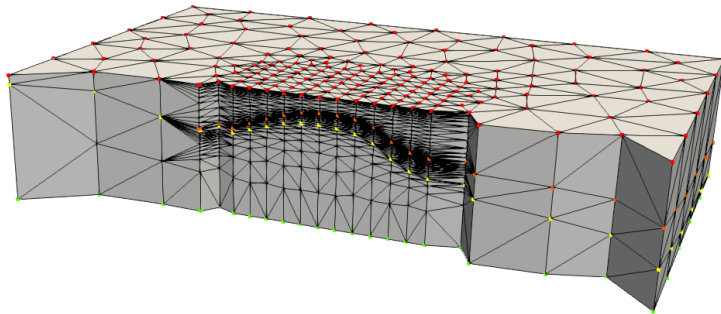


**Figure 24:** sectional view of the tetrahedralized computing domain (Step 13). The stratigraphic surfaces that represent the constraints in the process of generating the 3D grid are highlighted.

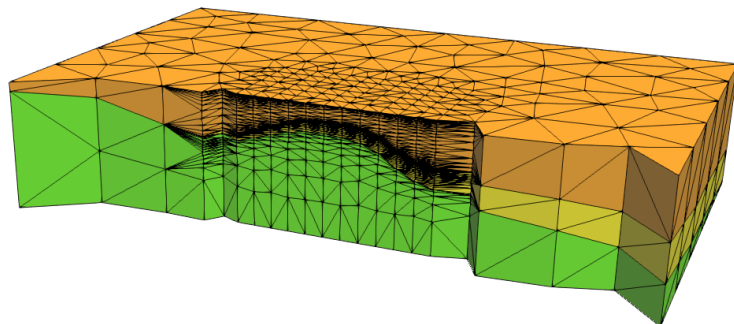


**Figure 25:** sectional view of the tetrahedralized computing domain. Regions identified by the *Tetgen* library (Step 12) are highlighted with different colors.

## Stratigraphical surface triangulation

The triangulation of the stratigraphic surfaces represents the first phase in the process of tetrahedrization of the computational domain. Figure 26 illustrates the steps of the implemented workflow. First, it provides a procedure for importing the stratigraphic surfaces point clouds which are supposed to be stored as a sequence of  $\mathbb{R}^3$  cartesian points coordinates ( $x$   $y$   $z$ ). At the same time, the feature for importing the surfaces according to vtkPolyData data structures formats made available by VTK (Schroeder et al., 2006) is set up. In addition, a dedicated flag allows one to distinguish between imported surfaces that need a further extension from those already extended to the edges of the model.

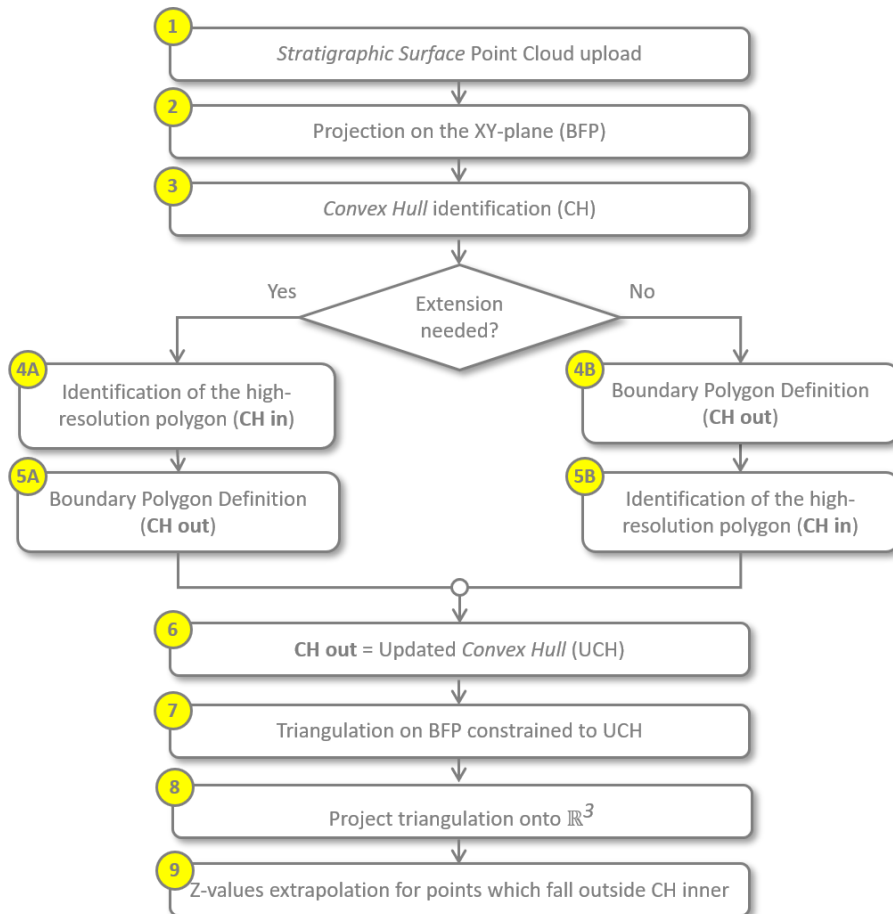


**Figure 26: stratigraphic surface reconstruction from 3D point cloud**

In the construction process of the model geometry, it is assumed that at least one stratigraphic surface is provided. Generally, when a single stratigraphic surface

is available, it corresponds to the *top of the reservoir*. Its point coordinates on the XY-plane are exploited to define a top and a bottom surface to limit the model. It is exactly the top surface, i.e., the seabed or the ground level, the reference surface to which the triangulation process is applied. The obtained discretization is then projected onto the underlying surfaces.

In general, the application of the triangulation algorithms available in *Triangle* requires the projection of the 3D surface point cloud on the plane that best approximates it (in the sense of least squares). However, for the intrinsic characteristic of stratigraphical surface point cloud, their BFP is assumed to coincide with the XY-plane of the current Cartesian coordinate system. In the absence of additional constraints, the *Triangle* library generates a 2D Delaunay triangulation constrained to the *Convex Hull* of the point cloud in the two-dimensional reference system. However, as shown in Figure 30a, (*Convex Hull* in red) the resulting triangulation, projected back to the three-dimensional space, is unacceptable as it is made up of triangles that join together points that should be tagged as boundary and/or triangles that do not conform to the shape of the original surface and characterized by minimum angles of the order of a tenth of a degree that could potentially generate numerical instabilities in the calculation of the stress and strain fields. From a general point of view, it should be necessary to update the boundary polygon to identify the *Concave Hull* that properly approximates the boundary of the 2D point cloud and it should be assigned as constraint to the triangulation algorithm. As an example, in Figure 30b is shown the triangulation obtained from the *Concave Hull* as boundary (green line). The algorithm proposed to define from the one of Park and Oh (Park and Oh, 2012) whose main idea was to incrementally “dig” the *Convex Hull* by splitting the current boundary edges in two sub-edges by including a point of the cloud that was previously classified as internal. The admissibility of the new boundary node is verified exploiting the *point-in-polygon* strategy whose implementation can be found in (*Graphics Gems IV*, 1994) and whose criticalities are discussed in (Schirra, 2008). Details in the implemented methodology can be found in (Serazio et al., 2021).

It is noticed that, when projected on the XY-plane, the point cloud results in a regular sampled set aligned with the coordinate axes or diagonals, as shown in Figure 27. Thus, the algorithm was specifically tailored exploiting this regular spatial pattern.

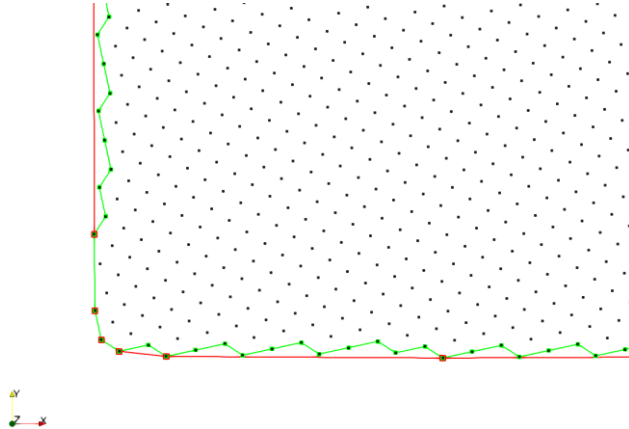


**Figure 27:** detail of the XY-plane point cloud projection (black). Points result equally spaced and aligned with diagonals. the initial *Convex Hull* and corresponding *Concave Hull*, in green and red, respectively.

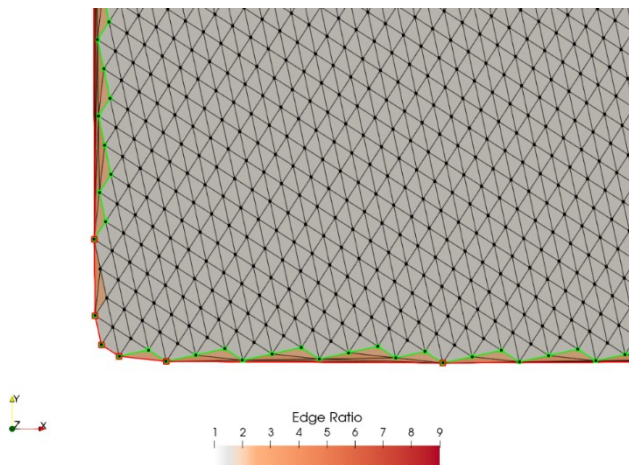


**Figure 28:** detail of the XY-plane point cloud projection. The colormap refers to edge ratio of the triangles of the triangulation constrained to the Convex Hull (red nodes). The mean value of the edge length distribution it is approximately 14. Triangles external to the final Concave Hull (green) show edge-ratio that deviate from the mean becoming candidates to be removed from the triangulation.

Initially, the mean and the standard deviation of the triangle edge length of the distribution of the triangulation constrained to the *Convex Hull* were calculated. Such quantities defined, in turns, the threshold used to discriminate if a triangle can concur to the refinement of the *Concave Hull* or not. To clarify this passage, let us consider a detail of the starting triangulation in Figure 28, where the color map describes the trend of the edge ratio, i.e., the measure of the mesh quality calculated as the ratio between the maximum and the minimum edge length of each triangle of the grid. Due to the regularity of the point sampling, it assumes values roughly

constant (about 1.4) over the whole domain. Triangles characterized by edge ratio that deviates from the mean value are exclusively close to the boundary polygon where the *Convex Hull* (in red) does not adequately describe the point cloud profile. Furthermore, it is observed that they are all external to the *Concave Hull* (in green) supporting the strategy that want to exclude such triangles from the discretization.

The proposed methodology proved to give satisfactory results in terms of surface reconstruction as shown in the two validation cases, denoted as *Surf Top* and *Erosional 50*, whose main parameters are summarized in Table 1 and the corresponding triangulations are shown in Figure 29-Figure 30 and Figure 31-Figure 32, respectively.

**Table 1: example of reconstruction of stratigraphic surfaces. The main parameters are reported: number of cloud points, sampling increment, dimension of the *Convex Hull* and the *Concave Hull* and corresponding triangulation (Serazio et al., 2021).**

<b>Case</b>	<b># Points</b>	<b>Sampling</b>	<b><i>Convex Hull</i></b>		<b><i>Concave Hull</i></b>	
			<b># nodes</b>	<b># triangles</b>	<b># nodes</b>	<b># triangles</b>
<i>Surf Top</i>	34635	150 x 150	32	69236	627	68641
<i>Erosional 50</i>	7335	50 x 50	23	14645	353	14315

However, the application of the proposed methodology directly to the surfaces who define a Geomechanical model can produce issues related to the resolution of the final volume tetrahedrization. In fact, since the triangulated surfaces represent the input constraints of the tetrahedrization procedure, the resulting tetrahedral mesh must comply with their triangle size to preserve conformity. It follows that, if the stratigraphical surface is sampled with a constant step for the whole spatial extension of the domain, the mesh could be inadequate to describe with sufficient accuracy the analyzed phenomena, or conversely, it could have a high level of refinement in zones were coarsening would be preferable.

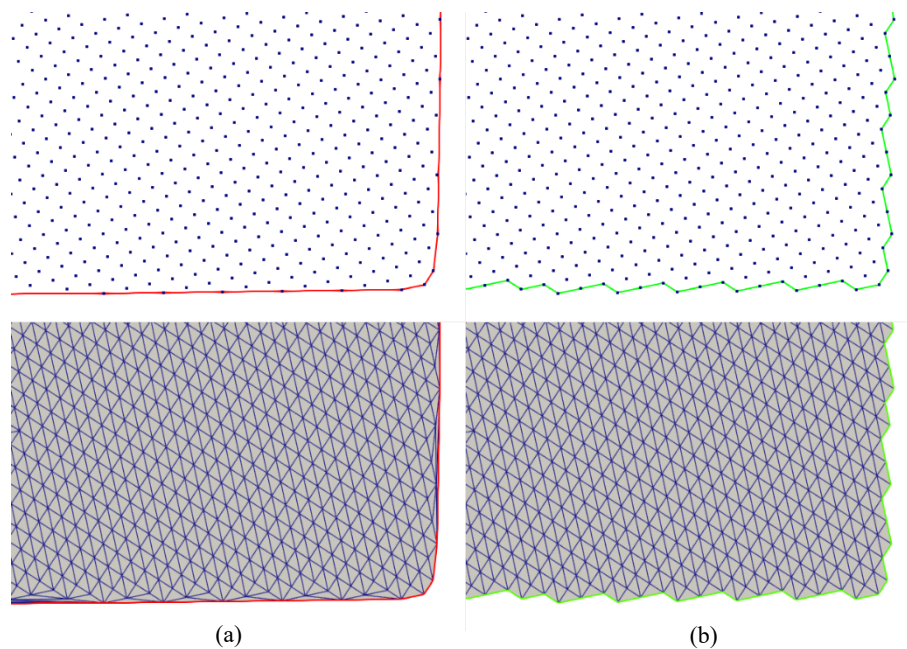


**Figure 29:** *case Surf Top - detail of the XY-plane point cloud projection: initial Convex Hull constrained triangulation (red) (a) and corresponding Concave Hull constrained triangulation (green) (b)* (Serazio et al., 2021).

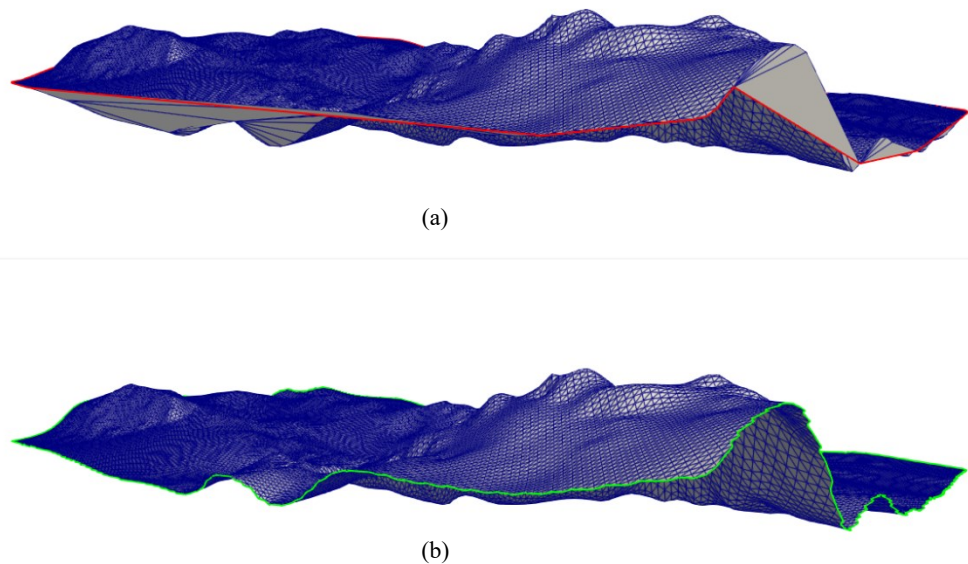


**Figure 30:** *case Surf Top - original Cartesian coordinate system comparison between the initial Convex Hull constrained triangulation (red) (a) and corresponding Concave Hull constrained triangulation (green) (b)* (Serazio et al., 2021).

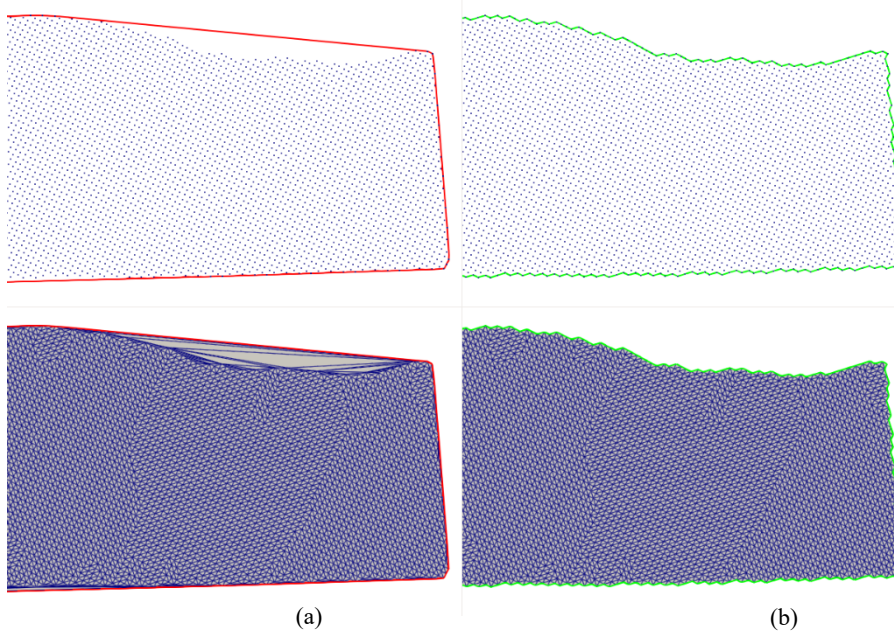


**Figure 31:** *case Erosional 50 - detail of the XY-plane point cloud projection: initial **Convex Hull** constrained triangulation (red) (a) and corresponding **Concave Hull** constrained triangulation (green) (b)* (Serazio et al., 2021).

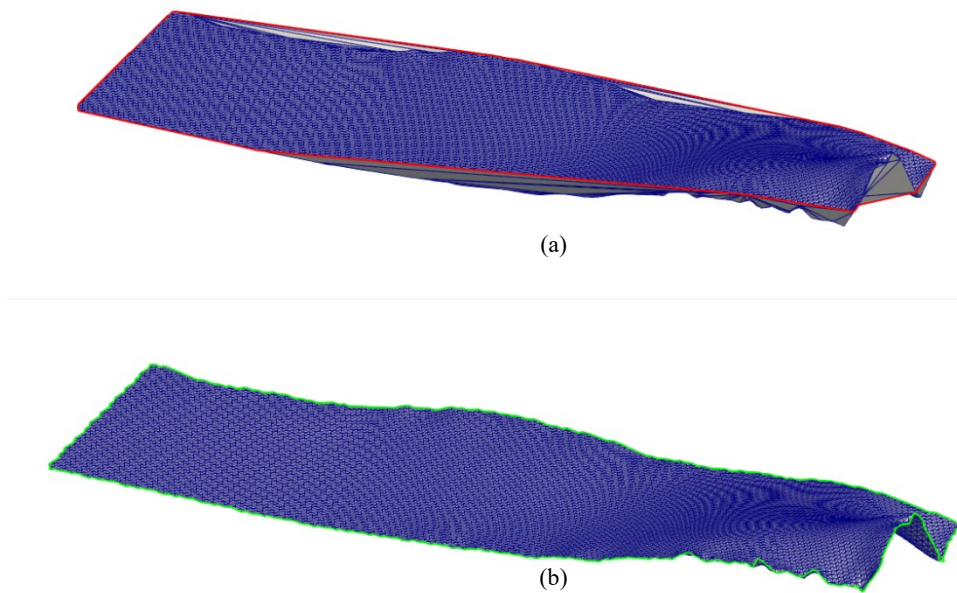


**Figure 32:** *case Erosional 50 - original Cartesian coordinate system comparison between the initial **Convex Hull** constrained triangulation (red) (a) and corresponding **Concave Hull** constrained triangulation (green) (b)* (Serazio et al., 2021).

For this reason, in the proposed workflow two further steps were implemented (step 4 and 5 of Figure 26), i.e., the identification of an inner area where constant high-resolution spacing is set ( $CH_{IN}$ ) and an outer zone where increasing triangle size is allowed ( $CH_{OUT}$ ). A distinction between surfaces that need extension and already extended surfaces was done, branch (a) and (b) of Figure 26, respectively.

In the case of an input stratigraphic surface that must be extended, the identification of the vertices of the polygon that delimits the geomechanical model  $CH_{OUT}$  is performed by extending  $CH_{IN}$  uniformly in both directions, i.e., extending the smallest quadrilateral containing the input surface projected on the XY-plane ( $CH_{IN} \rightarrow CH_{OUT}$ ). Alternatively,  $CH_{OUT}$  can be input as a convex polygon with arbitrary number of edges, thus the algorithm verifies that is the *Convex Hull* of the reference surface point cloud is included in the  $CH_{IN}$ . Sketch in Figure 33a.

The triangulation of the input point cloud is obtained exploiting the *Triangle* library through the imposition of a minimum angle constraint equal to  $30^\circ$  to the resulting mesh (Figure 34). This procedure allows for a high-level detail triangulation in the area of interest, with triangles of increasing size as you get closer to the edges of the model (Figure 36a), where variations of the stress and strain fields are negligible.

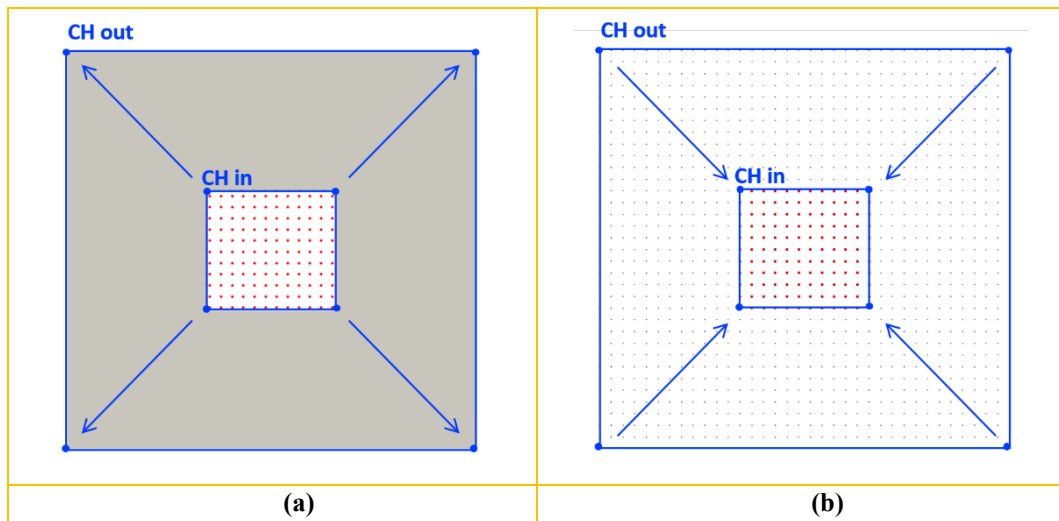


**Figure 33: XY-plane projections of stratigraphic surface point cloud.** In (a) the surface need extension and the outer boundary need to be identified: in red points at high-resolution and in gray the area occupied by the extended stratigraphic surface. In (b) the uploaded surface does not need extension. Conversely the high-resolution zone needs to be identified (points in red). In blue the boundary polygons defined in workflow in Figure 26, step 4-5, a and b, respectively.

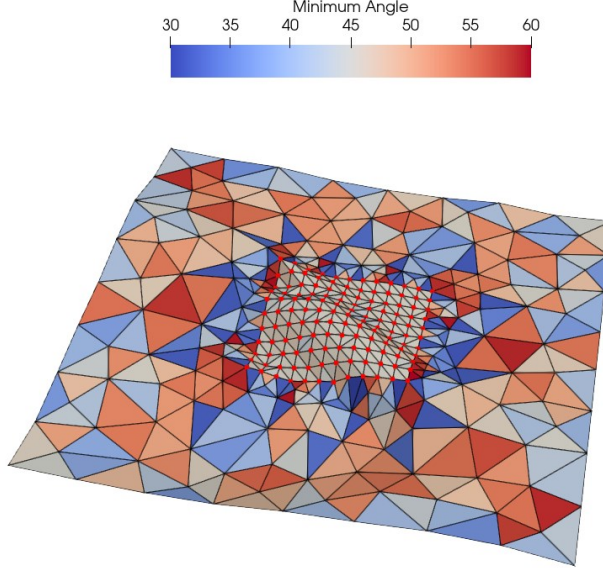


**Figure 34:** detail of the triangulation of an extended stratigraphic surface: measure of the quality mesh is given by the minimum angle of each triangle. Triangulation results from the  $30^\circ$  minimum angle constraints in the *Triangle* library routine.

In the case of an extended stratigraphic surface, instead,  $CH_{OUT}$  is defined by identifying the smallest quadrilateral containing the *Convex Hull* of the point cloud projected onto the XY-plane. Applying the inverse procedure defined for surface extension, the  $CH_{IN}$ , that delimits high-level detail area, is obtained by rescaling  $CH_{OUT}$  uniformly in both directions according to a constant factor ( $CH_{OUT} \rightarrow CH_{IN}$ ) as sketched in Figure 33b. There is also the possibility to set  $CH_{IN}$  as an arbitrary convex polygon that must be strictly included in the current  $CH_{OUT}$ .

The triangulation of an extended stratigraphic surface has therefore been reduced to a problem of triangulation of a surface that requires extension. This approach has the purpose of minimizing the complexity of the resulting grid, in terms of number of points and cells, and consequently to reduce the number of degrees of freedom characterizing the VEM problem solution. It guarantees a high-level of detail in the region of interest and a reduced one closer to the boundary where phenomenology relevance is minimal. In Figure 36a and Figure 36b a comparison between two triangulations of an extended surface is shown: in the former the high-resolution triangulation is guaranteed only in the area of interest, in the latter, instead, the level of detail of the stratigraphic surface is preserved for

the entire areal extension. This example wants to show how the adopted strategy can avoid an excessive increase in the computation cost required for the resolution of the geomechanical problem. However, the triangulation process of the reference stratigraphic surface requires the definition of additional points to preserve the effectiveness of the resulting mesh (Figure 35). Consequently, to complete the surface reconstruction process, it is necessary to assign to each of them an appropriate depth value. In the proposed process this evaluation is carried out applying the interpolation routines available in *Computational Geometry Algorithms Library* (CGAL) (The CGAL Project, 2021) to each input stratigraphic surface.

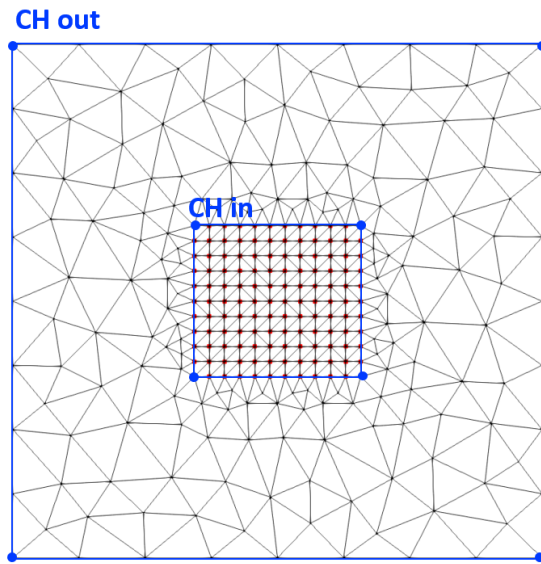


**Figure 35:** resulting triangulation of stratigraphic surface.

In detail, for each triangulation point for which the depth is unknown, a 2D linear interpolation algorithm is used (Flötotto, 2021): the estimated depth value is function of the depth values assigned to the neighboring points. Specifically, the algorithm allows to reconstruct the depth value of each point of the XY-plane within the 2D *Convex Hull* of the original surface input point cloud. In Figure 36 results of the interpolation process are shown: Figure 36a shows the triangulation resulting from the interpolation process applied to the extended surface of Figure 33b. In Figure 36b, instead, the original uniform sampling extended surface is shown. To appreciate the satisfactory level of agreement between the original and the reconstructed surface, a superimposition of the triangulations in the original  $\mathbb{R}^3$  space is shown in Figure 37.

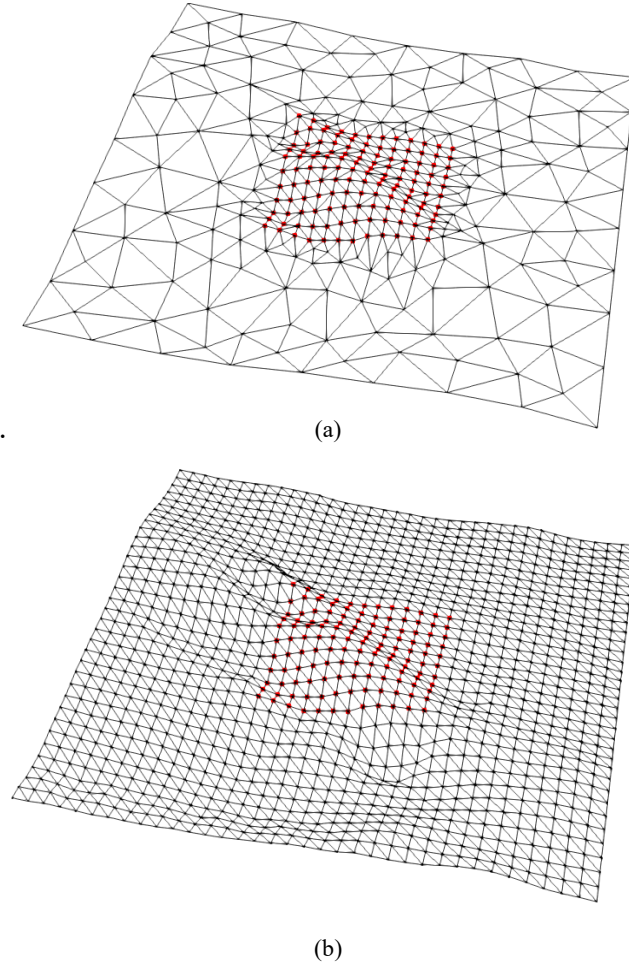


**Figure 36: comparison of two triangulation strategies.** Above (a) a high level of detail is preserved only on in the portion of interest of the investigation domain and extrapolation of depth values is applied. Below (b) a high level of detail is guaranteed for the entire extension of the geomechanical model and interpolation algorithm is applied outside the high-resolution zone.

Points external to the *Convex Hull* of the original point clouds are processed exploiting an extrapolation strategy: once calculated the barycenter ( $C$ ) of  $CH_{IN}$ , the depth associate to  $P$  is set equal to the depth value of point  $P'$  obtained by intersecting  $CH_{IN}$  with the segment that connects  $CP$  (Figure 38). In other words, the depths of the points ( $P'$ ) on the inner boundary  $CH_{IN}$  are projected to points ( $P$ ) which lies in the low-resolution zone or on the boundary of the model.  $CH_{OUT}$ .

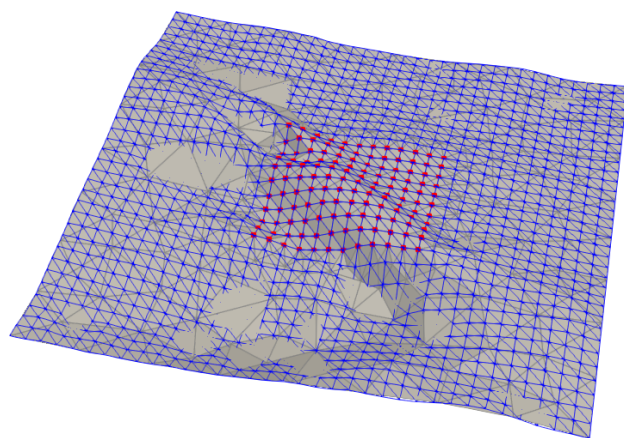


**Figure 37:** comparison between the stratigraphic surface extended obtained from the interpolation phase (grey) and the triangulation of the interpolated stratigraphic surface point cloud (blue). In the graph an amplification factor of 2 in the Z direction was applied to appreciate differences.

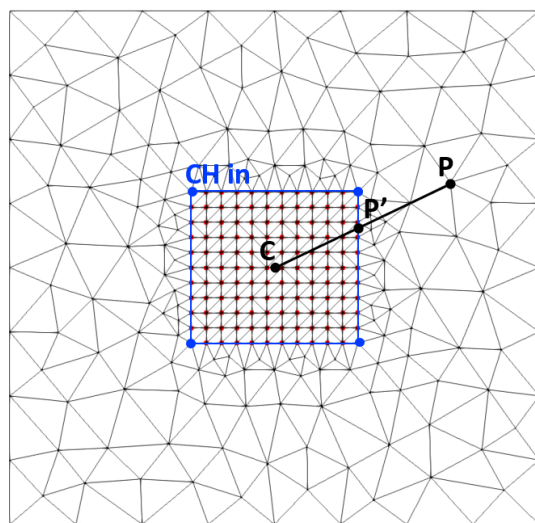


**Figure 38:** intersection  $P'$  on the XY plane between the *Convex Hull* (blue line) of the surface point cloud and the segment that connects the center of CH ( $C$ ) and the point  $P$  external to CH.

## Fault surface triangulation

The fault surface is the other type of input that contributes to the definition of the model geometry and to which the final grid must be constrained.

Preliminary analyses on the nature of the point cloud that defines a fault surface have determined the need to develop a dedicated algorithm for their triangulation. The proposed workflow, derived from the Park and Oh algorithm (Park and Oh, 2012), can be declined in the steps sketched in Figure 39.

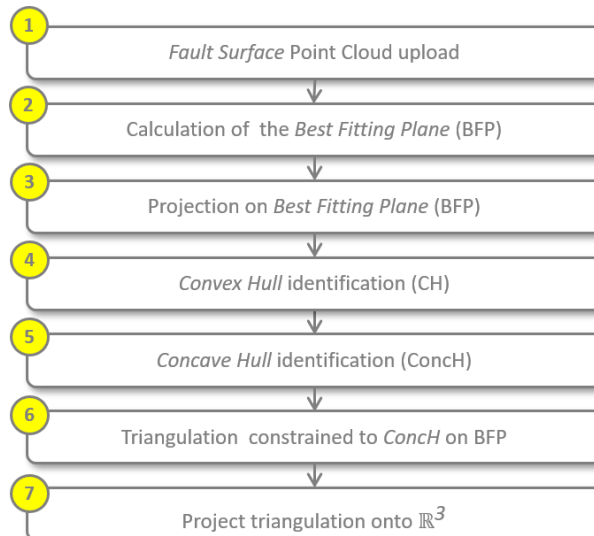


**Figure 39: fault surface reconstruction from 3D point cloud**

Unlike stratigraphic surfaces, faults are generally described with a loose sampling, if compared with their extension, and inhomogeneous in different directions. They are unlikely approximated by a plane and can be characterized by strongly irregular edges. Moreover, as extensively cited, the *Triangle* library supports only planar triangulations constrained to planar straight-line graphs. Therefore, unlike the case of stratigraphic surface point clouds, it becomes necessary to identify the best plane approximating the fault surface (BFP) (step 2), in the sense of least squares, on which to project the point cloud and successively identify the *Concave Hull* (Conch) (step 5) which accurately describes the boundary of the projected cloud.

The BFP identification was performed by exploiting the linear algebra algorithms available in the *Eigen library* (Guennebaud et al., 2010). In the specific case the principal components of the matrix consisting of the coordinates of the points of the cloud expressed respect to a Cartesian reference system centered in the barycenter of the cloud itself were calculated by solving the associated eigenvalue problem. In figure an example of fault surface point cloud (a), intersection with the calculated BFP in  $\mathbb{R}^3$  (b) and point cloud projection onto BFP (c), respectively.

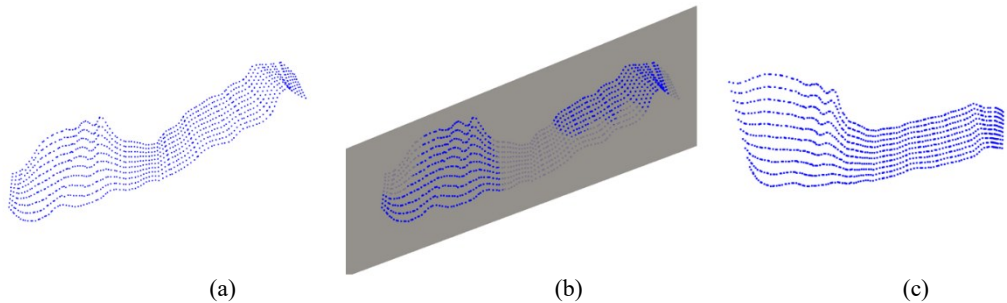


**Figure 40:** (a) point cloud in  $\mathbb{R}^3$ , representative of a fault surface. (b) Intersection of the point cloud with the BFP (grey) in  $\mathbb{R}^3$  (c) Point cloud projection on the BFP. (Serazio et al., 2021)

For the identification of the *Concave Hull*, as done for the stratigraphic surfaces, the starting polygon of the algorithm is the *Convex Hull* obtained as the output of *Triangle* and the depth to which the hull is iteratively "excavated" is determined by a parameter indicated as  $nDig \in [0,1]$ . Indeed, it defines the width of the neighborhood exploration through the relation  $r = \text{edgeLength} * nDig$ . The algorithm iterates over all the nodes of the actual boundary, and for each of them look for an internal node belonging to the neighborhood which can be classified as boundary. In Figure 41, as an example of the “digging” evolution, the initial *Convex Hull* (in red) and four concave hulls of increasing number of nodes (from orange to yellow) are represented. The resulting *Concave Hull* is the green boundary. In Table 2 are reported the key parameters of two validation case of the proposed algorithm and published in (Serazio et al., 2021) where details on the implementation of the proposed algorithm can be found. In both cases the boundary, once projected on the BFP plane present an irregular trend with concavities of different size. This is the main characteristic which made the attempt of applying the 2D  $\alpha$ -shapes strategies available in the CGAL module (Da, 2021) not satisfactory. Indeed, to obtain accurate representation of the boundary polygons a tuning of the  $nDig$  parameter was necessary and the final values reflect the different nature of the two surfaces

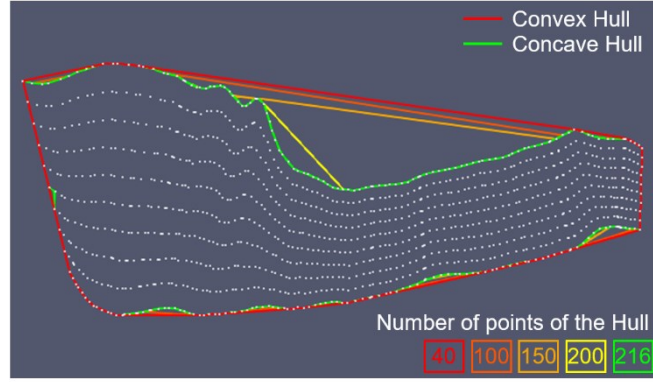


**Figure 41:** "digging" algorithm evolution example. Boundary polygons corresponding to five steps are shown. The initial **Convex Hull** (red) of 40 nodes, iterations at 100, 150, 200 nodes and the final **Concave Hull** (green) of 216 nodes. (Serazio et al., 2021)

The *Fault 12* represent an example of fault that cannot be approximated by a plane. Conversely the boundary shows an irregular shape, but not narrow changes in concavity, thus a relatively low value of  $nDig$  (0.4) produces the expected result as shown in Figure 42 and Figure 43 where the initial and the final triangulation are compared on the plane and on the original Cartesian coordinate system, respectively. The *H53* case, instead, is closer to a planar fault, but the boundary presents different concavities, very narrow, which are satisfactorily described with a high value of  $nDig$ . Comparison of the triangulation on the plane and in the original Cartesian coordinate system are shown in Figure 44 and Figure 45, respectively.

**Table 2:** example of reconstruction of fault surfaces. The main parameters are reported: number of the cloud points,  $nDig$ , dimension of the **Convex Hull** and the **Concave Hull** and corresponding triangulation (Serazio et al., 2021).

Case	# Points	$nDig$	<b>Convex Hull</b>		<b>Concave Hull</b>	
			# nodes	# triangles	# nodes	# triangles
<i>Fault 12</i>	1110	0.4	40	2178	216	2002
<i>H53</i>	1632	0.75	32	3230	436	2826

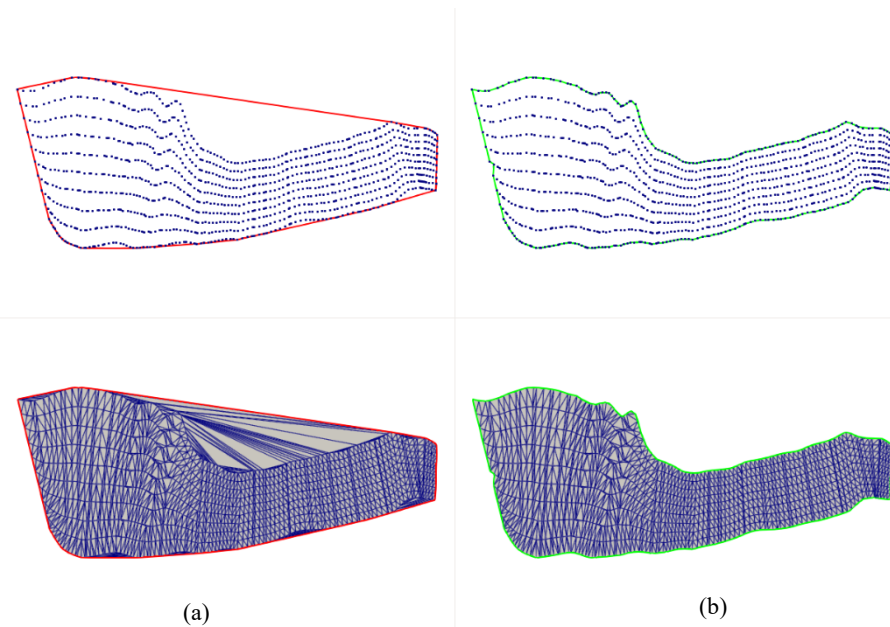


**Figure 42:** *case Fault 12 - XY-plane point cloud projection: initial Convex Hull constrained triangulation (red) (a) and corresponding Concave Hull constrained triangulation (green) (b)* (Serazio et al., 2021).

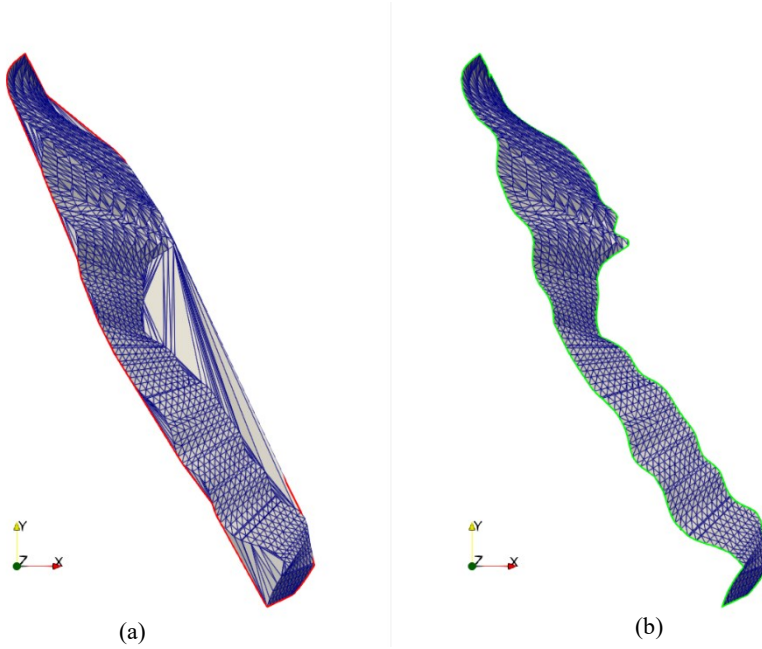


**Figure 43:** *case Fault 12 - original Cartesian coordinate system comparison between the initial Convex Hull constrained triangulation (red) (a) and corresponding Concave Hull constrained triangulation (green) (b)*. (Serazio et al., 2021).

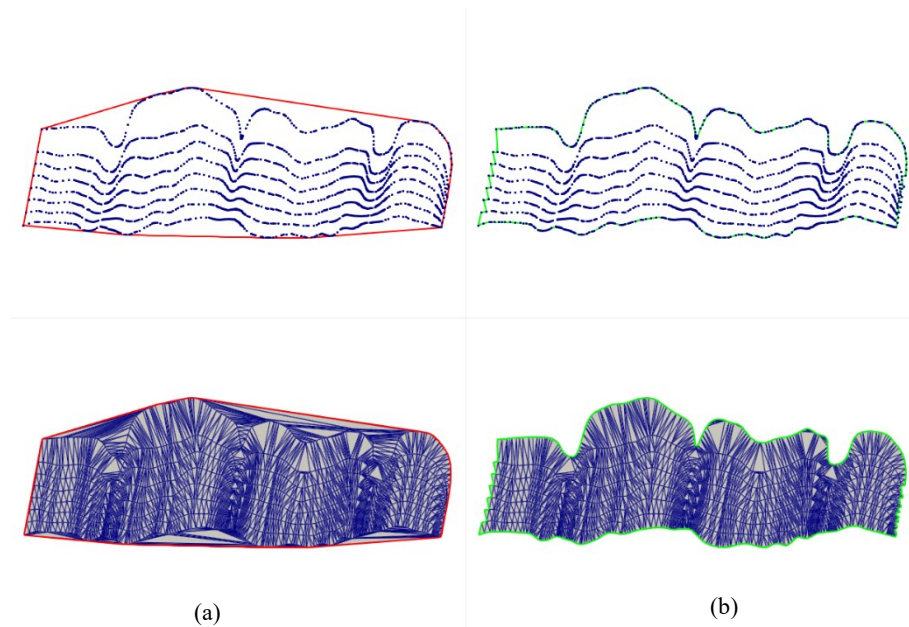


**Figure 44:** case H53 - XY-plane point cloud projection: initial *Convex Hull* constrained triangulation (red) (a) and corresponding *Concave Hull* constrained triangulation (green) (b)(Serazio et al., 2021)

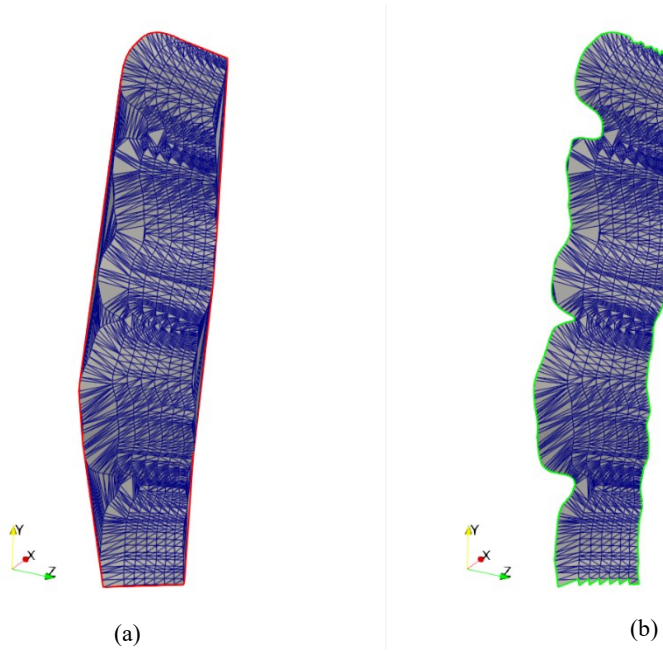


**Figure 45:** case H53 - - original Cartesian coordinate system comparison between the initial *Convex Hull* constrained triangulation (red) (a) and corresponding *Concave Hull* constrained triangulation (green) (b) (Serazio et al., 2021).

## Lateral surface triangulation

The lateral surface is the type of surface that identifies the external face of the model and allows to define the closed domain to be used as input for the *Tetgen* tetrahedrization library. The algorithm implemented for the triangulation of the lateral surfaces does not substantially differ from that used for the fault surfaces (Figure 39), except for the fact that the faces are well defined and known *a priori*; Figure 46 illustrates the steps of the proposed workflow.

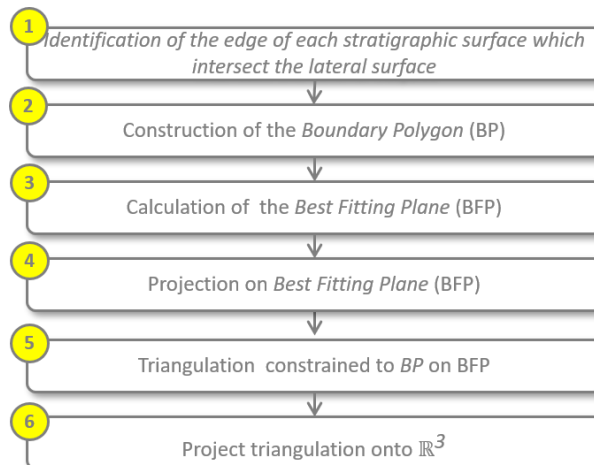


**Figure 46:** lateral surface triangulation workflow

Lateral surfaces are defined by the boundary edges of the extended stratigraphic surfaces which constitute the geomechanical model. They allow identification of the points that will constitute the lateral surface as well as the segments that will constitute the constraints for the triangulation library. Since no quality constraint are imposed to the *Triangle* function, the resulting triangulation will consist only of the points originally associated with the lateral faces of the stratigraphic surfaces; consequently, this triangulation procedure does not require the use of any interpolation algorithms for the assignment of the depth value to any additional points. Figure 47 shows the result of the triangulation process of the lateral surfaces relative to the example case shown in Figure 21 and Figure 22. It is observed that the triangulation is conforming to the associated stratigraphic surfaces.

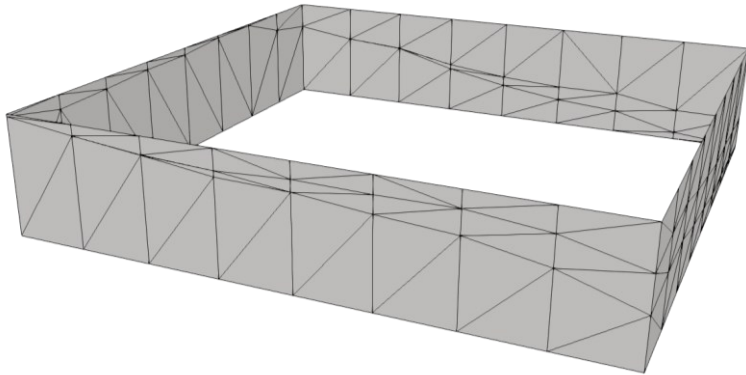


Figure 47: triangulation of the lateral faces of the model

## Intersection between faults and stratigraphic surfaces

The *Tetgen* library (Si, 2020), used for the discretization of the investigated domain, requires a conforming data structure, i.e. a set of points, segments and polygons without reciprocal intersection, *piecewise linear complex* (PLC), as an input; therefore, it is necessary to ensure that this constraint is respected for all the surface and fault triangulations that play a role in the construction of the discretized domain. It is observed that, by construction, the triangulations of stratigraphic and lateral surfaces are consistent. Conversely, the integration of fault surfaces requires appropriate checks since they are likely to intersect with one another and/or intersect the stratigraphic and lateral surfaces in points not belonging to the PLC, and this would represent an obstacle to the tetrahedrization of the geomechanical volume.

The identification of the intersection between two surfaces in a three-dimensional space can be reduced to the identification of the set of points in space where two surfaces coincide. This process is very onerous from a computational point of view, especially considering the extension of a geomechanical model and the numerosness of points and cells that constitute the triangulated surfaces. Furthermore, it should be noted that, since there is no function that describes the surfaces involved, it is not possible to analytically calculate their possible intersections (Patrikalakis et al., 2004), but it is necessary to exploit to suitable numerical algorithms.

In the dedicated literature the approaches for identifying the intersections between two surfaces are basically divided into two categories:

1. *Marching Methods*: given a known point of intersection between two surfaces, this algorithm's family iteratively identifies the next intersection point through suitable strategies of exploration of the domain (see for example (Barnhill and Kersey, 1990)). This type of approach has numerous disadvantages: the identification of an exploration algorithm suitable for the type of application, and also the additional cost due to the identification of the initial guess from which the exploration begins.

2. *Splitting Methods*: this second category includes algorithms which reduce the computationally onerous initial problem into sub-problems of identifying intersections on portions of the original domain through a splitting of the exploration domain (see as an example (Filip et al., 1986)). One of the disadvantages associated with this type of algorithm is represented by the difficulty of identifying an optimal domain subdivision strategy, sufficiently general and capable of minimizing calculation times and the computational cost.

Taking advantage of the available data structures, in the process of integrating the fault surfaces, the second type of algorithm has currently been proposed, i.e. the application of a *divide et impera* methodology.

The definition of the exploration strategy exploits the fact that the construction of the PLC (*Tetgen* input) derives from the triangulation of all the surfaces making up the model. Therefore, the intersection identification problem is further reduced, and it consists in verifying the intersection (if any) between two triangles in  $\mathbb{R}^3$ . In the technical literature there are numerous algorithms dedicated to this task, however, most of them return a Boolean output, i.e. if the two triangles do or do not show an intersection, without identifying its actual position in the space. To retrieve this information, functionality available in the *Tetgen* library were exploited: given a pair of triangles, it returns the presence of any intersections, combined with a series of accessory attributes useful for their spatial identification. Starting from this information, an *ad hoc* algorithm was developed that made it possible to identify the trace of the intersection between two surfaces. As an example, an application of the implemented algorithm is shown to the stratigraphic surface represented in orange in Figure 22, which is intersected by two fault surfaces (respectively blue and red surfaces in Fig. 24); in particular, in the sequence Fig. 23-Fig. 27 the evolution of the triangulations of the stratigraphic surface and of the fault surfaces afterward the integration of the intersections, the blue fault at first (Fig. 25), and in succession the red one (Fig. 26 and Fig. 27)

---

In the next step of the workflow, the identified intersection is integrated within the PLC input to *Tetgen*, thus allowing one to manage geometries that foresee the presence of fault surfaces.

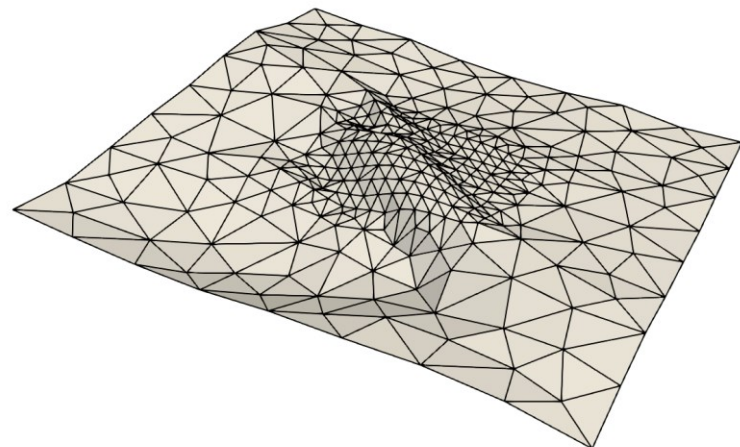


**Figure 48:** stratigraphic surface sample (orange in Figure 22) used to illustrate the evolution of triangulation afterward the identification of intersections with fault surfaces.

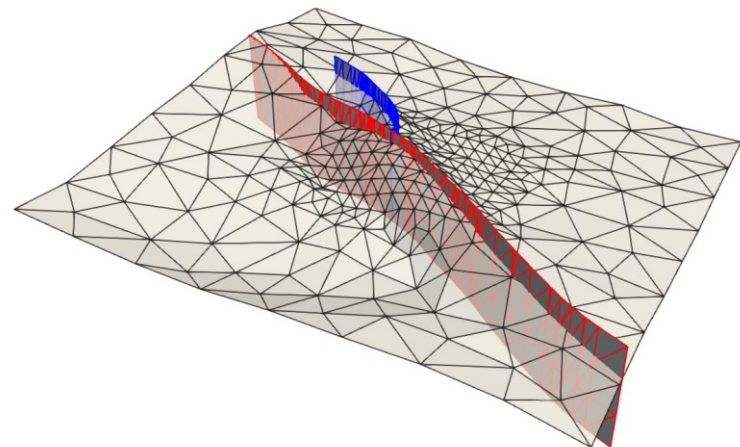


**Figure 49:** spatial position of the fault surfaces (in red and blue) with respect to the sample stratigraphic surface

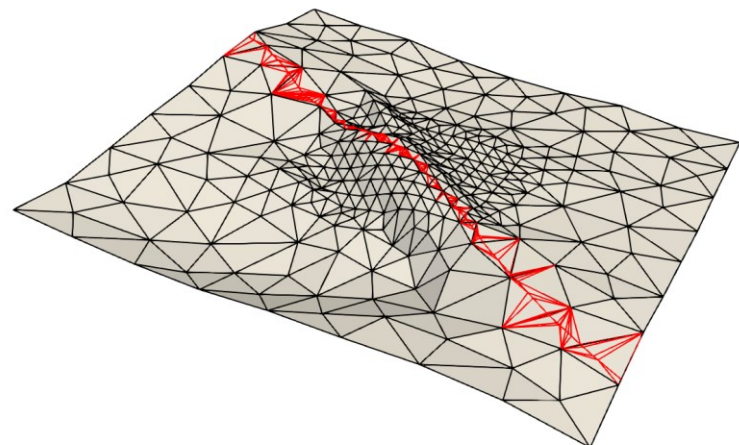


**Figure 50:** updating of the stratigraphic surface triangulation after the identification of intersections with the red fault surface of Figure 49. Added points and segments with respect to the starting triangulation are highlighted in red.

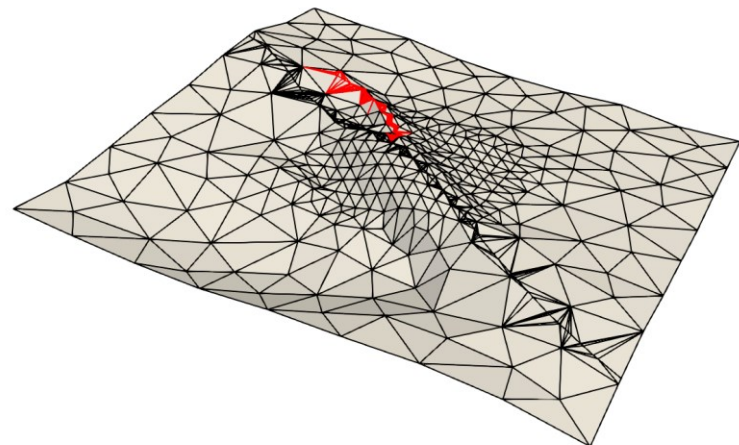


**Figure 51:** updating of the stratigraphic surface triangulation after the identification of intersections with the blue fault surface of Figure 49. Added points and segments with respect to the starting triangulation are highlighted in red.

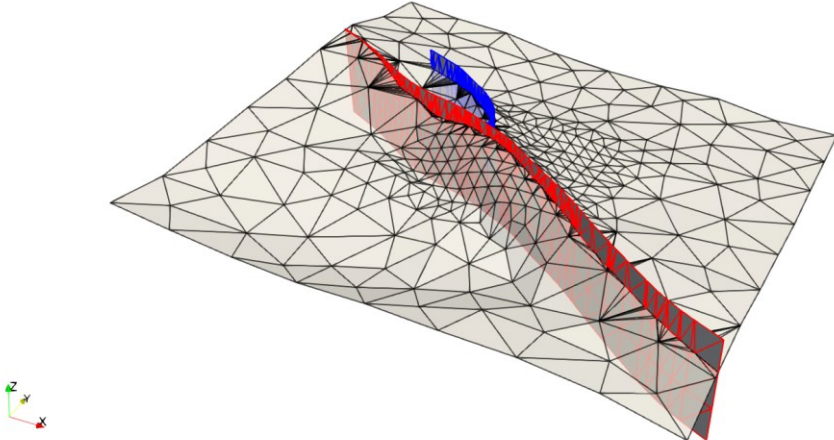


**Figure 52:** conforming triangulation resulting from the identification of intersections between the sample stratigraphic surface and the fault surfaces.

## Domain vertical refinement

To represent with sufficient accuracy the stress-deformation response of the geomechanical model in the region affected by subsidence, a high-level areal discretization is not sufficient, and an adequate vertical representation is also necessary.

Usually, the stratigraphic surfaces available to the user for the definition of the geomechanical model are not sufficient to ensure an acceptable vertical discretization. A possible strategy to overcome this problem is to insert fictitious surfaces (“numerical layers”) between two stratigraphic surfaces. Although the method is feasible, the inclusion of these layers raises two main problems:

- The first is related to the presence of fault surfaces in the geomechanical model. In fact, they greatly complicate the insertion of any numerical layers, as for their definition the vertical and areal extension of all the fault surfaces involved as well as the induced dislocations must be considered. Furthermore, the definition of numerical layers makes the verification and imposition of the compliance constraints of the input PLC to the Tetgen library more onerous.
- The second problem is associated with the characterization of the geomechanical model. As it will be described in detail in § 2.6, the model is populated by assigning properties to each region identified by the surfaces. The insertion of numerical layers between two stratigraphic

---

surfaces involves the subdivision of the defined regions into sub-regions, further complicating the property assignment phase.

Following these considerations, different solutions have been explored to define a vertical refinement suitable for geomechanical modeling.

The *Tetgen* library constructs a Delaunay tetrahedrization bounded to the input PLC, possibly respecting specific mesh quality parameters; in particular, *Tetgen* allows the definition of the desired level of detail in terms of the maximum volume of the generated tetrahedra (switch -a) and in terms of the maximum length of the arcs that constitute them (switch -m) by applying a mesh dimensioning function defined by user. The limitation to the use of these options is due to the impossibility of specifying the constraints differentiating them in different directions. Consequently, by specifying the same quality constraints both in the areal and vertical direction, the obtained meshes count a number of cells and nodes unacceptable to perform geomechanical study. By way of example, let us consider the orange region of Figure 25 delimited by the red and orange stratigraphic surfaces of Figure 22; at the center of the reservoir the two surfaces are about 200 m apart in the vertical direction. Since the volume where deformations occur must be discretized with a good level of detail, it is desirable to refine the grid in the orange region. It is assumed a maximum volume limit is applied to each tetrahedron which belongs to that region, so that the vertical detail is approximately 10 m. To satisfy the imposed constraint, the library inserts some additional points (*Steiner* points) into the region, reducing not only the vertical discretization, but also the areal one of the whole modeled volume, leading to a volume tetrahedrization exaggeratedly thicker than necessary, significantly increasing the computational cost of the geomechanical problem solution and without any improvement of the whole solution. For this reason, the proposed algorithm consists in forcing the insertion of a list of additional points to the PLC input to the *Tetgen* library (switch -i) that satisfy the desired vertical detail. Each stratigraphic surface has been associated with a thickness (expressed in m), to be used in the high-resolution area (red in Figure 33), which represents the level of desired vertical detail close to the stratigraphic surface. The vertical progression of the points between two successive stratigraphic surfaces can be linear or logarithmic, at the user's discretion. It is also possible to specify additional degrees of freedom in the vertical point progression definition by associating thickness values in correspondence of intermediate depth between the two surfaces. In Figure 53 an example of discretization is shown, relative to the case of Figure 21-Figure 25, where the following constraints have been imposed with respect to the stratigraphic surfaces illustrated in Figure 21:

- 10 m at ground level (red)
- 50 m on the average “fictitious” surface (white) defined starting from ground level and the underlying stratigraphic surface (orange)
- 10 m on the orange surface
- 30 m on the yellow surface
- 500 m on the model base (green)

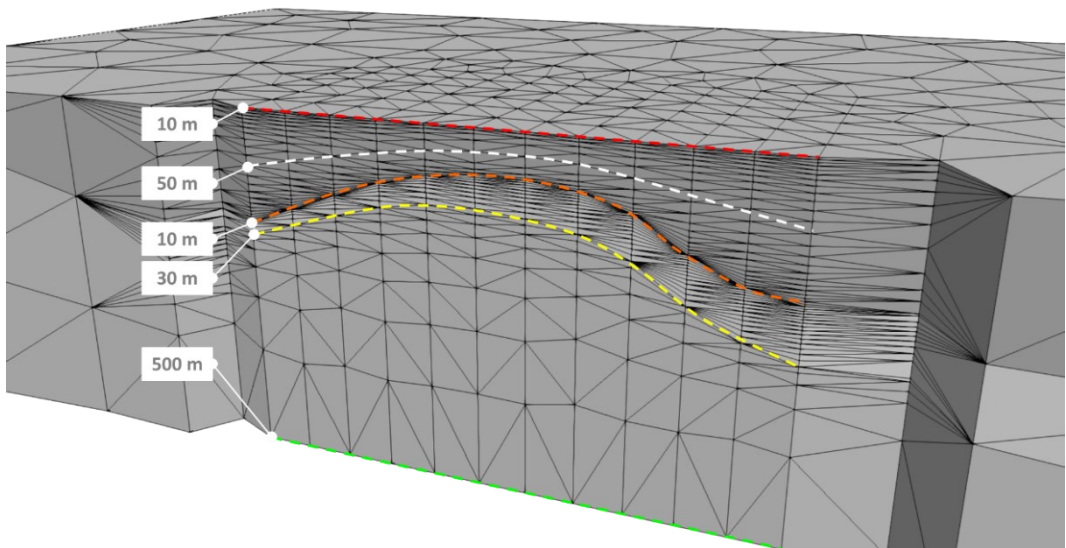


**Figure 53:** vertical discretization of the geomechanical model constrained by the depth values assigned to each surface of the model (white boxes)

## Region identification and characterization

The process of defining the model properties is carried out by defining geomechanical classes (i.e., volumes with homogeneous geomechanical characteristics); since the idea of characterizing one by one each cell belonging to the domain is impractical, the class assignment is supported by the region identification process. In particular, the identification of regions delimited by stratigraphic and fault surfaces, as well as by the lateral surfaces, was performed applying the available functionalities through an appropriate command line switch; *Tetgen* allows one to assign a marker to each tetrahedron, so that all the tetrahedra belonging to the same region are associated to the same marker; Figure 25 shows the result of the identification process of the regions applied to the example case.

In general, the number of geomechanical classes may not coincide with the number of regions that can be identified. Therefore, it is useful to be able to use

additional fictitious surfaces to have a unique correspondence between geomechanical classes and regions.

For each geomechanical class it is possible to define the corresponding pseudo-elastic parameters as well as the parameters required by the adopted yield criterion. The actual implementation involves the Mohr-Coulomb resistance criterion.

The characterization of a material with a transversely isotropic elastic behavior follows naturally from the isotropic case.

# Chapter 5

## Validation test in the linear-elastic domain

### VEM formalization for the solution of the elastic problem

The Virtual Elements Method (VEM), introduced in (Beirão da Veiga et al., 2014, 2013a, 2013b) is a generalization of the Finite Element Method (FEM) able to manage generic grids in a natural way. To this end, an appropriate abstract functional space is defined, containing the one exploited by FEMs, characterized by the fact that the functions in this space are not explicitly known (hence the adjective "virtual"), except on the edges of the grid. The space construction allows one to approximate the solution with a piecewise polynomial on each element of the grid and solve the problem using these polynomial approximations. In detail, the calculated VEM displacements are continuous functions belonging, on each polyhedron ( $E$ ), to the space  $V_h^E$  defined as

$$V_h^E = \{v \in H^1(E) : \Delta v \in \mathbb{P}_1(E), \quad v \in \mathbb{P}_1(e) \quad \forall e \in \partial E, \quad v \in C^0(\partial E)\} \quad (35)$$

where  $H^1(E)$  is the space of functions having a square-integrable gradient on  $E$ ,  $\partial E$  indicates the set of edges of the polyhedron,  $\mathbb{P}_1(E)$ , is the space of polynomials of degree lower than or equal to 1. It is possible to prove that a function

in such a space is uniquely determined by its values at the vertices of the polyhedron which coincide with the degrees of freedom of the problem.

The formulation of the linear momentum balance equation (6) with no displacement allowed on the domain boundary ( $\partial\Omega$ ) for a linear-elastic medium reduces to a Poisson's equation with homogeneous boundary conditions:

$$\begin{cases} \nabla \cdot \sigma(u) + b = 0 & \text{in } \Omega \\ u = 0 & \text{on } \Gamma^D \\ \sigma \cdot n = 0 & \text{on } \Gamma^N \end{cases} \quad (36)$$

where  $\Omega$  indicates the computational domain,  $\sigma$  is the stress tensor,  $b$  is a forcing term per unit of volume and  $\mathbf{u} = (u_1, u_2, u_3)^T$  is the displacement vector. Under the hypothesis of small deformations, the strain vector has expression (4) and the stress-strain relation for an isotropic linear elastic medium has expression (11) and Lamé coefficients in (12).

The continuous variational formulation of the problem in case of homogeneous boundary conditions, written in terms of the deformation  $\varepsilon(\nabla u)$  is:

$$\begin{aligned} & \int_{\Omega} 2\mu\varepsilon(\nabla u) : \varepsilon(\nabla v) d\Omega + \int_{\Omega} \lambda \nabla \cdot u \nabla \cdot v d\Omega \\ &= \int_{\Omega} b v d\Omega \quad \forall v \in H_{0,\Gamma^D}^1(\Omega) \end{aligned} \quad (37)$$

where  $H_{0,\Gamma^D}^1(\Omega)$  is the space of the functions of the Sobolev space  $H^1(\Omega)$  that cancels on the portion of boundary  $\Gamma^D$  where homogeneous Dirichlet conditions are defined. This formulation cannot be directly discretized with the VEMs, because the basis functions of the space are not known analytically, and the integrals are therefore not computable. For this reason, polynomial projections of the basis functions are employed, adding a stabilization term to guarantee the non-singularity of the resulting matrix. The discrete problem results,  $\forall v_h \in V_h$

$$\begin{aligned}
& \int_{\Omega} 2\mu \varepsilon(\Pi_0^0(\nabla u_h)) : \varepsilon(\Pi_0^0(\nabla v_h)) d + \int_{\Omega} \lambda \Pi_0^0(\nabla \cdot u_h) \Pi_0^0(\nabla \cdot v_h) d\Omega \\
& + (2\mu + \lambda) S((\mathbb{I} - \Pi_1^0)u_h, (\mathbb{I} - \Pi_1^0)v_h) \\
& = \int_{\Omega} b \Pi_1^0(v_h) d\Omega
\end{aligned} \tag{38}$$

where the symbol  $\Pi_1^0$  indicates a suitable projection on the polynomials of the VEM function, which can be calculated from the degrees of freedom. As the stabilization form is  $S(\cdot, \cdot)$ , it is sufficient to choose the scalar product of the degrees of freedom of the two involved functions.

## Implementation details

The method was implemented in C++ language using a calculation procedure entirely based on the matrix product (see Appendix for details). To optimize the products, the classes and methods made available by the Eigen library were exploited (Guennebaud et al., 2010). As for the calculation of the polynomial projection matrices, reference was made to (Beirão da Veiga et al., 2016b, 2014).

It is also noticed that, from the point of view of the computational cost, the dimensions of the resulting linear system make a direct resolution impractical. The preconditioned conjugate gradient method was then applied (Saad, 2003).

The known-term calculations, instead, was set equal to the delta pore pressure  $\Delta p$  recorded between two states of the system, i.e., before starting production and at the end of the primary production phase, or in the specific UGS context, the pressure difference recorded between the beginning and the end of a cycle (injection or production).

$$b = -\nabla \cdot (\Delta p \mathbb{I}) = - \begin{pmatrix} \frac{\partial(\Delta p)}{\partial x} \\ \frac{\partial(\Delta p)}{\partial y} \\ \frac{\partial(\Delta p)}{\partial z} \end{pmatrix} \tag{39}$$

The divergence value was determined by applying a finite difference scheme, i.e., by calculating an approximation of the normal derivative to each face using the pressure values of the neighboring cells. (See Appendix for further details)

## Validation

### Disk-shaped reservoir model

As introduced in the “Theoretical Background” Chapter, analytical solutions were developed in case of systems with simplified geometry and characterized by isotropic homogeneous and constant parameters. This is the case of a disk-shaped reservoir with vertical axis of symmetry and thickness vs radius ratio ( $H/R$ ) of the order of 0.1. The induced subsidence profile in a cylindrical coordinate system was proposed by Geertsma (Geertsma, 1973b) and recalled in equations (32) and (33).

As a preliminary validation test of the VEM implementation, a comparison was made between the FEM commercial software Visage (Schlumberger, 2020b), the VEM code profiles and the Geertsma’s analytical solution.

It is observed that the analytical solution of Geertsma is calculated on a semi-space by means of the *strain nuclei* concept thus no boundary conditions are imposed. It follows that the domain of investigation of the numerical solvers needs to be sufficiently extended so that the boundary effects on the calculated solution can be considered negligible. In the specific case, the box domain has an extension of 14 km x 14 km x 10 km as sketched in Figure 54a. The model parameters are listed in Table 3.

Two different volume discretizations were defined. The unstructured grid, based on the VTK framework and the Tetgen library, was set up through the identification of the reservoir region and of a refinement volume, defined as a cylinder with vertical axes and areal extension sufficient to cover the subsidence bowl, characterized by an absolute vertical displacement higher than 0.5 cm (Figure 54b). In parallel, the corner-point grid procedure was run in the Petrel E&P platform and a coherent domain was defined. In this case the refinement option relies on the Cartesian structure of the grid, resulting in a *tartan* refinement which spans the whole extension of the domain.

**Table 3: Geertsma's test model parameters**

Parameter	Description	Value
$H$	Reservoir thickness [m]	100 m
$R$	Reservoir radius	1000 m
$C$	Reservoir depth	400 m
$E$	Young's Modulus	2 GPa
$\nu$	Poisson's Ratio	0.25
$\Delta p$	Imposed reservoir pore pressure variation	-3 MPa

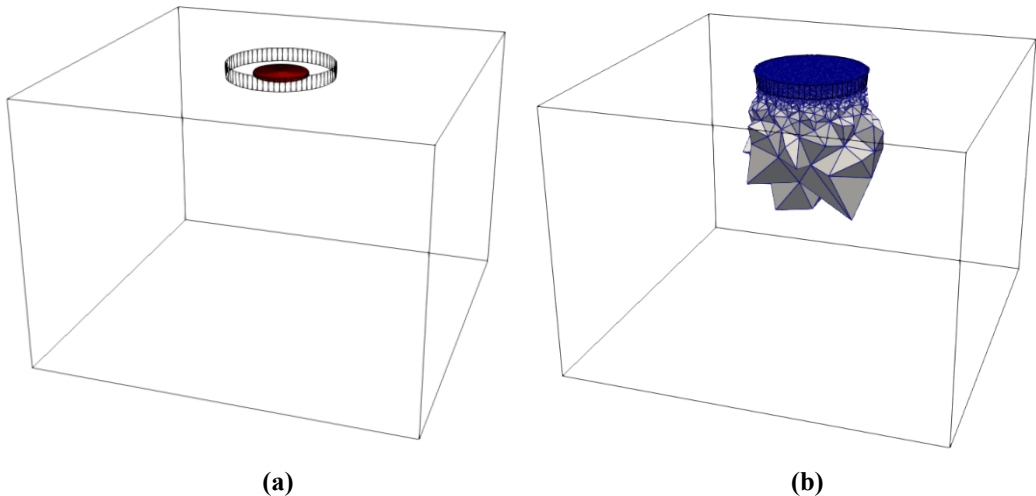


**Figure 54:** sketch of the model defined for the comparison of VEM numerical solution against Geertsma analytical one. (a) disk-shaped reservoir in red and black boundary of the refinement cylinder. (b) cells of the domain interested by a vertical displacement higher than 0.5 cm in absolute value.

The resulting discretization accounts for about  $3.5 \cdot 10^5$  tetrahedra of the unstructured grid and  $4.8 \cdot 10^5$  hexahedra of the corner-point grid. In Figure 55, the trend of the cell volumes for the two grids along a y-plane clip shows the higher flexibility of the unstructured grid with respect to the pillar gridding where the refinement of the mesh exclusively applies to the zone of interest while preserving

the quality of the mesh in the entire volume as shown in Figure 56 (the color map refers to the edge ratio associated to each element).

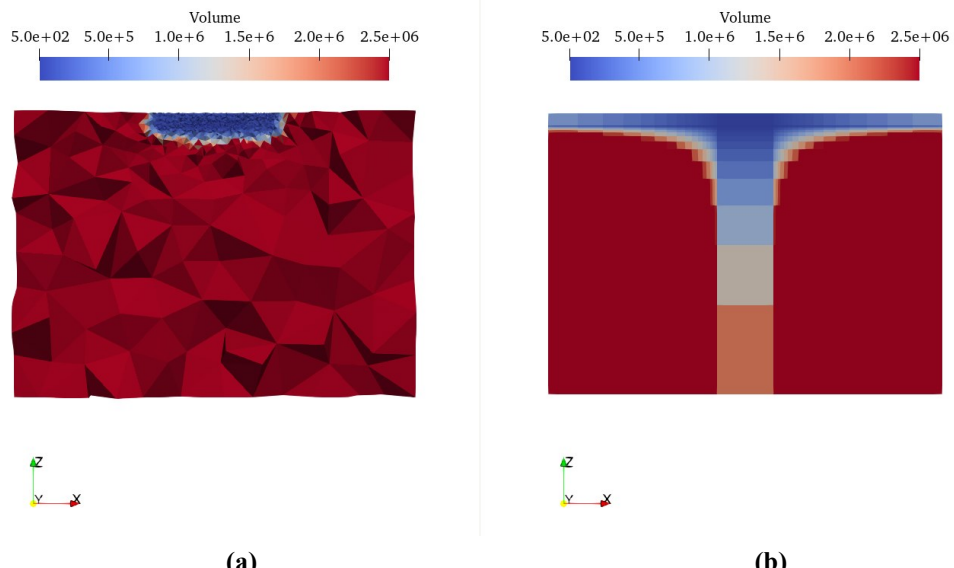


**Figure 55:** section orthogonal to Y-axis of the volume discretization with unstructured grid (a) and corner-point grid (b). The color map refers to the cell volumes ( $\text{m}^3$ )

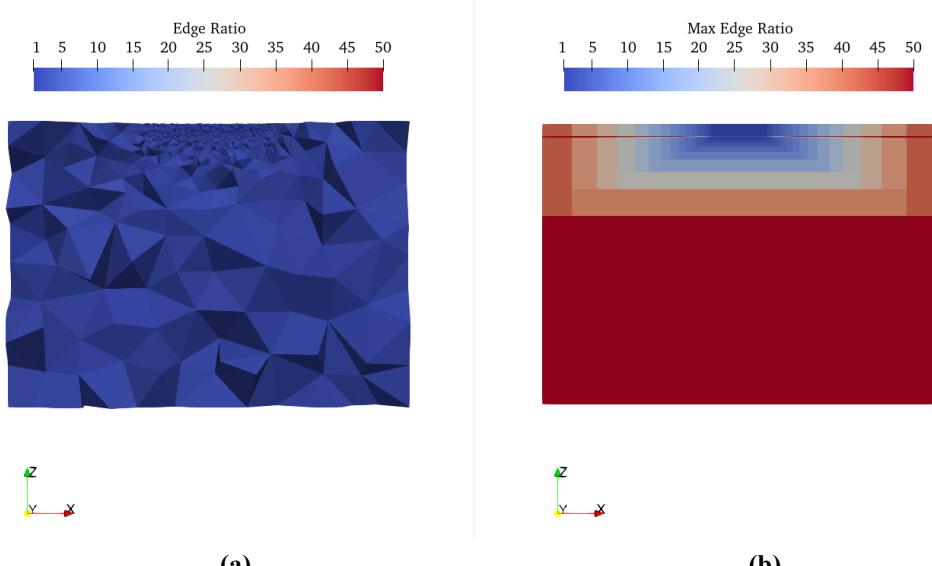
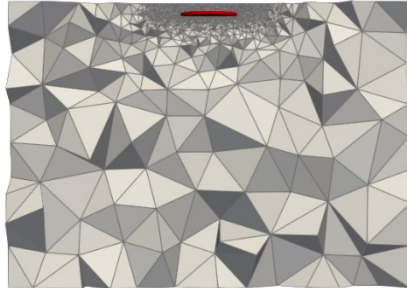
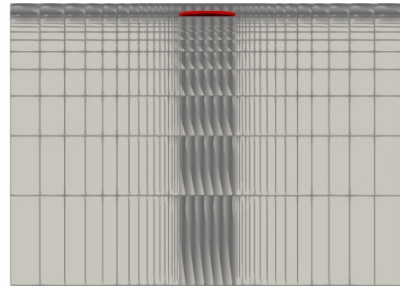


**Figure 56:** section orthogonal to Y-axis of the volume discretization with unstructured grid (a) and corner-point grid (b). The color map refers to the cell quality (edge ratio)

In Figure 57 and in Figure 58, the y-plane clip and the top view of the two models are shown. The reservoir, where the variation of pore pressure is imposed, is highlighted in red.

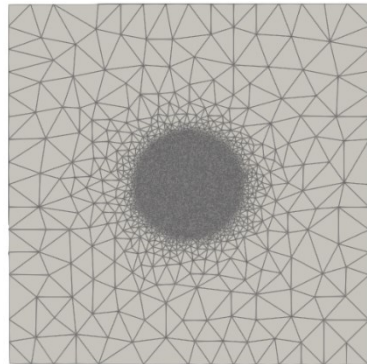


(a)

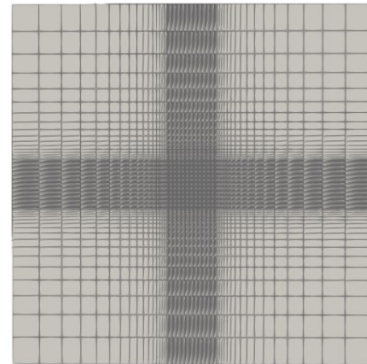


(b)

**Figure 57:** section orthogonal to Y-axis of the two grid models: on the left (a) unstructured grid for VEM simulation and, on the right (b), corner-point grid for FEM simulation, respectively. In red the reservoir where pore pressure variation is imposed.



(a)



(b)

**Figure 58:** top view of the two grid models: on the left (a) unstructured grid for VEM simulation and, on the right (b), corner-point grid for FEM simulation, respectively. In both grids a refinement zone in correspondence of the subsidence bowl was defined.

The solution comparison in terms of displacement field is performed on a section HH' of the top surface ( $z = 0$  m) as shown in Figure 59a where the colormap refers to the subsidence of the VEM solution expressed in cm. In Figure 59b the comparison of the z-direction displacement, calculated with the three methods along the HH' section, shows a satisfactory correspondence.

Analogous colormap and plot are depicted for the displacement along the x-direction in Figure 60a and Figure 60b, respectively. Due to the radial symmetry, the x-direction component of the numerical solver is compared with the radial one proposed by Geertsma in equation (33). Analogous comparison was performed for the variation of the stress field induced by imposed  $\Delta p$  as shown in Figure 61 and Figure 62 where  $\Delta\sigma_{xx}$  and  $\Delta\sigma_{yy}$  are shown, respectively.

Agreement among the solutions was also verified through a section along the vertical segment OO'. The vertical displacement is depicted in Figure 63, while the stress components  $\Delta\sigma_{xx}$  and  $\Delta\sigma_{zz}$  are shown in Figure 64 and Figure 65, respectively.

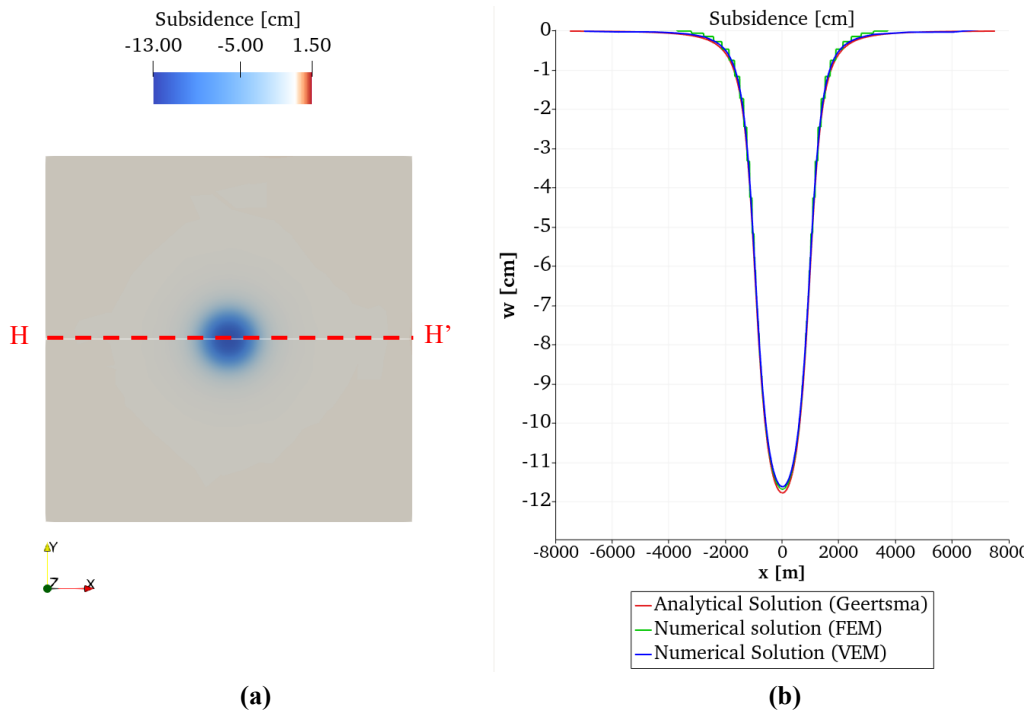


**Figure 59:** (a) top view of the model. The colormap refers to the subsidence expressed in cm. (b) comparison of the subsidence along the dotted red segment HH' in (a).

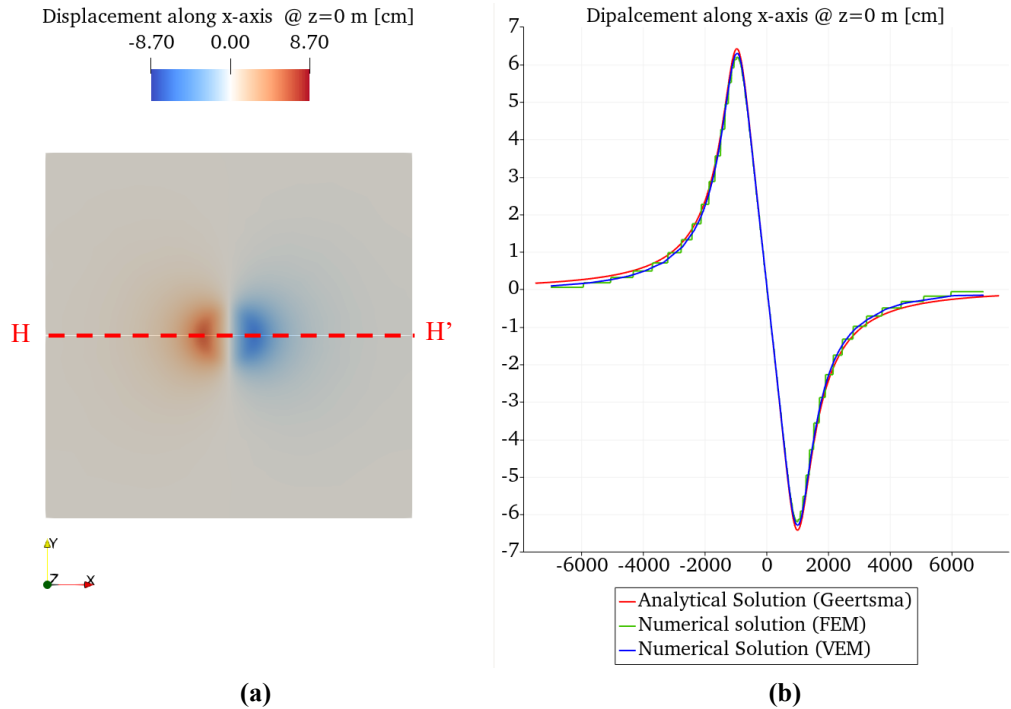


Figure 60: (a) top view of the model. The colormap refers to the displacement along x-axis expressed in cm. (b) comparison of the subsidence along the dotted red segment  $HH'$  in (a).

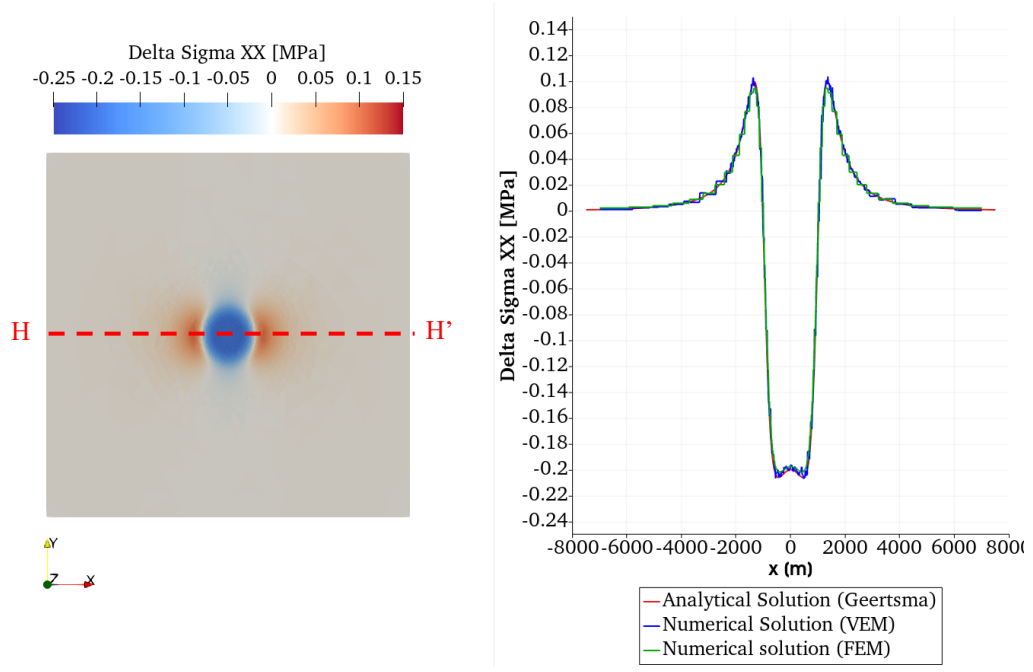
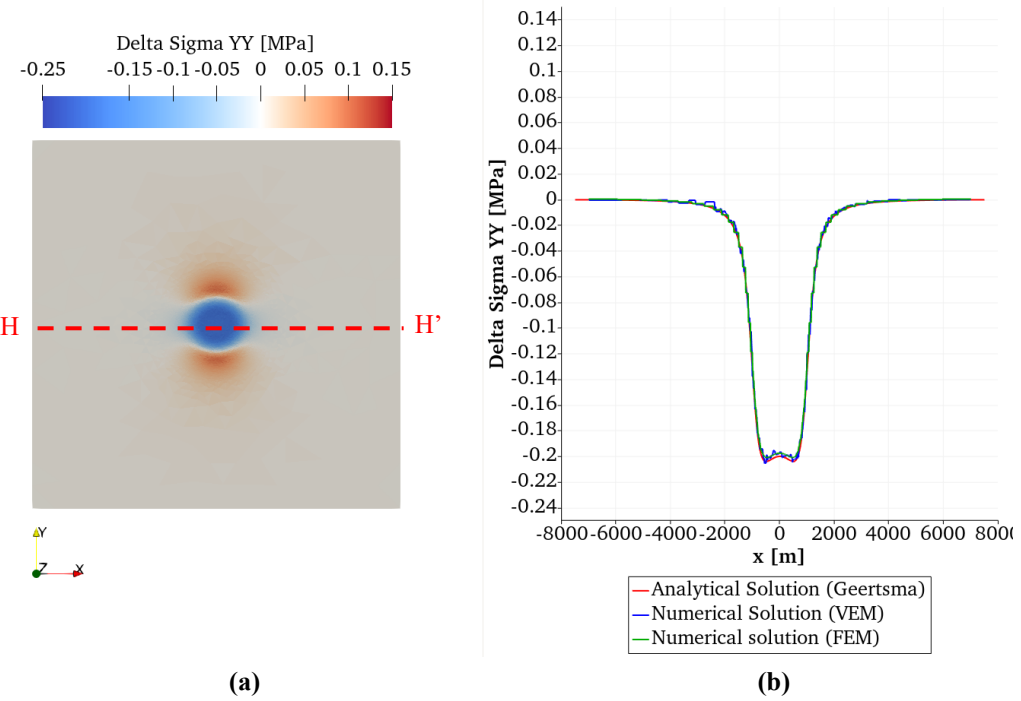
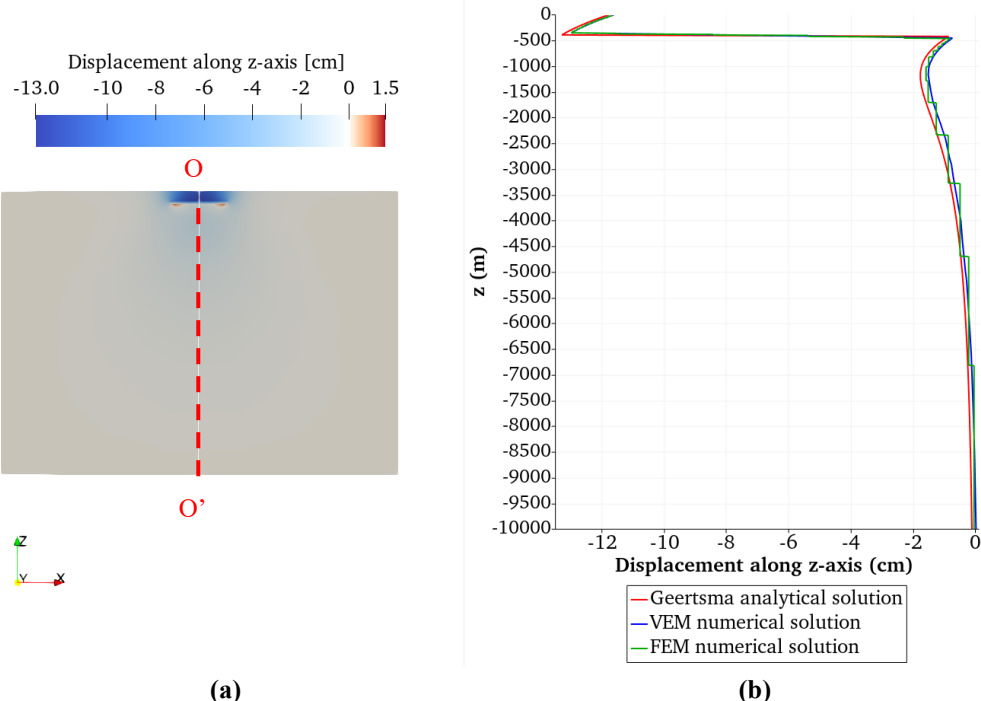


Figure 61: (a) top view of the model. The colormap refers to  $\Delta\sigma_{xx}$ , expressed in MPa, induced by the imposed  $\Delta p$ . (b) comparison of the induced  $\Delta\sigma_{xx}$  along the dotted red segment  $HH'$  in (a).



**Figure 62:** (a) top view of the model. The colormap refers to  $\Delta\sigma_{yy}$ , expressed in MPa, induced by the imposed  $\Delta p$ . (b) comparison of the induced  $\Delta\sigma_{yy}$  along the dotted red segment HH' in (a).



**Figure 63:** (a) section orthogonal to Y-axis of the model. The colormap refers to the displacement along z-axis expressed in cm. (b) comparison of the z-axis displacement along the dotted red segment OO' in (a)

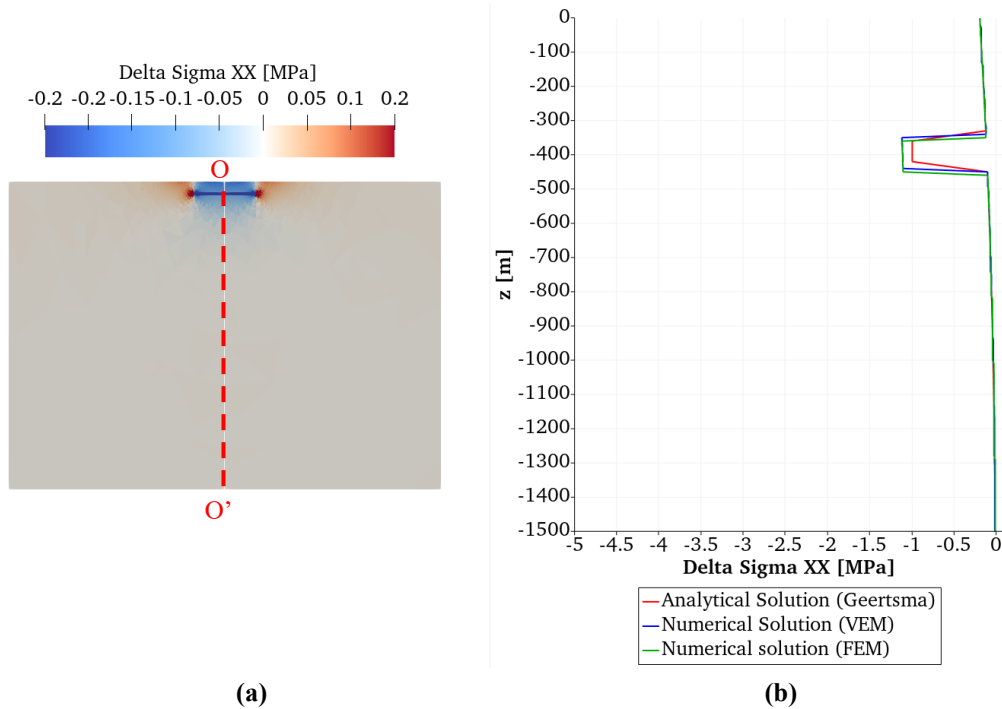


**Figure 64:** (a) section orthogonal to Y-axis of the model. The colormap refers to  $\Delta\sigma_{xx}$ , expressed in MPa, induced by the imposed  $\Delta p$ . (b) comparison of the induced  $\Delta\sigma_{xx}$  along the dotted red segment HH' in (a).

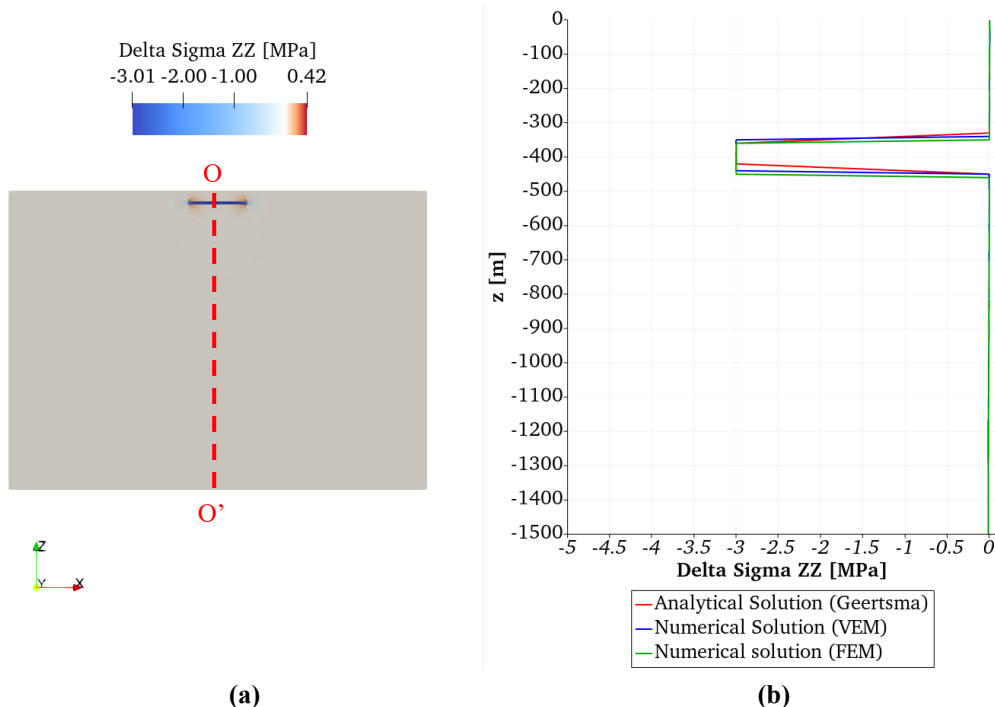


**Figure 65:** (a) section orthogonal to Y-axis of the model. The colormap refers to  $\Delta\sigma_{zz}$ , expressed in MPa, induced by the imposed  $\Delta p$ . (b) comparison of the induced  $\Delta\sigma_{zz}$  along the dotted red segment HH' in (a).

## Offshore Adriatic model

To test the grid generation process and the VEM solver, a synthetic geological model was constructed that reproduces a typical example of the stratigraphic/structural set-up of the North Adriatic offshore. The definition of the case study was based on the outcome of project carried out under an agreement between Politecnico di Torino and the Ministry of Economic Development, involving a detailed survey of all the reservoirs located in the area and the review of the relevant bibliography. Details about the seismic sections and well data collection and the geological classification of the analyzed area were provided in a technical report (SEADOG center, 2017) and are currently being published in a journal paper.

### *Geological classification of the area*

The study area belongs to the North Adriatic Basin delimited by three collisional chains: Dinarides to the East, Southern Alps to the North and Northern Apennines to the West. During the Cenozoic, the North Adriatic basin represented the foredeep-foreland system of the three collisional chains. Its current geological configuration is the result of the orogenic evolution that occurred during the Paleocene-Eocene (Dinaric system), Miocene-Upper Pliocene (southern Alpine system) and Pliocene-Pleistocene (Apennine system) (Cazzini et al., 2015).

Between the Upper Permian and the Middle Triassic, the area was affected by the first phases of extensional tectonics which favored the deposition of limestone, dolomite and evaporites; the extensional regime continued throughout the Mesozoic up to the lower Eocene and led to the development of structural highs with neritic sedimentation (carbonate platforms) separated by deep basins with predominantly pelagic sedimentation (Donda et al., 2013).

The subsequent development of a compressional regime between the Paleocene and Miocene, linked to the convergence between the European and African plate, resulted in an increase in terrigenous sediment supply within the basin with a consequent sedimentation of hemipelagic marl (Marl of Gallare).

During the Pliocene, the flexuration, triggered by the east north-east migration of the Apennine front, caused the rapid subsidence of the internal margin of the basin and a sudden marine transition which in turn favored the deposition of hemipelagic clays in the foreland and foreland ramp areas (Fm. Argille del

Santerno), as well as the deposition of turbidite sequences in the deepest areas of the foredeep domain (Fm. Porto Corsini and Porto Garibaldi) (Velić et al., 2015).

Between the Upper Pliocene and the Lower Pleistocene, the filling of the basin recorded the transition from a deep sea to a delta system controlled by the gradual decrease of the compressional tectonic forces of the Apennines and by an increase in the sediment supply from the Po River. The delta system progradation produced the consequent migration of the Adriatic foredeep towards south-east. Between the Pleistocene and the Holocene, the Apennine progradation was accompanied by the onlap deposition of foredeep turbidites on the foreland margin deepening to the west. These deposits have a basin-scale tabular geometry developing on gentle anticlines which formed during differential compaction of Plio-Pleistocene turbidites (Carola and Ravenna Formation) (Ghielmi et al., 2010; Malvić et al., 2011; Velić and Malvić, 2011).

#### *Geomechanical Model Construction*

The model reproduces a typical gas-bearing reservoir of the North Adriatic area. The reservoir formation is composed of a Pleistocene sedimentary sequence characterized by an alternation of sands and clays. The reservoir consists of a single pool, at an average depth of 730 m. The structural trap is an anticline with a NW-SE direction, while the hydraulic seal is ensured by a clayey formation above the mineralized volume. The areal extension of the field is about 8 km x 7 km as shown in Figure 66 and has an average thickness of 100 m.

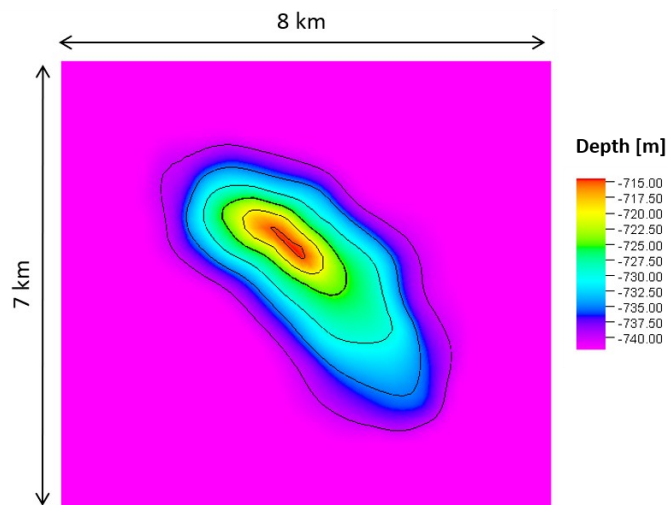


**Figure 66: Structural top of the reservoir**

The geomechanical model has an areal extension of 35 km x 35 km with a thickness of about 3.2 km. The zoning and geomechanical classes of the model are shown in Tab. 4 and Tab. 5, respectively, while the vertical sections are represented in Figure 67 and in Figure 68. The stratigraphic surfaces used for the construction of the model are listed in Tab. 1. It is observed that the Carola formation appears to be in an onlap relationship with the underlying Santerno.

**Table 4: zoning of the geomechanical model on the basis of the stratigraphy**

Age	Formation	Lithology	Zone in 3D model	Top Surface	
Holocene	Ravenna	Marine sands	0	Sea Bottom	
Pleistocene		Clay with local sand interlayer	1	Top 1 Ravenna	
			2	Top 2 Ravenna	
Pliocene	Carola	Alternating thin sands and clays	3	Top Carola	
			4	Top Reservoir	
			5	Bottom Reservoir	
			6	Top Santerno	
			7	Top Basement	
Cenozoic-Mesozoic	Santerno	Clays			
	Carbonate Substratum	Marls and calcareous marls			

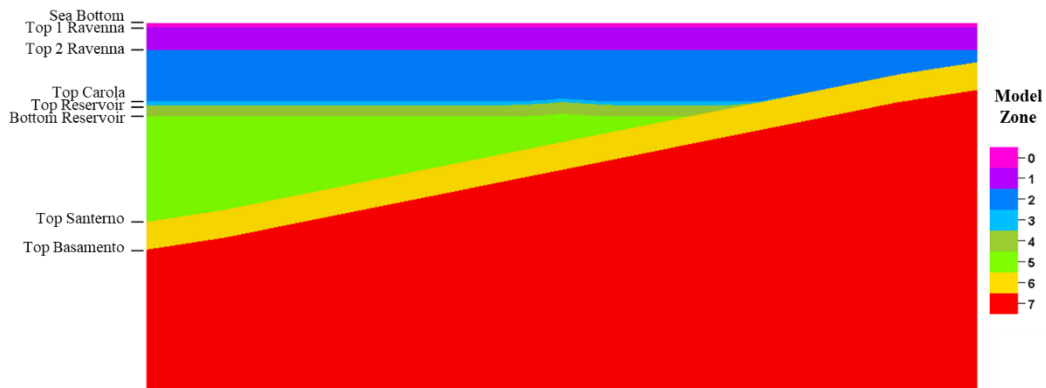


**Figure 67: zoning of the geomechanical model (thicknesses amplification factor of 5 applied in the z-direction)**

**Table 5: geomechanical classes defined in the model.**

Geomechanical Classes	Young's Modulus	Poisson's Ratio	Bulk density	Biot's Coefficient	
	E GPa	$\nu$	$\rho$ g/cm <sup>3</sup>	$\alpha$	
1	0.03	0.38	1.8	1	
2	0.4		1.9		
3	0.0046 z + 0.3082		2.1		
4			2.2		
5			2.3		
6	65		2.6		

**Figure 68: geomechanical classes defined in the model (thicknesses amplification factor of 5 applied in the z-direction)**

As far as the pressure map is concerned, it has been assumed that, after 4 years of gas production (22/03/2018-22/03/2022), the production is interrupted, and the pressure re-equilibrates in the system. The measured pressure variation is thus homogeneous throughout the reservoir and equal to 4 MPa (in Figure 69 a sectional view).

The domain discretization was performed by exploiting both the pillar-gridding process implemented in Petrel E&P and the workflow for unstructured grid

construction illustrated in the “Unstructured grid construction workflow” section. The former is characterized by a *tartan* refinement and counts  $2.9 \cdot 10^5$  nodes. In Figure 70a and Figure 70b the grid top and a 3D view are shown, respectively. The latter is made up of  $1.9 \cdot 10^5$  nodes. In Figure 71a and Figure 71b the corresponding top and 3D view are shown.

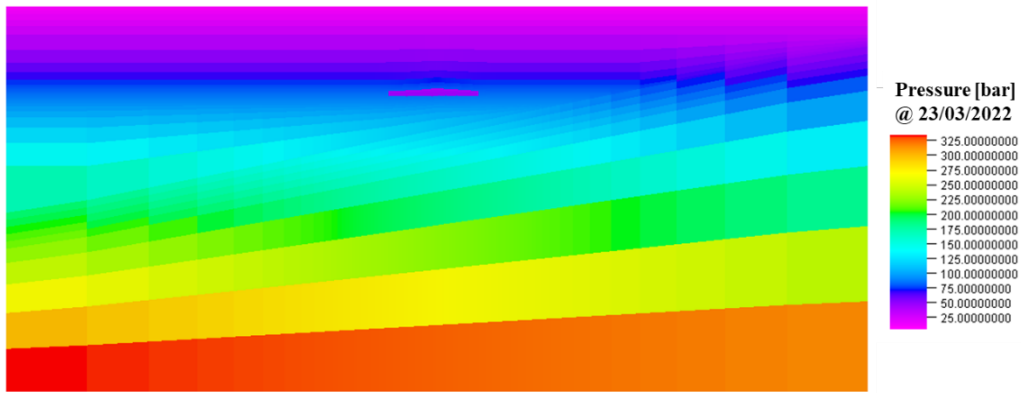


**Figure 69:** sectional view of the pressure map @ 23/03/2022 model (thicknesses amplification factor of 5 applied in the z-direction).

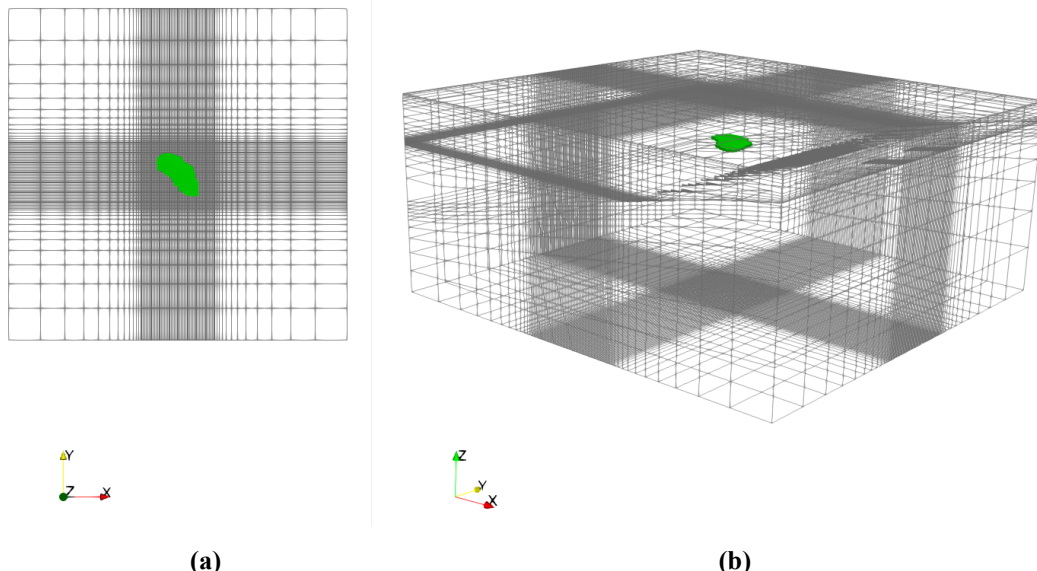


**Figure 70:** domain discretization by pillar-gridding: (a) top view and (b) 3D view. Reservoir cells are highlighted in green. In (b) a thicknesses amplification factor of 5 applied in the z-direction) to highlight the progression of the discretization.

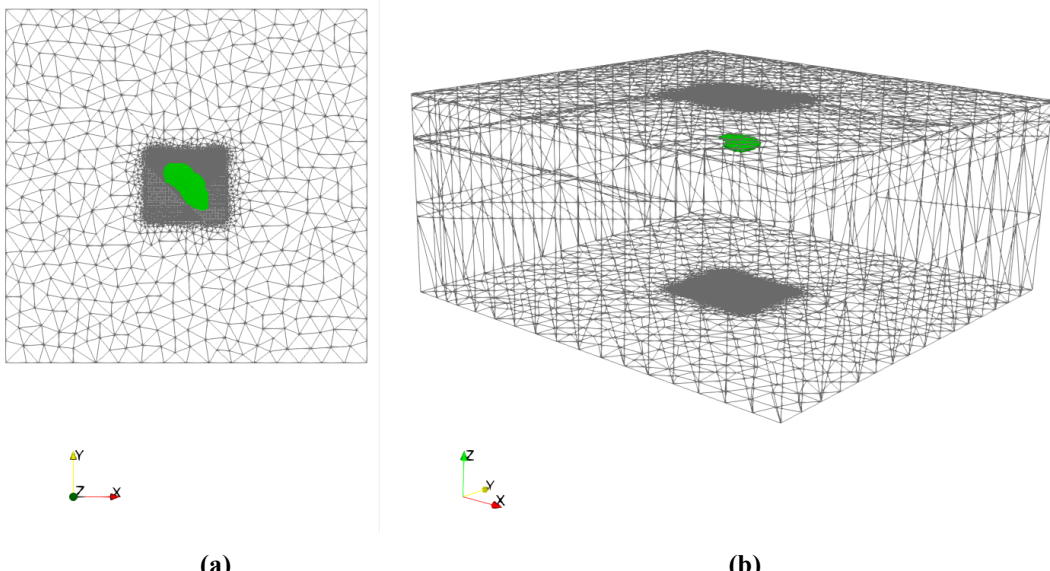


**Figure 71:** domain discretization by unstructured grid construction workflow: (a) top view and (b) 3D view. Reservoir cells are highlighted in green. In (b) a thicknesses amplification factor of 5 applied in the z-direction to highlight the progression of the discretization.

The set of sampled surfaces which were used as constraints for the unstructured grid construction (step 1 of the workflow of Figure 19) are shown in Figure 72. Since the sampling step is of 150 m x 150 m and would generate a too coarse grid, a refinement zone of about 7500 m x 7500 m is defined (yellow area). The presence of *pinch-out* (orange and green surfaces) made necessary to verify the presence of duplicated points and surface intersections. To make such operations easier, the triangulation performed on the top surface (“*Sea Bottom*”) was projected on the underlying surfaces. The drawback of this approach is the resulting discretization in the lower region of the model, where unnecessary cells were defined - as it happens for the corner point grid with *tartan* refinement.

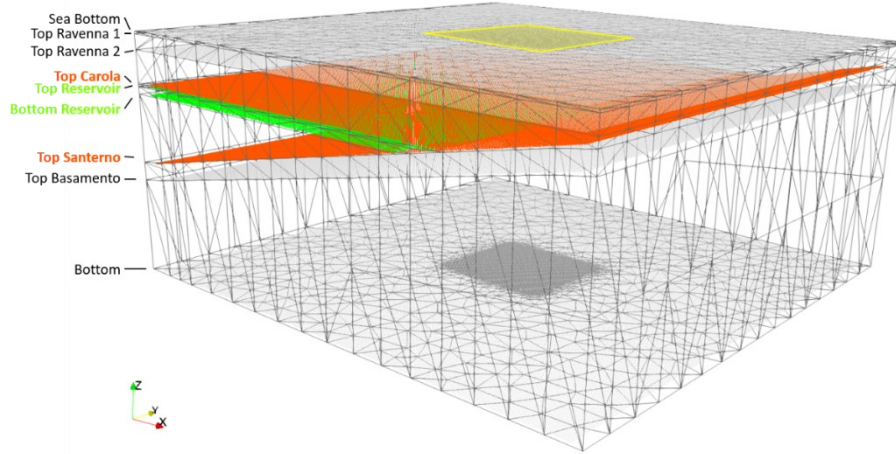


**Figure 72:** surfaces constraining the unstructured grid. Amplification factor of 5 applied in the z-direction.

The comparison of the vertical section between the two grids is shown in Figure 73a and Figure 73b. In both cases it is observed how the grid could be optimized in the underburden zone by introducing a coarsen triangulation of the constraining surfaces or applying a *gluing* approach which defines polyhedral (not necessarily convex) cells by the union of two or more tetrahedra.

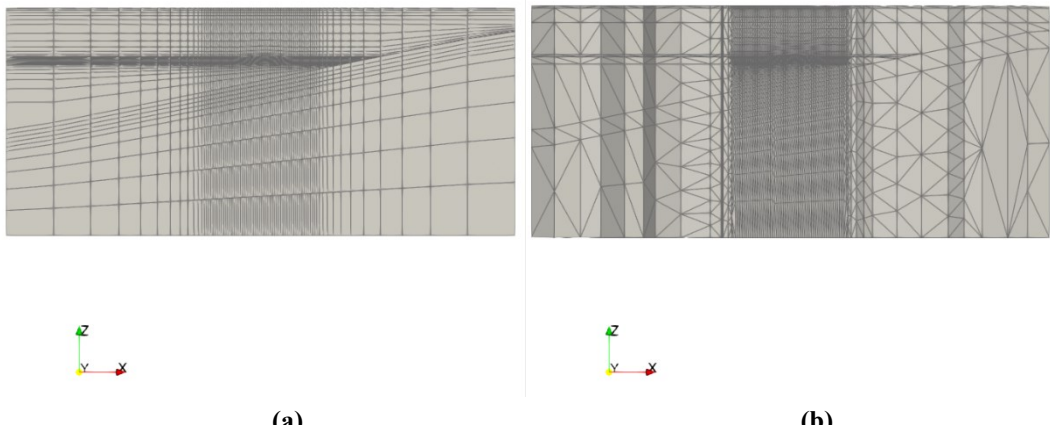


**Figure 73:** vertical section of the defined grid: (a) corner-point grid and (b) unstructured grid. Amplification factor of 5 applied in the z-direction.

Once the grid was defined and the regions identified (Figure 74), the mechanical properties were appropriately assigned. Figure 75 shows the trend of Young's module, whose value can depend on the cell centroid depth as specified in Table 5.

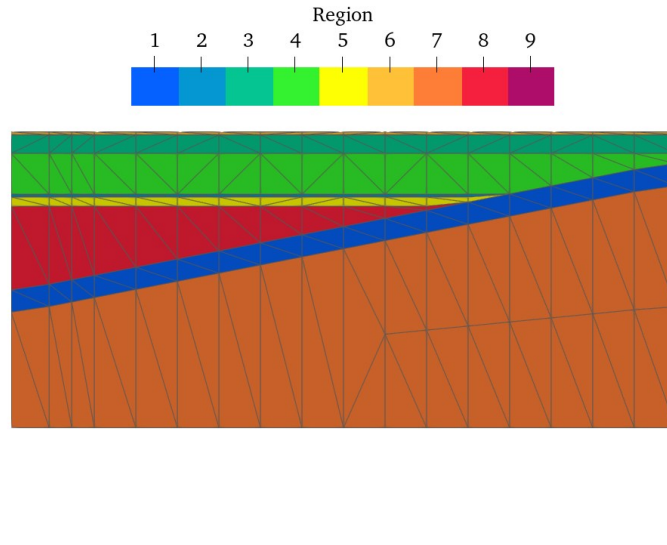


**Figure 74:** region identification from tetrahedralization process. Amplification factor of 5 applied in the z-direction.

The assignment of the pore pressure forcing term requires the correct identification of the reservoir cells. This objective is achieved by applying a dedicated workflow which requires two inputs: the region identification and the depth of the gas-water contact (GWC), if available. The resulting superposition of the reservoir corner-point grid discretization (green) to the unstructured tetrahedrization (blue-lines) is shown in Figure 76. It is observed that the faces of hexahedra, defined through the pillar-gridding process, are not necessarily planar and in the analyzed model they occur especially in correspondence of the reservoir cells due to the presence of the smooth anticlinal. Conversely, the VEM theoretical framework and the corresponding tested implementation involve polyhedral cells with planar faces, thus, if applied to grids which violate such hypothesis, can lead to the reduction of the solution accuracy. To verify the impact of not-planar grid cells two different grid refinements were introduced in correspondence of the reservoir cells as shown in Figure 17.

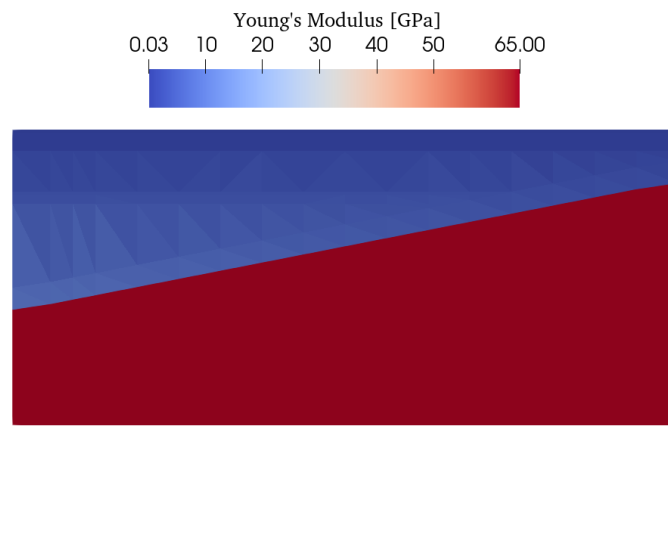


**Figure 75:** Young's modulus assignment. Amplification factor of 5 applied in the z-direction.

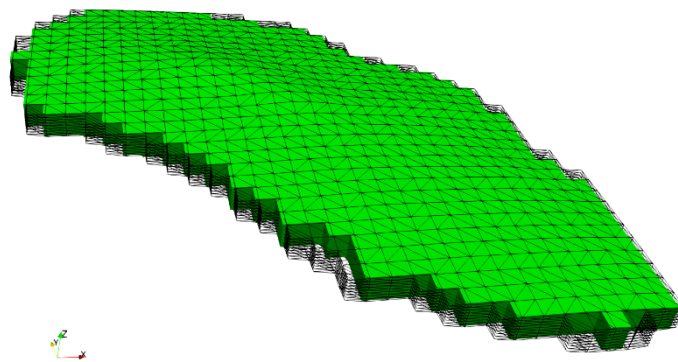


**Figure 76:** reservoir's cells identification

The resulting sequence of grids to be compared are: (a) hexahedral corner-point grid, (b) hexahedral corner-point grid “split faces”, i.e. reservoir hexahedral cells characterized by not-planar cells are substituted by polyhedrons obtained by adding a node in correspondence of the barycenter of the not-planar faces, (c) hexahedral corner-point grid “refine reservoir”, i.e. reservoir polyhedral cells are decomposed in tetrahedra. In Figure 77 the grid sequence and the reservoir top view are represented.

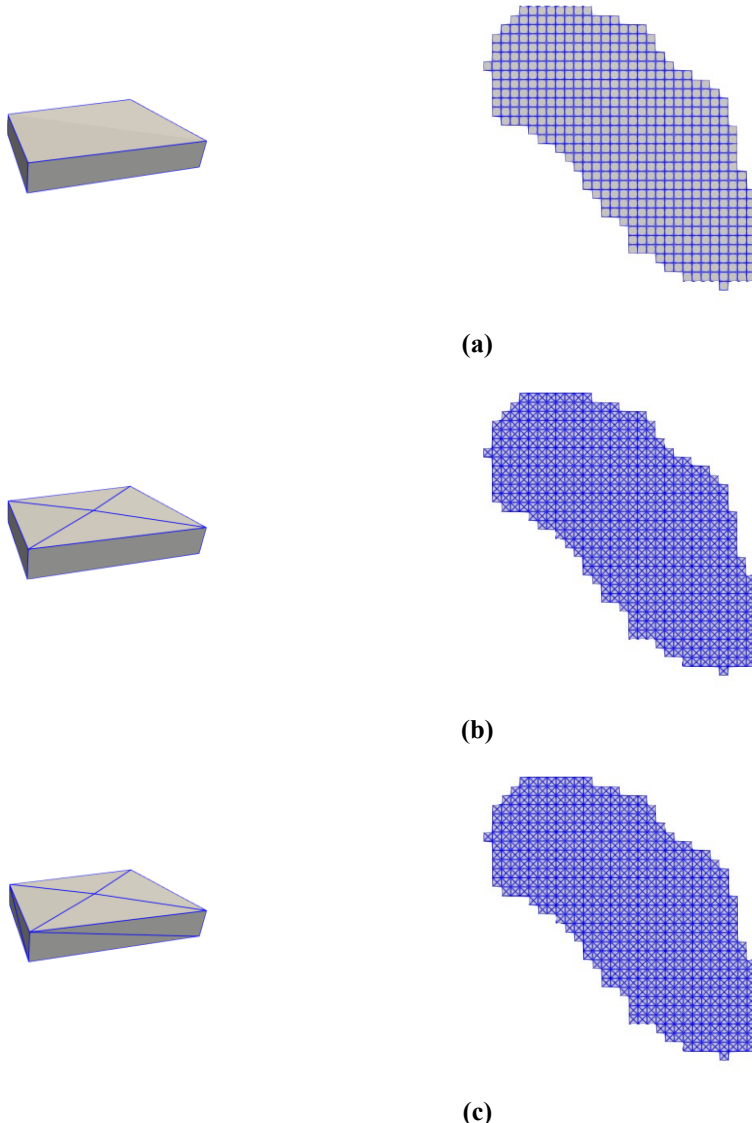


**Figure 77:** top view of the reservoir cells: (a) corner-point hexahedral grid, (b) polyhedral grid obtained by adding a node in correspondence of the barycenter of not planar faces in (a), (c) tetrahedral grid from decomposition of polyhedron in (b).

The assessment of the impact of the not planar faces in the VEM computed solution was performed in terms of relative discrepancy of the displacement z-component ( $w$ ). The FEM solution calculated on the original hexahedral pillar grid was taken as the reference value (see Figure 78 and Figure 79 for the top view and y-axis section, respectively). The relative discrepancy, instead, was defined as:

$$\text{discrepancy} = \frac{|w_{VEM} - w_{FEM}|}{\max(|w_{FEM}|)} \cdot 100 \quad (40)$$

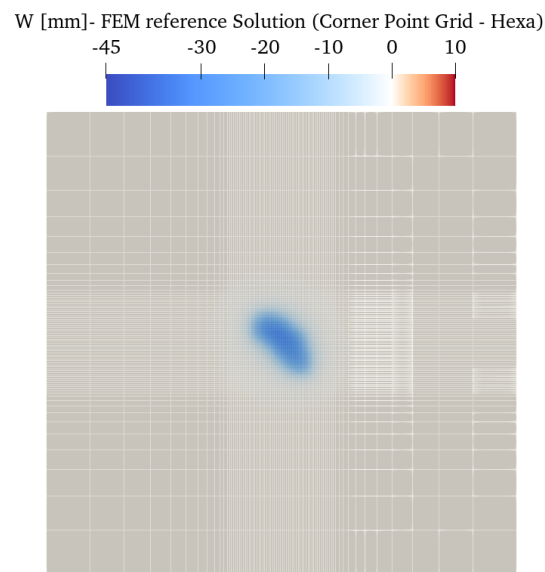


**Figure 78:** top view of the model. Colormap refers to the z-component of the FEM displacement. It ranges between 45mm and 10 mm.

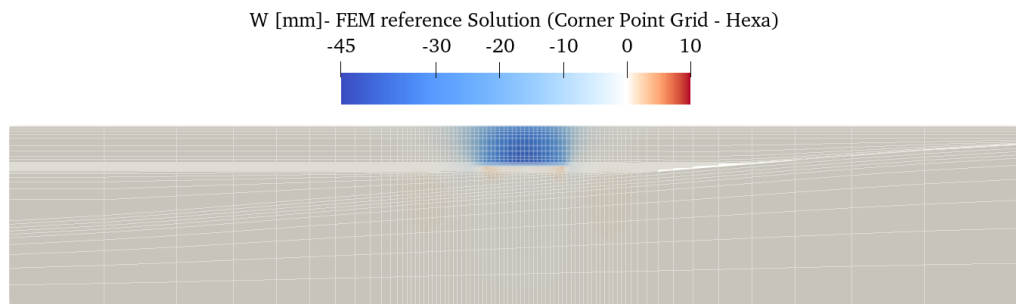


**Figure 79:** y-axis orthogonal section of the model. Colormap refers to the z-component of the FEM displacement. It ranges between 45mm and 10 mm.

The top view of the reservoir cells is shown in Figure 80,. The colormap refers to the relative discrepancy defined in (40). It is observed that no significant discrepancy is observed among the solutions calculated on different grids. This proves that the presence of not planar faces, due to the smooth anticlinal characterizing the current model, does not cause a reduction in the solution accuracy. The maximum recorded relative discrepancy is of the order of 5% and it refers to the boundary reservoir cells. Here the discontinuity of the imposed forcing term (constant delta pore pressure in the reservoir and zero outside) exasperates the effects of different strategies of refinement. For completeness, the top view and the y-axis orthogonal section of the model are shown in Figure 81 and Figure 82, respectively. Colormap refers to the z-component displacement relative discrepancy between FEM reference solution and VEM solution calculated on the original hexahedral corner-point grid (a), in the “spit faces” grid (b) and in the “refine reservoir” grid (c). The vertical displacement appears to be satisfactorily described. On the top surface the subsidence maximum discrepancy is about 2%. On the y-axis orthogonal section, instead, the discrepancy reaches the same magnitude as for the reservoir cells, about 5%.

Eventually, a comparison of the FEM Corner-Point Grid and the VEM Unstructured Grid (Figure 70) is shown. Preliminarily the subsidence bowls identified by the two solutions were compared, as shown in Figure 83, where cells are filtered using the minimum displacement of 0.5 mm as the threshold, i.e. values below that value are considered negligible. It is observed that both the planar and the vertical extension are in agreement, showing that the phenomenon is macroscopically captured. Since the solutions were calculated on different discretization nodes, a qualitative comparison was performed through line plots along a top surface segment as already shown for the Geertsma’s model validation test. The comparison of the three components of displacement (along the segment HH’ of Figure 84a) are shown in Figure 84b, Figure 85b and Figure 86b, respectively. A good agreement is observed between solutions especially in the x and y direction. In the refinement zone, indeed, the two grids share the same areal discretization. In the vertical direction, instead, a slight overestimation of the subsidence is observed. The vertical discretization can play a role, but it is also noticed that the maximum subsidence values are -29.8 mm and -31.8 mm for the FEM and VEM, respectively, which lead to a relative discrepancy of 4.5% - in line with the one observed in the previous tests.

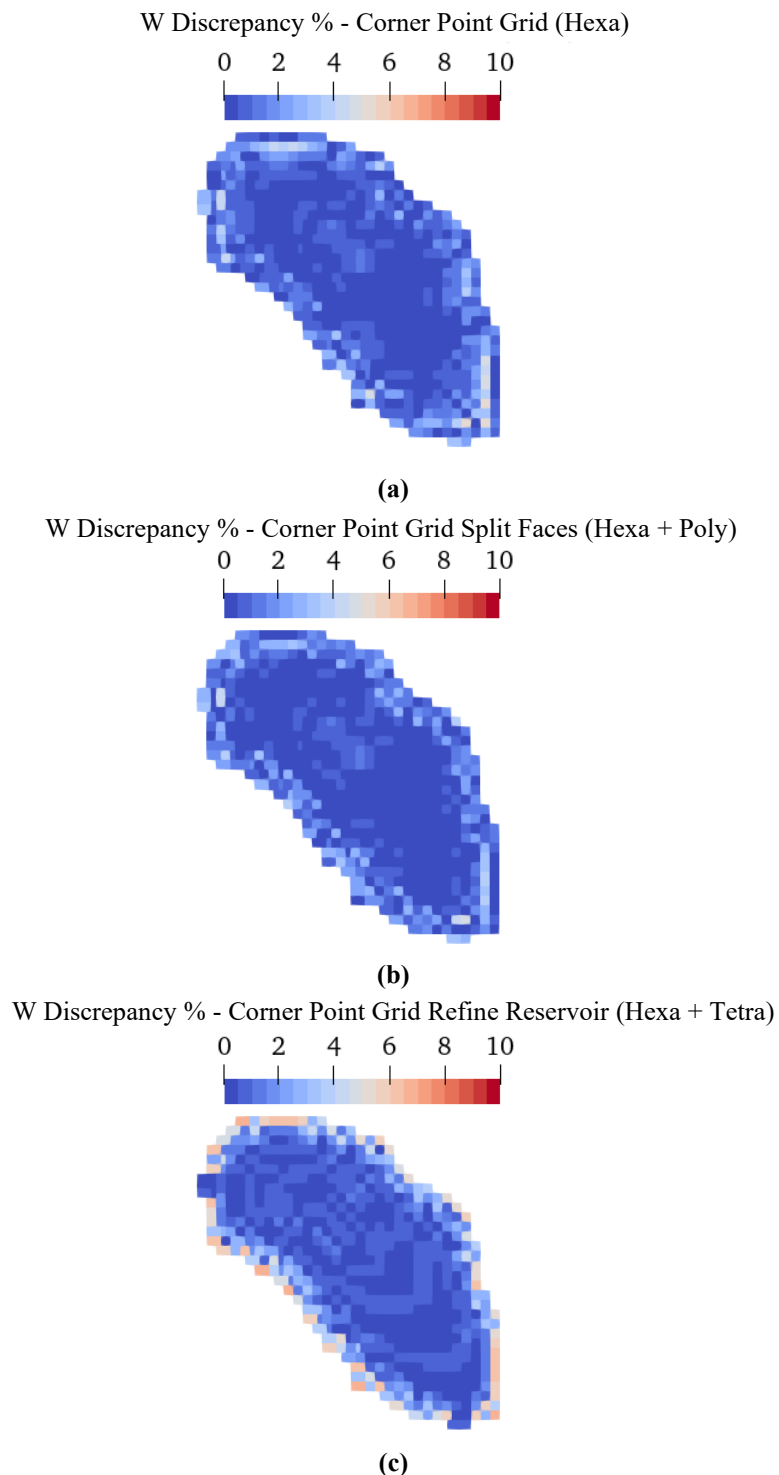


Figure 80: Top view of the reservoir cells. The colormap refers to the z-component displacement relative discrepancy between FEM reference solution and VEM solution calculated on the original hexahedral corner-point grid (a), in the “spit faces” grid (b) and in the “refine reservoir” grid.

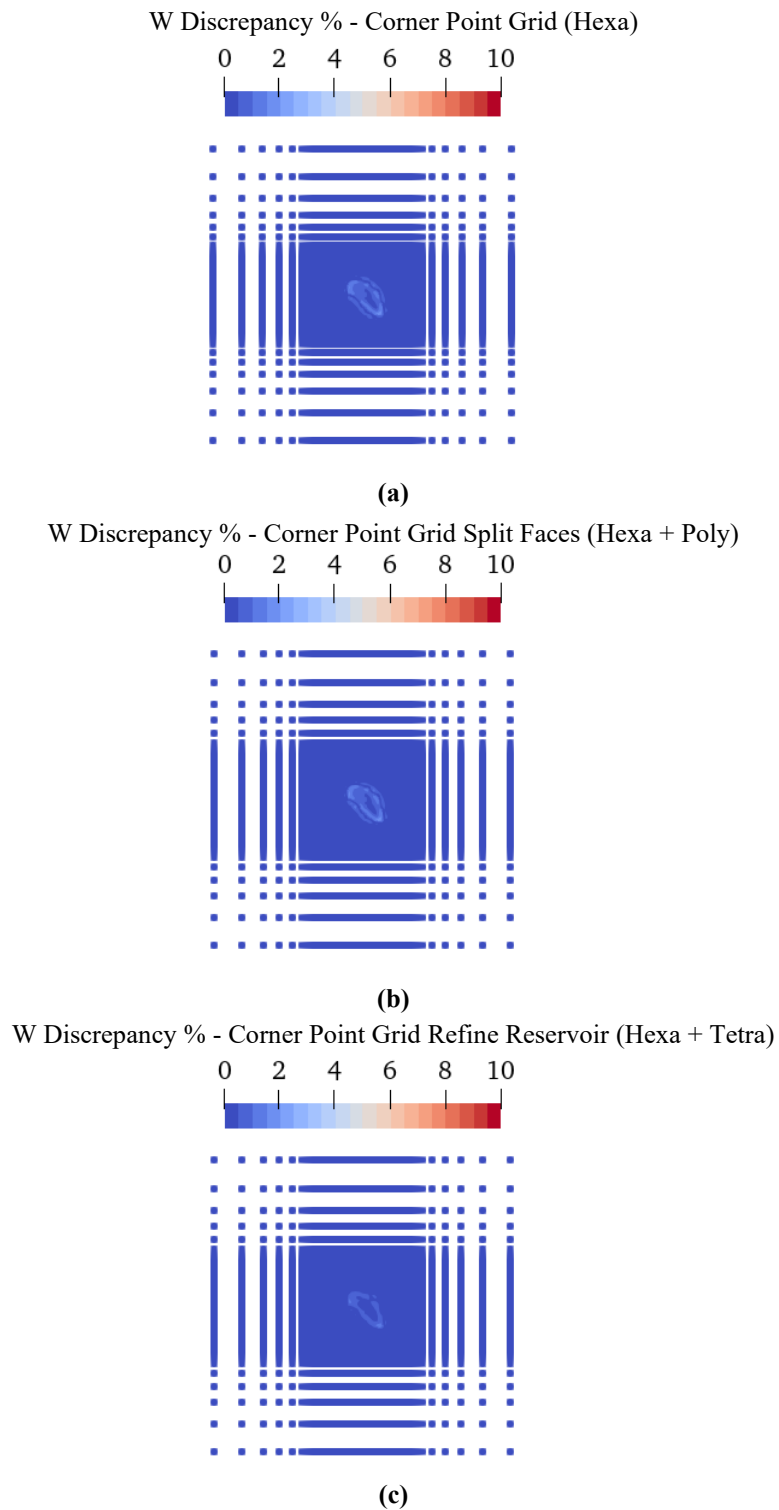
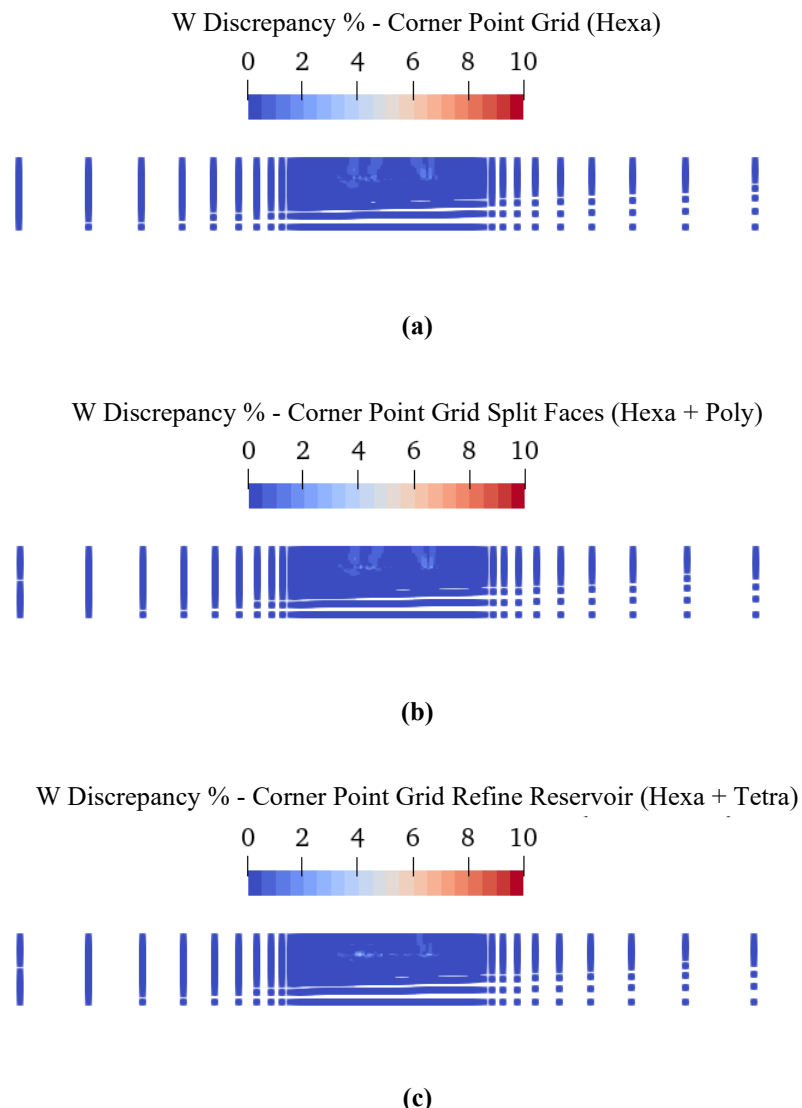
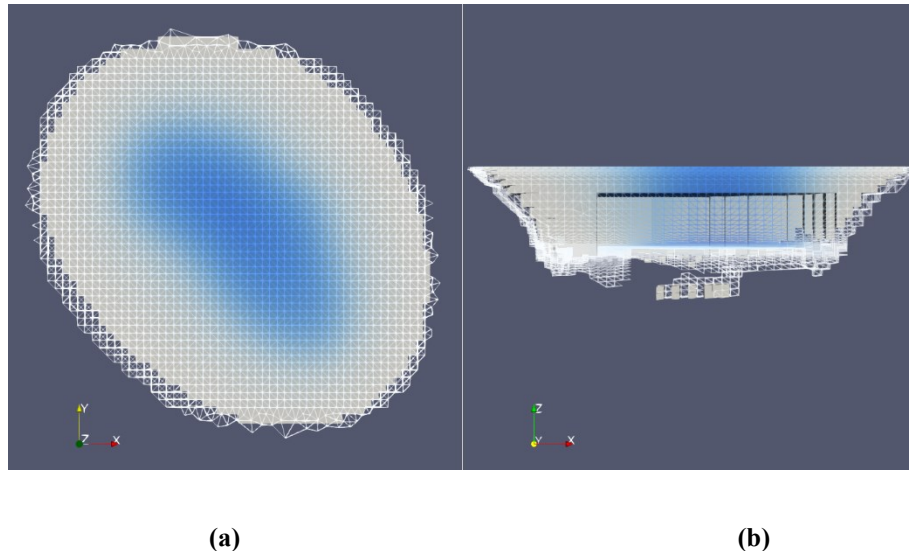


Figure 81: top view of the model. The colormap refers to the z-component displacement relative discrepancy between FEM reference solution and VEM solution calculated on the original hexahedral corner-point grid (a), in the “spit faces” grid (b) and in the “refine reservoir” grid.



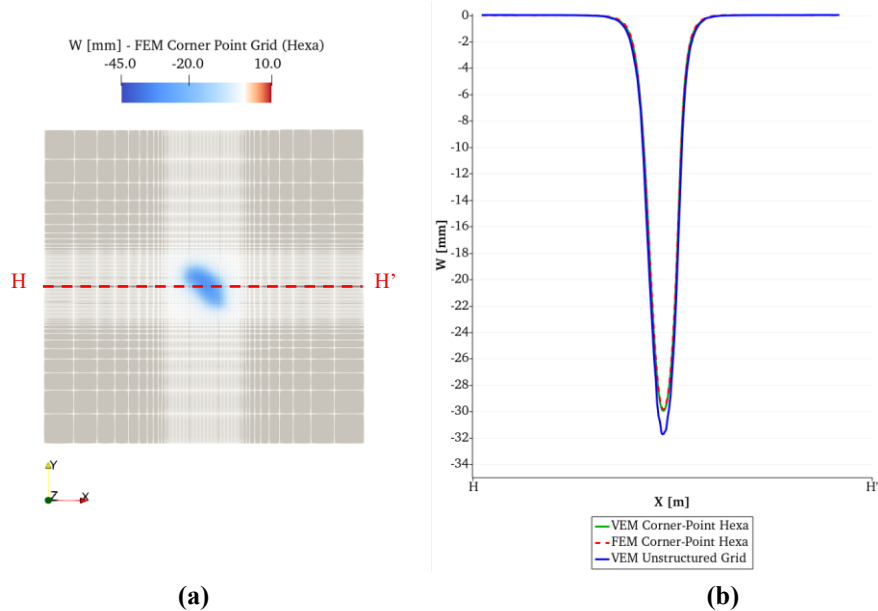
**Figure 82:** y-axis orthogonal section of the model. The colormap refers to the z-component displacement relative discrepancy between FEM reference solution and VEM solution calculated on the original hexahedral corner-point grid (a), in the “split faces” grid (b) and in the “refine reservoir” grid.



(a)

(b)

**Figure 83:** (a) top view and (b) y-axis orthogonal section of the subsidence bowl identified by the FEM solution calculated on the Corner-Point Grid (surface) and the VEM solution calculated on the Unstructured Grid (wireframe). Amplification factor of 2 applied in the z-direction.



(a)

(b)

**Figure 84:** (a) model top-view. Colormap refers to the z-component of displacement (subsidence  $W$ ) obtained by FEM on the original Corner-Point Grid. (b) Plot along the  $HH'$  line shown in (a). Comparison between the reference FEM solution on the corner point grid (hexa) (dotted red) against the VEM solutions calculated on the hexa corner point-grid (green) and on the tetra unstructured grid (blue) is shown.

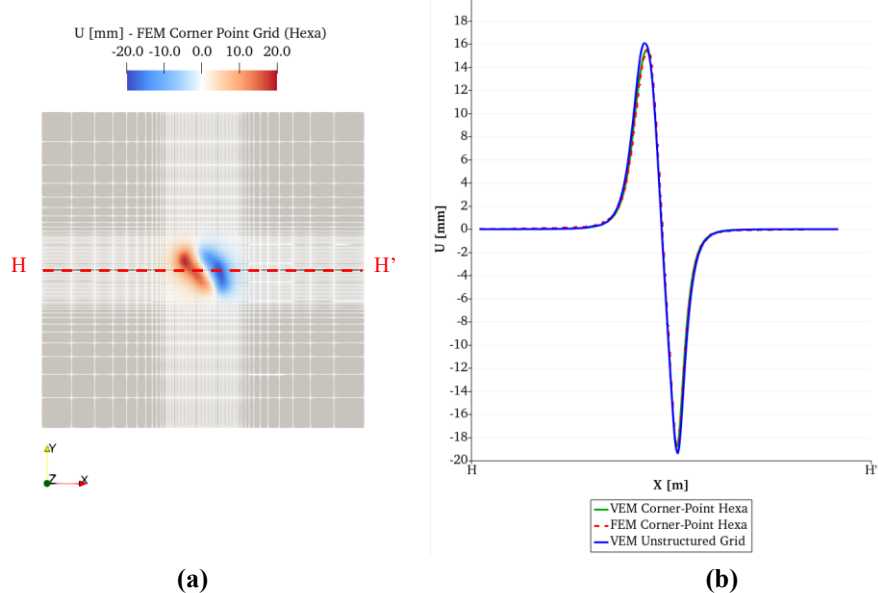


**Figure 85:** (a) model top-view. Colormap refers to the x-component of displacement ( $U$ ) obtained by FEM on the original Corner-Point Grid. (b) Plot along the  $HH'$  line shown in (a). Comparison between the reference FEM solution on the corner point grid (hexa) (dotted red) against the VEM solutions calculated on the hexa corner point-grid (green) and on the tetra unstructured grid (blue) is shown.

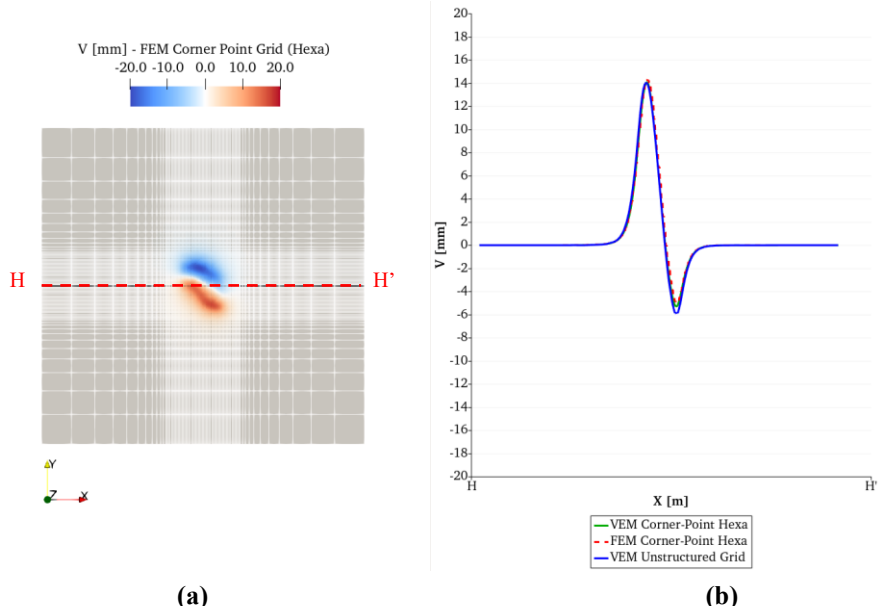


**Figure 86:** (a) model top-view. Colormap refers to the y-component of displacement ( $V$ ) obtained by FEM on the original Corner-Point Grid. (b) Plot along the  $HH'$  line shown in (a). Comparison between the reference FEM solution on the corner point grid (hexa) (dotted red) against the VEM solutions calculated on the hexa corner point-grid (green) and on the tetra unstructured grid (blue) is shown.

## UGS model

The analyzed Offshore Adriatic model was used to perform a validation test on a storage scenario. In the Carola formation, characterized by an alternation of sands and clays, seven superimposed gas pools were defined, representing a typical formation of the Italian landscape. The key parameters characterizing the corresponding dynamic model are listed in Table 6. Realistic petrophysical parameters were assigned. Figure 87 shows the discretized formation volume used for dynamic simulations; the wells defined to design the UGS strategy are also shown. The reservoir main production mechanism is gas expansion. The resulting UGS strategy was straightforward: 12 vertical wells were defined with the same completion data. They produce from all the layers simultaneously with control mode on bottom hole pressure (*BHP*): minimum pressure equal to 1 MPa and maximum pressure equal to 7 MPa during production and injection periods, respectively.

**Table 6: UGS dynamic model parameters**

Parameter	Description	Value
<i>FPR</i>	Average Field Pressure	7.034 MPa
<i>RGIP</i>	Reservoir Gas in Place	$9.3 \cdot 10^9 \text{ sm}^3$
<i>NTG</i>	Net to Gross	0.7
<i>SW</i>	Water Saturation	0.266
<i>PHI</i>	Porosity	0.3
<i>PERMX</i>	Absolute Permeability	250 mD

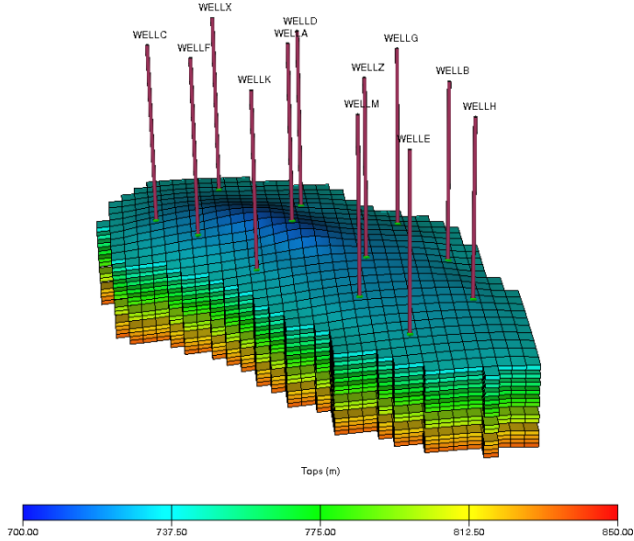


**Figure 87: UGS dynamic model: 7 superimposed gas pools are simulated. UGS strategy considered 12 wells.**

A UGS cycle was defined by 6 months of gas withdrawal followed by six months of gas injection with a week of closure in between. The dynamic simulations considered 10 cycles. The resulting gas rate and field pressure evolution are shown in Figure 88 and Figure 89, respectively. Due to the imposed pressure constraint the injected volume is maximized without exceeding the initial reservoir pressure. Moreover, as already mentioned, the only presence of depletion drive makes the UGS response balanced and stabilized both in terms of reservoir static pressures and injected/produced gas volume: each cycle is characterized by the same withdrawn/injected volume with a corresponding pressure variation  $\Delta p = 6.2$  MPa. Due to the constant pressure variation cycle after cycle and to the linearity of the considered constitutive law the induced displacement is expected to replicate the trend shown by pressure. Geomechanical analyses were then performed on the first cycle (highlighted in red in Figure 89) and a sequence of two simulations were performed imposing a withdrawal  $\Delta p_1 = -\Delta p$  and an injection  $\Delta p_2 = \Delta p$ .

The grid construction of the geomechanical model was performed through the already mentioned pillar-gridding workflow. The resulting model has an areal extension of 55 km x 50 km and a thickness of 3.2 km. The number of nodes is about  $2.67 \times 10^5$ . For the geomechanical characterization the classes defined in Table 5 were assigned according to the scheme in Figure 68. y-axis orthogonal slice of

the geomechanical grid is shown in Figure 90. Colored cells identify the reservoir where pressure variation (the forcing term) is applied.

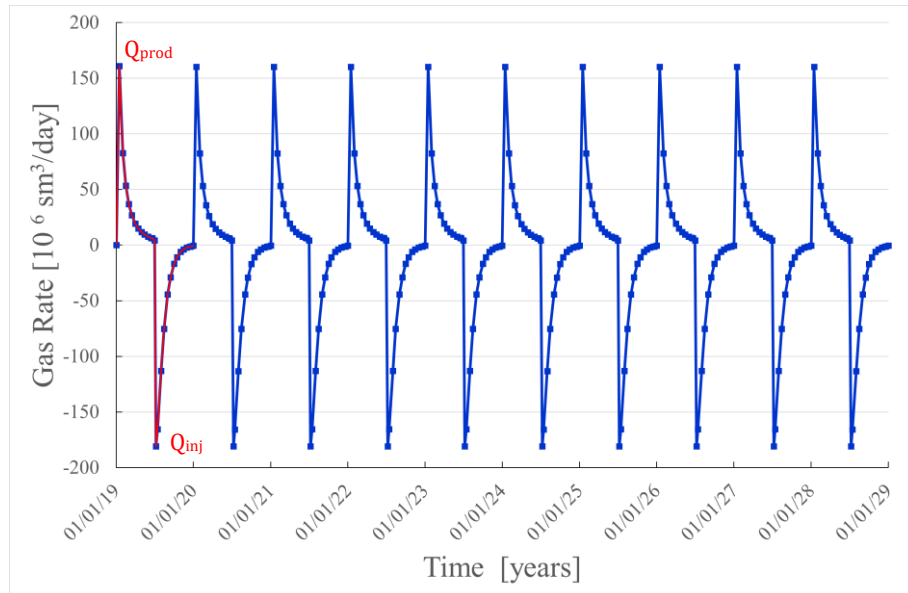


**Figure 88:** gas rate history of the UGS scenario: 10 gas storage cycles of 6 months of production followed by 6 months of injection. A week of closure between two cycles. In red the cycle under analysis.

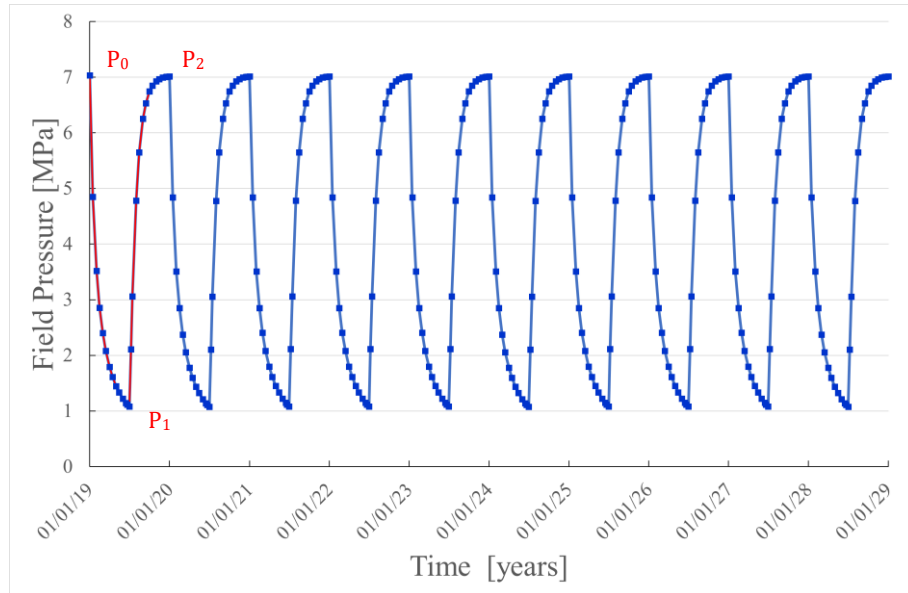


**Figure 89:** field gas pressure history of the UGS scenario. In red the cycle under analysis

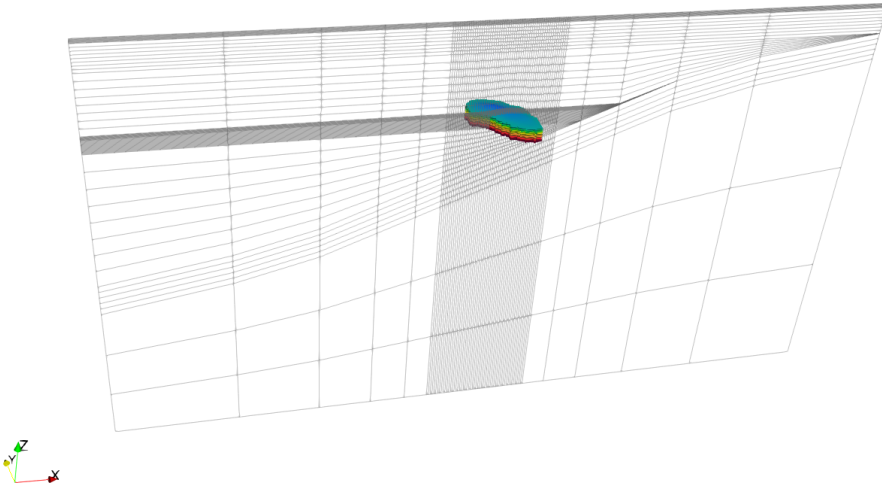


**Figure 90: y-axis orthogonal slice of the geomechanical grid. Colored cells represent the reservoir. Amplification factor of 10 applied in the z-direction.**

As a preliminary validation the subsidence bowls identified by the two solutions were compared. The threshold was set equal to -0.05 mm. The top view and the y-axis orthogonal section are shown in Figure 91a and Figure 91b, respectively. Colored cell surfaces represent the FEM solution and wireframe corresponds to the VEM one. A good agreement between the two is observed and is verified that the extension of the refinement region is adequate to capture the analyzed phenomena.

In the sequences Figure 92-Figure 94 and Figure 97-Figure 99, comparisons of the displacement components of the two solutions are shown along the segment HH' on the top surface (Figure 92a). Indices 1 and 2 identify the withdrawal and injection results, respectively. It is observed that in the second step, where the rebound compensates the subsidence induced by gas production, the resulting vertical displacement is barely of 0.05 cm against the 17 cm shown at the end of production. Despite the different order of magnitude, a satisfactory agreement of the two solutions is observed. Analogous comparison is performed in terms of increment of the effective stress components along the vertical segment OO' (Figure 95a) of the y-axis orthogonal section. The xx and zz components, which show a not negligible variation are shown in Figure 95-Figure 96 and Figure 100-Figure 101. As expected, values different from zero are observed in correspondence of the reservoir cells where the load is applied.

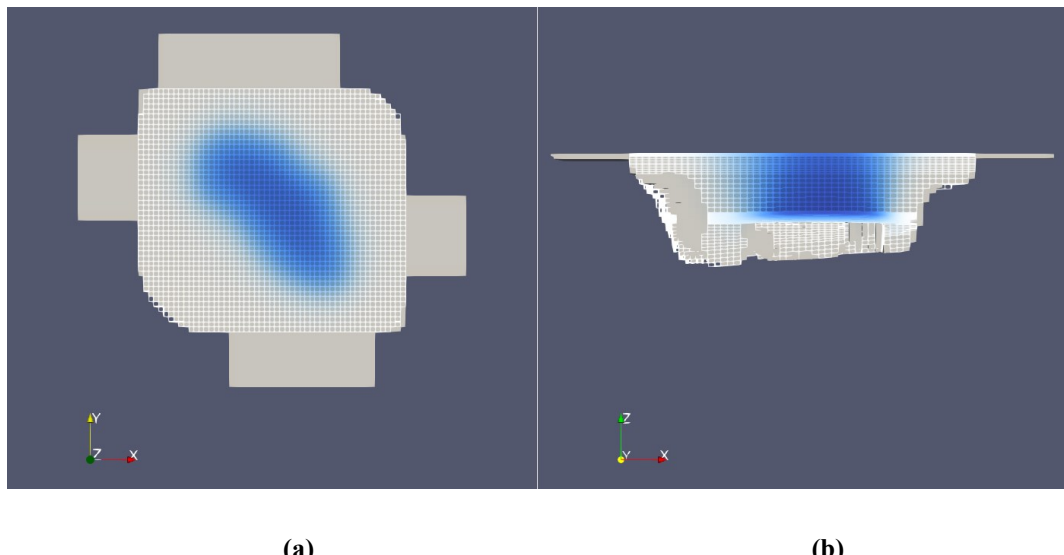


Figure 91: (a) top view and (b) y-axis orthogonal section of the subsidence bowl identified by the FEM (surface) and the VEM (wireframe) solution. Amplification factor of 2 applied in the z-direction.

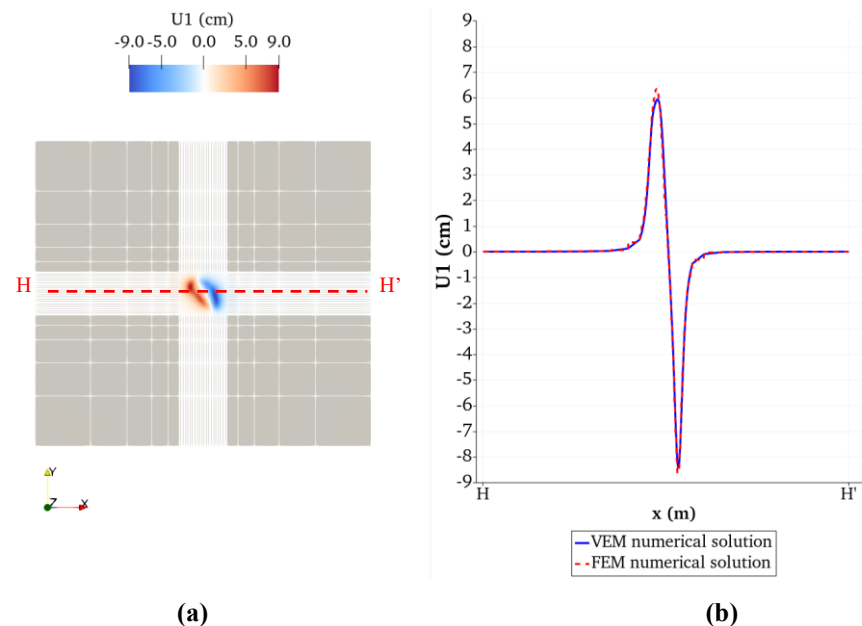
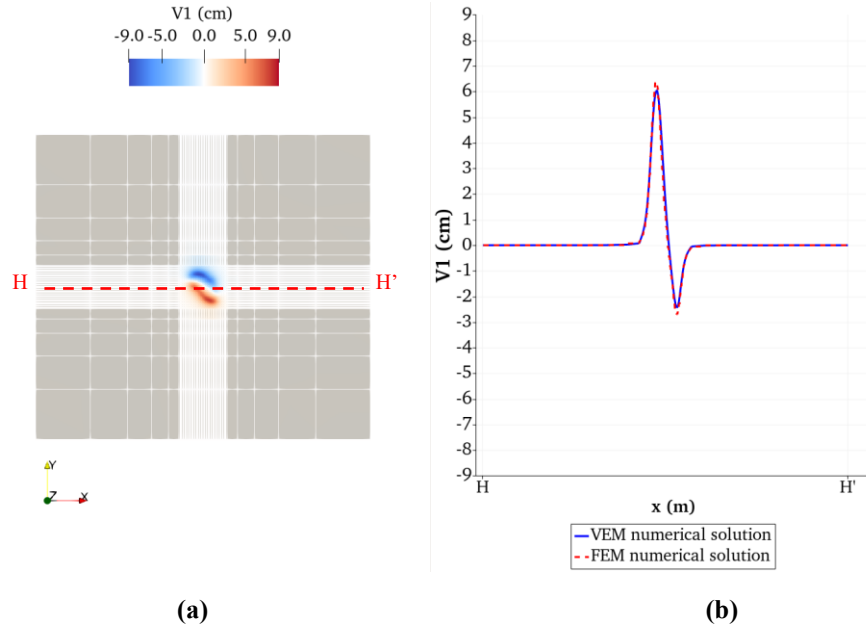
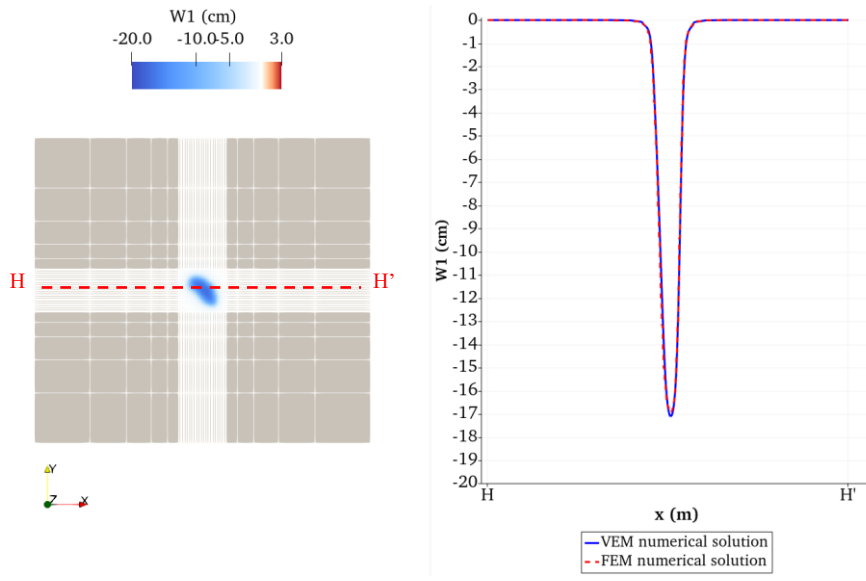


Figure 92: (a) model top-view. Colormap refers to the x-component of displacement ( $U$ ) obtained by FEM at the end of production ( $\Delta p_1$ ). (b) Plot along the  $HH'$  line shown in (a). Comparison between the reference FEM solution on (dotted red) against the VEM solutions (blue) is shown.



**Figure 93:** (a) model top-view. Colormap refers to the y-component of displacement ( $V$ ) obtained by FEM at the end of production ( $\Delta p_1$ ). (b) Plot along the  $HH'$  line shown in (a). Comparison between the reference FEM solution on (dotted red) against the VEM solutions (blue) is shown.



**Figure 94:** (a) model top-view. Colormap refers to the z-component of displacement ( $W$  subsidence) obtained by FEM at the end of production ( $\Delta p_1$ ). (b) Plot along the  $HH'$  line shown in (a). Comparison between the reference FEM solution on (dotted red) against the VEM solutions (blue) is shown.

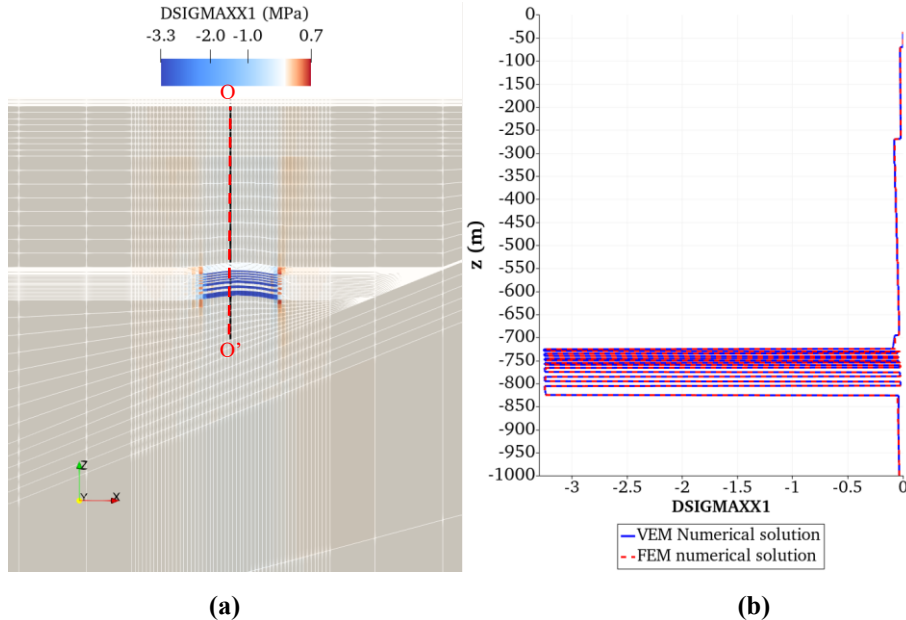


**Figure 95:** (a) y-axis orthogonal section view of the model. Colormap refers to variation of the xx-effective stress component obtained by FEM at the end of production ( $\Delta p_1$ ). (b) Plot along the OO' segment shown in (a). Comparison between the reference FEM solution on (dotted red) against the VEM solutions (blue) is shown.

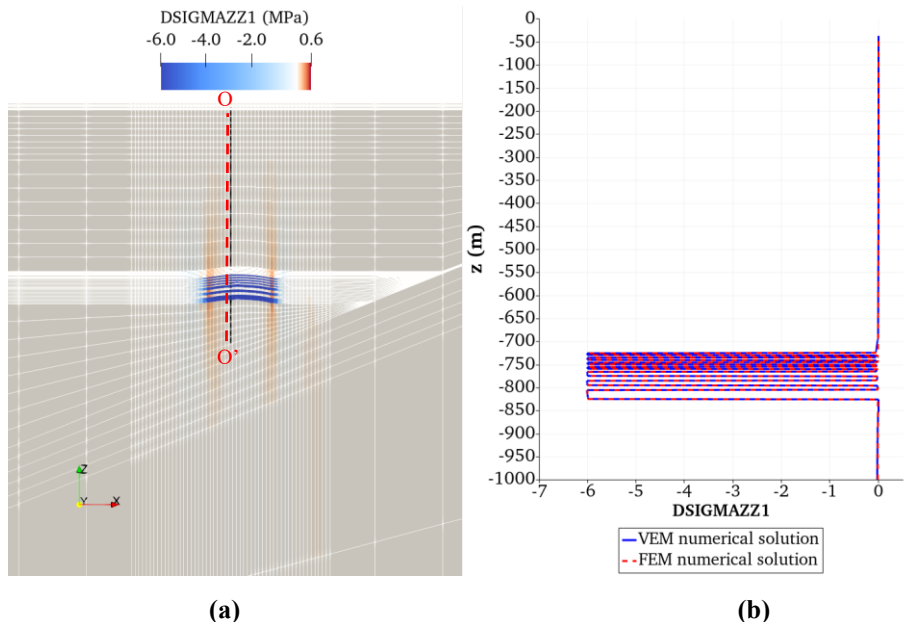


**Figure 96:** (a) y-axis orthogonal section view of the model. Colormap refers to variation of the zz-effective stress component obtained by FEM at the end of production ( $\Delta p_1$ ). (b) Plot along the OO' segment shown in (a). Comparison between the reference FEM solution on (dotted red) against the VEM solutions (blue) is shown.

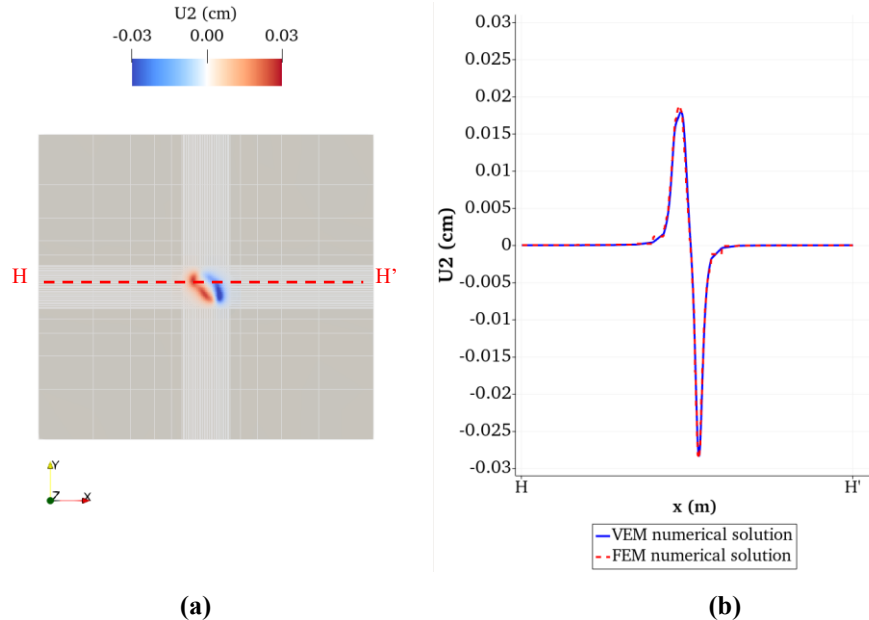


**Figure 97:** (a) model Top-view. Colormap refers to the x-component of displacement ( $U$ ) obtained by FEM at the end of injection ( $\Delta p_2$ ). (b) Plot along the  $HH'$  line shown in (a). Comparison between the reference FEM solution on (dotted red) against the VEM solutions (blue) is shown.

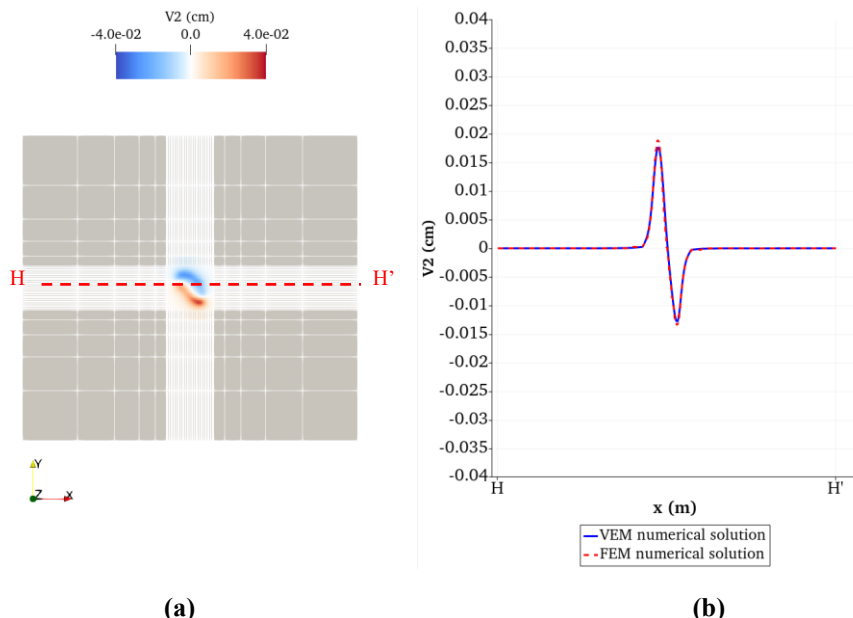


**Figure 98:** (a) model Top-view. Colormap refers to the y-component of displacement ( $V$ ) obtained by FEM at the end of injection ( $\Delta p_2$ ). (b) Plot along the  $HH'$  line shown in (a). Comparison between the reference FEM solution on (dotted red) against the VEM solutions (blue) is shown.

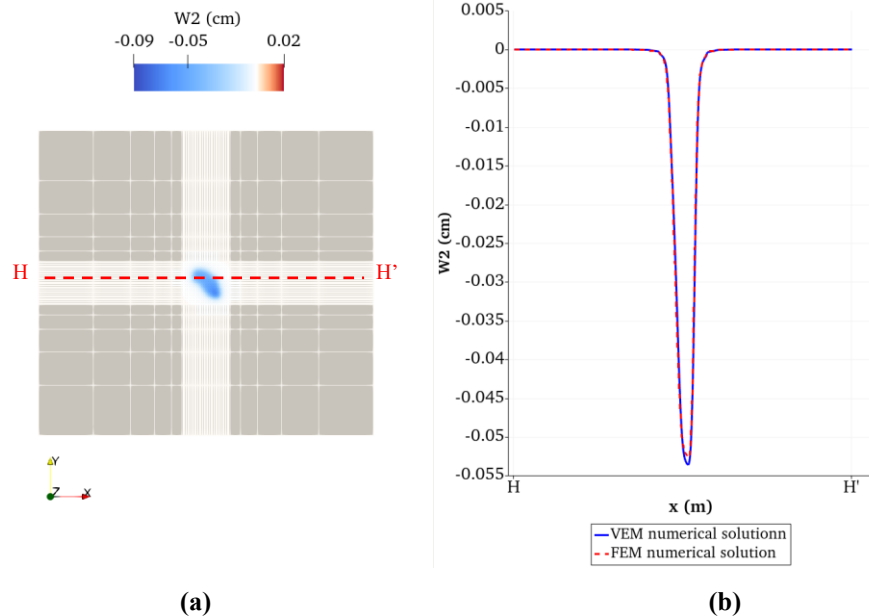


Figure 99: (a) model Top-view. Colormap refers to the z-component of displacement ( $W$  subsidence) obtained by FEM at the end of injection ( $\Delta p_2$ ). (b) Plot along the  $HH'$  line shown in (a). Comparison between the reference FEM solution on (dotted red) against the VEM solutions (blue) is shown.

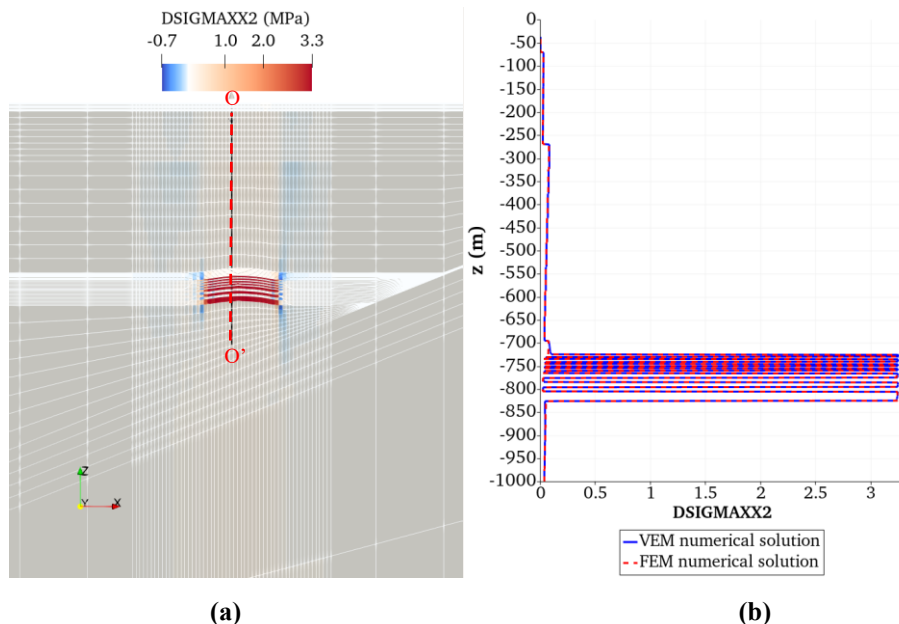
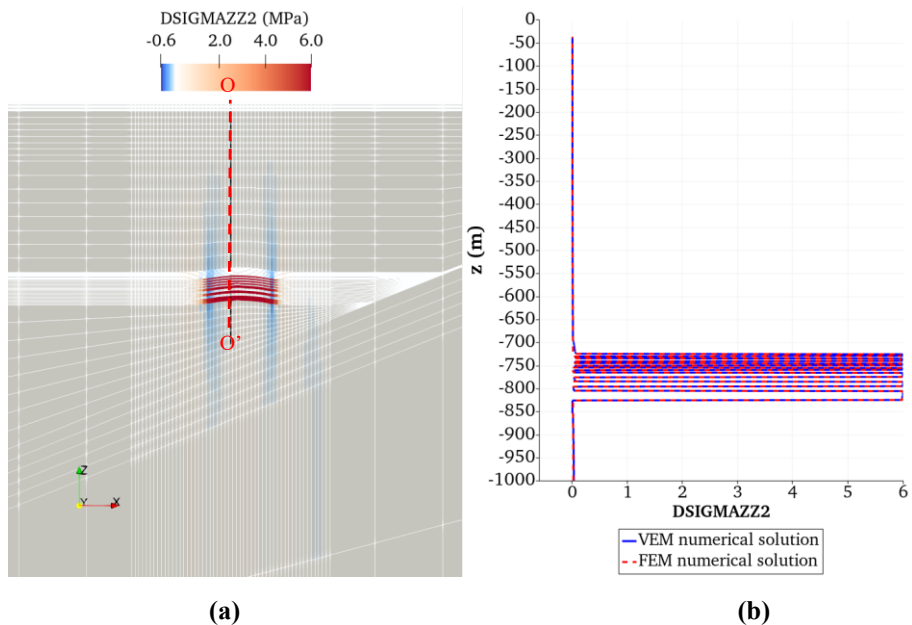


Figure 100: (a) y-axis orthogonal section view of the model. Colormap refers to variation of the xx-effective stress component obtained by FEM at the end of injection ( $\Delta p_2$ ). (b) Plot along the  $OO'$  segment shown in (a). Comparison between the reference FEM solution on (dotted red) against the VEM solutions (blue) is shown.



**Figure 101:** (a) y-axis orthogonal section view of the model. Colormap refers to variation of the zz-effective stress component obtained by FEM at the end of injection ( $\Delta p_2$ ). (b) Plot along the OO' segment shown in (a). Comparison between the reference FEM solution on (dotted red) against the VEM solutions (blue) is shown.

# Chapter 6

## Validation test in the elasto-plastic domain

In the case of an elasto-plastic material, i.e. a material whose response depends on the load path to which it is subject, the model resolution process requires the integration of an additional algorithm able to assess the plastic component of strain.

In the following a model is implemented to that end. The model an isotropic linear elastic (ILE) (i.e. constitutive law:  $\sigma' = D\epsilon^e$ ), perfectly plastic ( $\dot{\kappa} = 0$ ) yield surface, defined by Mohr-Coulomb failure criteria with non-associated plastic flow (i.e. the yield surface and the plastic potential do not coincide).

Techniques successfully applied to FEM for solving elasto-plastic problems can be broadly distinguished in methods that recompute the stiffness matrix at each load step and/or iteration, and methods that keep the stiffness matrix constant and only update the loads. Tangential and secant stiffness methods belong to the first group; conversely, initial strain and initial stress methods belong to the second group. In the initial strain family, the increase of the plastic strain during a load increment is calculated and treated as an initial strain, for which the elastic stress distribution is adjusted. In the initial stress approach, the stress-strain relation is adjusted to take plastic deformations into account for every load increment; the strain increments define the stress uniquely. With a properly specified elasto-plastic

matrix, this incremental elasticity approach can successfully treat perfect plasticity, as well as hardening plasticity.

In the framework of the constitutive problem introduced in the “Elasto-plastic constitutive models” section, the basic computational principles of the initial stress method (Zienkiewicz et al., 1969) are summarized below.

Let's suppose to apply a load increment which causes a displacement increment and, consequently, a total strain increment. Then the constitutive stress-strain relation can be expressed as:

$$\boldsymbol{\sigma}' = D^{ep} \boldsymbol{\varepsilon} \quad (41)$$

where  $D^{ep}$  represents the *elasto-plastic constitutive matrix*. By using relations (10), (14) and (17), (41) becomes

$$D^{ep} = D - \frac{D \frac{\partial \Psi}{\partial \boldsymbol{\sigma}'} \left( \frac{\partial \Phi}{\partial \boldsymbol{\sigma}'} \right)^T D}{\left( \frac{\partial \Phi}{\partial \boldsymbol{\sigma}'} \right)^T D \frac{\partial \Psi}{\partial \boldsymbol{\sigma}'}} \quad (42)$$

Eq. (42) uniquely defines the stress increment due to a total strain increment. Moreover, it is noticed that  $D^{ep}$  depends on the current stress state, thus introducing a non-linear relation in the discretized equilibrium equations implemented in the FEM and VEM. It follows that an iterative procedure must be introduced for determining  $D^{ep}$ .

A family of algorithms denoted as return-mapping are commonly applied to solve such constitutive problem (Neto et al., 2008)

## Return-mapping algorithms

Constitutive problems can also be equivalently formulated as initial value problem in the strain variable:

$$\begin{aligned}\dot{\boldsymbol{\varepsilon}}^e &= \dot{\boldsymbol{\varepsilon}} - \dot{\gamma} \nabla \Phi(\boldsymbol{\sigma}') \\ \dot{\gamma} &\geq 0 \quad \Phi(\boldsymbol{\sigma}') \leq 0 \quad \dot{\gamma} \Phi(\boldsymbol{\sigma}') = 0\end{aligned}\tag{43}$$

where the initial value  $\boldsymbol{\varepsilon}^e(t_0)$  is known and the history of the infinitesimal strain tensor  $\boldsymbol{\varepsilon} = \boldsymbol{\varepsilon}(t) = \boldsymbol{\varepsilon}^e(t) + \boldsymbol{\varepsilon}^p(t)$  is assumed to be known;  $t$  denotes the pseudo-temporal variable which determines variations of strain and stress fields.

In Figure 102 the main steps of the implemented resolution algorithm, denoted as *Implicit Return-Mapping* algorithm, are outlined. The first step of the solution algorithm involves the pseudo-temporal discretization of equations (43). In this case, an Implicit Euler scheme is applied, in which the increase in total deformation is assumed to be known  $\Delta\varepsilon$ :

$$\begin{aligned}\boldsymbol{\varepsilon}_{n+1}^e &= \boldsymbol{\varepsilon}_n^e + \Delta\varepsilon - \Delta\gamma \nabla \Phi(\boldsymbol{\sigma}'_{n+1}) \\ \Delta\gamma &\geq 0 \quad \Phi(\boldsymbol{\sigma}'_{n+1}) \leq 0 \quad \Delta\gamma \Phi(\boldsymbol{\sigma}'_{n+1}) = 0\end{aligned}\tag{44}$$

expression  $\Delta(\cdot)$  refers to  $(\cdot)_{n+1} - (\cdot)_n$ , while the subscripts  $n, n + 1$  identify the "updated" (unknown) state and the current state (known), respectively. Then a TRIAL elastic step follows where the stress state is assumed to be in the elastic domain ( $\Delta\gamma = 0$ ). If the evaluation of the yield surface  $\Phi(\boldsymbol{\sigma}'_{n+1}^{TRIAL})$  is negative or null, the TRIAL solution is feasible, and therefore it is possible to update the variables and proceed to the next loading step. Otherwise, a plastic correction step projects the solution onto the yield surface, so that the stress state can be classified as admissible. The workflow for the application of the Implicit Return-Mapping algorithm for the solution of the initial value elasto-plastic constitutive problem is schematized in Figure 102. Figure 103 shows a qualitative scheme of the two steps Return-Mapping algorithm.

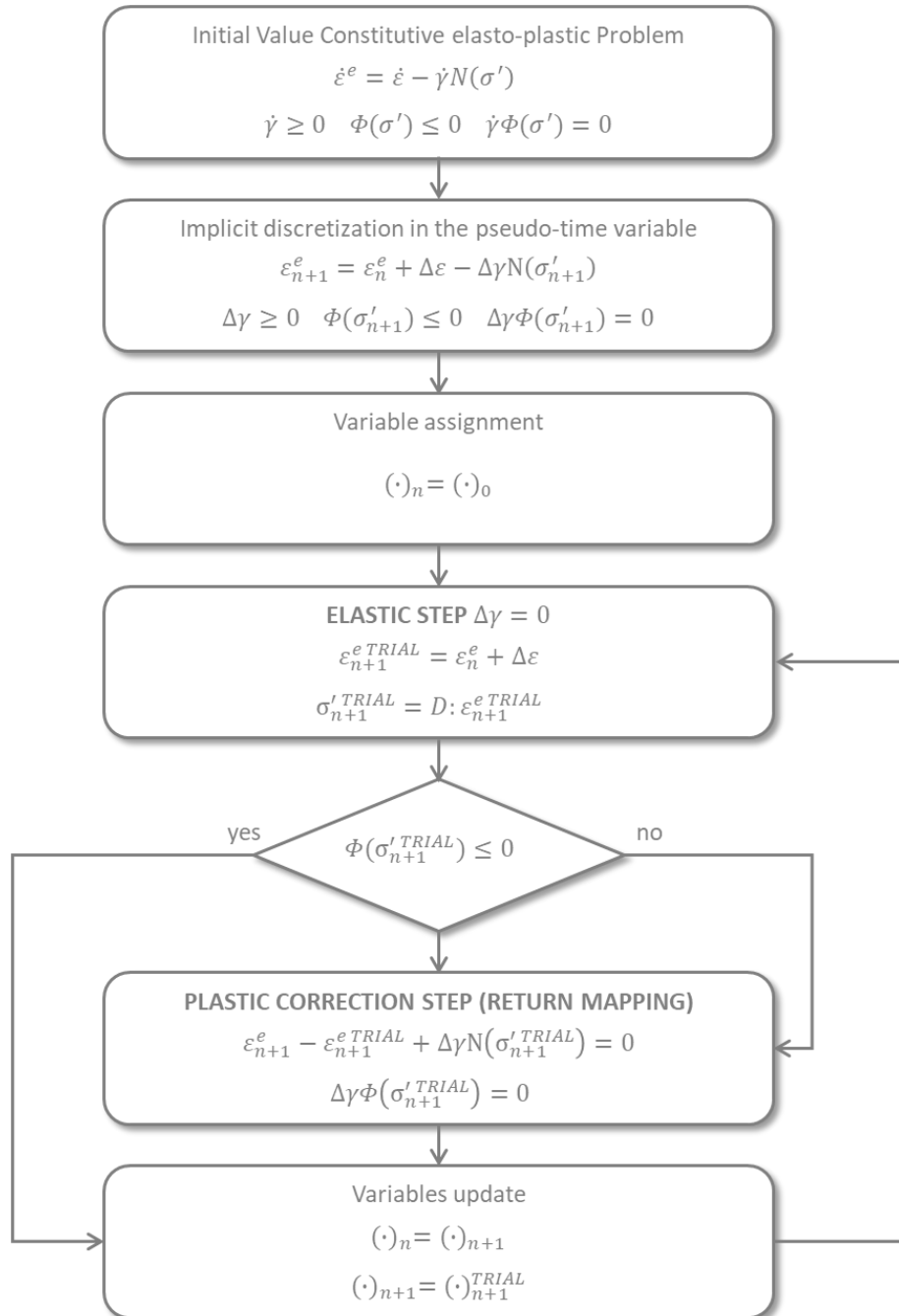


**Figure 102:** implicit Return-Mapping Algorithm for the solution of the initial value elasto-plastic constitutive problem.

The implementation of the plastic correction step requires the evaluation of  $N(\sigma'_{n+1}^{TRIAL})$ , i.e. the flow vector corresponding to the TRIAL stress state. In the case of the Mohr-Coulomb criterion the potential surface ( $\Psi$ ) is convex, but not differentiable, as shown in Figure 104, where the projection on the deviatoric plane is sketched. The non-univocity of the direction of the derivative represents one of the difficulties in implementing the method.

The code tested in this project implements an Implicit Return-Mapping algorithm based on sub-differential operators (Sysala et al., 2017) applied to a C2 continuous approximation to the Mohr-Coulomb yield surface (Abbo et al., 2011). Implementation details can be found in the reference publications.

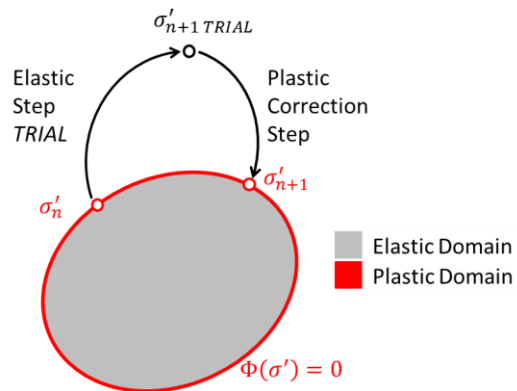


Figure 103: qualitative scheme of the Return-Mapping algorithm.

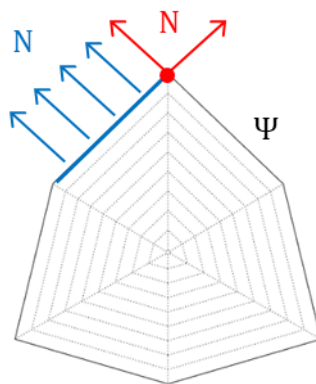


Figure 104: representation on the deviatoric plane of the flow potential  $\Psi$  deriving from the Mohr-Coulomb criterion. Flow vectors normal to the surface are identified by  $N$ .

## Validation

### Analytical scaled model

As a preliminary step of validation of the solution developed for the constitutive sub-problem, the choice was made to compare results of the VEM C++ implementation with the SS-MC-NP-3D code developed by the Institute of Geonics of the Czech Academy of Sciences in collaboration with VŠB-Technical University of Ostrava. The code is developed in the Matlab® environment, is distributed under the GNU General Public License and can be downloaded from the institutional page <http://www.ugn.cas.cz/>. SS-MC-NP-3D implements an elastic-perfectly plastic constitutive law with Mohr-Coulomb yield surface with non-associated plastic flow.

The model represents a scale test case. The domain is represented by a unitary cube and the imposed forcing term has the expression:

$$\Delta p(x, y, z) = \Delta p_{MAX} \frac{(a - x)(a - y)(a - z)(b - x)(b - y)(b - z)}{\left(a - \frac{1}{2}\right)^3 \left(b - \frac{1}{2}\right)^3} \quad (45)$$

Where the parameters assume the values  $\Delta p_{MAX} = 0.61$  MPa,  $a = 0$  and  $b = 1$ . A section view (XZ plane) of the function  $\Delta p(x, y, z)$  is represented in Figure 105.

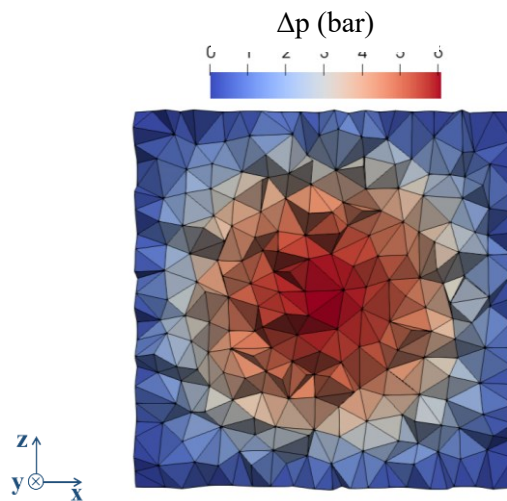


**Figure 105:** section view (XZ plane) of the pore pressure variation imposed as forcing term.

---

The parameters which characterize the elasto-plastic constitutive model are listed in Table 7.

**Table 7: parameters of the elasto-plastic constitutive model**

Parameter	Value
Cohesion ( $c$ )	0.13 MPa
Friction angle ( $\varphi$ )	7°
Young's modulus ( $E$ )	3 GPa
Poisson's ratio ( $\nu$ )	0.35
Dilatancy angle ( $\psi$ )	5°

The two codes were tested on two different volume discretization. The SS-MC-NP-3D code was tested on a hexahedron structured grid, characterized by a fixed number of nodes in the 3 directions: in the specific case  $15 \times 15 \times 15 = 3375$ . The VEM code was tested on an unstructured grid of the same order of magnitude consisting of 4576 nodes and 21140 cells. The comparison between the two solutions was carried out in terms of the maximum value of the yield function obtained at each load step. Here the forcing term was divided in 100 load steps. As shown in Figure 106, there is a good agreement between the two solutions that reach the plasticization state for nearly the same load step. For completeness, Figure 107 also shows a qualitative comparison between the total vertical displacements obtained by the two solvers on the XY plane for  $z = z_{\max}$ . It is confirmed that a good agreement is observed between the two solvers.

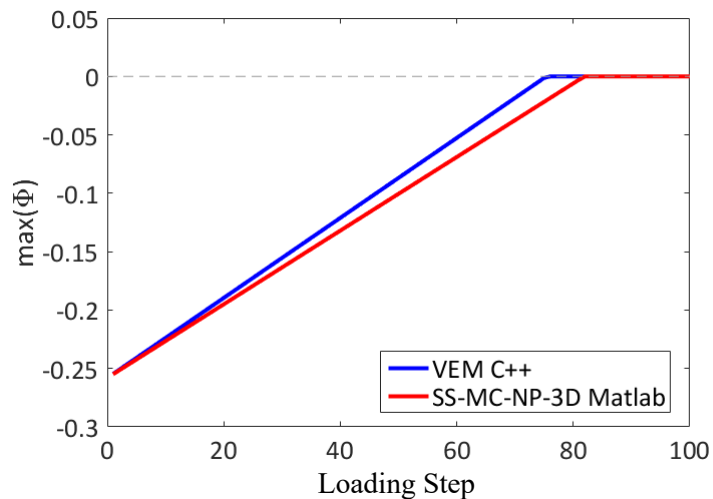


**Figure 106:** Comparison between the SS-MC-NP-3D Matlab (red line) and the VEM C++ (blue line) trend of the maximum value of the yield function ( $\Phi$ ) over the entire domain with respect to the load steps

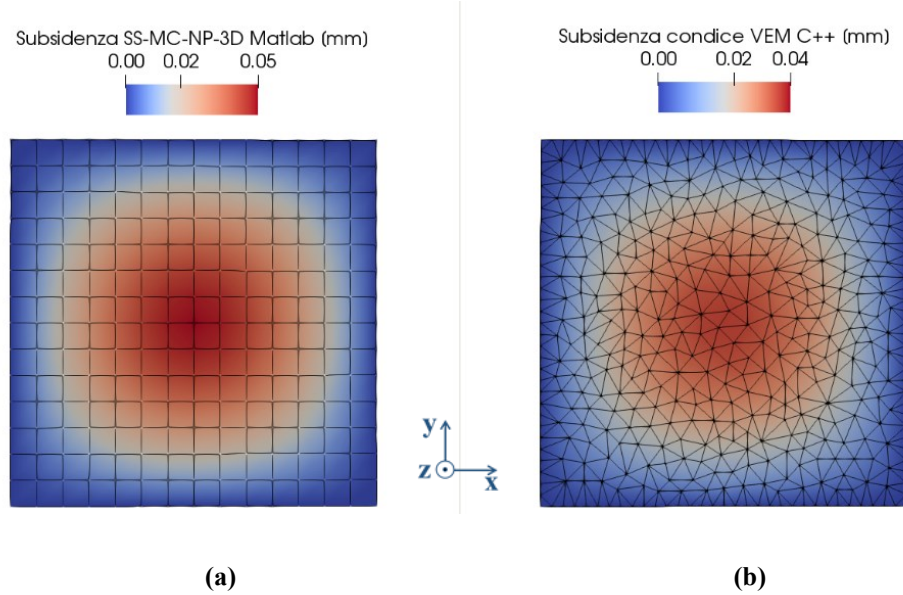


**Figure 107:** Comparison between the vertical displacement  $W$  (cm) on the XY plane calculated by the SS-MC-NP-3D code (a) and the VEM solver (b).

## Disk-shaped reservoir model

A second step of validation was performed on the disk-shaped reservoir model introduced in the “Disk-shaped reservoir model” section. The model is characterized by homogeneous parameters, listed in Table 8. The Mohr-Coulomb yield surface is completely defined by two parameters, i.e. friction angle ( $\varphi$ ) and cohesion (c). Plastic flow is non-associated, thus a dilatancy angle ( $\psi$ ) was assigned. No hardening parameters were set due to the perfect plasticity hypothesis. To force some nodes of the disk to reach plasticity it was necessary to impose a pore pressure variation of 2.5 MPa at a depth of 400 m (where the initial value is of the order of 4 MPa).

Simulations were initially run in the elastic domain and the resulting displacement and stress fields variations were compared to verify the agreement between the two solutions. The top view and a line plot of the horizontal,  $u$ , and vertical,  $w$ , components of the displacement at the top surface shown satisfactory agreement (Figure 109 and Figure 110). Analogous results were obtained along the y-axis orthogonal section and the corresponding line plot (Figure 118 and Figure 119). A comparison of vertical displacement,  $w$ , and variation of the  $\sigma'_{xx}$  and  $\sigma'_{zz}$  are shown in Figure 120.

**Table 8: disk-shaper reservoir model. Load term and elasto-plastic constitutive model parameters**

Parameter	Description	Value
$\Delta p$	Imposed reservoir pore pressure variation	2.5 MPa
$E$	Young's Modulus	2 GPa
$\nu$	Poisson's Ratio	0.25
$\varphi$	Friction angle	25°
c	Cohesion	0.16 MPa
$\psi$	Dilatancy angle	5°

The Safety Factors,  $S$ , introduced in the “Safety Factor” section was calculated for the disk-shaped reservoir cells where shear failure can occur. As an example case, in Figure 108 there are shown the two reservoir cells, belonging to the unstructured (green) and corner-point grid (blue), whose  $S$  values are given in Figure 108. As expected, the  $S$  values increase after injection due to a shift towards lower effective stresses - as shown by Mohr’s circle representation of Figure 114. Due to the different grid and consequently different centroid position in space, a discrepancy between the safety factor calculated from the FEM and VEM computed solutions can be observed. However, both exceed unity thus violating the yielding criterion and revealing plasticity occurred.

The subsequent step was to test the implemented return-mapping algorithm on the generalized Mohr-Coulomb yield surface. The investigated volume has extension 14 km x 14 km x 4.5 km and counts about  $4.3 \cdot 10^5$  nodes. Unfortunately, preliminary tests carried out so far highlighted convergence issues of the implemented Newton’s algorithm. The method, indeed, guarantees only local convergence, i.e. only when the trial step is close enough to the searched solution, the solution can be successfully identified. Conversely, there are globally converging methods, such as the conjugate gradient family, which have the tendency to stagnation, i.e. the solution does not change for several iterative steps (Atkinson, 1989; Saad, 2003). The high non-linearity of the problem makes necessary further investigation on the influence of the characteristic parameters of the model to identify a suitable strategy to be applied.

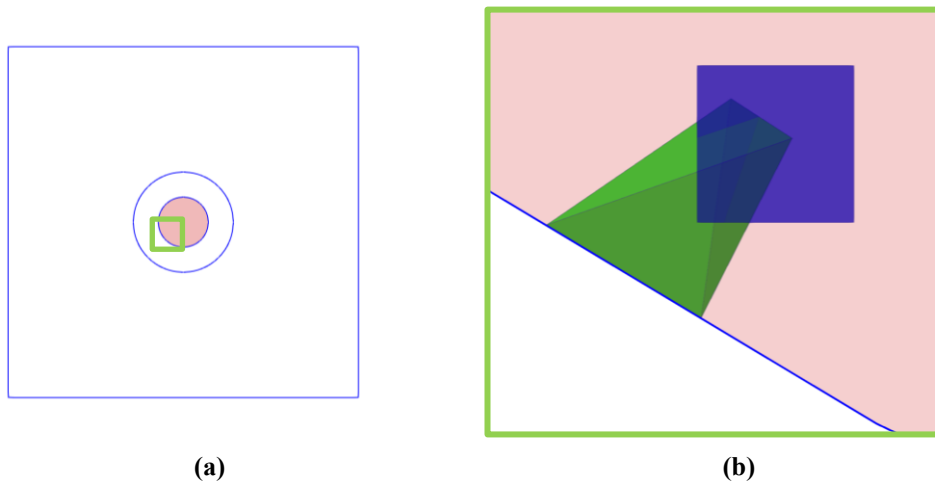
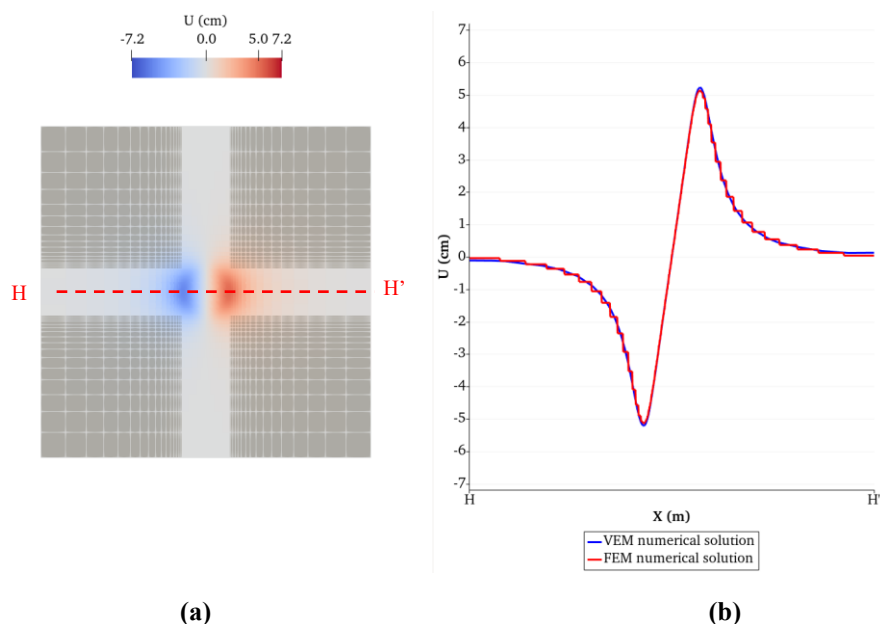


Figure 108: (a) top view of the model scheme: disk-shaped reservoir (in red) with the identification of the zone (green square) zoomed in (b), where are shown VEM tetrahedron (green) and FEM hexahedron (blue) cells whose safety factors are compared in Table 9.

**Table 9: Safety Factor calculated in correspondence of the centroid of test cell of the disk-shaped reservoir, both at the initial equilibrium ( $t_0$ ) and after injection ( $t_1$ )**

	FEM	VEM
<i>Coordinates of the cell centroid</i>	6512.5 m	6499.32 m
	6162.5 m	6154.4 m
	-387.5 m	-393.32 m
<i>Safety Factor @ <math>t_0</math></i>	0.6	0.6
<i>Safety Factor @ <math>t_1</math></i>	1.04	1.1



**Figure 109:** (a) model top-view. Colormap refers to the x-component of displacement ( $U$ ) obtained by FEM at the end of injection ( $\Delta p$ ). (b) Plot along the HH' line shown in (a). Comparison between the reference FEM solution on (dotted red) against the VEM solutions (blue) is shown.

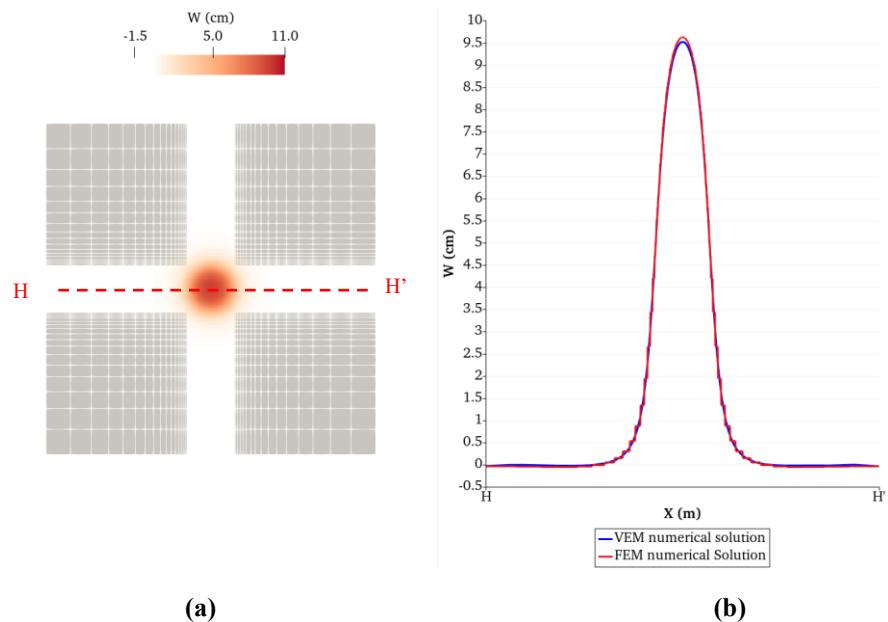


**Figure 110:** (a) model Top-view. Colormap refers to the z-component of displacement ( $W$  rebound) obtained by FEM at the end of production ( $\Delta p$ ). (b) Plot along the HH' line shown in (a). Comparison between the reference FEM solution on (dotted red) against the VEM solutions (blue) is shown.

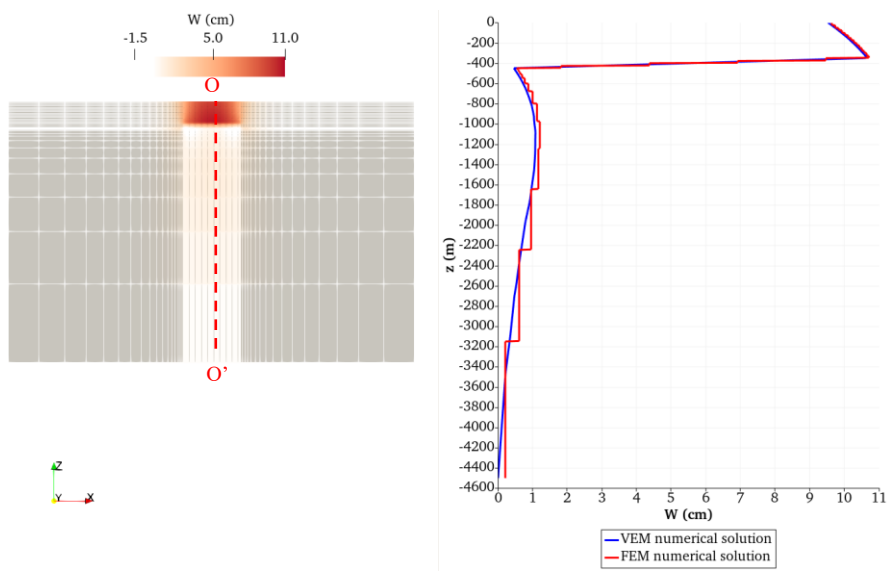


**Figure 111:** (a) y-axis orthogonal section view of the model with a thicknesses amplification factor of 2 applied along the z-direction. Colormap refers to the z-component of displacement (W rebound) at the end of injection ( $\Delta p$ ). (b) Plot along the OO' segment shown in (a). Comparison between the reference

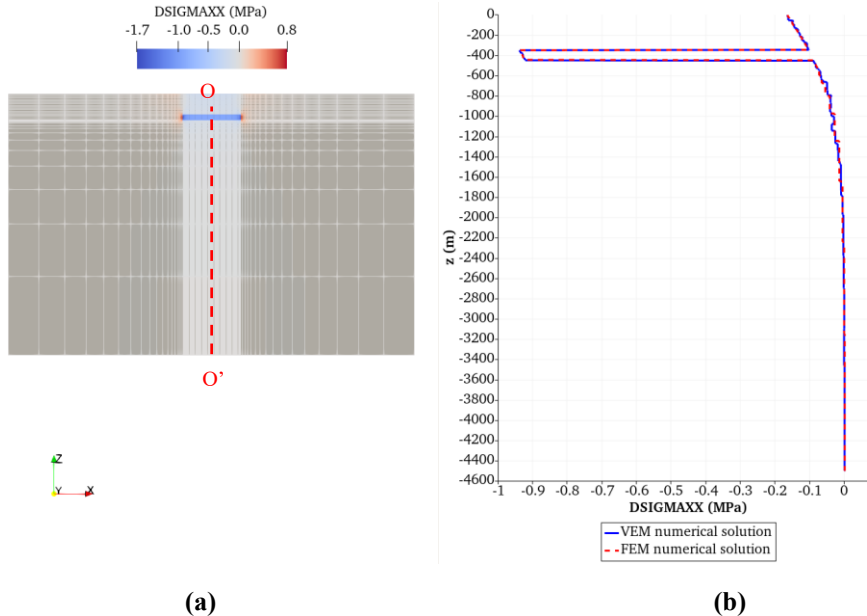


**Figure 112:** (a) y-axis orthogonal section view of the model with a thicknesses amplification factor of 2 applied along the z-direction. Colormap refers to variation of the xx-effective stress component obtained by FEM at the end of injection ( $\Delta p$ ). (b) Plot along the OO' segment shown in (a). Comparison between the reference FEM solution on (dotted red) against the VEM solutions (blue) is shown.

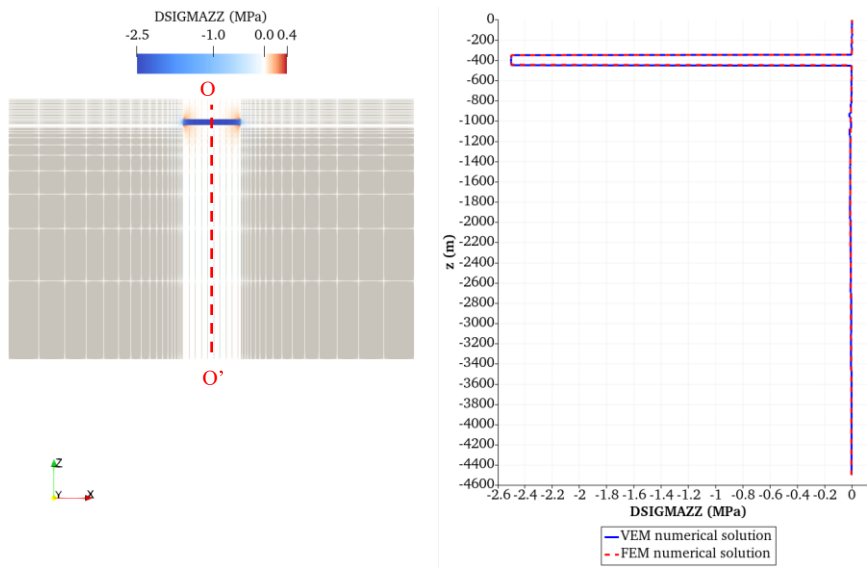


**Figure 113:** (a) y-axis orthogonal section view of the model with a thicknesses amplification factor of 2 applied along the z-direction. Colormap refers to variation of the xx-effective stress component obtained by FEM at the end of injection ( $\Delta p$ ). (b) Plot along the OO' segment shown in (a). Comparison between the reference FEM solution on (dotted red) against the VEM solutions (blue) is shown.

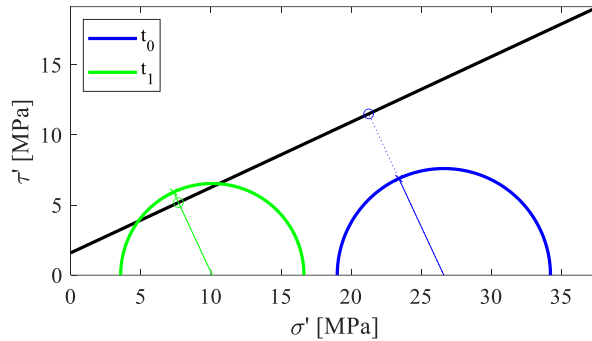


**Figure 114: Mohr's circle representation of the initial state of stress (blue) and the one assessed after injection (green) in correspondence of the centroid of a disk-shaped reservoir cell. Mohr-Coulomb failure criteria is represented as a black line.**

## Underground Natural Gas Storage Test

To complete the set of the tests to verify whether plasticity occurred, the calculation of the Safety Factor was also applied to an underground natural gas storage. The UGS model is the same as that introduced in the “UGS model” section. One standard storage cycle of gas withdrawal followed by gas injection step was taken into consideration; the maximum reservoir pressure at the end of the injection phase is approximately equal to the initial formation pressure.

**Table 10: Mohr-Coulomb yield criteria parameters**

Geomechanical Classes	Cohesion C	Friction Angle $\varphi$	Dilatancy Angle $\psi$
	MPa	°	°
1	0.1	38	
2	0.2	30	
3	1	30	
4	1.5	28	5
5	0.63	30	
6	4	45	

As expected, the calculated safety factor  $S$  shows a decrease after gas withdrawal ( $t_1$ ) and an increase (to approximately the initial value) after gas

injection ( $t_2$ ). As an example case, values calculated in the correspondence of the centroid of a selected reservoir cell are listed in Table 11; the corresponding Mohr's circle representation is depicted in Figure 115. Such results are supported by the technical literature analyzing the surveys of ground movements induced by the storage activities in the Po Plain, Italy. Ground movements monitoring with the Interferometric Synthetic Aperture Radar (InSAR) technique on large areas (A. Ferretti et al., 2001; Berardino et al., 2003) showed a consistent correlation between pressure variations due to gas injection/withdrawal and subsidence/rebound at the surface level (Benetatos et al., 2020; Codegone et al., 2016; Coti et al., 2018). Furthermore, the upward/downward ground movements indicate that the formations behave elastically (Ferronato et al., 2013; P. Teatini et al., 2011).

**Table 11: Safety Factor values of a reservoir and a caprock cells at the initial state ( $t_0$ ), at the end of primary production ( $t_1$ ) and after an injection period ( $t_2$ )**

	FEM	VEM
<i>Coordinates of the cell centroid</i>	3.3353e+07 m	3.3353e+07 m
	4.98178e+06 m	4.98178e+06 m
	-810.089 m	-810.089 m
<i>Safety Factor @ <math>t_0</math></i>	0.3190	0.3190
<i>Safety Factor @ <math>t_1</math></i>	0.3768	0.3771
<i>Safety Factor @ <math>t_2</math></i>	0.3193	0.3193

The management strategies of a UGS usually aim at maximizing the volume of stored gas that can be available to marketplace (working gas) and to enhance the storage performance (gas rates that can be delivered). To this end it is a common option to operate storage at a maximum working pressure in excess of the initial formation pressure (*delta-pressuring*). In the Italian panorama this is a possible practice provided that the maximum pressure does not exceed 107% of the initial pressure. For the case study under consideration this means that the final reservoir pressure should not exceed 7.5 MPa. The results of the simulations performed for the scenario in which a 107% delta-pressure is applied, are provided in Figure 116-

Figure 120. The solutions obtained with FEM and VEM are compared in terms of displacement and effective stress variations. The z-component along the HH' segment on the top surface is plotted in Figure 117: the delta-pressure condition causes a lift of the order of 1.5 cm at the surface. The corresponding values of the safety factor are listed in Table 12 and the Mohr's circle represented in Figure 121. All the obtained results confirm the case studies published in the reference literature and reinforce that simulation can be carried out in the elastic domain as a standard step of the geomechanical safety assessment.

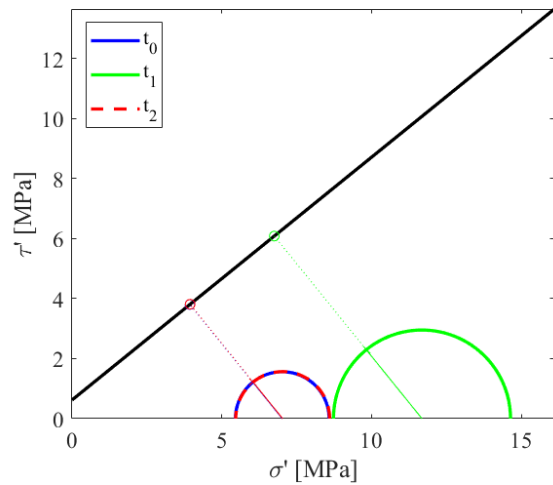


**Figure 115:** Mohr's circle representation of the state of stress for the selected reservoir cell obtained from VEM solution. Three states are represented: initial (blue), end of primary production (green) and end of injection period (dotted red). Projections on the Mohr-Coulomb failure line are used to evaluate the Safety Factor.

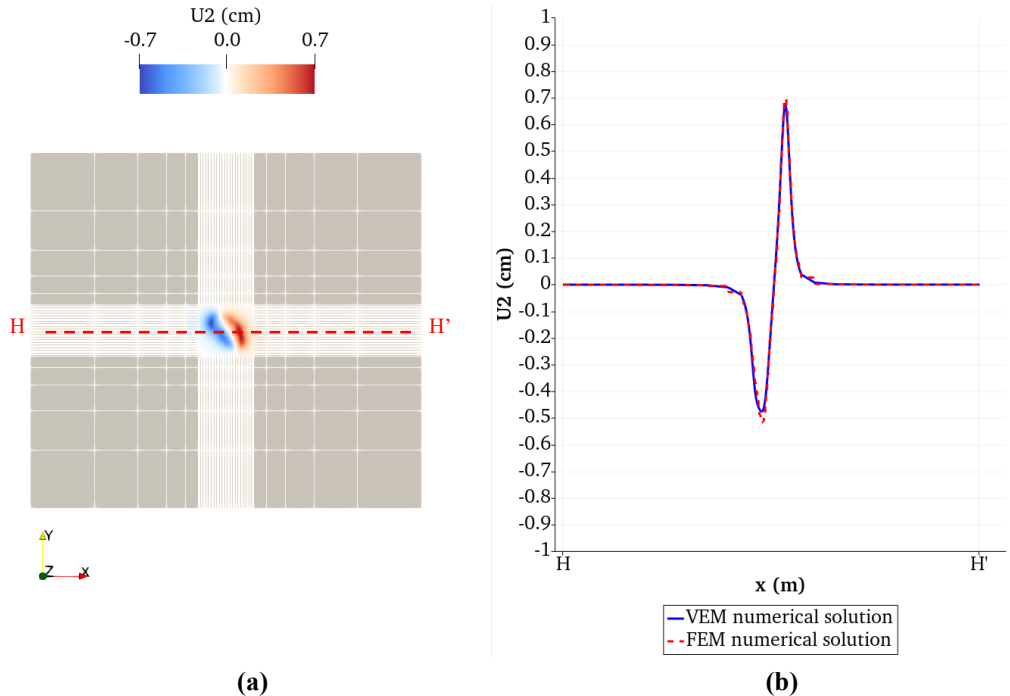


**Figure 116:** (a) model top-view. Colormap refers to the x-component of displacement ( $U$ ) obtained by FEM at the end of injection ( $\Delta p_2$ ). (b) Plot along the  $HH'$  line shown in (a). Comparison between the reference FEM solution on (dotted red) against the VEM solutions (blue) is shown.

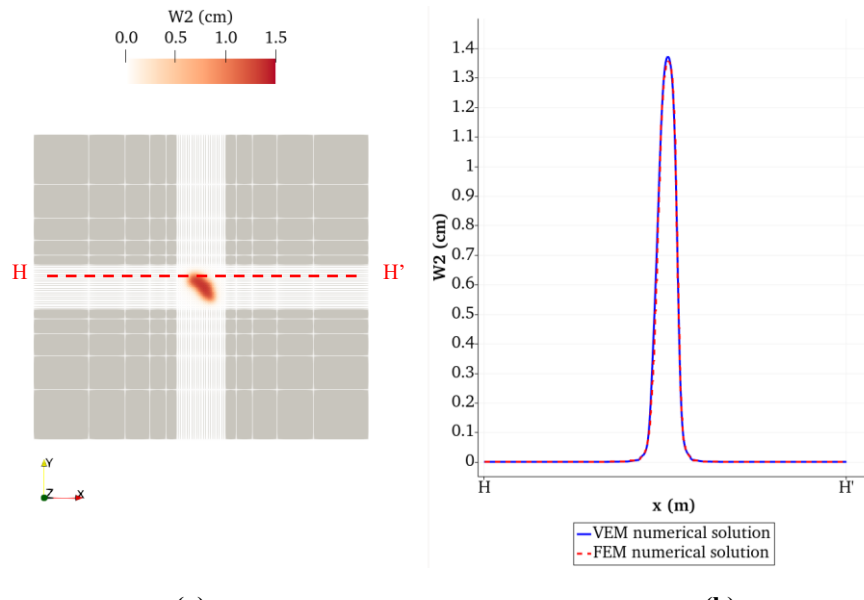


**Figure 117:** (a) model top-view. Colormap refers to the z-component of displacement ( $W$  subsidence) obtained by FEM at the end of production ( $\Delta p_2$ ). (b) Plot along the  $HH'$  line shown in (a). Comparison between the reference FEM solution on (dotted red) against the VEM solutions (blue) is shown.

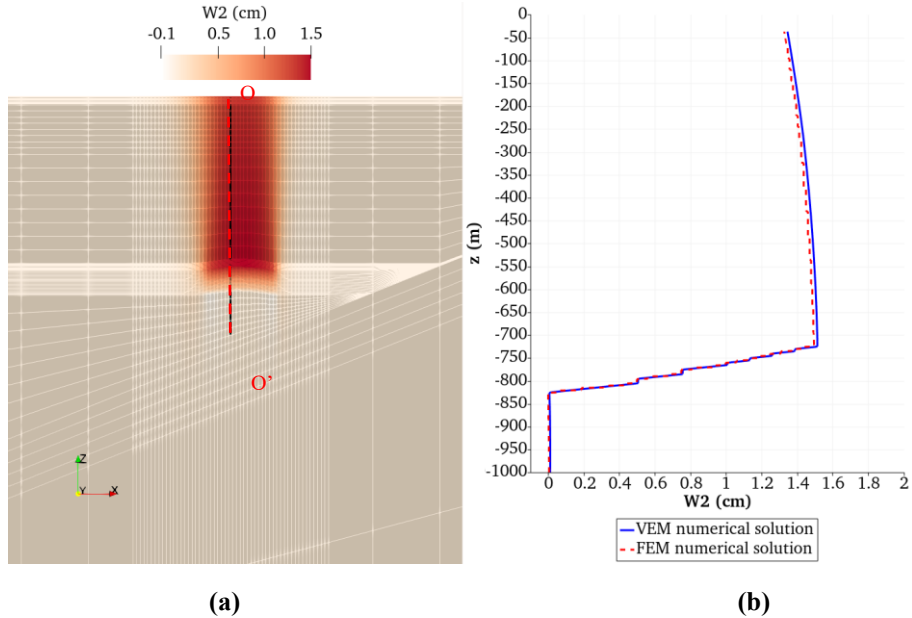


**Figure 118:** (a) y-axis orthogonal section view of the model. Colormap refers to the z-component of displacement ( $W$  subsidence) at the end of injection ( $\Delta p_2$ ). (b) Plot along the  $OO'$  segment shown in (a). Comparison between the reference FEM solution on (dotted red) against the VEM solutions (blue) is shown.

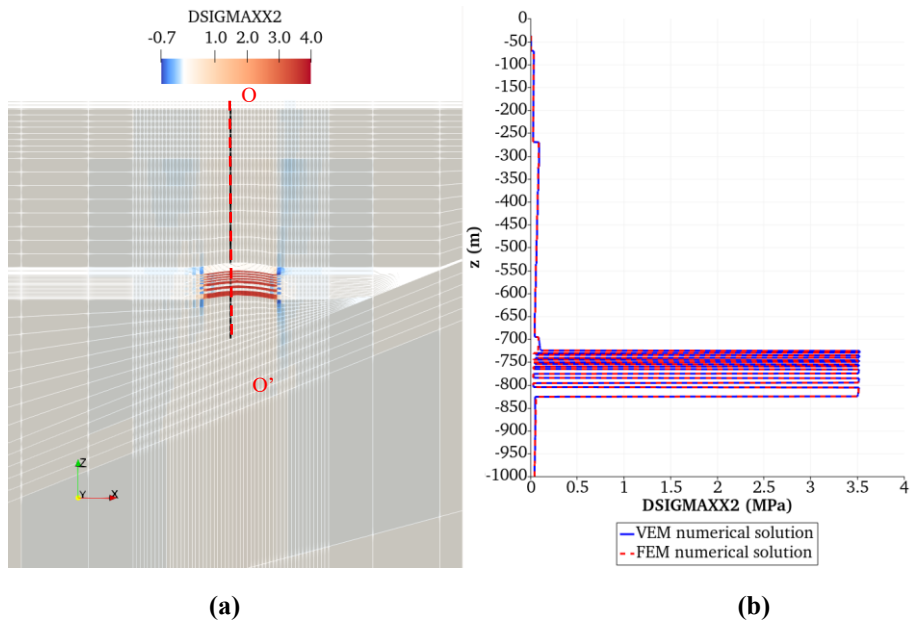


**Figure 119:** (a) y-axis orthogonal section view of the model. Colormap refers to variation of the xx-effective stress component obtained by FEM at the end of injection ( $\Delta p_2$ ). (b) Plot along the  $OO'$  segment shown in (a). Comparison between the reference FEM solution on (dotted red) against the VEM solutions (blue) is shown.

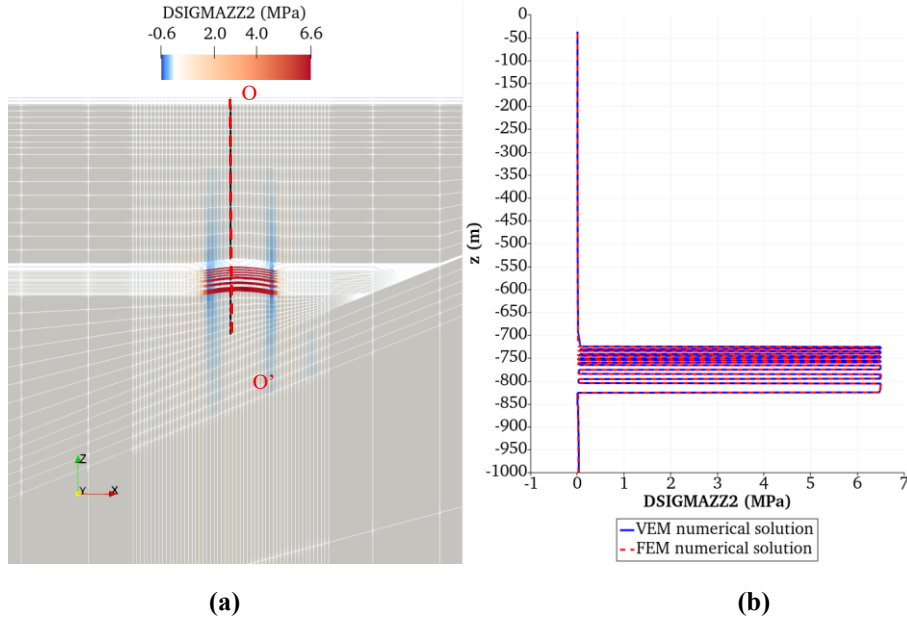


**Figure 120:** (a) y-axis orthogonal section view of the model. Colormap refers to variation of the zz-effective stress component obtained by FEM at the end of injection ( $\Delta p_2$ ). (b) Plot along the OO' segment shown in (a). Comparison between the reference FEM solution on (dotted red) against the VEM solutions (blue) is shown.

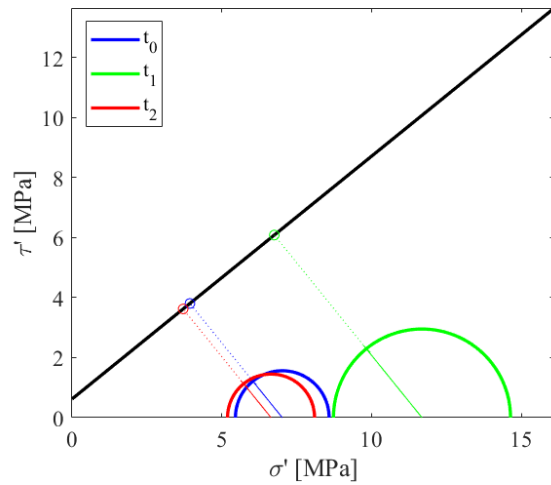


**Figure 121:** Mohr's circle representation of the state of stress for the selected reservoir cell obtained from VEM solution. Three states are represented: initial (blue), end of primary production (green) and end of injection period (red). Projections on the Mohr-Coulomb failure line are used to evaluate the Safety Factor.

**Table 12: Safety Factor values of a reservoir and a caprock cells at the initial state ( $t_0$ ), at the end of primary production ( $t_1$ ) and after an injection period ( $t_2$ )**

	<b>FEM</b>	<b>VEM</b>
<i>Coordinates of the cell centroid</i>	3.3353e+07 m	3.3353e+07 m
	4.98178e+06 m	4.98178e+06 m
	-810.089 m	-810.089 m
<i>Safety Factor @ <math>t_0</math></i>	0.3190	0.3190
<i>Safety Factor @ <math>t_1</math></i>	0.3768	0.3771
<i>Safety Factor @ <math>t_2</math></i>	0.3114	0.3114

# **Chapter 7**

## **Code development and GUI prototyping for model validation and data analysis**

The present project has seen, during the entire development, the adoption of different development tools. This was the optimal and preferred choice for different parts of the research due to the presence of pre-existing libraries and modules originally developed on two different systems: Microsoft Windows Systems and GNU/Linux. Indeed, it is well known that software compiled for Microsoft Windows does not work on GNU/Linux systems and vice versa. It follows that for the integration of piece of code written for different system into a prototype application as well as the construction of the validation process here described, it was necessary to identify the development actors that were most suitable for making the resulting workflow as independent as possible from the platform were the code was developed and compiled.

In Table 13 are summarized the pre-existing application development ecosystem actors characterizing the two development environments that needed to be integrated.

**Table 13: pre-existing Software Development Ecosystem Actors**

<b>Operating System</b>	Microsoft Windows 7 Microsoft Window 10	GNU/Linux
<b>User Interface</b>	GUI	Bash shell
<b>Development Tools</b>	Matlab® Mathworks Visual Studio® Microsoft Eclipse IDE Paraview Kitware	GCC compiler for C++ Vim editor Paraview Kitware Bitbucket
<b>Languages</b>	C# C++ Java/AWT VTK/Java wrapper Python	C C++
<b>Data Formats</b>	Schlumberger Proprietary GRDECL and SIMOPT Open-source Legacy VTK and VTU	Generic ASCII Open-source Legacy VTK and VTU
<b>Framework and Toolkits</b>	Matlab Eclipse RCP VTK as visualization toolkit and reader/parser Eigen Tetgen Triangle CGAL	Eigen Tetgen Triangle VTK as an open-source format data container and reader/parser

The development of the project tasks involved the subdivision of the activities between the functionalities for gridding and visualizations and the solution of equations. The former included the *Gridding Library* and GUI, the latter the *GeDim* and *VemElast* libraries. For sake of effectiveness and because of the pre-existing codes and libraries, related to the two sets of activities, were implemented in different environments, therefore, their integration in the prototype application architecture (sketched in Figure 122) required to adapt the model that was initially hypothesized.

On the other side, the underlying adopted strategy, by which the main functions were isolated in logical units, was very effective to develop each of them independently and give to the resulting code a modular structure. Each logical unit

was designed as a single library according to the MS Windows *Dynamic Linking Library* (dll) model, completely analogous to that of the Shared Objects of the Linux world. In this pattern, once a list of input and outputs parameters are coded, the internal functioning of the library is transparent, and it can be included in the main application even when not all its functionalities are already implemented. Such a choice, indeed, allows to modify the code locally without undermining the structure of the whole application.

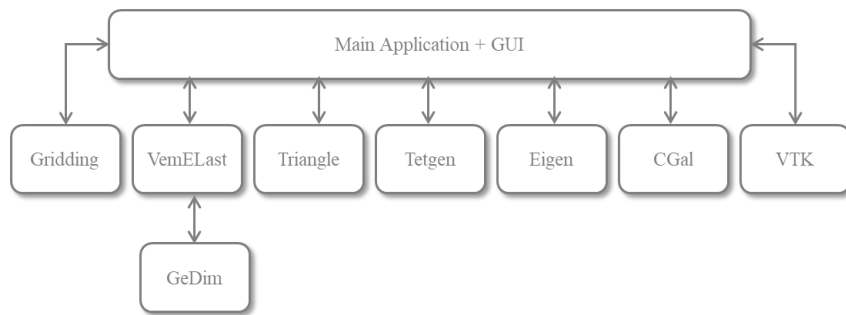


**Figure 122: Software architecture**

Some of the tools were added during the project development while some were abandoned. Consequently, entire pieces of code have been completely rewritten to incorporate the experience gained during the integration process. The main steps which retrace the evolution process of the application prototype and of the development environment can be summarized as follows:

- STEP 1: The *Main Application* and the *Gridding* libraries are developed with Visual Studio on Microsoft Windows. The *GeDim* (Generic Discretization Method) library, instead, runs on GNU/Linux. A sketch of the configuration can be found in Figure 123. The two environments do not have points of contact. Input and output data needs to be coded and a VEM implementation for the solution of the linear elastic boundary value problem is required.
- STEP 2: the *VemElast* (3D VEM implementation for the solution of the linear elastic boundary value problem) library is connected to the *GeDim* library on GNU/Linux. In this phase input and output data are codified as VTK legacy format in ASCII files and VTK framework is used as data container and reader/parser. A basic *Graphical User Interface* (GUI) developed in Qt is integrated in the *Main Application* together with the *Gridding* library. The user can now call grid importing functions without modifying the code. However, to perform a simulation, it is necessary to physically move data from workstations

running the *Main Application* on MS Windows to other running *VemElast* library on GNU/Linux. A sketch in depicted in Figure 124.

- STEP 3: the *VemElast* and some functionalities of the *GeDim* libraries are ported from GNU/Linux to MS Windows. Running the code is now simpler: the GUI has importing functions and it can directly call *Gedim+VemElast* at runtime avoiding export and re-import data from ASCII files. The development tool used is Visual Studio making compatibility with GNU/Linux platform difficult.
- STEP 4: the *Main Application* code is migrated to the open-source development environment made up of *QT Creator + CMake + MinGW*. The testing phase of the new environment required time and tuning but this new setting allowed to unify both GNU/Linux and MS Windows library development processes in the same environment (see Figure 125). Data structures are now shared inside the main application and ASCII files were no longer required.
- STEP 5: the GUI is developed in the Qt framework exploiting native classes which allows the coupling between Qt and VTK. Now, parameters, data and results can be passed from/to the *Main Application* and from/to libraries at run time, using slots and signals mechanism from Qt (The Qt Company, 2021a), thus it is possible to produce simple visualizations of imported grids and results from the *Gedim+VemElast* simulations. The sequence of actions which exemplifies the main functions implemented in the *Main Application* GUI are shown in the sequence of screenshot Figure 128-Figure 134.

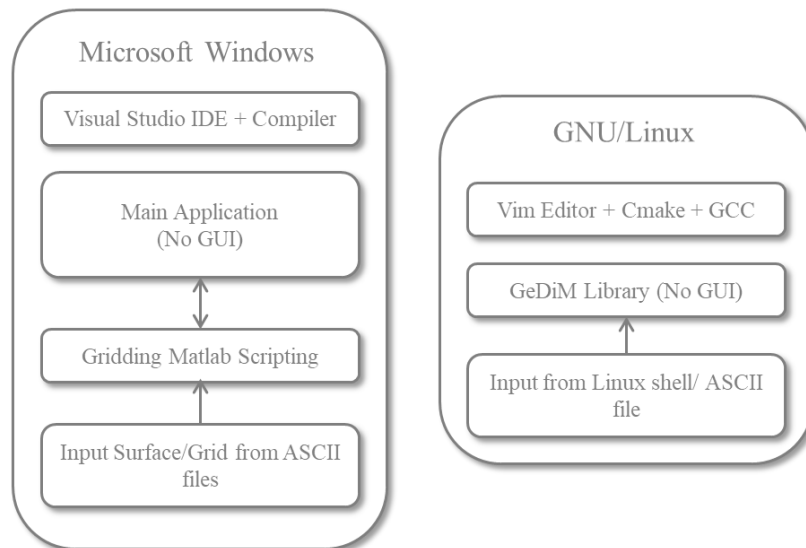


**Figure 123:** sketch of STEP1 of the evolution process.

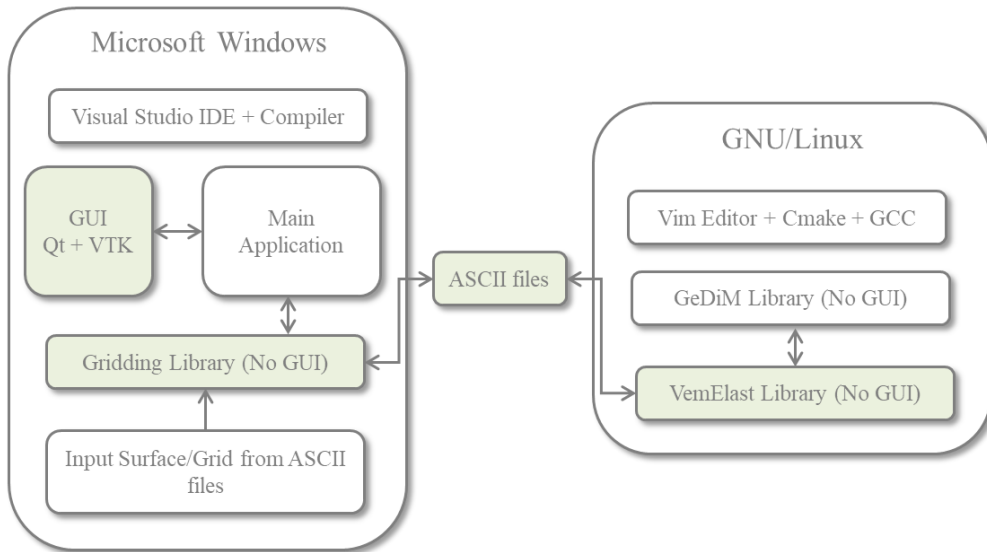


Figure 124: sketch of STEP2 of the evolution process.

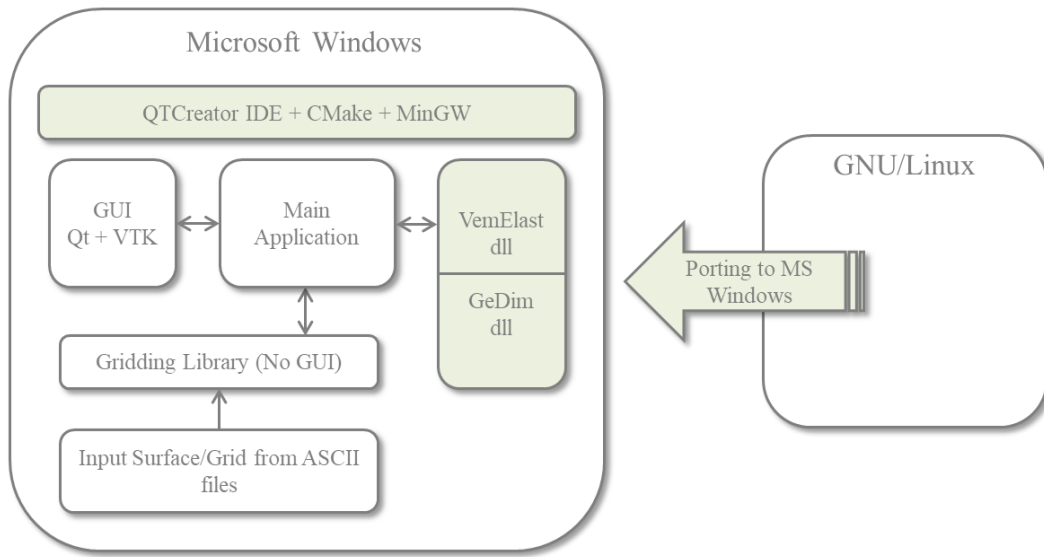


Figure 125: sketch of STEP4 of the evolution process.

Among the many advantages deriving from the use of the Qt framework, two are to be underlined as key aspects: the communication system commonly known as "*Signals and Slots*" (The Qt Company, 2021a) and the low-level API *QThread* (The Qt Company, 2021b).

Signal and slots are a peculiar implementation of communication between objects implemented in the Qt frameworks. This is a solution alternative to the original *Callback* pointers to functions commonly used in the communication between widgets in a GUI. The logical scheme of slot/signal communication mechanism is depicted in Figure 126. Signals are emitted when a particular event occurs. A signal is emitted by an object when its internal state has changed. Then the slots (C++ functions) connected to it are executed independently of any GUI event loop. The main advantage in using such a mechanism is that signals are automatically generated by the program that handles Qt's C++ extensions (Meta-Object Compiler) and must not be implemented in the cpp files, making coding faster. The mechanism is type safe through signal signature verification at runtime overcoming errors in type-correctness of callback arguments. This development pattern is widely used in GUI interfaces but is also used extensively in multi-threading management.

Signals and Slots, indeed, are also founding tools for Qt multi-threading implementation. Substantial feature of QThread is that it's not a thread, but it is a wrapper around a thread object. This wrapper provides signals, slots and methods to easily implement the thread object within a Qt project ([wiki.qt.io](https://wiki.qt.io)). The need to use multi-threading in an application is directly linked to the availability, especially in the most recent workstations, of many processors: the capability to execute several parallel operations reduces the execution time of even very simple tasks and the user experience can benefit from this mechanism.

The combined use of the QThread Class and the "Signals and Slots" pattern provides the programmer with an easy-to-use tool to achieve this goal. From the simple need not to freeze the GUI while executing a process that takes a long time, such as loading an ASCII file, to the possibility of parallelizing a complex calculation, these two tools open a world of possibilities. Only a few rules are required to manage the execution of multiple tasks in parallel. Particular attention must be paid to the way shared resources are accessed and the intertwining of possible errors that could be generated by a System that can reach a high degree of complexity.

The parallelization of the deepest computational parts is beyond this type of management and have been structured with the use of more complex and specialized models, linked to the area of competence of the *GeDim* library.

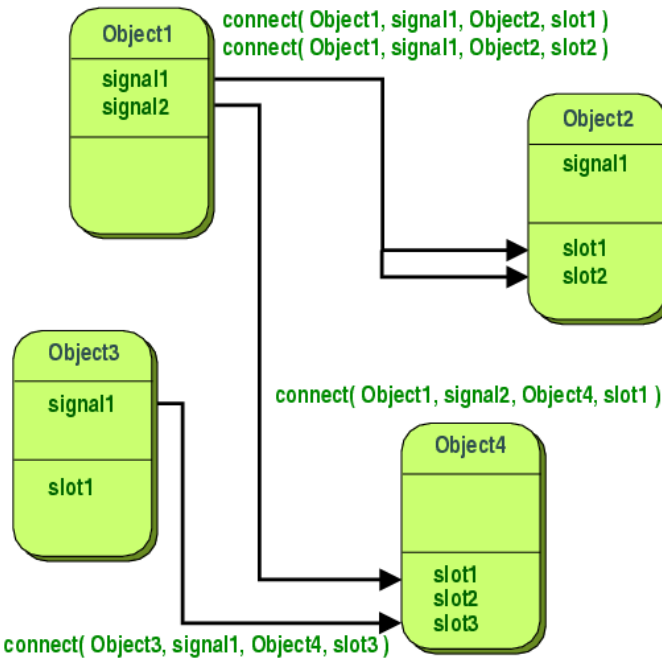


Figure 126: scheme of signal/slot connection between objects (The Qt Company, 2021a)

The resulting development flowchart (sketched in Figure 127) is made up of four main actors

- *Qt Creator* (The Qt Company, 2021c): a cross-platform C++, JavaScript and QML Integrated Development Environment (IDE). which simplifies GUI application development. It is part of the SDK for the Qt GUI application development framework and uses the Qt API, which encapsulates host OS GUI function calls.
- *CMake* (Kitware, 2021): cross-platform free and open-source software for build automation, testing, packaging and installation of software by using a compiler-independent method. CMake is not a build system but rather it generates another system's build files.
- • *MinGW and MinGW-w64* (Mingw-w64, 2021): native Windows port of the GNU Compiler Collection (GCC), commonly referred to as a toolchain . They both contain freely distributable import libraries and header files for building native Windows applications; they include extensions to the MSVC runtime to support C99 functionality. These toolchains are re-distributed by *QT Creator* package. Qt versions up to 4.8.6 target MinGW toolchain; newer Qt 4.8 binary packages ship with MinGW-w64 based toolchain.

- *Code Versioning* tools allow to easily redistribute code and test new ideas. Their introduction in the development environment facilitates asynchronous remote working model, i.e. team members do not have to necessarily work in the same geographical location and at the same time. There were set up:
  - *GitLab* (Gitlab inc., 2021): web-based DevOps<sup>1</sup> lifecycle tool that provides a Git repository manager providing wiki, issue-tracking and continuous integration and deployment pipeline features (GitLab inc., 2021), the core features are distributed under a MIT open-source license,
  - *Bitbucket* (Atlassian, 2021): is a Git-based source code repository hosting service owned by Atlassian.



**Figure 127: Current Development Flowchart**

---

<sup>1</sup> Practices that combine software development (Dev) and IT operations (Ops)

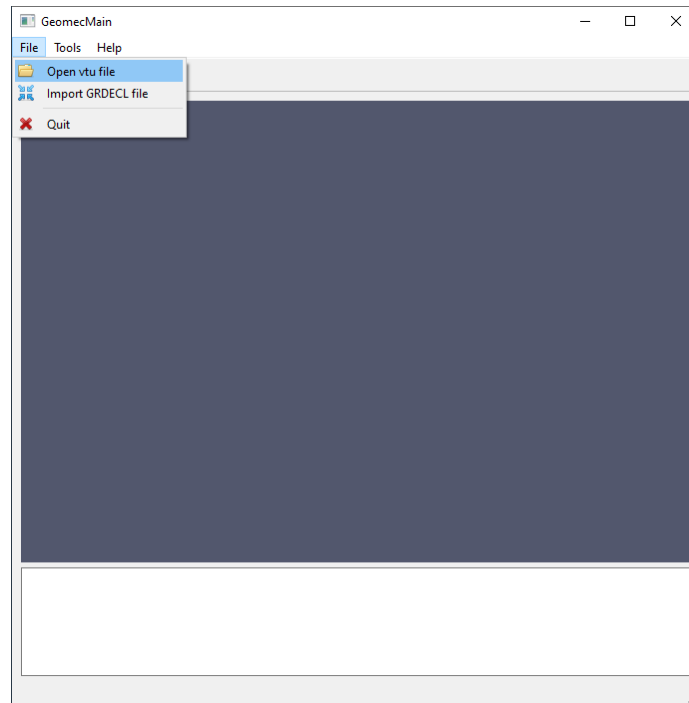


**Figure 128:** Main Application GUI – menu item for selection of the grid file to be processed

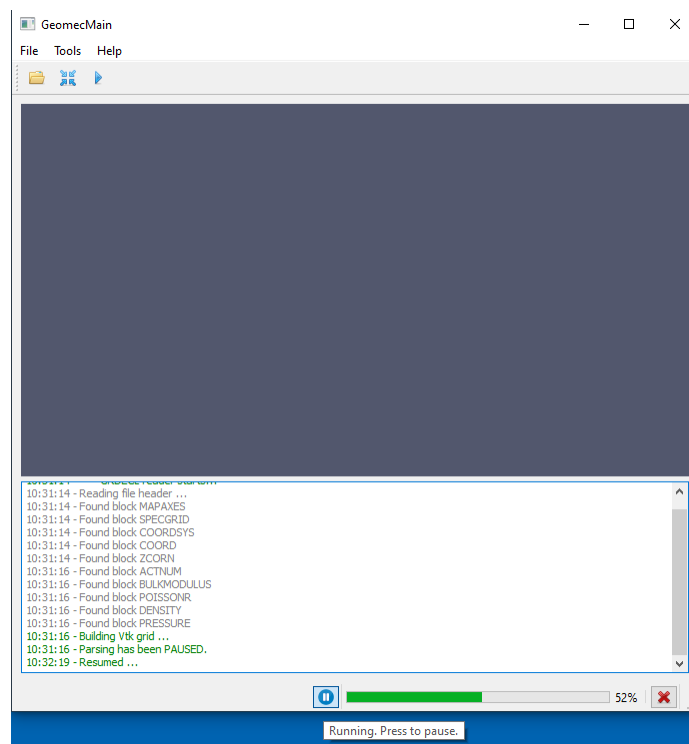


**Figure 129:** Main Application GUI – logging window for grid upload

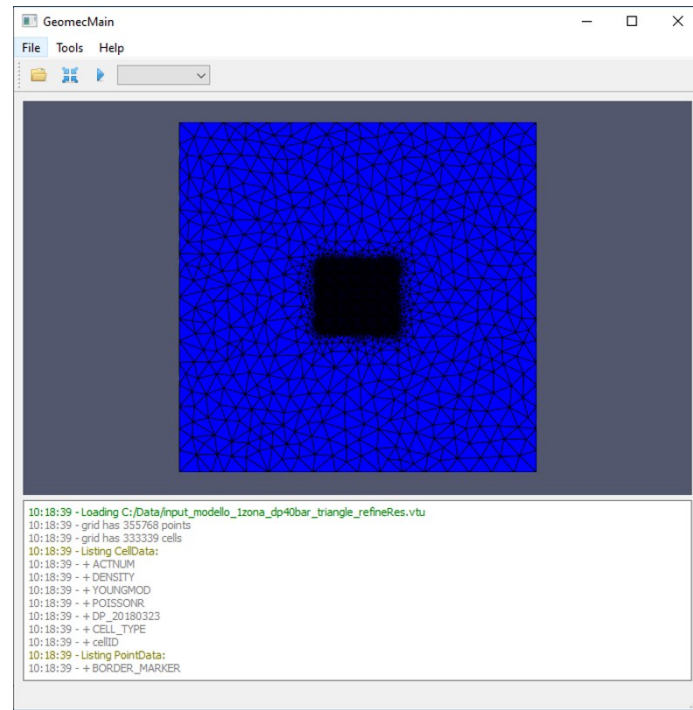


**Figure 130: Main Application GUI – successful upload of unstructured gridding with attributes**

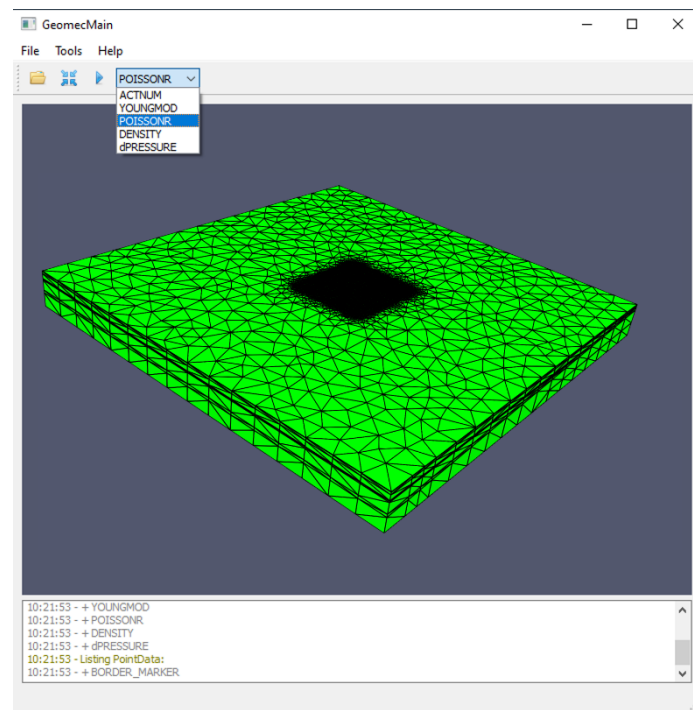


**Figure 131: Main Application GUI – grid attributes visualization through combobox**

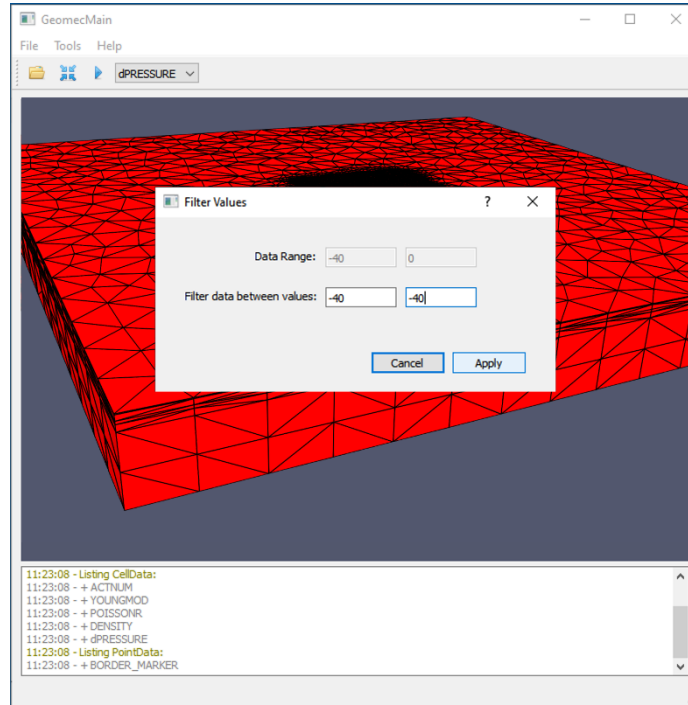


**Figure 132: Main Application GUI – dialog box for threshold filtering. By way of example, reservoir is identified by selecting cells with associated dP equal to 40 bar.**

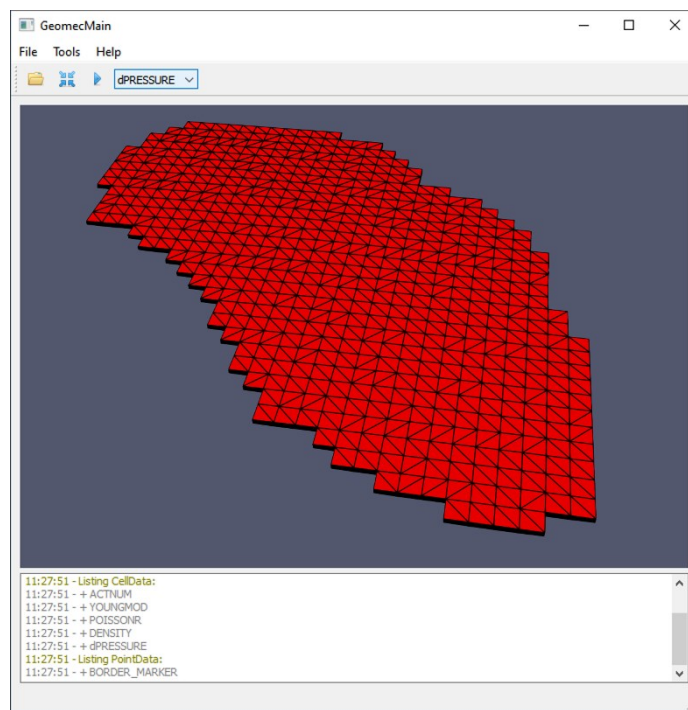


**Figure 133: Main Application GUI – visualization of the threshold filter's output**

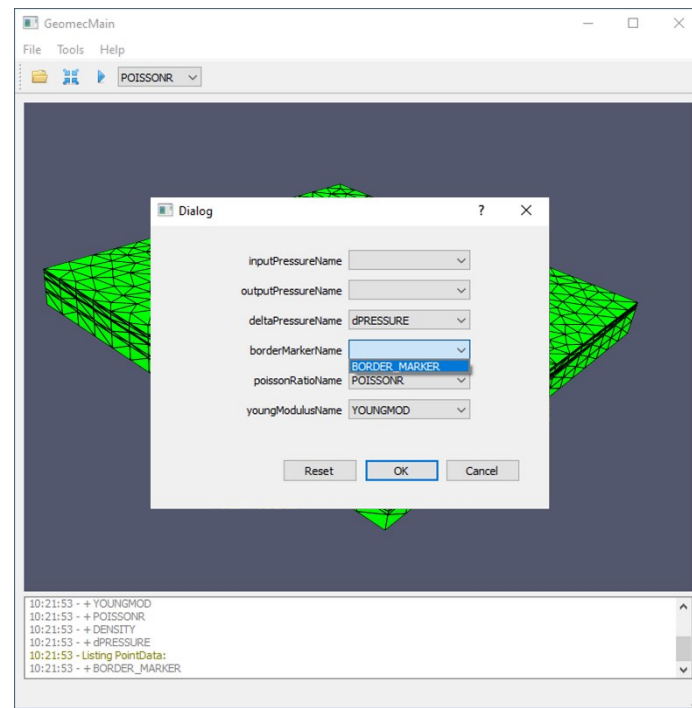


**Figure 134: Main Application GUI – dialog box for association of grid attributes to the VEM simulation input parameters**

# **Chapter 8**

## **Conclusion and future development**

The renewed interest in underground fluid storage systems in the perspective of energy transition and decarbonization was the starting point of this project. CO<sub>2</sub> confinement in deep geological formations and in saline aquifers could significantly contribute to reduce greenhouse gases in the atmosphere and mitigate climate change effects. H<sub>2</sub> underground storage is currently under investigation as an option to store chemical energy obtained from the excess of electrical power production from renewable sources, which are unstable and intermittent by nature and unsuited to match the electricity demand.

Underground fluid storage implies rock stress state variations, induced in the geological formations by the pressure changes due to fluid injection and withdrawal. If the variations of the rock stress state are significant, they could jeopardize the formation integrity and induce (micro)fracturing, potential faults (re)activation and rock deformation, which can propagate to the surface and induce ground movements. Because of the complexity of the problem, 3D geomechanical models are needed to assess that safety conditions can be guaranteed during the storage lifetime.

The goal of this research was to apply the recently formalized Virtual Element Method (VEM) to build 3D geomechanical models and address the safety issues associated to fluid storage in deep geological formations, namely rock integrity and compaction/expansion due to fluid withdrawal/injection causing ground level subsidence/rebound. The advantage of using VEM mainly resides in their versatility

to reproduce complex geometries while maintaining a certain computational “simplicity” without losing solution accuracy. Indeed, VEM is based on a theoretical framework sufficiently general to allow to overcome some of the FEM limitations such as typology of elements used to discretize the domain or the applicability to non-conforming grids (Gain et al., 2014): VEM allows the presence of hanging nodes and hybrid grids, i.e. the use of elements of different types and different degrees of approximation, reaching an adequate representation of the structural model and reproducing the solution with great accuracy only on the portions of main interest of the domain, with a consequent saving in terms of computational cost.

The first step of the research project was the implementation of a new workflow for the generation of the mechanical model grid. It was formalized starting from the minimal structural constraint set, that is the domain boundaries, at least one stratigraphic surface (already adjusted to the stratigraphic sequence intercepted by the wells) and fault surfaces, if any. The following step consisted in the tetrahedrization of the volume of interest, using the above geologic elements as constraints. An unstructured grid was obtained, with a refinement in the portion of the volume of interest where the investigated phenomena, that is compaction/expansion due to fluid withdrawal/injection and induced ground level subsidence/rebound, are occurring.

Because the geomechanical safety assessments necessarily follow the geologic modeling and the fluid-flow simulations, the main targets of the project also brought about the need for integration with other software. In fact, the mechanical analysis of deep geologic formations requires also relies on information deriving from the static and dynamic models. In turn, this implies the ability to correctly transfer or manipulate data, such adapting the grids and scaling the properties (such as the petrophysical properties or the pressure values) from the static and dynamic models to set up a coherent mechanical model. This is the reason why integrated platforms were developed to manage the whole workflow from geological modelling to mechanical analyses. The relevant technical literature mentions several codes which were specifically developed to integrate the output of geo-modelers and simulators devoted to different physical phenomena in an unified workflow (Fischer et al., 2021; Nakaten and Kempka, 2014; Park et al., 2014; Sentís and Gable, 2017). Among them, a reference tool in the oil and gas field is the Petrel E&P Software Platform, which uses proprietary data structures and gridding, by Schlumberger. Petrel is used for geologic modeling while Eclipse is the applied to dynamic simulations; the module Visage was developed for mechanical analyses

(Schlumberger, 2020b). Therefore, in parallel with the generation of a new gridding procedure for the mechanical model, these additional activities were performed: the construction of a C++ parser able to read the grid generated by Petrel (but potentially from any other software used for static modeling) and to convert it into the open source format vtu (Visualization Toolkit Unstructured grid) (Schroeder et al., 2006) as well as the implementation of a routine to extract the calculated pressure values from the dynamic simulator Eclipse (but potentially from any other software used for dynamic modeling).

Subsequently, the identified geological regions and/or layers were characterized based on preliminary defined geomechanical classes (i.e. rock characterized by homogeneous and constant isotropic strain and deformation parameters).

Once the volume discretization and the characterization of the geological formations were completed, the VEM method was applied and the approximated solutions of the PDEs were calculated on a fixed number of points, which can be the vertices or the centers of each element of the grid. Tests on the underground volume to be included in the simulations to avoid boundary effects and grid refinement were carried out. Furthermore, tests were also performed both on pillar grids generated by Petrel E&P and on unstructured grids built ad hoc according to the developed workflow. Eventually, to validate the methodology and the VEM solver implemented by the Numerical Analysis and Scientific Computing Group of the Department of Mathematical Sciences of Politecnico di Torino, tests were made on cases representative of natural gas underground storages in the Italian panorama. The VEM solution was compared with the FEM solution calculated with the Visage module in terms of subsidence/rebound induced by UGS operations in the linear elastic field. In fact, the analysis of ground movement surveys induced by the storage systems located in the Po Plain, Italy, shows a consistent relation between pressure variations and corresponding subsidence/rebound at the surface level (Benetatos et al., 2020; Codegone et al., 2016; Coti et al., 2018). This UGS-related pressure variations due to the withdrawal/injection phases affect the formation cyclically and over relatively short periods (typically 5-7 months) and the correlation between gas injection/withdrawal and upward/downward ground movements indicates that the formations behave elastically (Ferronato et al., 2013; P. Teatini et al., 2011).

The implemented constitutive model also includes the possibility of simulating the behavior of the rock in an elasto-plastic regime with a Mohr-Coulomb yield

surface and analyses on models largely representative of the Adriatic/Po Plain scenario were also performed. The calculation of a safety factor, which expressed the risk of shear failure, indicates if plasticity occurred in the investigated geological volume. However, convergence issues highlighted the need to modify the iterative algorithm implemented to solve the constitutive problem to obtain consistent results under any investigated scenario.

# Appendix

In this section the VEM formulation on polygonal and polyhedral elements is briefly introduced, with focus on the computation of the local stiffness matrix and the forcing term associated to the model problem defined in (36). A short overview of the abstract framework necessary to apply the VEM is shown, however the discussion on discretization process is limited to elements of accuracy order equal to 1. Theoretical details can be found in (Ahmad et al., 2013; Beirão da Veiga et al., 2014, 2013a).

## *VEM discrete approximations*

The strong expression of the set of equations which describes the behavior of the linear elastic medium is given in (36). If the solution  $u$  and test functions belong to the Sobolev space  $H_{0,\Gamma^D}^1(\Omega)$ , the corresponding variational formulation becomes

$$\int_{\Omega} \sigma(u) : \nabla v d\Omega = \int_{\Omega} b v d\Omega \quad \forall v \in H_{0,\Gamma^D}^1(\Omega) \quad (\text{a.1})$$

where  $\Omega \subseteq \mathbb{R}^3$  is the domain with boundary  $\Gamma$  partitioned in disjoint non-trivial segments  $\Gamma^D$  and  $\Gamma^N$  and mixed homogeneous boundary conditions are implicitly supposed, i.e.

$$\begin{aligned} u &= 0 && \text{on } \Gamma^D \\ \sigma \cdot n &= 0 && \text{on } \Gamma^N \end{aligned} \quad (\text{a.2})$$

Combining (a.1) with the hypothesis of small deformation in the generalized Hooke's law, the symmetric bilinear form is defined as

$$a(u, v) := \int_{\Omega} \sigma(u) : \varepsilon(v) d\Omega \quad (\text{a.3})$$

and, consequently, the model problem can be formulated as:

$$\text{find } u \in V: a(u, v) = (b, v) \quad \forall v \in V \quad (\text{a.4})$$

where  $V := H_{0,\Gamma^D}^1(\Omega)$ ,  $b \in L^2(\Omega)$  and the  $(\cdot, \cdot)$  is the  $L^2$ -scalar product.

The solution of the model problem through VEM is performed introducing a discrete approximation of the domain  $\Omega$ , the solution space  $V$ , the bilinear form  $a$  and the forcing term  $b$ .

Let us consider a tessellation  $\{\mathcal{T}_h\}_h$  of  $\Omega$  into disjoint non-overlapping polyhedral elements  $E$ . It is supposed that there exists a positive real number  $\gamma$  such that

- for every element  $E$ , for every face  $f$  of  $E$ , and for every edge  $e$  of  $f$   

$$h_e \geq \gamma h_f \geq \gamma^2 h_E$$

here  $h_e$ ,  $h_f$  and  $h_E$  are edge, face, and element diameters, respectively
- every element  $E$  is star-shaped with respect to all the points of a sphere of radius  $\geq \gamma h_E$
- every face  $f$  is star-shaped with respect to all the points of a sphere of radius  $\geq \gamma h_f$ .

Then the maximum diameter of the decomposition can be set as  $h := \max_{E \in \mathcal{T}_h} h_E$ .

In accordance with the Galerkin approximation, for each  $h$ , it is possible to introduce a finite dimensional space  $V_h \subset V$

$$V_h = \{v_h \in V: v_h|_E \in V_h(E) \quad \forall E \in \mathcal{T}_h\} \quad (\text{a.5})$$

and to split the symmetric bilinear form ( $a^E$ ) on each element  $E$ :

$$a(u_h, v_h) = \sum_{E \in \mathcal{T}_h} a^E(u_h, v_h) \quad \forall u_h, v_h \in V_h \quad (\text{a.6})$$

so as, the discrete model problem becomes

$$\text{find } u_h \in V_h: a(u_h, v_h) = \langle b, v_h \rangle \quad \forall v_h \in V_h \quad (\text{a.7})$$

The solution of (a.7) requires the computation of the local stiffness matrix on each element, i.e., the calculation of weak form integrals through evaluation of interpolation functions in the interior of the element. Since functions in  $V_h$  and its basis are in general non-polynomial functions, high order quadrature rules are adopted to reduce integral approximation errors, making the computational cost prohibitive.

VEM core idea it is to define adequate (virtual) space  $V_h$  such that functions contain the polynomial of degree  $\leq k$  (where  $k$  is the order of accuracy of the method), plus additional functions (in general not polynomials) that are never required to be computed thanks to the careful choice of the degrees of freedom and the introduction of an approximation  $a_h$  of the bilinear form. Operatively, it is necessary to construct a local projector on the space of polynomials of degree  $\leq k$ .

Substituting the approximated bilinear form  $a_h: V_h \times V_h \rightarrow \mathbb{R}$ :

$$\text{find } u_h \in V_h: a_h(u_h, v_h) = \langle b_h, v_h \rangle \quad \forall v_h \in V_h \quad (\text{a.8})$$

and supposing to split on each element  $E$

$$a_h(u_h, v_h) = \sum_{E \in \mathcal{T}_h} a_h^E(u_h, v_h) \quad \forall u_h, v_h \in V_h \quad (\text{a.9})$$

where  $a_h^E(\cdot, \cdot): V_h(E) \times V_h(E) \rightarrow \mathbb{R}$  and  $b_h \in V_h'$  approximates the forcing term. The VEM model problem has the form:

$$\text{find } u_h \in V_h : a_h(u_h, v_h) = \langle b_h, v_h \rangle \quad \forall v_h \in V_h \quad (\text{a.10})$$

Let us introduce, as basis for the space of polynomials  $\mathbb{P}_1(\mathcal{E})$  of degree 1 on the  $d$ -dimensional object  $\mathcal{E}$  (i.e.  $d = 2$  for polygon,  $d = 3$  for polyhedron), the set of scaled monomials of degree less than or equal to  $|\alpha|$ :

$$\mathcal{M}_1(\mathcal{E}) := \left\{ m_s : m_s = \left( \frac{\mathbf{x} - \mathbf{x}_{\mathcal{E}}}{h_{\mathcal{E}}} \right)^{\alpha} \text{ for } \alpha \in \mathbb{N}^d \text{ with } |\alpha| \leq 1 \right\} \quad (\text{a.11})$$

where  $x_{\mathcal{E}}$  and  $h_{\mathcal{E}}$  are the barycenter and the diameter of the object  $\mathcal{E}$ , respectively. The multi-index notation denotes:  $\alpha := (\alpha_1, \dots, \alpha_d)$ ,  $|\alpha| := \sum_{i=1}^d \alpha_i$  and  $x^{\alpha} := \prod_{i=1}^d x_i^{\alpha_i}$ . The number of elements in  $\mathcal{M}_k(\mathcal{E})$  is equal to  $n = (\prod_{i=1}^d (1+i))/d!$ . It follows that on polygon  $n_{mf} = 3$  and on polyhedron  $n_{mE} = 4$ .

$\mathbb{P}_0(\mathcal{E})$  is, instead the space of constant valued function on the  $d$ -dimensional object  $\mathcal{E}$ . And recall that  $\mathbb{P}_{-1}(\mathcal{E}) = \{0\}$ . To define the virtual space of the trial function it is necessary to introduce the following elementwise projection operators for each object  $\mathcal{E}$ .

- $H^1(\mathcal{E})$ -orthogonal projection operator  $\Pi_{1,\mathcal{E}}^V : H^1(\mathcal{E}) \rightarrow \mathbb{P}_1(\mathcal{E})$

$$\begin{aligned} (\nabla p, \nabla \Pi_{1,\mathcal{E}}^V v)_{\mathcal{E}} &= (\nabla p, \nabla v)_{\mathcal{E}} \quad \forall v \in H_1(\mathcal{E}), \forall p \in \mathbb{P}_1(\mathcal{E}) \\ (1, \nabla \Pi_{1,\mathcal{E}}^V v)_{\partial\mathcal{E}} &= (1, v)_{\partial\mathcal{E}} \quad \forall v \in H^1(\mathcal{E}) \end{aligned} \quad (\text{a.12})$$

- $L^2(\mathcal{E})$ -orthogonal projection operator  $\Pi_{1,\mathcal{E}}^0 : L^2(\mathcal{E}) \rightarrow \mathbb{P}_1(\mathcal{E})$

$$(p, \Pi_{1,\mathcal{E}}^0 v)_{\mathcal{E}} = (p, v)_{\mathcal{E}} \quad \forall v \in L^2(\mathcal{E}), \forall p \in \mathbb{P}_1(\mathcal{E}) \quad (\text{a.13})$$

- $L^2(\mathcal{E})$ -orthogonal projection operator of derivatives  $\Pi_{0,\mathcal{E}}^0 \nabla : H^1(\mathcal{E}) \rightarrow \mathbb{P}_0(\mathcal{E})$

$$\left( p, \Pi_{0,\varepsilon}^0 \frac{\partial v}{\partial x_i} \right)_\varepsilon = \left( p, \frac{\partial v}{\partial x_i} \right)_\varepsilon \quad \forall v \in H^1(\mathcal{E}), \forall p \in \mathbb{P}_0(\mathcal{E}) \quad (\text{a.14})$$

The construction of the three-dimensional virtual element space lies on the two-dimensional framework. To this end let us introduce the sequence of spaces defined on the boundary of a face ( $\partial f$ ) and on the face itself ( $f$ ). In particular, the enhanced version of the virtual spaces ( $\mathbb{W}_1$ ) are introduced to guarantee the evaluation of  $\Delta$ -operator on the polyhedron and its faces. Details on the construction of such spaces can be found in (Ahmad et al., 2013; Beirão da Veiga et al., 2016b, 2013a).

$$\mathbb{B}_1(\partial f) := \{v: v \in C^0(\partial f) \text{ and } v|_e \in \mathbb{P}_1(e) \quad \forall e \in \partial f\} \quad (\text{a.15})$$

where  $\mathbb{P}_1(e)$  is the space of polynomials of degree  $\leq 1$  on the edge  $e$ .  $\mathbb{B}_1(\partial f)$  is a linear space of dimension equal to the number of edges ( $n_{vf}$ ). Thus, the enhanced virtual space for each face has expression:

$$\mathbb{W}_1(f) := \left\{ \begin{array}{l} w \in H^1(f): w|_{\partial f} \in \mathbb{B}_1(\partial f), \Delta w \in \mathbb{P}_1(f) \text{ and} \\ (w, m_s)_{0,f} = (\Pi_{1,f}^\nabla w, m_s)_{0,f} \quad \forall m_s \in \mathcal{M}_1(f), s = 0,1 \end{array} \right\} \quad (\text{a.16})$$

$\mathbb{W}_1(f)$  is made up of functions which are linear on each edge and are completely determined by their value at the  $n_{vf}$  vertices. In  $\mathbb{W}_1(f)$  the  $n_{vf}$  values of  $w$  at the vertices are chosen as degrees of freedom. Analogously on the boundary of the polyhedron is defined the space:

$$\mathbb{B}_1(\partial E) := \{v: v \in C^0(\partial E) \text{ and } v|_f \in \mathbb{W}_1(f) \quad \forall f \subset \partial E\} \quad (\text{a.17})$$

where functions are continuously linked on the faces and are linear if restricted to the edges. And the enhanced virtual space defined on the polyhedron  $\mathbb{W}_1(E)$  has expression:

$$\mathbb{W}_1(E) := \left\{ \begin{array}{l} w \in H^1(E) : v|_{\partial E} \in \mathbb{B}_1(\partial E), \Delta w \in \mathbb{P}_1(E) \text{ and} \\ (w, m_s)_{0,E} = (\Pi_{1,E}^\nabla w, m_s)_{0,E} \quad \forall m_s \in \mathcal{M}_1(E), s = 0,1 \end{array} \right\} \quad (\text{a.18})$$

The space has dimension  $N^E = n_{vE}$  (i.e., the number of vertices of the polyhedron) and the choice of the degrees of freedom coincides with the values of  $w$  at the  $n_{vE}$  vertices of the polyhedron  $E$ . In the discretization process here described it is assumed that that  $V_h(E) := \mathbb{W}_1(E)$ . It is observed that, for order 1,  $\Pi_{1,\mathcal{E}}^\nabla \equiv \Pi_{1,\mathcal{E}}^0$ , as shown below.

The introduction of such spaces allows to define the approximation of the bilinear form:

$$a_h^E(u_h, v_h) := a^{E,\nabla}(u_h, v_h) + S^{E,\nabla}(u_h, v_h) \quad \forall u_h, v_h \in V_h(E) \quad (\text{a.19})$$

where the two terms  $a^{E,\nabla}(u_h, v_h)$  and  $S^{E,\nabla}(u_h, v_h)$  ensure consistency and stability of the method, respectively. In the specific case the two terms of (a.19) reduce to:

$$\begin{aligned} a^{E,\nabla}(u_h, v_h) &= \int_E \sigma(\Pi_{0,E}^0 \nabla u_h) : \varepsilon(\Pi_{0,E}^0 \nabla v_h) dE \\ S^{E,\nabla}(u_h, v_h) &= (2\mu + \lambda) S \left( (\mathbb{I} - \Pi_{1,E}^\nabla) u_h, (\mathbb{I} - \Pi_{1,E}^\nabla) v_h \right) \end{aligned} \quad (\text{a.20})$$

The computation of (a.20), i.e. the construction of the local stiffness matrix, in the VEM framework requires the introduction of a series of key elements, such as the computation of the orthogonal projectors defined in (a.12) (a.13) and (a.14). It follows a brief description of their construction on polygonal faces and their extension to polyhedron.

### *VEM on Polygonal Faces*

#### Quadrature and Vandermonde Matrices

Let us consider a polygonal face  $f$  with  $n_{vf}$  vertices (which is equal to the number of edges). To preserve the hypothesis of planarity the face  $f = \bigcup_{i=1}^{n_{vf}} \tau_i$  is decomposed  $n_{vf}$  triangles with vertices  $[e(0), e(1), c_f]$ , i.e., they coincide with the

extremes of the current edge  $e$  and the barycenter  $c_f$  of the polygonal face, respectively. On the reference element  $\hat{\tau}$  a second order quadrature Gaussian formula is defined: this means that the 3 quadrature internal points, and the corresponding weights, are stored in a  $\hat{\mathbf{P}}^f \in \mathbb{R}^{2 \times 3}$  and  $\hat{\mathbf{W}}^f \in \mathbb{R}^{3 \times 1}$  matrices, respectively. The reference triangle  $\hat{\tau}$  is mapped to each triangle  $\tau_i$ , thus the storage of the whole quadrature formula on  $f$  requires two matrices  $\mathbf{P}^f \in \mathbb{R}^{2 \times 3n_{vf}}$  and  $\mathbf{W}^f \in \mathbb{R}^{3n_{vf} \times 1}$ .

$$\begin{aligned}\mathbf{P}^f &= [\mathbf{P}_1^f \quad \dots \quad \mathbf{P}_{n_{vf}}^f] \text{ and } \mathbf{P}_i^f = [p_i^1 \ p_i^2 \ p_i^3] = \begin{bmatrix} x_1 & x_2 & x_3 \\ y_1 & y_2 & y_3 \end{bmatrix} \\ \mathbf{W}^f &= [\mathbf{W}_1^f \quad \dots \quad \mathbf{W}_{n_{vf}}^f]^T \text{ and } \mathbf{W}_i^f = [w_i^1 \ w_i^2 \ w_i^3]\end{aligned}\tag{a.21}$$

where for the generic triangle  $\tau_i$ :  $\mathbf{P}_i^f = \mathbf{J}_i \hat{\mathbf{P}}^f + \mathbf{b}_i$  and  $\mathbf{W}_i^f = |\mathbf{J}_i| \hat{\mathbf{W}}^f$ .

On the boundary a Gauss-Lobatto quadrature formula of order 1 is assumed. The quadrature points coincide with the  $n_{vf}$  polygon vertices and the corresponding matrix  $\mathbf{P}^{\partial f} = [p_1^{\partial f} \dots p_{n_{vf}}^{\partial f}] \in \mathbb{R}^{2 \times n_{vf}}$ . Analogously to the internal points, a map between the reference 1D edge  $[0,1]$  (with weights  $[\hat{w}_{e_0}^{\partial} \ \hat{w}_{e_1}^{\partial}]$ ) to the 2D edge  $e$  is performed. At each boundary point  $p_i^{\partial}$  the weight is defined as  $w_i^{\partial f} = \hat{w}_0^{\partial} |J_{e_0}| + \hat{w}_1^{\partial} |J_{e_1}|$  where  $e_0$  and  $e_1$  are the two edges which have the vertex  $i$  as extrema. If the normal outward versor for each edge  $e_i$  is defined as  $[n_x^{e_i}, n_y^{e_i}]^T$  the corresponding weighted component are

$$\begin{aligned}w_i^{\partial f} n_x &= n_x^{e_0} \hat{w}_0^{\partial} |J_{e_0}| + n_x^{e_1} \hat{w}_1^{\partial} |J_{e_1}| \\ w_i^{\partial f} n_y &= n_y^{e_0} \hat{w}_0^{\partial} |J_{e_0}| + n_y^{e_1} \hat{w}_1^{\partial} |J_{e_1}|\end{aligned}\tag{a.22}$$

resulting in 3 matrices  $\mathbf{W}^{\partial f}, \mathbf{W}_{n_x}^{\partial f}, \mathbf{W}_{n_y}^{\partial f} \in \mathbb{R}^{n_{vf} \times 1}$ .

Let now consider the monomial basis  $\mathcal{M}_1(f)$  of dimension  $n_{mf} = 3$ . The multi-index  $\alpha$  has expression

$$\alpha = \begin{bmatrix} 0 & 0 \\ 1 & 0 \\ 0 & 1 \end{bmatrix} \quad (\text{a.23})$$

To calculate efficiently integrals required for the construction of the local stiffness matrix, monomial and their partial derivatives evaluated on the quadrature points (internal and on boundary), are stored in Vandermonde matrices where the index  $i := 4(k - 1) + q$   $j = 1, \dots, n_{mf}$ ,  $k = 1, \dots, n_{vf}$  and  $q = 1, \dots, 3$ :

$$\begin{aligned} V^f &\in \mathbb{R}^{3n_{vf} \times n_{mf}} & V_{ij} &= m_j(p_k^q) \\ V_x^f &\in \mathbb{R}^{3n_{vf} \times n_{mf}} & \frac{\partial V_{ij}}{\partial x} &= \frac{\partial m_j}{\partial x}(p_k^q) \\ V_y^f &\in \mathbb{R}^{3n_{vf} \times n_{mf}} & \frac{\partial V_{ij}}{\partial y} &= \frac{\partial m_j}{\partial y}(p_k^q) \end{aligned} \quad (\text{a.24})$$

and in the following it is supposed  $i = 1, \dots, n_{vf}$   $j = 1, \dots, 3$ :

$$\begin{aligned} V^{\partial f} &\in \mathbb{R}^{n_{vf} \times n_{mf}} & V_{ij}^{\partial f} &= m_j(p_i^{\partial f}) \\ V_x^{\partial f} &\in \mathbb{R}^{n_{vf} \times n_{mf}} & \frac{\partial V_{ij}^{\partial f}}{\partial x} &= \frac{\partial m_j}{\partial x}(p_i^{\partial f}) \\ V_y^{\partial f} &\in \mathbb{R}^{n_{vf} \times n_{mf}} & \frac{\partial V_{ij}^{\partial f}}{\partial y} &= \frac{\partial m_j}{\partial y}(p_i^{\partial f}) \end{aligned} \quad (\text{a.25})$$

### Computation of $\Pi_{1,f}^V$

Once numbered the degrees of freedom, from 1 to  $n_{vf}$ , let us introduce the operator  $\chi_i: \mathbb{W}_1(f) \rightarrow \mathbb{R}$  as

$$\chi_i(v) := i - \text{th degree of freedom of } v \quad i = 1: n_{vf} \quad (\text{a.26})$$

and the local basis function  $\varphi_i \in \mathbb{W}_1(f)$  defined as the canonical basis function:

$$\chi_i(\varphi_j) := \delta_{ij} \quad i, j = 1 : n_{vf} \quad (\text{a.27})$$

It follows the Lagrange-type interpolation identity:

$$v_h = \sum_{i=1}^{n_{vf}} \chi_i(v_h) \varphi_i \quad \forall v_h \in \mathbb{W}_1(f) \quad (\text{a.28})$$

Moreover, since  $\Pi_{1,f}^V v_h \in \mathbb{P}_1(f)$ , it is possible to represent it in the basis of  $\mathcal{M}_1(f)$

$$\Pi_{1,f}^V v_h = \sum_{\beta=1}^{n_{mf}} s^\beta(v_h) m_\beta \quad \forall v_h \in \mathbb{W}_1(f) \quad (\text{a.29})$$

From the definition of the operator (a.12) and substituting  $\nabla p = \nabla m_\alpha$  and (a.28)

$$\begin{aligned} \sum_{\beta=1}^{n_m} s^\beta (\nabla m_\alpha, \nabla m_\beta)_f &= (\nabla m_\alpha, \nabla v_h)_f \quad \alpha = 1, \dots, n_m \\ \left( 1, \sum_{\beta=1}^{n_m} s^\beta m_\beta \right)_{\partial f} &= (1, v_h)_{\partial f} \quad \forall v_h \in \mathbb{W}_1(f) \end{aligned} \quad (\text{a.30})$$

The system has expression

$$\mathbf{G}_f \mathbf{s} = \tilde{\mathbf{b}}_f \quad (\text{a.31})$$

where  $\mathbf{s}$  is the vector of the components of  $\Pi_{1,f}^V v_h$  in the monomial basis and

$$\mathbf{G}_f = \begin{bmatrix} (1, m_1)_{\partial f} & (1, m_2)_{\partial f} & (1, m_3)_{\partial f} \\ 0 & (\nabla m_2, \nabla m_2)_f (\nabla m_2, \nabla m_3)_f \\ 0 & (\nabla m_3, \nabla m_2)_f (\nabla m_3, \nabla m_3)_f \end{bmatrix} \quad (a.32)$$

$$\tilde{\mathbf{b}}_f = \begin{bmatrix} (1, v_h)_{\partial f} \\ (\nabla m_2, \nabla v_h)_f \\ (\nabla m_3, \nabla v_h)_f \end{bmatrix}$$

The computation of the matrix  $\mathbf{G}_f \in \mathbb{R}^{n_{mf} \times n_{mf}}$  requires only to evaluate integrals of polynomials on the face  $f$

$$(\nabla m_i, \nabla m_j)_f = \sum_{k=1}^{n_{vf}} \sum_{q=1}^3 \left[ \frac{\partial m_i}{\partial x}(p_k^q) w_k^q \frac{\partial m_j}{\partial x}(p_k^q) + \frac{\partial m_i}{\partial y}(p_k^q) w_k^q \frac{\partial m_j}{\partial y}(p_k^q) \right] \quad i, j = 2, 3 \quad (a.33)$$

The first row, instead is defined

$$(1, m_j)_{\partial f} = \sum_{k=1}^{n_{vf}} m_j(p_k^{\partial f}) w_k^{\partial f} \quad j = 1, \dots, n_m \quad (a.34)$$

and in compact form it can be written as:

$$\mathbf{G}_f = \begin{bmatrix} (\mathbf{W}^{\partial f})^T \mathbf{V}^{\partial f} \\ \mathbf{V}_x^f {}^T \text{diag}(\mathbf{W}^f) \mathbf{V}_x^f + \mathbf{V}_y^f {}^T \text{diag}(\mathbf{W}^f) \mathbf{V}_y^f \end{bmatrix} \quad (a.35)$$

Let us observe that, applying the divergence theorem, it is possible to write the right term in (a.30) as

$$(\nabla m_i, \nabla v_h)_f = - \int_f \Delta m_i v_h df + \int_{\partial f} \frac{dm_i}{d\mathbf{n}} v_h ds \quad \forall i \quad (a.36)$$

Since  $m_i \in \mathbb{P}_1(f)$  the  $\Delta m_i$  is equal to zero thus, the computation of  $\tilde{\mathbf{b}}_f$  reduces to:

$$\begin{aligned}\tilde{\mathbf{b}}_{f1} &= (1, v_h)_{\partial f} = \sum_{k=1}^{n_{vf}} \chi_k(v_h)(1, \varphi_k)_{\partial f} = \sum_{k=1}^{n_{vf}} \chi_k(v_h) \int_{\partial f} \varphi_k ds \\ \tilde{\mathbf{b}}_{fi} &= (\nabla m_i, \nabla v_h)_f = \int_{\partial f} \frac{dm_i}{d\mathbf{n}} v_h ds = \sum_{k=1}^{n_{vf}} \chi_k(v_h) \int_{\partial f} \frac{dm_i}{d\mathbf{n}} \varphi_k ds\end{aligned}\quad (a.37)$$

Since  $\varphi_k|_{\partial f} \in \mathbb{B}_1(\partial f)$  thus the integrand function is a polynomial of degree 1. The evaluation of the (a.37) with a Gauss-Lobatto quadrature rule with 2 points guarantees order 1 precision, so as

$$\begin{aligned}\int_{\partial f} \varphi_k ds &= \sum_{i=1}^{n_{vf}} w_i^{\partial f} \varphi_k(p_i^{\partial f}) = \sum_{i=1}^{n_{vf}} w_i^{\partial f} \delta_{ik} = w_k^{\partial f} \\ \int_{\partial f} \frac{dm_i}{d\mathbf{n}} \varphi_k ds &= \sum_{i=1}^{n_{vf}} \left[ \frac{\partial m_i}{\partial x}(p_i^{\partial f}) w_i^{\partial f} n_x + \frac{\partial m_i}{\partial y}(p_i^{\partial f}) w_i^{\partial f} n_y \right] \varphi_k(p_i^{\partial f}) \\ &= \sum_{i=1}^{n_{vf}} \left[ \frac{\partial m_i}{\partial x}(p_i^{\partial f}) w_i^{\partial f} n_x + \frac{\partial m_i}{\partial y}(p_i^{\partial f}) w_i^{\partial f} n_y \right] \delta_{ik} \\ &= \frac{\partial m_k}{\partial x}(p_k^{\partial f}) w_k^{\partial f} n_x + \frac{\partial m_k}{\partial y}(p_k^{\partial f}) w_k^{\partial f} n_y\end{aligned}\quad (a.38)$$

It follows that the computation of  $\tilde{\mathbf{b}}_f$  can be performed knowing only the  $\chi_k(v_h)$  on the face. Since the stiffness matrix involves uniquely the canonical basis, let now define the matrix  $\mathbf{B}_f \in \mathbb{R}^{n_{mf} \times n_{vf}}$ :

$$\begin{aligned}\mathbf{B}_f &= [\mathbf{b}_{f1}, \dots, \mathbf{b}_{fn_{vf}}] \\ &\begin{bmatrix} (1, \varphi_1)_{\partial f} & (1, \varphi_2)_{\partial f} & (1, \varphi_3)_{\partial f} & (1, \varphi_4)_{\partial f} \\ (\nabla m_2 \cdot \mathbf{n}, \varphi_1)_{\partial f} & (\nabla m_2 \cdot \mathbf{n}, \varphi_2)_{\partial f} & (\nabla m_2 \cdot \mathbf{n}, \varphi_3)_{\partial f} & (\nabla m_2 \cdot \mathbf{n}, \varphi_4)_{\partial f} \\ (\nabla m_3 \cdot \mathbf{n}, \varphi_1)_{\partial f} & (\nabla m_3 \cdot \mathbf{n}, \varphi_2)_{\partial f} & (\nabla m_3 \cdot \mathbf{n}, \varphi_3)_{\partial f} & (\nabla m_3 \cdot \mathbf{n}, \varphi_4)_{\partial f} \end{bmatrix}\end{aligned}\quad (a.39)$$

$$= \left[ (\mathbf{W}^{\partial f})^T \right. \\ \left. + \left( \mathbf{V}_x^{\partial f} \right)^T \text{diag}(\mathbf{W}_{n_x}^{\partial f}) + \left( \mathbf{V}_y^{\partial f} \right)^T \text{diag}(\mathbf{W}_{n_y}^{\partial f}) \right]$$

It follows that the computation of  $\Pi_{1,f}^\nabla \varphi_i$  has the compact expression

$$\boldsymbol{\Pi}_{1,f}^{\nabla*} = [\mathbf{s}_1, \dots, \mathbf{s}_{n_v}] = \mathbf{B}_f^{-1} \mathbf{G}_f \quad (\text{a.40})$$

This is the matrix representation  $\boldsymbol{\Pi}_{1,f}^{\nabla*} \in \mathbb{R}^{n_{mf} \times n_{vf}}$  of the projection operator acting from  $\mathbb{W}_1(f) \rightarrow \mathbb{P}_1(f)$ . However, it is necessary to compute projectors respect to the canonical basis, i.e. interpreting the operator as acting  $\mathbb{W}_1(f) \rightarrow \mathbb{W}_1(f)$ :

$$\Pi_{1,f}^\nabla \varphi_i = \sum_{j=1}^{n_{vf}} \chi_j(\Pi_{1,f}^\nabla \varphi_i) \varphi_j \quad i = 1, \dots, n_{vf} \quad (\text{a.41})$$

Substituting the representation (a.29) of  $\varphi_j$ :

$$\begin{aligned} \Pi_{1,f}^\nabla \varphi_i &= \sum_{\alpha=1}^{n_{mf}} s^\alpha(\varphi_i) m_\alpha = \sum_{\alpha=1}^{n_{mf}} s^\alpha(\varphi_i) \sum_{j=1}^{n_{vf}} \chi_j(m_\alpha) \varphi_j \\ &= \sum_{j=1}^{n_{vf}} \left( \sum_{\alpha=1}^{n_{mf}} s^\alpha(\varphi_i) \chi_j(m_\alpha) \right) \varphi_j \quad i = 1, \dots, n_{vf} \end{aligned} \quad (\text{a.42})$$

It follows that

$$\chi_j(\Pi_{1,f}^\nabla \varphi_i) = \sum_{\alpha=1}^{n_{mf}} s^\alpha(\varphi_i) \chi_j(m_\alpha) \quad i, j = 1, \dots, n_{vf} \quad (\text{a.43})$$

Let now define the matrix  $\mathbf{D}_f \in \mathbb{R}^{n_{vf} \times n_{mf}}$

$$\mathbf{D}_f := \begin{bmatrix} \chi_1(m_1) & \chi_1(m_2) & \chi_1(m_3) \\ \chi_2(m_1) & \chi_2(m_2) & \chi_2(m_3) \\ \chi_3(m_1) & \chi_3(m_2) & \chi_3(m_3) \\ \chi_4(m_1) & \chi_4(m_2) & \chi_4(m_3) \end{bmatrix} \quad \text{with } n_{vf} = 4 \text{ and } n_{mf} = 3 \quad (\text{a.44})$$

In the analyzed case, since the dof coincide with the vertices of the face, it follows that  $\mathbf{D}_f \equiv \mathbf{V}^{\partial f}$ . Thus, in compact form the projector matrix  $\Pi_{1,f}^{\nabla} \in \mathbb{R}^{n_{vf} \times n_{vf}}$  in the canonical basis has expression

$$\Pi_{1,f}^{\nabla} = \mathbf{D}_f \mathbf{G}_f^{-1} \mathbf{B}_f = \mathbf{V}^{\partial f} \Pi_{1,f}^{\nabla*} \quad (\text{a.45})$$

#### Computation of $\Pi_{1,f}^0$

From the definition  $L^2(f)$ -orthogonal projection operator in (a.13)

$$(m_\alpha, \Pi_{1,f}^0 v_h)_f = (m_\alpha, v_h)_f \quad \forall v_h \in W_1(f), \forall m_\alpha \in \mathcal{M}_1(f) \quad (\text{a.46})$$

and, as done for the  $\Pi_{1,f}^{\nabla*}$ , let express each function respect to the monomial basis

$$\Pi_{1,f}^{0*} v_h = \sum_{\beta=1}^{n_{mf}} t^\beta(v_h) m_\beta \quad (\text{a.47})$$

It follows that

$$\sum_{\beta=1}^{n_{mf}} (m_\alpha, m_\beta)_f t^\beta(v_h) = (m_\alpha, v_h)_f \quad (\text{a.48})$$

$$\forall v_h \in W_1(f), \forall m_\alpha, m_\beta \in \mathcal{M}_1(f)$$

The system has expression

$$\mathbf{H}_1^f \mathbf{t} = \tilde{\mathbf{c}}^f \quad (\text{a.49})$$

where  $\mathbf{t}$  is the vector of the components of  $\Pi_{1,f}^0 v_h$  in the monomial basis and

$$\begin{aligned} \mathbf{H}_1^f &= \begin{bmatrix} 1 & (1, m_2)_f & (1, m_3)_f \\ (m_2, 1)_f & (m_2, m_2)_f & (m_2, m_3)_f \\ (m_3, 1)_f & (m_3, m_2)_f & (m_3, m_3)_f \end{bmatrix} \text{ with } n_{mf} = 3 \\ \tilde{\mathbf{c}}^f &= \begin{bmatrix} (1, v_h)_f \\ (m_2, v_h)_f \\ (m_3, v_h)_f \end{bmatrix} \end{aligned} \quad (\text{a.50})$$

$\mathbf{H}_1^f \in \mathbb{R}^{n_{mf} \times n_{mf}}$  is called mass matrix and can be calculated as

$$\mathbf{H}_1^f = \mathbf{V}^{f T} \text{diag}(\mathbf{W}^f) \mathbf{V}^f \quad (\text{a.51})$$

For the calculation of the  $\tilde{\mathbf{c}}^f$ , it is exploited the enhancement property, which allows to evaluate integrals through the actual degree of freedom of the resulting polynomial, i.e.

$$\tilde{c}_i^f = (m_i, v_h)_f = \int_f m_i v_h df = \int_f m_i \Pi_{1,f}^\nabla v_h df \quad (\text{a.52})$$

If it is defined the corresponding matrix  $\mathbf{C}_1^f \in \mathbb{R}^{n_{mf} \times n_{vf}}$  with elements

$$c_{ij}^f = (m_i, \varphi_j)_f = (m_i, \Pi_{1,f}^\nabla \varphi_j)_f \quad (\text{a.53})$$

in the compact form it reduces

$$\mathcal{C}_1^f = \mathbf{H}_1^f \boldsymbol{\Pi}_{1,f}^{\nabla*} \quad (\text{a.54})$$

consequently, the expression of the  $L^2(f)$ -orthogonal projection operator, for order 1 has expression

$$\boldsymbol{\Pi}_{1,f}^{0*} = \boldsymbol{\Pi}_{1,f}^{\nabla*} \quad (\text{a.55})$$

At last, the projector can be expressed in terms of VEM basis function by

$$\boldsymbol{\Pi}_{1,f}^0 = \mathbf{V}^{\partial f} \boldsymbol{\Pi}_{1,f}^{0*} \quad (\text{a.56})$$

### Computation of $\boldsymbol{\Pi}_{0,f}^0 \nabla$

From the definition of the  $H^1(f)$ -orthogonal projection operator of derivatives in (a.14) and considering that the monomial basis reduces to  $m_1 = 1$ , we have

$$\begin{aligned} \left( m_1, \boldsymbol{\Pi}_{0,f}^0 \frac{\partial v_h}{\partial x} \right)_f &= \left( m_1, \frac{\partial v_h}{\partial x} \right)_f \\ \left( m_1, \boldsymbol{\Pi}_{0,f}^0 \frac{\partial v_h}{\partial y} \right)_f &= \left( m_1, \frac{\partial v_h}{\partial y} \right)_f \end{aligned} \quad \forall v_h \in \mathbb{W}_1(f) \quad (\text{a.57})$$

Considering the composition of the projector and the partial derivative, let's define the operators  $\boldsymbol{\Pi}_{0,f}^{0,x}$  and  $\boldsymbol{\Pi}_{0,f}^{0,y}$  that, in the trivial case of  $\mathbb{P}_0(f)$ , reduce to

$$\begin{aligned} \boldsymbol{\Pi}_{0,f}^{0,x} v_h &= \tilde{t}_1^x(v_h) m_1 \\ \boldsymbol{\Pi}_{0,f}^{0,y} v_h &= \tilde{t}_1^y(v_h) m_1 \end{aligned} \quad \forall v_h \in \mathbb{W}_1(f) \quad (\text{a.58})$$

Thus, for the single element of the basis of  $\mathbb{W}_1(f)$

$$\begin{aligned}\Pi_{0,f}^{0,x} \varphi_i &= t_{1i}^x(\varphi_i) m_1 & \forall i = 1, \dots, n_{vf} \\ \Pi_{0,f}^{0,y} \varphi_i &= \tilde{t}_{1i}^y(\varphi_i) m_1\end{aligned}\quad (\text{a.59})$$

Applying again the divergence theorem the right term of (a.57) can be written as:

$$\begin{aligned}\left( m_1, \frac{\partial \varphi_i}{\partial x} \right)_f &:= \int_f \frac{\partial \varphi_i}{\partial x} df = \int_{\partial f} \varphi_i n_x \\ \left( m_1, \frac{\partial \varphi_i}{\partial y} \right)_f &:= \int_f \frac{\partial \varphi_i}{\partial y} df = \int_{\partial f} \varphi_i n_y\end{aligned}\quad (\text{a.60})$$

where it is assumed that  $\nabla m_1 = 0$ . In this simple case the mass matrix  $\mathbf{H}_0^f$  reduces to a scalar value equal to 1. Thus, in compact form the projector respect to the monomial basis of  $\mathbb{P}_0(f)$  can be expressed as

$$\begin{aligned}\boldsymbol{\Pi}_{0,f}^{0,x*} &= \left( \mathbf{V}_x^{\partial f}(:,1) \right)^T \text{diag}(\mathbf{W}_{nx}^{\partial f}) \\ \boldsymbol{\Pi}_{0,f}^{0,y*} &= \left( \mathbf{V}_y^{\partial f}(:,1) \right)^T \text{diag}(\mathbf{W}_{ny}^{\partial f})\end{aligned}\quad (\text{a.61})$$

$\mathbf{V}_x^{\partial f}(:,1)$  and  $\mathbf{V}_y^{\partial f}(:,1)$  represents the first column of the corresponding complete Vandermonde matrices.  $\boldsymbol{\Pi}_{0,f}^{0,x*}$  and  $\boldsymbol{\Pi}_{0,f}^{0,y*} \in \mathbb{R}^{1 \times n_{vf}}$ .

### VEM on Polyhedron

Operators and the matrix representation introduced on faces can be naturally extended to polyhedrons. In the following only key elements are briefly introduced.

#### Quadrature and Vandermonde Matrices

Let us consider a star-shaped polyhedron  $E$  with  $n_{vE}$  vertices and  $n_{fE}$  faces  $f$ . The polyhedron is decomposed in tetrahedra  $E = \bigcup_{i=1}^{n_{TE}} T_i$  where  $n_{TE} = \sum_{k=1}^{n_{fE}} n_{vf}^k$  and  $n_{vf}^k$  is the number of vertices (coincides with the number of edges) of the face

$k$ . Once calculated the barycenter  $c_E$ , each tetrahedron is defined as  $[e_f(0), e_f(1), c_f, c_E]$  where  $[e_f(0), e_f(1)]$  and  $c_f$  are one of the edges and the barycenter of the current face, respectively. On the reference element  $\widehat{T}$  a second order quadrature Gaussian formula is defined: this means that 4 quadrature internal points, and the corresponding weights, are stored in a  $\widehat{\mathbf{P}}^f \in \mathbb{R}^{3 \times 4}$  and  $\widehat{\mathbf{W}}^f \in \mathbb{R}^{4 \times 1}$  matrices, respectively. The reference tetrahedron  $\widehat{T}$  is mapped to each  $T_i$ , thus the storage of the whole quadrature formula on  $E$  requires two matrices  $\mathbf{P}^E \in \mathbb{R}^{3 \times 4n_{TE}}$  and  $\mathbf{W}^E \in \mathbb{R}^{4n_{TE} \times 1}$ . On the boundary, quadrature formulas defined for faces are exploited. In particular, the number of the boundary quadrature points are  $n_{\partial E} = \sum_{k=1}^{n_{fE}} n_{vf}^k$ , and matrices

$$\begin{aligned}\mathbf{P}^{\partial E} &= \left[ \mathbf{P}_1^{\partial f}, \dots, \mathbf{P}_{n_{fE}}^{\partial f} \right] \in \mathbb{R}^{3 \times 3n_{\partial E}} \\ \mathbf{W}^{\partial E} &= \left[ \mathbf{W}_1^{\partial f}, \dots, \mathbf{W}_{n_{fE}}^{\partial f} \right] \in \mathbb{R}^{3n_{\partial E} \times 1}\end{aligned}\tag{a.62}$$

Analogously  $\mathbf{W}_{n_x}^{\partial E}$ ,  $\mathbf{W}_{n_y}^{\partial E}$ ,  $\mathbf{W}_{n_z}^{\partial E} \in \mathbb{R}^{3n_{\partial E} \times 1}$ . The monomial basis  $\mathcal{M}_1(E)$  has dimension  $n_{mE} = 4$  and the multi-index  $\alpha$  has expression

$$\alpha = \begin{bmatrix} 0 & 0 & 0 \\ 1 & 0 & 0 \\ 0 & 1 & 0 \\ 0 & 0 & 1 \end{bmatrix}\tag{a.63}$$

As done for faces, Vandermonde matrices on polyhedron are defined to store values of monomial basis on the selected quadrature points. For the internal points, there are defined  $\mathbf{V}^E, \mathbf{V}_x^E, \mathbf{V}_y^E, \mathbf{V}_z^E \in \mathbb{R}^{4n_{TE} \times n_{mE}}$  and  $\mathbf{V}^{\partial E}, \mathbf{V}_x^{\partial E}, \mathbf{V}_y^{\partial E}, \mathbf{V}_z^{\partial E} \in \mathbb{R}^{3n_{\partial E} \times n_{mE}}$ . The construction of the stiffness matrix requires the evaluation of  $\Pi_{0,E}^0 \nabla \varphi_i$  on the quadrature nodes respect to the VEM basis. The computation of such operator exploits the fact that the  $n_{vf}$  dof of each face belongs to  $n_{vE}$  dof of the polyhedron. This means that, for each face, the product  $(\mathbf{V}^f(:,1))^T \Pi_{0,f}^{0*} \in \mathbb{R}^{3n_{vf} \times n_{vf}}$  is interpreted as the evaluation at the quadrature points of the canonical basis on  $f \subset \partial E$  respect to the canonical basis on  $E$ . Thus, the complete matrix  $\bar{\mathbf{V}}^{\partial E}$  belongs to  $\mathbb{R}^{n_{\partial E} \times n_{mE}}$ .

### Computation of $\Pi_{1,E}^\nabla$

The extension to the three-dimensional case is straightforward and the linear system which allows to compute  $\mathbf{s}_j$ , the vector of the components of  $\Pi_{1,E}^\nabla \varphi_j$  in the monomial basis has expression

$$\mathbf{G}_E \mathbf{s}_j = \mathbf{b}_E^j \quad (\text{a.64})$$

with

$$\begin{aligned} \mathbf{G}_E &= \begin{bmatrix} (1, m_1)_{\partial E} & (1, m_2)_{\partial E} & (1, m_3)_{\partial E} & (1, m_4)_{\partial E} \\ 0 & (\nabla m_2, \nabla m_2)_E (\nabla m_2, \nabla m_3)_E (\nabla m_2, \nabla m_4)_E \\ 0 & (\nabla m_3, \nabla m_2)_E (\nabla m_3, \nabla m_3)_E (\nabla m_3, \nabla m_4)_E \\ 0 & (\nabla m_4, \nabla m_2)_E (\nabla m_4, \nabla m_3)_E (\nabla m_4, \nabla m_4)_E \end{bmatrix} \\ \mathbf{b}_E^j &= \begin{bmatrix} (1, \varphi_j)_{\partial E} \\ (\nabla m_2, \nabla \varphi_j)_E \\ (\nabla m_3, \nabla \varphi_j)_E \\ (\nabla m_4, \nabla \varphi_j)_E \end{bmatrix} \end{aligned} \quad (\text{a.65})$$

Analogously to what done on faces, it is possible to write

$$\begin{aligned} \mathbf{G}_E &= \begin{bmatrix} (\mathbf{W}^{\partial E})^T \mathbf{V}^{\partial E} \\ (\mathbf{V}_x^E)^T \text{diag}(\mathbf{W}^E) \mathbf{V}_x^E + (\mathbf{V}_y^E)^T \text{diag}(\mathbf{W}^E) \mathbf{V}_y^E \end{bmatrix} \\ \mathbf{B}_E &= \begin{bmatrix} (\mathbf{W}^{\partial E})^T \bar{\mathbf{V}}^{\partial E} \\ ((\mathbf{V}_x^{\partial E})^T \text{diag}(\mathbf{W}_{nx}^{\partial E}) + (\mathbf{V}_y^{\partial E})^T \text{diag}(\mathbf{W}_{ny}^{\partial E}) + (\mathbf{V}_z^{\partial E})^T \text{diag}(\mathbf{W}_{nz}^{\partial E})) \bar{\mathbf{V}}^{\partial E} \end{bmatrix} \end{aligned} \quad (\text{a.66})$$

Thus, the whole matrix  $\Pi_{1,E}^\nabla \in \mathbb{R}^{n_{mE} \times n_{vE}}$  with  $\mathbf{G}_E \in \mathbb{R}^{n_{mE} \times n_{mE}}$  and  $\mathbf{B}_E \in \mathbb{R}^{n_{mE} \times n_{vE}}$  has expression:

$$\Pi_{1,E}^\nabla = \mathbf{G}_E^{-1} \mathbf{B}_E \quad (\text{a.67})$$

### Computation of $\Pi_{0,E}^0 \nabla$

Extending again to the polyhedron expression calculated for each face, it is possible to compute the operator

$$\begin{aligned}\boldsymbol{\Pi}_{0,E}^{0,x} &= \left( \boldsymbol{V}_x^{\partial E}(:,1) \right)^T \text{diag}(\boldsymbol{W}_{nx}^{\partial E}) \bar{\boldsymbol{V}}^{\partial E} \\ \boldsymbol{\Pi}_{0,E}^{0,y} &= \left( \boldsymbol{V}_y^{\partial E}(:,1) \right)^T \text{diag}(\boldsymbol{W}_{ny}^{\partial E}) \bar{\boldsymbol{V}}^{\partial E} \\ \boldsymbol{\Pi}_{0,E}^{0,z} &= \left( \boldsymbol{V}_z^{\partial E}(:,1) \right)^T \text{diag}(\boldsymbol{W}_{nz}^{\partial E}) \bar{\boldsymbol{V}}^{\partial E}\end{aligned}\quad (\text{a.68})$$

$\boldsymbol{\Pi}_{0,E}^{0,x}$ ,  $\boldsymbol{\Pi}_{0,E}^{0,y}$ ,  $\boldsymbol{\Pi}_{0,E}^{0,z} \in \mathbb{R}^{1 \times n_{vE}}$ . This means that the gradient of the projected VEM basis evaluated on the internal quadrature points  $\Pi_{0,E}^0 \nabla \varphi(\boldsymbol{P}^E)$  can be stored in 3 matrices  $\mathbb{R}^{4n_{TE} \times n_{vE}}$  with column  $j$  defined as

$$\begin{aligned}\Pi_{0,E}^{0,x} \varphi_j(\boldsymbol{P}^E) &= \left( \boldsymbol{V}^E(:,1) \right)^T \boldsymbol{\Pi}_{0,E}^{0,x}(j) \\ \Pi_{0,E}^{0,y} \varphi_j(\boldsymbol{P}^E) &= \left( \boldsymbol{V}^E(:,1) \right)^T \boldsymbol{\Pi}_{0,E}^{0,y}(j) \\ \Pi_{0,E}^{0,z} \varphi_j(\boldsymbol{P}^E) &= \left( \boldsymbol{V}^E(:,1) \right)^T \boldsymbol{\Pi}_{0,E}^{0,z}(j)\end{aligned}\quad (\text{a.69})$$

### *Computation of the local stiffness matrix*

The evaluation of the approximated bilinear form  $\boldsymbol{a}_h^E$  defined in (a.19) requires the calculation of the two terms introduced in (a.20). In particular, the first term  $\boldsymbol{a}^{E,\nabla}$  can be then evaluated exploiting the introduced canonical basis function projections. Exploiting the expression in (a.69), it is possible to define the  $\boldsymbol{\epsilon}$  strain tensor respect to the canonical basis evaluated at the internal quadrature points. Each of the 6 components belongs to  $\mathbb{R}^{4n_{TE} \times 3n_{vE}}$ , and they are defined as rows of block-matrix of size  $4n_{TE} \times n_{vE}$ :

$$\begin{aligned}
\boldsymbol{\varepsilon}_{11} &= [\Pi_{0,E}^{0,x}\varphi(\mathbf{P}^E) \quad 0 \quad 0] \\
\boldsymbol{\varepsilon}_{21} &= \left[ \frac{1}{2}\Pi_{0,E}^{0,y}\varphi(\mathbf{P}^E) \quad \frac{1}{2}\Pi_{0,E}^{0,x}\varphi(\mathbf{P}^E) \quad 0 \right] \\
\boldsymbol{\varepsilon}_{22} &= [0 \quad \Pi_{0,E}^{0,y}\varphi(\mathbf{P}^E) \quad 0] \\
\boldsymbol{\varepsilon}_{31} &= \left[ \frac{1}{2}\Pi_{0,E}^{0,z}\varphi(\mathbf{P}^E) \quad 0 \quad \frac{1}{2}\Pi_{0,E}^{0,x}\varphi(\mathbf{P}^E) \right] \\
\boldsymbol{\varepsilon}_{32} &= \left[ 0 \quad \frac{1}{2}\Pi_{0,E}^{0,z}\varphi(\mathbf{P}^E) \quad \frac{1}{2}\Pi_{0,E}^{0,y}\varphi(\mathbf{P}^E) \right] \\
\boldsymbol{\varepsilon}_{33} &= [0 \quad 0 \quad \Pi_{0,E}^{0,z}\varphi(\mathbf{P}^E)]
\end{aligned} \tag{a.70}$$

The stress tensor, which depends linearly on the strain tensor, can be calculated substituting the expression below

$$\boldsymbol{\sigma}_{ij} = 2\mu\boldsymbol{\varepsilon}_{ij} + \lambda\text{tr}(\boldsymbol{\varepsilon})\delta_{ij} \quad \text{with } 1 \leq i, j \leq 3 \tag{a.71}$$

with

$$\lambda\text{tr}(\boldsymbol{\varepsilon}) = \text{diag}(\lambda)[\Pi_{0,E}^{0,x}\varphi(\mathbf{P}^E) \quad \Pi_{0,E}^{0,y}\varphi(\mathbf{P}^E) \quad \Pi_{0,E}^{0,z}\varphi(\mathbf{P}^E)] \tag{a.72}$$

It follows that the bilinear form  $\int_E \boldsymbol{\sigma}(\Pi_{0,E}^0 \nabla \varphi) : \boldsymbol{\varepsilon}(\Pi_{0,E}^0 \nabla \varphi) dE$  can be computed as

$$\sum_{i=1}^3 \left( \boldsymbol{\varepsilon}_{ij}^T \text{diag}(\mathbf{W}^E) \boldsymbol{\sigma}_{ij} + 2 \sum_{j=1}^{i-1} \boldsymbol{\varepsilon}_{ij}^T \text{diag}(\mathbf{W}^E) \boldsymbol{\sigma}_{ij} \right) \tag{a.73}$$

The stabilization term  $S^{E,\nabla}$  in (a.20) is evaluated defining as (Beirão da Veiga et al., 2014, 2013a; Gain et al., 2014)

$$\begin{aligned}
& S \left( (\mathbb{I} - \Pi_1^\nabla) \varphi_i, (\mathbb{I} - \Pi_1^\nabla) \varphi_j \right) \\
& := \sum_{k=1}^{n_{vE}} \chi_k((\mathbb{I} - \Pi_1^\nabla) \varphi_i) \chi_k((\mathbb{I} - \Pi_1^\nabla) \varphi_j)
\end{aligned} \tag{a.74}$$

Recalling that  $\chi_k(\varphi_i) = \delta_{ki}$  and that analogously to (a.44)  $\mathbf{D}_E \in \mathbb{R}^{n_{vE} \times n_{mE}}$  is defined as  $D_{Eij} = \chi_i(m_j)$

$$S^{E,\nabla} = (2\mu + \lambda) |h_E| (\mathbf{I} - \mathbf{D}_E \boldsymbol{\Pi}_1^{\nabla*})^T (\mathbf{I} - \mathbf{D}_E \boldsymbol{\Pi}_1^{\nabla*}) \tag{a.75}$$

$|h_E|$  is the diameter of the polyhedron.

Computation of the stiffness matrix is thus obtained summing up the two terms in (a.73) and (a.75)

*Computation of the forcing term*

At last, the computation of the forcing term requires the evaluation of the integral of each element of the element basis

$$\langle b_h, \varphi_i \rangle_E := - \int_E \nabla \cdot (\Delta p \mathbb{I}) \varphi_i dE \tag{a.76}$$

Applying divergence theorem and the L2-projectors it is possible to write

$$\langle b_h, \varphi_i \rangle_E = - \int_E \Delta p \nabla \varphi_i dE = - \int_E \Delta p \Pi_{0,E}^0 \nabla \varphi_i dE \tag{a.77}$$

Let us define  $\Delta \mathbf{p} \in \mathbb{R}^{4n_{TE} \times 1}$  as the pore pressure variation evaluated on the internal quadrature point of  $E$  that is supposed constant on the polyhedron. It follows that the forcing term results, evaluated respect to the VEM basis results in a 3-block vector

$$\boldsymbol{b}_h^E = \begin{bmatrix} \left( \Pi_{0,E}^{0,x} \varphi(\boldsymbol{P}^E) \right)^T (\Delta \boldsymbol{p} \circ \boldsymbol{W}^E) \\ \left( \Pi_{0,E}^{0,z} \varphi(\boldsymbol{P}^E) \right)^T (\Delta \boldsymbol{p} \circ \boldsymbol{W}^E) \\ \left( \Pi_{0,E}^{0,z} \varphi(\boldsymbol{P}^E) \right)^T (\Delta \boldsymbol{p} \circ \boldsymbol{W}^E) \end{bmatrix} \in \mathbb{R}^{3n_{vE} \times 1} \quad (\text{a.78})$$

# References

- A. Ferretti, C. Prati, F. Rocca, 2001. Permanent scatterers in SAR interferometry. *IEEE Trans. Geosci. Remote Sens.* 39, 8–20. <https://doi.org/10.1109/36.898661>
- Abbo, A.J., Lyamin, A.V., Sloan, S.W., Hambleton, J.P., 2011. A C2 continuous approximation to the Mohr-Coulomb yield surface. *Int. J. Solids Struct.* 48, 3001–3010.
- Ahmad, B., Alsaedi, A., Brezzi, F., Marini, L.D., Russo, A., 2013. Equivalent projectors for virtual element methods. *Comput. Math. Appl.* 66, 376–391. <https://doi.org/10.1016/j.camwa.2013.05.015>
- Andersen, O., Nilsen, H.M., Raynaud, X., 2017. Virtual element method for geomechanical simulations of reservoir models. *Comput. Geosci.* <https://doi.org/10.1007/s10596-017-9636-1>
- Atkinson, J., 1993. An Introduction to the Mechanics of Soils and Foundations: Through Critical State Soil Mechanics, McGraw-Hill international series in civil engineering. McGraw-Hill Book Company.
- Atkinson, K.E., 1989. An introduction to Numerical analysis. Wiley.
- Atlassian, 2021. Bitbucket | The Git solution for professional teams [WWW Document]. Bitbucket. URL <https://bitbucket.org/product> (accessed 7.1.21).
- Barnhill, R.E., Kersey, S.N., 1990. A marching method for parametric surface/surface intersection. *Comput. Aided Geom. Des.* 7, 257–280. [https://doi.org/10.1016/0167-8396\(90\)90035-P](https://doi.org/10.1016/0167-8396(90)90035-P)
- Beirão da Veiga, L., Brezzi, F., Cangiani, A., G, M., Marini, L.D., Russo, A., 2013a. Basic principles of virtual element methods. *Math. Models Methods Appl. Sci.* 23, 199–214. <https://doi.org/10.1142/S0218202512500492>
- Beirão da Veiga, L., Brezzi, F., Marini, L.D., Russo, A., 2016a. Virtual Element Implementation for General Elliptic Equations, in: Barrenechea, G.R., Brezzi, Franco, Cangiani, A., Georgoulis, E.H. (Eds.), Building Bridges: Connections and Challenges in Modern Approaches to Numerical Partial Differential Equations. Springer International Publishing, Cham, pp. 39–71. [https://doi.org/10.1007/978-3-319-41640-3\\_2](https://doi.org/10.1007/978-3-319-41640-3_2)
- Beirão da Veiga, L., Brezzi, F., Marini, L.D., Russo, A., 2016b. Virtual Element Method for general second-order elliptic problems on polygonal meshes.

- Math. Models Methods Appl. Sci. 26, 729–750. <https://doi.org/10.1142/S0218202516500160>
- Beirão da Veiga, L., Brezzi, F., Marini, L.D., Russo, A., 2014. The Hitchhiker's Guide to the Virtual Element Method. *Math. Models Methods Appl. Sci.* 24, 1541–1573. <https://doi.org/10.1142/S021820251440003X>
- Beirão da Veiga, L., Dassi, F., Russo, A., 2017. High-order Virtual Element Method on polyhedral meshes. *Comput. Math. Appl.* <https://doi.org/10.1016/j.camwa.2017.03.021>
- Beirão da Veiga, L., F, B., D, M.L., 2013b. Virtual Elements for Linear Elasticity Problems. *SIAM J. Numer. Anal.* 51, 794–812. <https://doi.org/10.1137/120874746>
- Benedetto, M.F., Berrone, S., Borio, A., 2016. The Virtual Element Method for Underground Flow Simulations in Fractured Media, in: Ventura, G., Benvenuti, E. (Eds.), *Advances in Discretization Methods: Discontinuities, Virtual Elements, Fictitious Domain Methods*. Springer International Publishing, Cham, pp. 167–186. [https://doi.org/10.1007/978-3-319-41246-7\\_8](https://doi.org/10.1007/978-3-319-41246-7_8)
- Benetatos, C., Codegone, G., Ferraro, C., Mantegazzi, A., Rocca, V., Tango, G., Trillo, F., 2020. Multidisciplinary Analysis of Ground Movements: An Underground Gas Storage Case Study. *Remote Sens.* 12. <https://doi.org/10.3390/rs12213487>
- Benetatos, C., Málek, J., Verga, F., 2013. Moment tensor inversion for two micro-earthquakes occurring inside the Háje gas storage facilities, Czech Republic. *J. Seismol.* 17, 557–577. <https://doi.org/10.1007/s10950-012-9337-0>
- Benetatos, C., Salina Borello, E., Peter, C., Rocca, V., Romagnoli, R., 2019. Considerations on energy transition. *GEAM Geoing. Ambient. E MINERARIA* 158, 26–31.
- Berardino, P., Costantini, M., Franceschetti, G., Iodice, A., Pietranera, L., Rizzo, V., 2003. Use of differential SAR interferometry in monitoring and modelling large slope instability at Maratea (Basilicata, Italy). *Remote Sens. Monit. Landslides* 68, 31–51. [https://doi.org/10.1016/S0013-7952\(02\)00197-7](https://doi.org/10.1016/S0013-7952(02)00197-7)
- Biot, M.A., 1941. General Theory of Three-Dimensional Consolidation. *J. Appl. Phys.* 12, 155–164. <https://doi.org/10.1063/1.1712886>
- Bouteca, M., Guéguen, Y., 1999. Mechanical Properties of Rocks: Pore Pressure and Scale Effects. *Oil Gas Sci. Technol. - Rev IFP* 54, 703–714. <https://doi.org/10.2516/ogst:1999060>
- Brady, B.H.G., 2012. Rock Mechanics: For Underground Mining. Springer Netherlands.

- Brown, E.T., Hoek, E., 1978. Trends in relationships between measured in-situ stresses and depth. *Int. J. Rock Mech. Min. Sci. Geomech. Abstr.* 15, 211–215. [https://doi.org/10.1016/0148-9062\(78\)91227-5](https://doi.org/10.1016/0148-9062(78)91227-5)
- Capasso, G., Mantica, S., 2006. Numerical Simulation of Compaction and Subsidence Using ABAQUS.
- Cazzini, F., Zotto, O.D., Fantoni, R., Ghielmi, M., Ronchi, P., Scotti, P., 2015. Oil and Gas in the Adriatic Foreland, Italy. *J. Pet. Geol.* 38, 255–279. <https://doi.org/10.1111/jpg.12610>
- Codegone, G., Rocca, V., Verga, F., Coti, C., 2016. Subsidence Modeling Validation Through Back Analysis for an Italian Gas Storage Field. *Geotech. Geol. Eng.* 34, 1749–1763. <https://doi.org/10.1007/s10706-016-9986-9>
- Coti, C., Rocca, V., Sacchi, Q., 2018. Pseudo-Elastic Response of Gas Bearing Clastic Formations: An Italian Case Study. *Energies* 11. <https://doi.org/10.3390/en11092488>
- Coulomb, C.A., 1776. *Essai sur une application des règles de maximis & minimis à quelques problèmes de statique, relatifs à l'architecture*. Paris: De l'Imprimerie Royale.
- Cuss, R.J., Rutter, E.H., Holloway, R.F., 2003. The application of critical state soil mechanics to the mechanical behaviour of porous sandstones. *Int. J. Rock Mech. Min. Sci.* 40, 847–862. [https://doi.org/10.1016/S1365-1609\(03\)00053-4](https://doi.org/10.1016/S1365-1609(03)00053-4)
- Da, T.K.F., 2021. 2D Alpha Shapes, in: CGAL User and Reference Manual. CGAL Editorial Board.
- Davis, R.O., Selvadurai, A.P.S., 2002. Plasticity and Geomechanics. Cambridge University Press, Cambridge. <https://doi.org/10.1017/CBO9780511614958>
- DIANA FEA, 2021. DIANA Finite Element Analysis [WWW Document]. URL <https://dianafea.com/> (accessed 6.18.21).
- Donda, F., Civile, D., Forlin, E., Volpi, V., Zecchin, M., Gordini, E., Merson, B., De Santis, L., 2013. The northernmost Adriatic Sea: A potential location for CO<sub>2</sub> geological storage? *Spec. Issue Geol. Periadriatic Basin Adriat. Sea, Special Issue: The Geology of the Periadriatic Basin and of the Adriatic Sea* 42, 148–159. <https://doi.org/10.1016/j.marpetgeo.2012.10.006>
- Drucker, D.C., 1956. On Uniqueness in the theory of plasticity. *Q. Appl. Math.* 14, 35–42.
- Emerson, 2021. SKUA-GOCAD Software Suite [WWW Document]. URL <https://www.pdgm.com/products/skua-gocad/> (accessed 6.18.21).

- European Commission Website, 2016. 2030 climate & energy framework [WWW Document]. Clim. Action - Eur. Comm. URL [https://ec.europa.eu/clima/policies/strategies/2030\\_en](https://ec.europa.eu/clima/policies/strategies/2030_en)
- Ferronato, M., Castelletto, N., Gambolati, G., Janna, C., Teatini, P., 2013. II cycle compressibility from satellite measurements. *Géotechnique* 63, 479–486. <https://doi.org/10.1680/geot.11.P.149>
- Filip, D., Magedson, R., Markot, R., 1986. Surface algorithms using bounds on derivatives. *Comput. Aided Geom. Des.* 3, 295–311. [https://doi.org/10.1016/0167-8396\(86\)90005-1](https://doi.org/10.1016/0167-8396(86)90005-1)
- Firme, P.A.L.P., Quispe, R.Q., Roehl, D., Oliveira, M.F., Parotidis, M., Glassborow, B., 2014. A Comparative Study of Constitutive Models for Reservoir Compaction and Surface Subsidence.
- Fischer, K., Gärtner, B., Schönher, S., Wessendorp, F., 2021. Linear and Quadratic Programming Solver, in: CGAL User and Reference Manual. CGAL Editorial Board.
- Fjær, E., Holt, R.M., Horsrud, P., Risnes, R., Raaen, A.M., 2008. Petroleum Related Rock Mechanics, Developments in Petroleum Science. Elsevier Science & Technology.
- Flötotto, J., 2021. 2D and Surface Function Interpolation, in: CGAL User and Reference Manual. CGAL Editorial Board.
- Fokker, P.A., Orlic, B., 2007. Semi-Analytic Modelling of Subsidence. *Math. Geol.* 38, 565–589. <https://doi.org/10.1007/s11004-006-9034-z>
- Gain, A.L., Talischi, C., Paulino, G.H., 2014. On the Virtual Element Method for three-dimensional linear elasticity problems on arbitrary polyhedral meshes. *Comput. Methods Appl. Mech. Eng.* 282, 132–160. <https://doi.org/10.1016/j.cma.2014.05.005>
- Geertsma, J., 1973a. Land Subsidence Above Compacting Oil and Gas Reservoirs. *J. Pet. Technol.* 25, 734–744. <https://doi.org/10.2118/3730-PA>
- Geertsma, J., 1973b. A basic theory of subsidence due to reservoir compaction: The homogeneous case. *Verh. Kon Ned Geol Mijnbouwk Gen* 28, 43–62.
- Ghielmi, M., Minervini, M., Nini, C., Rogledi, S., Rossi, M., Vignolo, A., 2010. Sedimentary and tectonic evolution in the eastern Po-Plain and northern Adriatic Sea area from Messinian to Middle Pleistocene (Italy). *RENDICONTI LINCEI* 21, 131–166. <https://doi.org/10.1007/s12210-010-0101-5>
- Gitlab inc., 2021. GitLab 14.0 [WWW Document]. URL <https://about.gitlab.com/releases/2021/06/22/gitlab-14-0-released/> (accessed 7.1.21).

- GitLab inc., 2021. Set up Automated Continuous Integration (CI) Systems with GitLab [WWW Document]. URL <https://about.gitlab.com/stages-devops-lifecycle/continuous-integration/> (accessed 7.1.21).
- Gockenbach, M.S., 2006. Understanding and implementing the Finite Element Method, Other Titles in Applied Mathematics. Society for Industrial and Applied Mathematics.
- Graphics Gems IV, 1994. . Elsevier. <https://doi.org/10.1016/C2013-0-07360-4>
- Gringarten, E.J., Arpat, G.B., Haouesse, M.A., Dutranois, A., Deny, L., Jayr, S., Tertois, A.-L., Mallet, J.-L., Bernal, A., Nghiem, L.X., 2008. New Grids for Robust Reservoir Modeling. <https://doi.org/10.2118/116649-MS>
- Guennebaud, G., Jacob, B., others, 2010. Eigen v3.
- Itasca Consulting Group, 2021. FLAC [WWW Document]. URL <http://www.itascacg.com/software/FLAC> (accessed 6.18.21).
- Jing, L., Hudson, J.A., 2002. Numerical methods in rock mechanics. *Numer. Methods Rock Mech.* 39, 409–427. [https://doi.org/10.1016/S1365-1609\(02\)00065-5](https://doi.org/10.1016/S1365-1609(02)00065-5)
- K. Ponting, D., 1989. Corner Point Geometry in Reservoir Simulation. Presented at the ECMOR I - 1st European Conference on the Mathematics of Oil Recovery, European Association of Geoscientists & Engineers, Cambridge, UK. <https://doi.org/10.3997/2214-4609.201411305>
- Kitware, 2021. CMake [WWW Document]. URL <https://cmake.org/> (accessed 7.1.21).
- Kitware, I., 2021. VTK: vtkUnstructuredGrid Class Reference 8.2 [WWW Document]. URL <https://vtk.org/doc/nightly/html/classvtkUnstructuredGrid.html#details> (accessed 6.22.21).
- Lamberti, A., Garino, N., Sacco, A., Bianco, S., Chiodoni, A., Gerbaldi, C., 2015. As-grown vertically aligned amorphous TiO<sub>2</sub> nanotube arrays as high-rate Li-based micro-battery anodes with improved long-term performance. *Electrochimica Acta* 151, 222–229. <https://doi.org/10.1016/j.electacta.2014.10.150>
- Lancellotta, R., 2012. Geotecnica, IV. ed. Zanichelli.
- LANL, 2016. LaGriT [WWW Document]. URL <https://lagrit.lanl.gov/> (accessed 6.18.21).
- Lie, K., Krogstad, S., Ligaarden, I.S., Natvig, J.R., Nilsen, H.M., Skaflestad, B., 2012. Open-source MATLAB implementation of consistent discretisations on complex grids. *Comput. Geosci.* 16, 297–322. <https://doi.org/10.1007/s10596-011-9244-4>

- Lie, K.-A., 2019. An Introduction to Reservoir Simulation Using MATLAB/GNU Octave: User Guide for the MATLAB Reservoir Simulation Toolbox (MRST). Cambridge University Press, Cambridge. <https://doi.org/10.1017/9781108591416>
- Lipnikov, K., Manzini, G., Shashkov, M., 2014. Mimetic finite difference method. *Phys.-Compat. Numer. Methods* 257, 1163–1227. <https://doi.org/10.1016/j.jcp.2013.07.031>
- Luenberger, D.G., Ye, Y., others, 1984. Linear and nonlinear programming. Springer.
- Mallet, J.-L., 2004. Space-Time Mathematical Framework for Sedimentary Geology. *Math. Geol.* 36, 1–32. <https://doi.org/10.1023/B:MATG.0000016228.75495.7c>
- Malvić, T., Đureković, M., Šikonja, Ž., Čogelja, Z., Ilijaš, T., Kruljac, I., 2011. Exploration and production activities in northern Adriatic Sea (Croatia), successful joint venture INA (Croatia) and ENI (Italy). *Nafta* 62, 287, 293–292, 296.
- Mao, P., Shimada, H., Hamanaka, A., Wahyudi, S., Oya, J., Naung, N., others, 2020. Three-Dimensional Analysis of Gate-Entry Stability in Multiple Seams Longwall Coal Mine Under Weak Rock Conditions. *Earth Sci. Res.* 9, 1–72.
- Mase, G.T., Mase, G.E., 1999. Continuum Mechanics for Engineers, Computational Mechanics and Applied Analysis. CRC-Press.
- Matos, C.R., Carneiro, J.F., Silva, P.P., 2019. Overview of Large-Scale Underground Energy Storage Technologies for Integration of Renewable Energies and Criteria for Reservoir Identification. *J. Energy Storage* 21, 241–258. <https://doi.org/10.1016/j.est.2018.11.023>
- Mattax, C.C., Dalton, R.L., Engineers (U.S.), S. of P., 1990. Reservoir Simulation, Henry L. Doherty series. Henry L. Doherty Memorial Fund of AIME, Society of Petroleum Engineers.
- Mindlin, R.D., 1936. Force at a Point in the Interior of a Semi-Infinite Solid. *Physics* 7, 195–202. <https://doi.org/10.1063/1.1745385>
- Mindlin, R.D., Cheng, D.H., 1950. Thermoelastic Stress in the Semi-Infinite Solid. *J. Appl. Phys.* 21, 931–933. <https://doi.org/10.1063/1.1699786>
- Mingw-w64, 2021. Mingw-w64 - GCC for Windows 64 & 32 bits [mingw-w64] [WWW Document]. URL <http://mingw-w64.org/doku.php> (accessed 7.27.21).
- Mission Innovation, 2021. URL <http://mission-innovation.net/> (accessed 7.1.21).

- Montone, P., Mariucci, M.T., 2015. P-wave Velocity, Density, and Vertical Stress Magnitude Along the Crustal Po Plain (Northern Italy) from Sonic Log Drilling Data. *Pure Appl. Geophys.* 172, 1547–1561. <https://doi.org/10.1007/s00024-014-1022-5>
- Morita, N., Whitfill, D.L., Nygaard, O., Bale, A., 1989. A Quick Method To Determine Subsidence, Reservoir Compaction, and In-Situ Stress Induced by Reservoir Depletion. *J. Pet. Technol.* 41, 71–79. <https://doi.org/10.2118/17150-PA>
- Nagel, N.B., 2001. Compaction and subsidence issues within the petroleum industry: From wilmington to ekofisk and beyond. *Phys. Chem. Earth Part Solid Earth Geod.* 26, 3–14. [https://doi.org/10.1016/S1464-1895\(01\)00015-1](https://doi.org/10.1016/S1464-1895(01)00015-1)
- Nakaten, B., Kempka, T., 2014. Workflow for fast and efficient integration of Petrel-based fault models into coupled hydro-mechanical TOUGH2-MP - FLAC3D simulations of CO<sub>2</sub> storage, in: 12th International Conference on Greenhouse Gas Control Technologies, GHGT-12. Presented at the 12th International Conference on Greenhouse Gas Control Technologies, GHGT-12, Austin, Texas US, pp. 3576–3581. <https://doi.org/10.1016/j.egypro.2014.11.387>
- Neto, E.A. de S., Peric, D., Owen, D.R.J., 2008. Computational Methods for Plasticity: Theory and Applications. Wiley.
- Park, C.-H., Shinn, Y.J., Park, Y.-C., Huh, D.-G., Lee, S.K., 2014. PET2OGS: Algorithms to link the static model of Petrel with the dynamic model of OpenGeoSys. *Comput. Geosci.* 62, 95–102. <https://doi.org/10.1016/j.cageo.2013.09.014>
- Park, J.-S., Oh, S.-J., 2012. A New Concave Hull Algorithm and Concaveness Measure for n-dimensional Datasets. *J. Inf. Sci. Eng.* 28, 587–600.
- Patrikalakis, N.M., Maekawa, T., Ko, K.H., Mukundan, H., 2004. Surface to Surface Intersections. *Comput.-Aided Des. Appl.* 1, 449–457. <https://doi.org/10.1080/16864360.2004.10738287>
- Pellerin, J., Botella, A., Bonneau, F., Mazuyer, A., Chauvin, B., Lévy, B., Caumon, G., 2017. RINGMesh: A programming library for developing mesh-based geomodeling applications. *Comput. Geosci.* 104, 93–100. <https://doi.org/10.1016/j.cageo.2017.03.005>
- Rodrigues, E.M.G., Godina, R., Santos, S.F., Bazuayehu, A.W., Contreras, J., Catalão, J.P.S., 2014. Energy storage systems supporting increased penetration of renewables in islanded systems. *Energy* 75, 265–280. <https://doi.org/10.1016/j.energy.2014.07.072>

- Rubin, E., Meyer, L., de Coninck, H., 2005. IPCC Special Report on Carbon Dioxide Capture and Storage: Prepared by Working Group III of the Intergovernmental Panel on Climate Change. Intergov. Panel Clim. Change Camb. UK.
- S. Kwon, W.J. Cho, J.O. Lee, 2013. An analysis of the thermal and mechanical behavior of engineered barriers in a high-level radioactive waste repository. *Nucl. Eng. Technol.* 45, 41–52. <https://doi.org/10.5516/NET.06.2012.015>
- Saad, Y., 2003. Iterative Methods for Sparse Linear Systems, Other Titles in Applied Mathematics. Society for Industrial and Applied Mathematics. <https://doi.org/10.1137/1.9780898718003>
- Scalia, A., Zaccagnini, P., Armandi, M., Latini, G., Versaci, D., Lanzio, V., Varzi, A., Passerini, S., Lamberti, A., 2021. Tragacanth Gum as Green Binder for Sustainable Water-Processable Electrochemical Capacitor. *ChemSusChem* 14, 356–362. <https://doi.org/10.1002/cssc.202001754>
- Schirra, S., 2008. How Reliable Are Practical Point-in-Polygon Strategies?, in: *Lect. Note. Comput. Sci.* pp. 744–755. [https://doi.org/10.1007/978-3-540-87744-8\\_62](https://doi.org/10.1007/978-3-540-87744-8_62)
- Schlumberger, 2020a. Petrel - E&P Software Platform [WWW Document]. URL <https://www.software.slb.com/products/petrel> (accessed 6.18.21).
- Schlumberger, 2020b. VISAGE [WWW Document]. URL [/products/visage](#) (accessed 6.18.21).
- Schlumberger, 2020c. ECLIPSE - Industry Reference Reservoir Simulator [WWW Document]. URL <https://www.software.slb.com/products/eclipse> (accessed 6.18.21).
- Schlumberger, 2020d. ECLIPSE 2020.4 Reference Manual.
- Schofield, A.N., Wroth, P., 1968. Critical State Soil Mechanics, European civil engineering series. McGraw-Hill.
- Schroeder, W., Martin, K., Lorensen, B., Kitware, I., 2006. The Visualization Toolkit: An Object-oriented Approach to 3D Graphics. Kitware.
- SEADOG center, 2017. Attività di ricerca e di supporto istituzionale per lo studio di approcci innovativi e per la definizione di linee guida in relazione alla tematica della sicurezza della produzione da giacimenti di idrocarburi situati a mare.
- Sen, B., 1951. Note on the stresses produced by nuclei of thermo-elastic strain in a semi-infinite elastic solid. *Q. Appl. Math.* 8, 365–369. <https://doi.org/10.1090/qam/37717>
- Sentís, M.L., Gable, C.W., 2017. Coupling LaGrit unstructured mesh generation and model setup with TOUGH2 flow and transport: A case study. *TOUGH*

- Symp. 2015 Recent Enhanc. TOUGH Fam. Codes Coupled Flow Geomech. Process. Model. 108, 42–49. <https://doi.org/10.1016/j.cageo.2017.06.012>
- Serazio, C., Tamburini, M., Verga, F., Berrone, S., 2021. Geological Surface Reconstruction from 3D point clouds. MethodsX 101398. <https://doi.org/10.1016/j.mex.2021.101398>
- Shewchuk, J.R., 1996. Triangle: Engineering a 2D Quality Mesh Generator and Delaunay Triangulator, in: Lin, M.C., Manocha, D. (Eds.), Applied Computational Geometry Towards Geometric Engineering: FCRC'96 Workshop, WACG'96 Philadelphia, PA, May 27–28, 1996 Selected Papers. Springer Berlin Heidelberg, Berlin, Heidelberg, pp. 203–222. <https://doi.org/10.1007/BFb0014497>
- Si, H., 2020. TetGen: A quality tetrahedral mesh generator and a 3D Delaunay triangulator (Version 1.6 — User's Manual).
- Si, H., 2015. TetGen, a Delaunay-Based Quality Tetrahedral Mesh Generator. ACM Trans Math Softw 41. <https://doi.org/10.1145/2629697>
- SINTEF, 2021. MRST Project [WWW Document]. URL <https://www.sintef.no/projectweb/mrst/> (accessed 6.21.21).
- Sperner, B., Müller, B., Heidbach, O., Delvaux, D., Reinecker, J., Fuchs, K., 2003. Tectonic stress in the Earth's crust: advances in the World Stress Map project. Geol. Soc. Lond. Spec. Publ. 212, 101. <https://doi.org/10.1144/GSL.SP.2003.212.01.07>
- Sysala, S., Cermak, M., Koudelka, T., Kruis, J., Zeman, J., Blaheta, R., 2017. Subdifferential-based implicit return-mapping operators in computational plasticity. ZAMM - J. Appl. Math. Mech. Z. Für Angew. Math. Mech. 96, 1318–1338. <https://doi.org/10.1002/zamm.201500305>
- Taherynia, M.H., Fatemi Aghda, S.M., Fahimifar, A., 2016. In-Situ Stress State and Tectonic Regime in Different Depths of Earth Crust. Geotech. Geol. Eng. 34, 679–687. <https://doi.org/10.1007/s10706-016-9978-9>
- Teatini, P., Castelletto, N., Ferronato, M., Gambolati, G., Janna, C., Cairo, E., Marzorati, D., Colombo, D., Ferretti, A., Baglioni, A., Bottazzi, F., 2011. Geomechanical response to seasonal gas storage in depleted reservoirs: A case study in the Po River basin, Italy. J. Geophys. Res. Earth Surf. 116. <https://doi.org/10.1029/2010JF001793>
- Teatini, Pietro, Gambolati, G., Ferronato, M., Settari, A. (Tony), Walters, D., 2011. Land uplift due to subsurface fluid injection. J. Geodyn. 51, 1–16. <https://doi.org/10.1016/j.jog.2010.06.001>
- Terzaghi, K., 1936. The Shearing Resistance of Saturated Soils and the Angle between the Planes of Shear. Presented at the 1st International Conference on Soil Mechanics and Foundation Engineering, pp. 54–56.

- The CGAL Project, 2021. CGAL User and Reference Manual, 5.2.2. ed. CGAL Editorial Board.
- The Paris Agreement | UNFCCC [WWW Document], 2016. . U. N. Framew. Conv. Clim. Change. URL <https://unfccc.int/process-and-meetings/the-paris-agreement/the-paris-agreement>
- The Qt Company, 2021a. Signals & Slots | Qt Core 5.15.5 [WWW Document]. URL <https://doc.qt.io/qt-5/signalsandslots.html> (accessed 7.1.21).
- The Qt Company, 2021b. Multithreading Technologies in Qt | Qt 5.15 [WWW Document]. URL <https://doc.qt.io/qt-5/threadstechologies.html> (accessed 7.1.21).
- The Qt Company, 2021c. Embedded Software Development Tools | Cross Platform IDE | Qt Creator [WWW Document]. URL <https://www.qt.io/product/development-tools> (accessed 7.1.21).
- Velić, J., Malvić, T., 2011. Depositional conditions during Pliocene and Pleistocene in Northern Adriatic and possible lithostratigraphic division of these rocks. *Nafta* 62, 25, 33–32, 38.
- Velić, J., Malvić, T., Cvetković, M., Velić, I., 2015. Stratigraphy and Petroleum Geology of the Croatian part of the Adriatic basin. *J. Pet. Geol.* 38, 281–300. <https://doi.org/10.1111/jpg.12611>
- Verga, F., 2018. What's Conventional and What's Special in a Reservoir Study for Underground Gas Storage. *Energies* 11. <https://doi.org/10.3390/en11051245>
- Wood, D.M., 1991. Soil Behaviour and Critical State Soil Mechanics. Cambridge University Press.
- Zang, A., Stephansson, O., 2009. Stress Field of the Earth's Crust. Springer Netherlands.
- Zang, A., Stephansson, O., Heidbach, O., Janouschkowetz, S., 2012. World Stress Map Database as a Resource for Rock Mechanics and Rock Engineering. *Geotech. Eng.* 30, 625–646. <https://doi.org/10.1007/s10706-012-9505-6>
- Zienkiewicz, O.C., Valliappan, S., King, I.P., 1969. Elasto-plastic solutions of engineering problems ‘initial stress’, finite element approach. *Int. J. Numer. Methods Eng.* 1, 75–100. <https://doi.org/10.1002/nme.1620010107>